PHD

Rotor Vibration Reduction and Control via Flexibly-Mounted Internal-Stator Magnetic Bearings

Lusty, Christopher

Award date:
2016

Awarding institution:
University of Bath

Rotor Vibration Reduction and Control via Flexibly-Mounted, Internal-Stator Magnetic Bearings

submitted by

Chris Lusty

for the degree of Doctor of Philosophy

of the

University of Bath

Department of Mechanical Engineering

September 2016

Summary

Consideration has been given to the question of reducing and controlling vibration occurring in active rotor systems. The subject is of importance due to the widespread use of rotors within many engineering applications, coupled with the fact that one of the most problematic issues faced by designers of rotor systems is that of vibration. Furthermore, it is identified that improvements in the ability to handle vibration in high speed rotor systems will open up new opportunities for novel machine design and associated new capabilities.

An overview of the history of rotor dynamics as a field is provided, highlighting both fundamental early work on the topic, as well as a range of research done with specific application to rotor vibration control.

A novel design of an active rotor-vibration-reduction system is then proposed, consisting of a hollow rotor coupled to a flexible internal secondary shaft via magnetic bearings. The unique features and benefits of this design are outlined, together with some numerical modelling of the vibration behaviour of such a system.

The project required the design and fabrication of a bespoke test rig, and details of this process and the resulting rig are discussed. Special attention is given to the design of the magnetic bearings of the system, which employ a soft magnetic composite material and a novel, internal-stator, homopolar geometry.

The test rig was run, and two different control strategies for the magnetic bearings were explored for the purposes of achieving vibration reduction - one a traditional PID method, and the other a model-based H_∞ technique. A range of results describing the behaviour of the system under each of these control systems - as well as in the uncontrolled state - is presented.

It is seen that the H_∞ controller can deliver substantial vibration reduction performance, and thereby the capability of the novel system topology for its designed purpose is proved.

Acknowledgements

This thesis serves as the chronicle of a course of research undertaken in the Department of Mechanical Engineering at the University of Bath between September 2012 and September 2016.

The project could not have been completed without the advice, support and help of a number of people, to all of whom I am extremely grateful.

To my main supervisor, Patrick Keogh, despite an enduring inability to remember my name, I am deeply indebted for an eclectic catalogue of engaging and amusing anecdotes, a quantity of coffee sufficient to support a medium-sized Peruvian coffee plantation for a year, and a number of quality film recommendations. The occasional passing thought on a technical subject was always equally welcome, even when confidently justified with the phrase "Trust me, I've never done it before".

Many thanks must also go to Necip Sahinkaya for his advice and guidance as my secondary supervisor during the early part of the project, as well as for providing worthy content for a number of Patrick's anecdotes.

The contribution of the technical support staff of the department can hardly be overstated. A particular mention is due to Paul Griffiths, who became chief fabricator for the majority of the test rig, for an eternally cheerful disposition and a real dedication to seeing the job through, despite uncounted redesigns, remakes and unexpected problems along the way. On this topic, thanks are also due to Paul Frith, on whose ingeniously simple yet effective idea the final test rig assembly is based.

My sincere gratitude also goes to Alan Jeffries, Clare Ball and Vijay Rajput, for each providing invaluable support and advice at various times during the project and generally "making things work", usually in spite of my woeful naivety and misguided optimism.

To my colleagues at the Technical University of Denmark, particularly Jonas Lauridsen, his supervisor Ilmar Santos and their group, and I'm grateful both for their technical contribution which lies behind the parameter identification work in this project, and for hosting my to visit to Copenhagen in May 2016.

It is gratefully acknowledged that the project was financially supported by a studentship provided by the James Dyson Foundation.

Contents

Chapter 1

Introduction

Across the modern engineering landscape, the use of rotating shafts for the transmission and conversion of power is ubiquitous. A rotating shaft may be employed in a "purely mechanical" application - such as transmitting torque from one location to another - or perhaps more commonly in combination with a working fluid, wherein the rotor is engaged in transferring power to and/or from the fluid. Examples of rotating machinery applications can be found in almost every engineering discipline, from the gas turbines of aircraft and power stations to the large scale pumps and compressors used in the petrochemical industry.

One of the most important issue that must be addressed while designing a system using rotors, regardless of application, is that of vibration. While there are numerous potential causes of vibration in rotating machinery, one stands pre-eminent as far the most common issue to be overcome: rotor unbalance. When a body rotates, if its centre of mass is not *exactly* aligned with its axis of rotation, the object will be subject to periodic forcing action by the out of balance mass, which causes the body to vibrate. In real world situations, nothing is ever exactly balanced - even in components designed with perfect rotational symmetry, manufacturing and assembly errors will always be present to some degree, and thus unbalance will always be introduced. In many applications, the vibration caused by this effect is so small as to be negligible. However, in other situations, the magnitude of the vibration can become so large as to cause catastrophic machine failure. In these situations, techniques to reduce the vibration to acceptable levels must be employed.

In dealing with rotor vibrations, an important distinction is made between two classifications of rotor; from an analysis point of view, rotors may be considered either as **rigid** bodies or as **flexible** bodies. Which of these two classifications applies for a given rotor is dependent on its properties, and on the operating conditions of its particular application. Operating speed especially is a key factor in determining whether a rotor is considered as rigid or flexible; generally speaking, almost all rotors behave rigidly at low speeds, and then as speed increases,

there comes a point (or speed) where they must be considered flexible. This transition speed is a function of a rotor's properties (e.g. geometry, material etc.) and loading, and thus is different for every rotor.

Controlling vibration in rotors that satisfy the conditions for rigid body definition is more or less trivial - the techniques are well understood and common industrial practice. Conversely, vibration control in rotors that behave flexibly is very difficult, and current technology for doing this is far from comprehensive.

With the progress of technology, it is inevitable that more and more machines will benefit from being able to employ rotors that behave flexibly. This is essentially a consequence of requiring machines to give a higher power density. Power density is a measure of power per unit size, so to get greater power out of the same (or smaller) sized rotor, it is necessary for the rotor to spin faster, pushing it towards flexible behaviour.

Thus the key motivation for this research project has been the potential to find a new technique which may allow more rotating machinery of the future to use high-speed, flexible rotors as a means of achieving smaller, lighter, higher performance designs, with the myriad benefits associated with such progress.

1.1 Applications and Research Impact

As stated above, the ultimate motivation for improving high speed rotor capabilities lies in opening up possibilities for new and improved machine design. Here, a brief overview is given of some of the technology that stands to benefit from such progress. Figures 1.1 and 1.2 depict a few such rotor applications, particularly where high speeds and vibration limitation are considerable factors.

One of the key industrial uses of rotating systems is in the field of turbo-machinery, particularly in the petrochemical and electricity generation industries. Such machines routinely operate supercritically, and therefore vibration management is of paramount importance to them. Machines of this type tend to run non-stop for weeks, months or even years at a time, and lie at the heart of processes critical to modern society, and representing enormous financial interest. Techniques, therefore, which can offer improved vibration handling, improved system longevity and reliability, improved economy or the possibility for improved system design are of great interest to the field.

One very current rotor system research area is in the field of flywheel energy storage devices. A number of commercial providers of such systems already exist, and they tend to find themselves in strong competition with alternative energy storage solutions - chiefly battery technology. In order to stay competitive, it is vital that flywheel technology continues to innovate, especially in the arena of power density; indeed given the squared relationship between rotational speed of

a flywheel and energy stored, the motivation for enabling higher speed operation is clear.

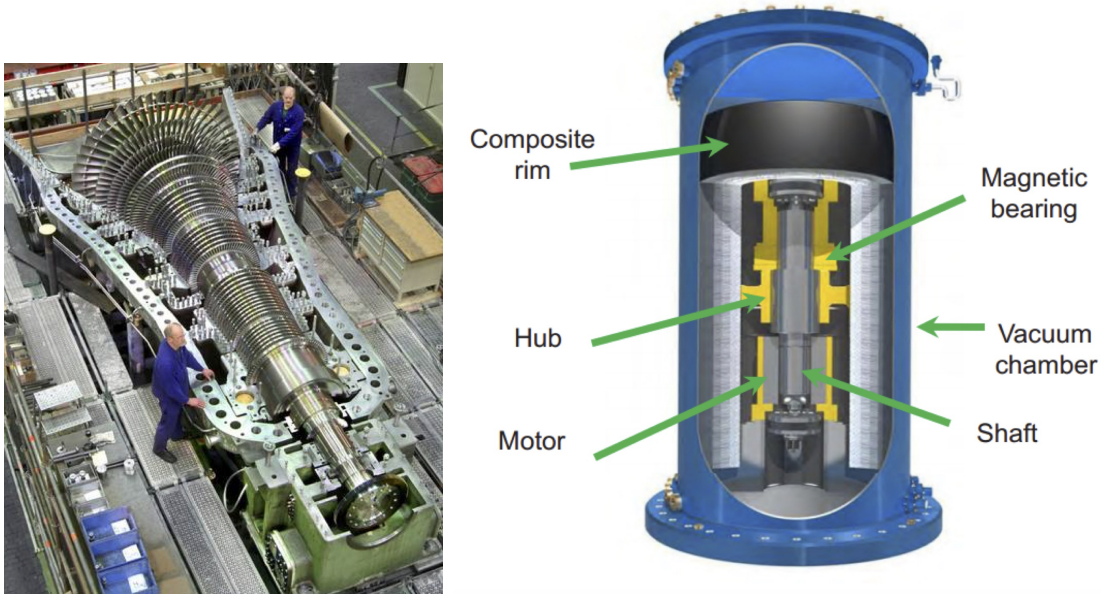

(a) (b)

Figure 1.1: Examples of rotor applications (a) large-scale steam turbine *Image courtesy: MAN SE*, (b) flywheel energy storage device *Image courtesy: Beacon POWER*

Another area of interest for rotor vibration reduction techniques may be machine tool spindles for high-speed, high-precision manufacturing tasks. In such an application the reduction of vibration has very obvious benefits in terms of the quality and precision of manufactured parts.

There again, in terms of vibration reduction opening possibilities in novel technologies, the micro-turbine presents an interesting study. This is essentially a gas turbine such as may be found in power generation and propulsive applications, but on a far smaller scale; they have promising prospects for use in distributed power generation systems (with associated potential for very substantial energy efficiency gains over traditional centralised power generation), as well as in emerging applications such as electric vehicles. Currently, the power density of available micro-turbines is not sufficient to stimulate significant market uptake - the advantages, then, of these engines being able to operate at higher speeds translate to considerable potential advances in other fields.

Indeed, a similar reasoning may be applied to many rotational devices used in the transport industry, particularly in aerospace applications - the greater the power density that can be achieved for any component, the smaller (and therefore lighter) it can be made. In areas where weight is critical for efficiency, this offers great prospective benefit. As a matter of fact, more-than-passing interest has been shown in the possibility of employing magnetic bearings in aircraft engines [1, 2] , and there is no question that such a design offers substantial performance

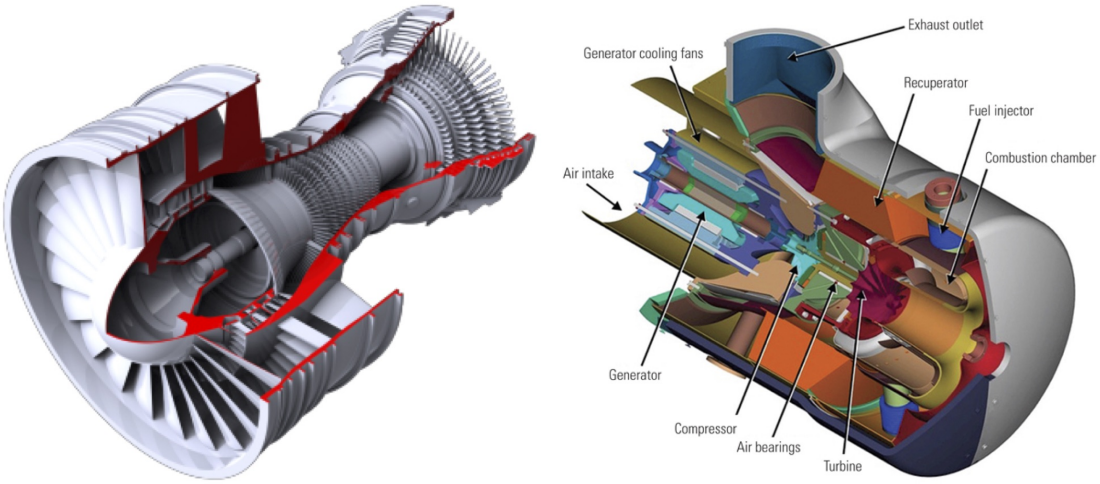

(a) (b)

Figure 1.2: Examples of rotor applications (a) gas turbine aircraft engine *Image courtesy: isromac-isimet.univ-lille1.fr*, (b) micro-turbine *Image courtesy: powermag.com*

benefits, not least in the field of vibration reduction. For now, safety considerations prevent such an application, but there is every possibility that new, improved techniques may one day make this a reality.

It is apparent, then, that techniques for the reduction of vibration in rotating machinery are of remarkable moment to technological progress across a wide range of fields, and it is on this justification that the current project is founded.

1.2 Thesis Outline

This thesis provides a detailed description of a project exploring the vibration reduction capabilities of a novel rotor system design. It takes the novel rotor system topology from conception, through mathematical analysis, design and construction of a specialised test rig, design and testing of possible control algorithms, and culminates in a series of experimental results illustrating the capabilities and potential of the proposed design.

To place this work in context, Chapter 2 provides a qualitative discussion of the various topics relevant to rotor dynamics. This begins with a brief historical perspective, and proceeds to outline key technical concepts in the field, touches on the antecedence of mathematical rotor analysis techniques, before taking a tour through the various techniques and technologies that have been employed to date to manage rotor vibration. The chapter concludes by introducing the specific technique which is considered in this project.

Chapter 3 takes a more quantitative approach to rotor dynamics, with an exposition of modern

finite element rotor analysis techniques. These techniques are then applied to an example system conforming to the topology explored in this project. The results of this analysis are justification for proceeding to the practical testing stage.

On this justification, Chapter 4 documents the process of design and construction of a test rig suitable for exploring the proposed topology. The chapter gives attention to practical details and specifications, as well as describing some of the difficulties experienced during the process, and the solutions devised. The test rig is an inherently mechatronic system, so for clarity the chapter is split to give separate consideration to each of mechanical, electrical and computational subsystems in turn.

The only part of the test rig not addressed by Chapter 4 is the magnetic bearings. In consideration of their relative complexity and central importance to the project, the magnetic bearings earn their own chapter - Chapter 5. Here there is presented a mathematical treatment of the active magnetic actuator, together with the design and material considerations which led to the final test rig bearings. This is complemented by the results of some standalone magnetic bearing tests designed to verify the capabilities of the finished items.

With the complete design and construction of the test rig covered, Chapter 6 turns its attention to bringing the rig online. This includes the development of a detailed numerical model of the rig based on the theory of Chapter 3, parameter identification for improved accuracy and model order reduction for simulation and control purposes. The chapter further presents results from a number of non-rotating experimental tests to establish rig characteristics.

In Chapter 7, consideration is given to the practicalities of running and controlling the rig. Results are presented - together with appropriate mathematical theory - showing the rig operating under both PID and model-based H_∞ control schemes. These results clearly illustrate the achievement of the original project goal, i.e. the capability of the novel topology to substantially improve the vibration behaviour of a flexible rotor.

Concluding remarks are collected in Chapter 8, being a summary of the project achievements, and a suggested outline of further work which may be undertaken to enhance the project at a later date.

Chapter 2

Rotor Vibrations - A Qualitative Discussion

THE purpose of this chapter is to consider the scope of the field of rotor dynamics, from its emergence as a distinct field of study through to its current state as a mature and well documented discipline. Particular attention is given to an understanding of some of the fundamental phenomena of rotor systems, as well as the various techniques that have been employed by researchers in the field to control and minimise rotor vibration.

Towards the end of the chapter, once a good understanding of the landscape of the rotor dynamics field has been gained, the particular novel concept to be addressed by the remainder of this project is presented. The idea is set within the context of existing works and techniques, with its unique qualities and advantages indicated.

2.1 A Brief History of Rotors

It's hard to define exactly when rotor dynamics, as a distinct subject, first came into existence. On the one hand it is apparent that mankind has made use of rotating devices for many thousands of years, right back to the stone age when logs were used as rollers to assist in the movement of heavy objects. On the other hand it's hard to justify that this sort of use of rotation merited anything in the nature of an academic study. Indeed, fast-forwarding though history, through the invention of the wheel as a means of transport, of the water-wheel and the windmill as a source of power, right up to the start of the Industrial Revolution with its steam engines, locomotives and industrial manufacturing machines, rotating machinery can generally be considered to have been used on a basis of experience and experimentation i.e. without any mathematical analysis - see also Figure 2.1.

In fact, it is only when one starts to try and rotate things at high speeds (i.e. pushing rotors into the flexible domain) that one begins to discover problems. Throughout history, from antiquity up to 300 or so years ago, the vast spectrum of machines using rotational motion operated at low speeds. Only once the Industrial Revolution took hold, and a variety of new machines began to take shape, did a need for things to rotate at high speeds emerge, and thus the field of rotor dynamics come into being.

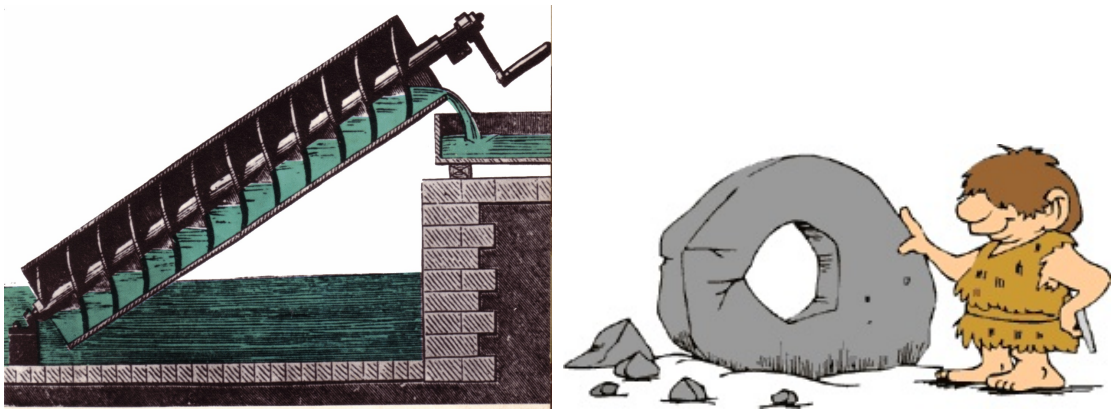

(a) (b)

Figure 2.1: Early uses of rotors worked without knowledge of rotor dynamics (a) Archimedes' screw; (b) the "wheel"

2.1.1 The Development of the Basic Rotor Model

One of the first people to subject the rotor a measure of educated consideration was the Scottish engineer and physicist William Rankine. In 1869 he analysed the spinning shaft, and postulated the existence of a *critical speed*, at which excessive vibration would make operation impossible [3]. Unfortunately, Rankine's understanding of the situation was incomplete (he took no account of damping effects), and thus while the fundamental idea of a critical speed is sound, Rankine predicted that speeds above this critical speed were entirely unattainable - a prediction later proved false.

Indeed the first supercritical rotation achieved in practice was just 14 years later in 1883. The machine was a steam turbine, built by the Swedish engineer and inventor Gustaf de Laval [4]. Curiously, Laval never really published any theoretical work on rotor dynamics, despite the strong likelihood that he must have given at least a little attention to the subject in order to achieve his turbine. Instead, the analytical work that might have been expected to precede a practical supercritical rotor came from a number of papers published separately over the following years, most notably from Dunkerley in 1894 [5], and Föppl in 1895 [6].

It is apparent that there was a lack of collaboration and cohesive understanding on the subject of rotor dynamics at the turn of the century. For instance the work of Rankine - an eminent

name in science and engineering at the time - was held (largely in consideration of his prestigious reputation) to be correct, but individual practical experiments seemed to be disproving his results. To remedy this, The Royal Society of London commissioned Henry Jeffcott to investigate the situation and clear up anomalies. The degree of his success in this venture is perhaps indicated by the fact that even today, the standard basic rotor model, commonly used to explain a range of rotor phenomena, is known as the Jeffcott Rotor. The paper propounding this model was published in 1919 in Philosophical Magazine [7]. In point of fact, virtually the same model had been published years earlier in 1895 by German August Föppl, however, he published in a German language journal of very limited readership, and thus the model is primarily attributed to Jeffcott.

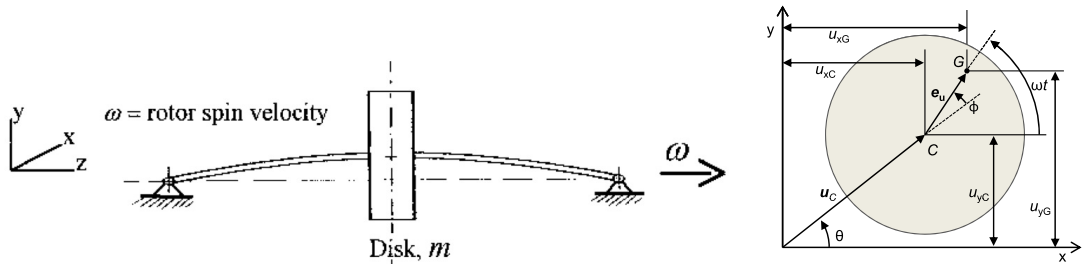

Figure 2.2: a) The Jeffcott Rotor, courtesy Adams [8]; b) Disc cross-section, courtesy Yoon et al [9]

The Jeffcott model consists of single rigid disk mounted at midspan on a massless elastic shaft, Figure 2.2a. The disk centre of mass is offset from its geometric centre by a nominal eccentricity e, Figure 2.2b. Employing a few simplifying assumptions and applying Newtonian mechanics (essentially $F = ma$), the differential equations of motion of the centre of the disc can be derived. It is then simply a mathematical exercise to find solutions to these equations under various conditions (e.g. force/free vibration), i.e. the time (or more usefully frequency) dependent coordinates of the centre of the disc, and thus draw conclusions about the nature of the disc/shaft vibration behaviour.

For the reader intrigued to further study, most standard rotor dynamics texts include a detailed Jeffcott rotor analysis, for instance Adams [8].

2.2 Rotor Dynamic Phenomena

It is salient here to break off from the story of the development of rotor dynamics, and to outline some of the key technical phenomena which underpin modern rotor dynamic theory. The concepts are well illustrated through consideration of the Jeffcott model, and can be understood without mathematical analysis.

Consider first a "perfect" Jeffcott rotor, with no unbalance, rotating at a constant, stable speed of Ω. If the system is then disturbed by an impulse and allowed to respond with no further interference, the whole shaft will precess in a bent shape around the equilibrium position. The precession will occur with a frequency ω, and depending on the direction of the initial impulse,may occur in either the same sense or the opposite sense to the shaft rotation Ω. These two eventualities are termed respectively forward and backward whirling, with ω_f and ω_b the forward and backward *natural whirling frequencies*. These may be thought of in a similar way to natural frequencies in other dynamic systems. Note that the precession frequency (ω) is a function of the rotor spin speed (Ω).

In the case that the Jeffcott rotor is "perfect", i.e. with the disk mounted exactly centrally, $\omega_f = \omega_b$, however if the model is modified such that the disk is no longer central but at any other location along the shaft, the forward and backward whirling frequencies are different, with $\omega_f > \omega_b$. This effect is due to the non-central disk twisting in the plane perpendicular to the rotor axis. As Ω increases, the difference between ω_f and ω_b also increases.

The model is now altered such that the disk has a centre of mass eccentric from its centre of rotation. As the shaft rotates, this unbalance causes a rotating force, deflecting the shaft from its equilibrium position. As with any dynamic system subject to periodic forcing, in the steady state, the system responds at the driving frequency, and thus the shaft will precess at Ω. Such forced whirling is termed *synchronous* whirling or vibration.

Now consider the case of an unbalance-driven whirling rotor having a rotational speed that happens to coincide with one of its natural whirling frequencies ($\Omega = \omega_f$ or $= \omega_b$). In such a case the system is effectively in resonance, and a (local) maximum amplitude of vibration is seen. In rotor dynamics, these speeds are termed *critical speeds*. Note that while all rotors have a critical speed at $\Omega = \omega_f$, not all system experience a critical speed at $\Omega = \omega_b$ - it depends whether the system geometry permits the unbalance forcing to feed energy into the backwards whirling mode.

2.3 Numerical Modelling Techniques

While the Jeffcott rotor model is very useful for providing an understanding of the fundamental principles of rotor vibration phenomena, it is severely limited in that it is only possible to apply it to the very simplest of systems. Most real world rotors are far too complex to analyse this way (for instance due to multiple discs, variable shaft diameter etc.), so analytical methods generally give way to numerical techniques, utilising the enormous processing power available in modern computers.

In many ways, therefore, the history of rotor dynamics continues with the history of numerical methods. Naturally, numerical methods for rotor analysis were not developed independently of the broader numerical analysis field, and this topic has a rich history and literature subset of

its own. However, the relevance of this topic is only tangential to the main focus of this project, and therefore a substantial survey of the field is omitted here. To the curios reader, however, Rao's "History of Rotating Machinery Dynamics" [10] is highly recommended as providing a thorough explanation of these topics.

Suffice to say then that the way for today's "standard" numerical rotor analysis technique was paved by the advent of the finite element techniques in the mid Twentieth Century - initiating in the arena of static analysis in civil structure, but today applied across a wide spectrum of applications.

A mathematical overview of the modern standard rotor finite element technique, which was derived in its current form by Nelson and McVaugh [11] and Nelson [12] and is used in this project, can be found in Chapter 3.

2.4 Rotor Vibration Control

2.4.1 Technique Classification

Having now arrived at a point where the existence of rotor dynamics as a subject is justified (understanding flexible rotor behaviour), the basic model of a flexible rotor is understood (Jeffcott), and the use of numerical techniques to analyse real life rotors has been presented, our rotor dynamics story is precipitated into modern times, and the focus turns to the current state of the art of rotor vibration management.

When categorising rotor vibration control techniques, perhaps the most fundamental division that can be drawn is between techniques that can be applied to rotors *in situ*, and those that require the rotor to be taken out of service to be adjusted. These classes are referred to as **on-line** and **off-line** respectively. Naturally, on-line methods have an intrinsic advantage over off-line ones, namely that they don't require an interruption of the process in which the rotor is involved (i.e. no machine down-time). On-line techniques also have the potential to be adaptable to changing operating conditions, which off-line techniques lack. However, on-line techniques are much more difficult to successfully implement, to such an extent that the vast majority of rotor vibration control today is done off-line.

The only real tactic available to off-line vibration control is that of balancing the rotor, i.e. of placing calculated masses at strategic locations along the length of the shaft to bring the overall centre-of-mass of the rotor closer to its axis of rotation. This is very common practice, right the way from large industrial turbines and rollers through to the wheels on cars.

However, it is important to highlight the difference between off-line balancing of low speed rotating devices compared to high speed ones. As outlined above, up to a certain point rotors can be modelled as rigid bodies, while at higher speeds they must be considered as flexible

components. Balancing of rigid rotors is more or less trivial in terms of concept and difficulty, whereas off-line balancing of flexible rotors present some significant challenges. To overcome these, two distinct methodologies have been developed during the second half of the Twentieth Century: **modal balancing** and the **influence coefficient technique**. Modal balancing involves placing correctional masses to independently balance each bending mode of a rotor, ensuring each mass placed does not affect any previously balanced modes. This can be difficult in systems with complex mode shapes and limited space for placement of balancing masses. The influence coefficient method involves minimising vibration at a chosen constant rotor speed by placing balancing masses at chosen locations. It requires more test runs to implement than modal balancing, but is more efficient. A more detailed explanation of these techniques is provided by Muszynska [13, p.731]

On-line techniques, as a class, come wielding a greater variety of tactics beyond just balancing, however before examining them individually, it is pertinent to introduce two sub-classes: **passive** and **active** methods. The difference between these two groups is simple: passive techniques rely purely on the forces implicit to the physics of the situation to apply correctional effects (e.g. inertia or centripetal force to move ball bearings), while active systems always involve some sort of controller, making decision about where, when and how much force and / or motion to apply, based on measured variables. The consensus from research conducted into passive techniques (for instance Olsson [14] and Meraz et al [15]) indicates that while they can be very effective in low speed applications, they have very limited promise in practical supercritical applications. This is largely due to the fact that any balancing device will naturally contain its own unbalances / inaccuracies of manufacture, which will themselves exacerbate vibration behaviour in the region of critical speeds. Active techniques therefore constitute the majority of the interesting research in the field.

2.4.2 Modern Research Topics

Currently there is only one industrially practical mechanism for active on-line management of vibration of a rotor, and that is through the use of active bearings; in all other cases, to reach supercritical speeds shafts must be carefully balanced by one of two off-line methods, either modal balancing or the influence coefficient method.

That said, a significant amount of research has been undertaken in designing and testing various promising methods of active vibration management, and an outline of that research follows.

Taking a broad view of the matter, active rotor vibration reduction techniques may be considered to split into three distinct groups:

- the first of these groups is concerned with active balancing, i.e. redistributing mass around the rotor system to remove the driving force of synchronous vibration. These methods

tend to be adaptations of off-line balancing methods.

- the second group concerns itself with directly applying forces to the rotor; generally this is by means of lateral forces at the supporting bearings, although other methods of force application have been researched
- the third group is a little less clearly defined in nature, but techniques here generally involve changing some physical property of the system (other than mass redistribution), for example stiffness or geometry, and thus alter vibration response

Note that of these three groups, only the first actually tries to remove the source of vibration, while the other two contain methods to deal with / mitigate any vibration that occurs. As a result of this, methods employing only active balancing can only deal with vibration due to out of balance masses (synchronous vibration) - vibration from outside sources (e.g. shock loading) cannot be handled by these systems, whereas they potentially can by force application and physical adjustment schemes. An overview of all vibration control techniques can be seen in Figure 2.3.

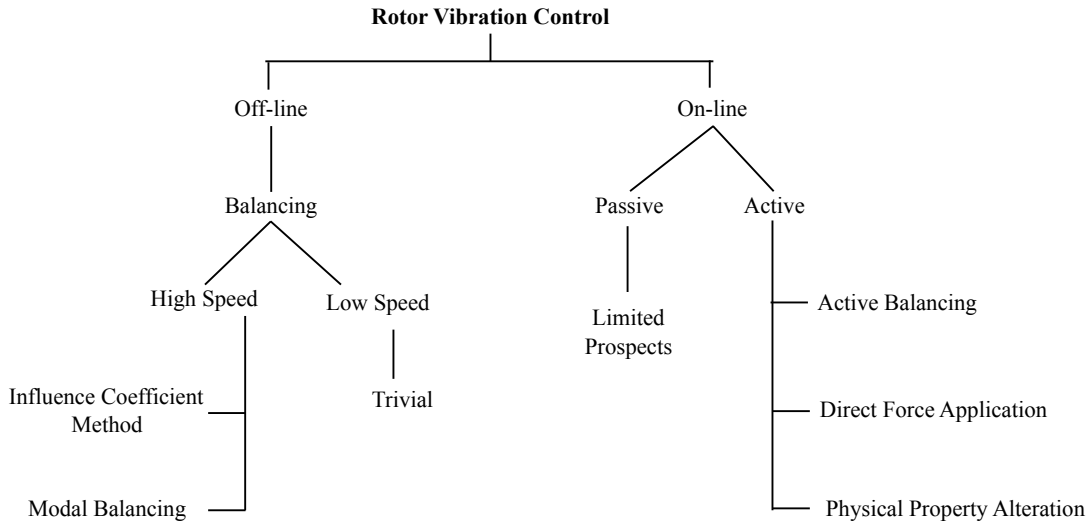

Figure 2.3: Vibration-control techniques tree

2.4.3 Active Balancing

On the front of active mass redistribution, Van De Vegte's 1964 paper [16] presents the first design of an active mass redistribution mechanism, consisting of masses mounted on the rotor with the ability to move along two perpendicular axes. From measurements of the vibration at the bearings, a correction position of the masses could be calculated by methods based on the off-line influence coefficient technique, with actuation provided by a servo-motor for each

axis of motion. While sound in theory (and indeed practicable at low speeds), Van De Vegte soon discovered that when approaching critical speeds, errors both in vibration measurement and in influence coefficient measurement lead to large errors in the placement of the correction mass.

In an attempt to overcome shortcomings of the control system, Van de Vegte undertook further work [17], [18] whereby each of the masses was positioned manually by operator control, trying different logic approaches to the order of moving the masses. Van de Vegte's experiments were not, practically speaking, a great success; however, the design of balancing head he proposed was adopted by several subsequent studies by other researches. For instance, Bishop's 1982 paper [19] dismisses Van de Vegte's balancing logic as overly complicated, and instead proposed a new method of using the same physical balancing head according to entirely different reasoning. Similarly, Gosiewski [20], [21] takes the same balancing head and adds to Van de Vegte's original influence coefficient control the use of a digital computer as a controller. Gosiewski's scheme assumes prior knowledge of influence coefficients for several ranges of spin speed, which are held in the computers memory. These data then allows the controller to work with rotors of non-constant spin speed - a notable advantage over previous works.

Further significant work was undertaken by Dyer and Ni, whose 2001 paper [22] presents a new design of balancer, which successfully uses influence coefficient control to reduce vibration. Their balancer consists of a pair of rings with known unbalance; the rotational positioning of these rings relative to one another allows the positioning of a single equivalent heavy spot anywhere within a certain radius. Dyer and Ni also use on-line calculation of influence coefficients (compared to Gosiewski's predetermined values), giving their system greater adaptability.

However, very little is commercially available on this front yet. What is available (for instance from German based Hofmann Precision Balancing) is highly specialised and is far from universally applicable (e.g. because of size constraints). On-line active balancers may therefore be considered largely still the domain of research, with a minimal industrial presence.

A good review of active rotor balancing research is provided by Zou and Shi [23].

2.4.4 Direct Force Control

The techniques in this section all share the common feature of having the capability to apply a lateral force to a rotor, and by doing this strategically they aim to effectively overpower vibrations.

One of the most promising active vibration management techniques explored to date is the use of magnetic bearings. The fundamental principle of magnetic bearings is simple: a rotor, rather than being supported by any form of contact bearing with either rolling or fluid elements, is levitated within a magnetic field. This type of bearing has the huge advantage, however, of

having the capability to be used as an active control mechanism. This quality is a function of the fact that magnetic bearings have hugely and rapidly adjustable stiffness characteristics, and may therefore be used as a force applicator to the rotor. It is proposed to make use of magnetic bearings in this PhD project, with aspects of the geometry and materials subject to unusual and novel design. As such a separate subsection, Section 2.4.6, explores the relevant literature of this field.

In addition to the magnetic variety, other species of active bearing have also been investigated with a view controlling rotor vibration. Santos [24] provides an overview of modern research into making oil-film bearings active devices. As with magnetic bearings, the focus is on altering stiffness and damping properties of the bearings, in addition to dealing with cross-coupling effects, which is a destabilising phenomenon occurring in this type of bearing.

Separately, Qui et al [25] explore a novel kind of tilting-pad gas bearing, with two out of three pads on each bearing are given piezo actuation to adjust the distance between the pad and the shaft, and so the adjust forces on the shaft. They used PID control to successfully illustrate a measure of vibration suppression.

A further possibility for the application of control forces at the bearings - regardless of what kind of bearings are in use - is to mount the bearings themselves on actuators. Through this means, one can achieve similar kind of control available with magnetic bearings with more traditional (and cheaper) types of bearing. The actuation force can be achieved through either hydraulic or piezoelectric means, although high stiffness and rapid response generally make piezoelectrics the more favoured choice. This idea is explored by Palazzolo et al [26].

2.4.5 Physical Property Alteration

This last group of techniques shows slightly less coherence than the others. The key link is that all techniques try to alter one or more of the physical properties of the rotor system that contribute to defining its natural frequencies/vibration behaviour. It is into this category that the techniques researched so far in the project fall, although no previous literature - as far as is known - exists directly describing these methods.

One technique that has been proposed involved dynamically altering the stiffness of a rotor. This is achieved by having one of its support bearings mobile, and thus changing the effective length of the rotor; as frequency of vibration is a function of length / support positions, this allows an altering of the resonant frequencies. Ortega presents a paper exploring this idea [27]. Clearly there is an intrinsic disadvantage to this technique, which is the requirement for lengths of the rotor shaft to be left free and available for the bearing to slide along, thus making the rotor (and conceivably the entire machine) larger than is necessary.

There is also another technique that has been the subject of some research involving the use of piezoelectric effects. Specifically the application of PZT patches (lead zirconate titinate -

a common piezoelectric material) to the surface of a rotor has been explored. The technique was initially used for non-rotating shafts (Hagood et al. [28]), and has since been adapted for rotors (Horst and Wölfel [29]). The basic idea is to bond a pair of PZT patches to a strategic station along a rotor's length, on opposite sides of the shaft. The patches can then be activated as an "antagonistic pair" to exert a bending moment on the shaft, thereby tending to counter a deflection resulting from vibration. Horst and Wölfel present a mathematical model of this arrangement and a limited practical implementation, but fail to demonstrate convincing active vibration reduction, citing the need for further work.

More recently, the use of shape memory alloys (SMAs) in rotor vibration reduction applications has been considered. SMAs have thermally influenced properties, particularly stiffness, as well as exhibiting substantial hysteresis during deflection leading to damping qualities. The application of an SMA ring in addition to traditional bearings is explored by Ma et al. [30]. The paper illustrates a capability to alter the rotor system properties (changing the critical speed) and by making use of this a modest reduction in peak vibration amplitude is achieved. Another concept involves using SMAs in the support/housing for one or more of the main bearings of the system. This idea is examined by Enemark et al. [31], where a comparison is drawn between using steel and SMA springs connected to one of the bearings of a vertically oriented rotor. They report significant, temperature-dependent capability to reduce maximum vibration amplitudes when passing critical speeds, but note that there are also more fundamental changes to the rotor dynamics caused by the use of the SMA, and thus a more complex, system level analysis is required to achieve optimum behaviour rather than simply directly replacing, say, steel components with SMA ones.

2.4.6 Magnetic Bearings

A vast amount of literature is published on the design and use of magnetic bearings. A brief survey of that material is presented here.

Early work in the field was focused on using a magnetic actuator as a "supplementary" bearing in a system already fully constrained on tradition bearings, for example oil-film bearings. It was found in this work [32, 33] that a very substantial reduction in vibration amplitudes could be achieved through the used of these "Active Magnetic Dampers" (AMDs).

In the early research, full shaft levitation (i.e. with useful stiffness and damping characteristics) was challenging and expensive, due to lack of availability of key technologies, particularly transistors for power amplification, and microprocessors for digital control. The rapid developments in these fields over the 1970s and 1980s provided a huge stimulus to development in the magnetic bearing field, and a number of works over those years explored the possibilities AMBs offer to rotor system performance [34, 35, 36].

In subsequent work, various authors have addressed specific tasks and applications relating

to the use of magnetic bearings: Clark et al. [1] presents a summary of work that has been done towards the use of AMBs in gas turbine engines; self-sensing (sensorless) techniques have been explored by Vischer and Bleuler [37] , and Noh and Maslen [38]; control of rotor/stator contact events have been addressed by Keogh et al. [39, 40, 41]; Komori et al. consider systems incorporating superconducting magnetic bearings [42, 43, 44].

One interesting topic in the magnetic bearing sphere is that of automatic balancing. The principle here is to use the magnetic bearing to generate a revolving force equal and opposite to the force caused by the shaft unbalance, and thus eliminate its effect. The technique is fundamentally open-loop, i.e. a feed-forward controller, which can be implemented via a magnetic bearing in addition to a feedback controller providing rotor levitation if necessary. This provides stability advantages over trying to compensate for unbalance via a feedback algorithm [45].

An algorithm to calculate such a compensating force was presented by Burrows and Sahinkaya [46]. A disadvantage of the original form of this technique was that it required prior analysis of the system to allow the calculation of control forces. In subsequent work, Burrows et al. [34] enhanced their algorithm to permit on-line estimation of system parameters, such that without any knowledge of the system beforehand, the appropriate control forces could be automatically determined. The work of Burrows et al. was considered as part of a program of experimental work by Knospe et al. [47, 48] who made particular note of the efficiency of the technique.

The technique of Burrows et al. was further enhanced by Abulrub et al. [49] to allow the facility to cope with sudden changes in a rotor unbalance (e.g. mass loss event). The alteration effectively made the original algorithm recursive, such that the control force to be applied is recalculated at the fundamental sampling rate of the system by means of a recursive Fourier transform.

Magnetic bearings have also found use in combination with other bearing types. One interesting example is the recent work on hybrid foil-magnetic bearings. In such devices, a traditional air-foil bearing is used concentrically within a magnetic bearing. By combining the advantages of both systems, a bearing can be made which is lighter and more resilient to power failure than an ordinary AMB, while reducing problems with coating wear and and rotor vibration which may trouble traditional passive air-foil bearings. The technology is well treated by Heshmet et al. [50]. Further works considering response to step unbalance change, system optimisation and rotordynamic performance of such systems have been presented, for example, by Jeong and Lee [51], Pham and Ahn [52], and Jeong et al. [53]. This is a field of ongoing research.

Another interesting use of electromagnetic actuators is described by Mahfoud and Der Hagopian [54]. In a similar way to the AMDs discussed above, the magnetic actuator is not used as a bearing per se, but rather as a supplementary device in a system already constrained by traditional bearings. The idea explored in this work is to use the actuator to change the system stiffness, and thus alter its vibration behaviour. Specifically the magnetic actuator is used in an open-loop configuration with a constant current through all coils. This results in a decrease

in overall system stiffness, and therefore a reduction in critical speeds. By selectively activating and de-activating the actuator, critical speeds can be "dodged" as a rotor spins up or down.

In addition to the material discussed above, good general background information on magnetic bearings and a more in depth literature review can be found in several books, for instance Maslen and Schweitzer's "Magnetic Bearings: Theory, Design, and Application to Rotating Machinery" [55]. Furthermore, in a recent paper [56], Schweitzer presents a brief overview of modern research topics in AMB technology, including high speed rotors, touchdown dynamics and advanced applications.

What remains substantially unexplored however, and is of specific interest to this project, is the use of magnetic bearings as a controllable coupling between two flexible systems - that is to say a new application for the existing technology. Usually if a flexible rotor is being considered, it is taken as read that the bearings are mounted on a rigid body. However it is proposed that if the bearings are mounted on a flexible body, they may effectively be used as a tuneable coupling, allowing the transfer of vibration energy from the rotor to these flexible bearing mounts (in which vibration is designed not be an issue). No literature directly bearing on this has been discovered.

2.5 A New Idea for Vibration Management

The concept proposed in this thesis for the reduction of rotor vibration is conceptually inspired by the use of tuned mass damping in traditional vibrations problems. Specifically the concept of including a secondary "body" to change the vibration behaviour of a primary "body" is exploited. In the context of this thesis, the idea consists of the following key points:

- a hollow tube rotor
- a secondary shaft that runs concentrically through the rotor with its own independent support
- an active coupling device, which enables the rotor to be selectively linked or un-linked from the secondary shaft

Figure 2.4 shows a simplified illustration of the proposed rotor layout. The rotor is a hollow tube of soft magnetic metal (e.g. steel) supported on external rolling element, or other passive bearings. The secondary shaft is supported entirely separately by non-rotating supports. The material for the non-rotating shaft is chosen on a basis of its stiffness qualities, and it need not have appreciable magnetic permeability. The fact that this shaft does not rotate gives the advantage that any unbalance present in the member does not add to or complicate the dynamics of the primary rotor when the two shafts are coupled. The active couplings are

achieved by internal-stator magnetic bearings. A conceptual cross-sectional view of such a device is provided in Figure 2.5.

The novel and original contribution of this project to the field can be summarised as:

- the characteristic of mounting a magnetic bearing on a shaft of comparable flexibility to the rotor whose vibration is to be reduced
- the original design (and use of non-traditional material) of a space-efficient internal-stator magnetic bearing core to facilitate the proposed system topology
- the control methods employed, specifically using measurements of relative displacement between two flexible bodies as the feedback variable to reduce the absolute vibration of one of those bodies

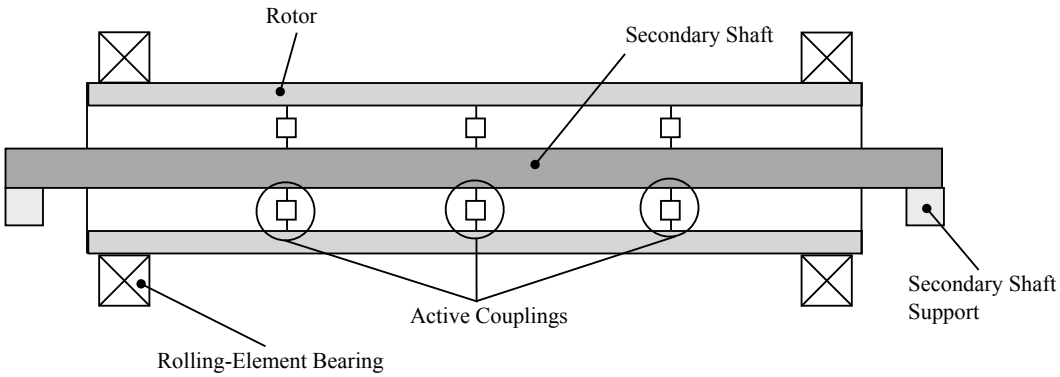

Figure 2.4: Schematic view of proposed novel rotor topology. The number and position of "Active Couplings" shown is arbitrary.

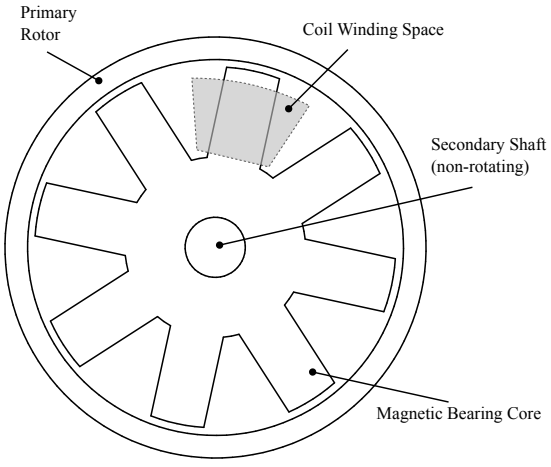

Figure 2.5: General schematic cross-section of internal stator magnetic bearing

Chapter 3

Modelling

In order to evaluate the merit of the proposed concentric-shaft concept for the purposes of vibration reduction, the arrangement is mathematically modelled via the finite element technique. The goal is to check that, for a given rotor operating under a give forcing (e.g. a specific out-of-balance mass) the magnitude of vibration of that rotor at its first critical speed can be reduced through the introduction of a secondary shaft and a magnetic coupling, as proposed.

This chapter has two parts: in the first part, the finite element method of rotor modelling is derived; in the second part the finite element method is applied to a specific rotor system corresponding to the proposed new topology, and the results of this analysis are presented to illustrate the potential of the scheme.

3.1 The Finite Element Method

In the analysis of structures generally, it is only ever possible to find an analytical representation in the simplest of cases. When considering beams and rotors, analytical description is usually confined to uniform cross-section geometries with straight-forward loading conditions. Most real beams and rotors have more complex, non-uniform cross-sections, and for these analytical description is generally impractical.

The solution to this difficulty is to consider the complex beam as being constructed from a number of smaller elements. Each individual element is defined such that it is of uniform cross-section, and thus is - in isolation - amenable to analytical consideration. The equations governing the individual elements are then collected together with conditions of continuity imposed on their ends, such that a larger set of equations governing the whole beam is acquired.

As such, it is required to consider the equations which govern the motion of a single, uniform

cross-section beam element, such as that shown in Figure 3.1. Note that, to keep the analysis concise, the beam element is only shown deflecting in a single plane - in practice of course an element will deflect in two orthogonal planes, but the equations for the second plane are identical to and independent of those for the first plane (at least as long as the beam is not rotating - see Section 3.1.1).

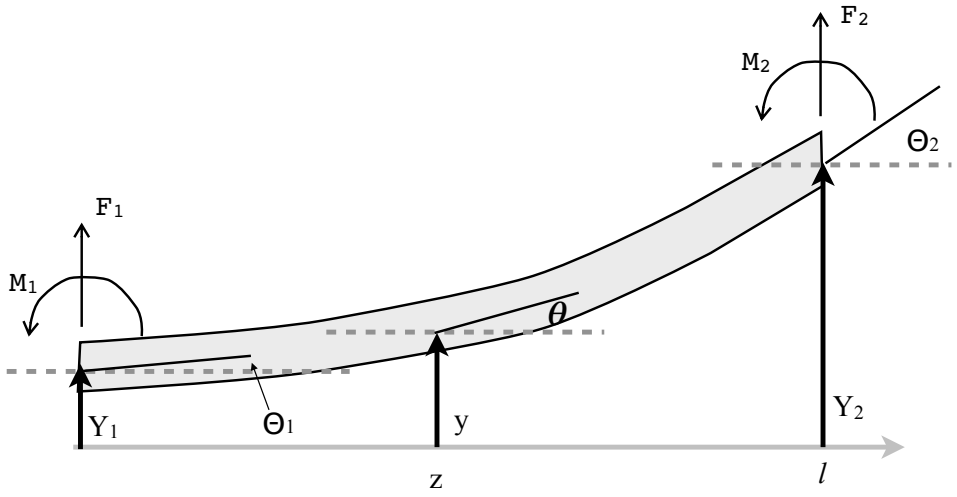

Figure 3.1: A general deflected beam element in one plane

The element under consideration in Figure 3.1 has four degrees of freedom: Y_1, Y_2, Θ_1 and Θ_2 which respond to the four imposed forces F_1, F_2, M_1 and M_2. These are generally collected in the following way:

$$\mathbf{q} = \begin{bmatrix} Y_1 \\ \Theta_1 \\ Y_2 \\ \Theta_2 \end{bmatrix} = \begin{bmatrix} q_1 \\ q_2 \\ q_3 \\ q_4 \end{bmatrix} \quad , \quad \mathbf{f} = \begin{bmatrix} F_1 \\ M_1 \\ F_2 \\ M_2 \end{bmatrix} = \begin{bmatrix} f_1 \\ f_2 \\ f_3 \\ f_4 \end{bmatrix}$$

At any mid-point location along the element, the internal displacements are represented by y and θ.

The ultimate goal of the analysis is to find equations relating the displacements at the end of the element to the forces acting at those ends.

Towards this goal, the first step taken is to establish a generalised expression for the deflection of the beam at any internal point, i.e. an expression for $y(z)$. For considerations of physical realism, it is required that this function has C^1 continuity. That is to say the function must itself be continuous, and its first derivative ($\frac{\partial y}{\partial z}$) must also be continuous. This is to ensure that

the curvature of the beam element (which is the physical interpretation of $\frac{\partial y}{\partial z}$) is smooth and continuous. The simplest such function is the Hermitian cubic shape function, and thus such a function is used to describe the deflected shape of the beam element. The general Hermitian cubic is expressed as:

$$y(z) = a_0 + a_1 z + a_2 z^2 + a_3 z^3 \tag{3.1}$$

Four boundary conditions can then be applied to this equation to transform it into an expression in terms of the element degrees of freedom, rather than arbitrary a values. The boundary conditions may be written:

$$\begin{aligned} y(0) &= Y_1 & \qquad y(L) &= Y_2 \\ \dot{y}(0) &= \Theta_1 & \qquad \dot{y}(L) &= \Theta_2 \end{aligned}$$

Applying these boundary conditions yields

$$\begin{aligned} y(0) &= a_0 = Y_1 \\ \dot{y}(0) &= a_1 = \Theta_1 \\ y(L) &= a_0 + a_1 L + a_2 L^2 + 3a_3 L^3 = Y_2 \\ \dot{y}(L) &= a_1 + 2a_2 L + 3a_3 L^2 = \Theta_2 \end{aligned} \tag{3.2}$$

The final two statements in Equation (3.2) can be solved as a pair of simultaneous equations for expressions for a_2 and a_3, and these (together with the values for a_0 and a_1 already derived) can be substituted into Equation (3.1).

This results in Equation (3.3):

$$y(z) = n_1 Y_1 + n_2 \Theta_1 + n_3 Y_2 + n_4 \Theta_2 \tag{3.3}$$

where

$$
\begin{aligned}
n_1 &= \frac{1}{L^3}(2z^3 - 3Lz^2 + L^3) \\
n_2 &= \frac{1}{L^3}(Lz^3 - 2L^2z^2 + L^3z) \\
n_3 &= \frac{1}{L^3}(-2z^3 + 3Lz^2) \\
n_4 &= \frac{1}{L^3}(Lz^3 - L^2z^2)
\end{aligned}
$$

Supposing for the moment that the deflection is merely static, it is possible to relate the forces and moments on the beam element to the deflections via standard Euler beam theory, as in:

$$
M = EI\frac{\partial^2 y}{\partial z^2} \qquad , \qquad F = \frac{\partial M}{\partial z} \tag{3.4}
$$

where E is the material Young's Modulus and I is the beam second moment of area.

Following these calculations through and evaluating in the cases of z = 0 and z = L yields the expression shown in Equation (3.5). The matrix relating the displacements to the forces is commonly referred to as the *stiffness matrix*, denoted **k**. Here, l is the element length.

$$
\begin{bmatrix} F_1 \\ M_1 \\ F_2 \\ M_2 \end{bmatrix} = \frac{EI}{l^3} \begin{bmatrix} 12 & 6l & -12 & 6l \\ 6l & 4l^2 & -6l & 2l^2 \\ -12 & -6l & 12 & -6l \\ 6l & 2l^2 & -6l & 4l^2 \end{bmatrix} \begin{bmatrix} Y_1 \\ \Theta_1 \\ Y_2 \\ \Theta_2 \end{bmatrix} \tag{3.5}
$$

This may also be more compactly expressed as:

$$
\mathbf{kq} = \mathbf{f} \tag{3.6}
$$

To extend the analysis to cover not only the *static* but also the *dynamic* behaviour of the beam element, we turn to the Euler-Lagrange equation, which is expressed:

$$
\frac{\partial^2}{\partial z}\left(EI\frac{\partial^2 y}{\partial z^2}\right) + \mu\frac{\partial^2 y}{\partial t^2} = f(z) \tag{3.7}
$$

where μ is the beam element mass per unit length.

The first term of Equation (3.7) is a stiffness term, and the second is an inertia term. It is this

inertia term which is of particular interest - the stiffness behaviour has already been derived in Equation (3.5). Thus we need only focus on the term:

$$\mu \frac{\partial^2 y}{\partial t^2}$$

which may be expanded by substituting in Equation (3.3) to:

$$\mu(n_1 \ddot{Y}_1 + n_2 \ddot{\theta}_1 + n_3 \ddot{Y}_2 + n_4 \ddot{\theta}_2) \tag{3.8}$$

It should be noted, however, that the expression derived for y(z) in Equation (3.3) can only strictly be applied to a static beam element. When used to consider inertial behaviour, which is inherently dynamic, there will be some degree of error. In order to minimise this, the standard Galerkin technique is employed; here, if Equation (3.8) is represented as $f(z,t)$, we may attempt to minimise errors by calculating:

$$\int_0^L n_i f(z,t) dz \tag{3.9}$$

where i = 1 - 4, giving a set of four equations. To expand each of these four equations fully would be very repetitive, so is omitted here - only first term of the case for $i = 1$ is expanded as a representative example, as follows:

$$\mu \ddot{Y}_1 \int_0^L n_1^2 dz = \frac{\mu \ddot{Y}_1}{L^6} \left[\frac{4}{7} z^7 - 2Lz^6 + \frac{9}{5} L^2 z^5 + L^3 z^4 - 2L^4 z^3 + L^6 z \right]_0^L = \frac{13}{35} \mu L \ddot{Y}_1 \tag{3.10}$$

Expanding all terms resulting from Equation (3.9) in the same way leads to the following expression, which is commonly called the *consistent mass matrix* and denoted **m**.

$$\mathbf{m} = \frac{\mu l}{420} \begin{bmatrix} 156 & 22l & 54 & -13l \\ 22l & 4l^2 & 13l & -3l^2 \\ 54 & 13l & 156 & -22l \\ -13l & -3l^2 & -22l & 4l^2 \end{bmatrix} \tag{3.11}$$

Note that the $\frac{13}{35}\mu L$ term of Equation (3.10) is seen as $\frac{156}{420}\mu L$ in the consistent mass matrix.

In combination with the stiffness matrix presented in Equation 3.5, the governing equation for

the 2D beam element now becomes:

$$\mathbf{m\ddot{q}} + \mathbf{kq} = \mathbf{f} \tag{3.12}$$

3.1.1 The 3D Case

As mentioned earlier, the beam element derivation was presented only for motion in a single plane. In general the motion occurs in two orthogonal planes, and the beam element representing the new degrees of freedom is shown in Figure 3.2.

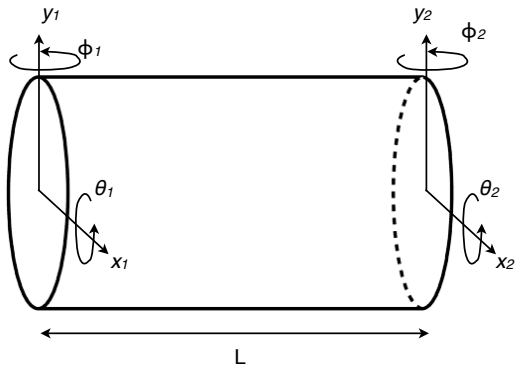

Figure 3.2: Degrees of freedom acting on a 3D beam element

In such a case, the vector $\mathbf{q}$ is redefined to include the degrees of freedom from the second plane, as follows:

$$\mathbf{q}(t) = (x_1(t), y_1(t), \theta_1(t), \phi_1(t), x_2(t), y_2(t), \theta_2(t), \phi_2(t))^T$$

As the two planes are orthogonal, the motion in each is independent, and therefore the results of the single-plane analysis can be directly applied to each plane separately. Thus the Equation (3.12) is still applicable, where $\mathbf{m}$ and $\mathbf{k}$ are "doubled up" (and possibly internally rearranged) to account for the extra degrees of freedom.

Thus far then, a model describing a 3D *beam* element has been described, which includes terms based on stiffness and inertia effects. When considering a rotor (i.e. a beam which rotates), there is a third term to be considered. This term is known as the *gyroscopic matrix*. It comes about as a result of the polar moment of inertia of the rotating beam element, which can "feed" energy into the vibration of the element if it has it has any angle other than perpendicular to the axis of rotation.

This gyroscopic term couples the previously orthogonal and independent axes of vibration of the element (i.e. the x and y directions), and is the cause of the splitting of forward and

backward natural whirling frequencies of a rotor, as described in Section 2.2.

A full mathematical derivation is omitted, but can found in a number of rotor dynamics text books, and in Nelson's paper [11], where this formulation of the finite element method was originally specified.

The gyroscopic matrix ($\mathbf{g}$) is dependent on the speed of the rotor (Ω), and can be added to the element equation of motion in Equation (3.12) as:

$$\mathbf{m}\ddot{\mathbf{q}} - \Omega\mathbf{g}\dot{\mathbf{q}} + \mathbf{k}\mathbf{q} = \mathbf{f} \tag{3.13}$$

The $\mathbf{g}$ matrix is explicitly defined in Appendix A, together with the expanded $\mathbf{m}$ and $\mathbf{k}$ matrices applicable to the 3D element.

3.1.2 Modelling a Whole Rotor

Up to this point, equations have been derived to allow the modelling of a single element of a rotor. It is now time to connect a number of such elements together to model a whole rotor, and illustrate how external fittings (e.g. bearings, discs etc) may be included in the model.

With each of the $\mathbf{m}$, $\mathbf{g}$ and $\mathbf{k}$ element matrices, a summation is made to include all elements in the overall model and yield an equation of motion for a multi-element rotor:

$$\mathbf{M}\ddot{\mathbf{Q}} - \Omega\mathbf{G}\dot{\mathbf{Q}} + \mathbf{K}\mathbf{Q} = \mathbf{F} \tag{3.14}$$

where $\mathbf{M}$, $\mathbf{K}$, $\mathbf{G}$, $\mathbf{F}$ and $\mathbf{Q}$ are the global equivalents of the elemental terms $\mathbf{m}$, $\mathbf{k}$, $\mathbf{g}$, $\mathbf{f}$ and $\mathbf{q}$, respectively.

The form of this summation is illustrated graphically in Figure 3.3. Here it is shown how n element mass matrices ($\mathbf{m}_1$ to $\mathbf{m}_n$), each of 8×8 size, are combined into a single global mass matrix $\mathbf{M}$ of size $4n + 4$. Note that the areas where element matrices are shown to overlap is where the relevant terms of those matrices are summed.

The process for forming global gyroscopic ($\mathbf{G}$) and stiffness ($\mathbf{K}$) matrices is identical.

Once in possession of a set of global mass, stiffness and gyroscopic matrices representing an entire rotor shaft, one may then furnish the shaft with any required assortment of disc and bearing elements. Each of these must be located at a junction of two of the model elements (a node). Mathematically, a disk mounted at node i will answer to the governing equation of:

$$\mathbf{m_d}\ddot{\mathbf{q}}_\mathbf{i} - \Omega\mathbf{g_d}\dot{\mathbf{q}}_\mathbf{i} = \mathbf{f_d} \tag{3.15}$$

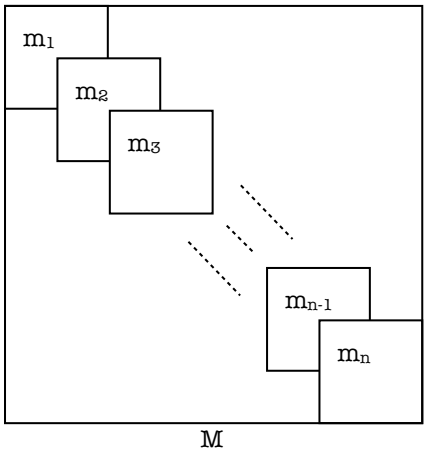

Figure 3.3: Addition of individual element matrices to form global matrices

with

$$\mathbf{m_d} = \begin{bmatrix} m_d & & & & \\ & m_d & & & \\ & & I_d & & \\ & & & I_d & \end{bmatrix} \qquad \mathbf{g_d} = \begin{bmatrix} 0 & & & \\ & 0 & & \\ & & 0 & -I_p \\ & & I_p & 0 \end{bmatrix} \tag{3.16}$$

where m_d, I_d and I_p are respectively the disk mass, diametral inertial and polar inertia.

Similarly, a bearing residing at node r will obey the mathematical model of:

$$\begin{bmatrix} k_{xx} & k_{xy} \\ k_{yx} & k_{yy} \end{bmatrix} \begin{bmatrix} x_r \\ y_r \end{bmatrix} + \begin{bmatrix} c_{xx} & c_{xy} \\ c_{yx} & c_{yy} \end{bmatrix} \begin{bmatrix} \dot{x_r} \\ \dot{y_r} \end{bmatrix} = \begin{bmatrix} f_{xr} \\ f_{yr} \end{bmatrix} \tag{3.17}$$

where k and c are bearing stiffness and damping characteristics (note that they may be different in the x and y directions, i.e. orthotropic bearings).

Discs and bearings can be added to the model by adding matrices containing their stiffness and damping properties to the appropriate global beam matrices at the relevant nodes. Example placement of such auxiliary component addition is illustrated in Figure 3.4.

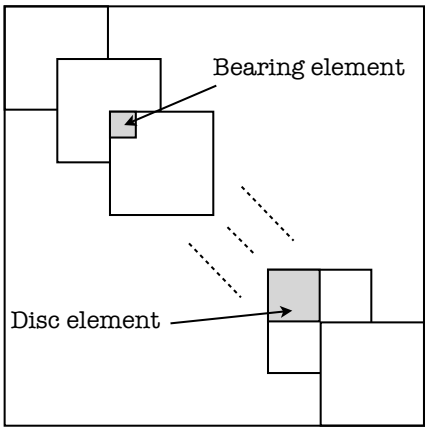

Figure 3.4: Positioning of disc and bearing elements in global matrices

3.1.3 Combining Multiple Shafts

The above derivation is a standard analysis in rotor dynamics and allows for the generation of a set of equations to describe the behaviour of a single beam or rotor. The concept proposed in this thesis includes a system with a non-rotating beam running concentrically through a hollow rotor, with active couplings between the two. To adapt the standard, single shaft methodology to this topology, we first define a new $\mathbf{Q}$ vector, which is now extended to include degrees of freedom for both the primary rotor ($\mathbf{Q_R}$) and the secondary shaft ($\mathbf{Q_S}$):

$$\mathbf{Q} = \begin{bmatrix} \mathbf{Q_R}^T & \mathbf{Q_S}^T \end{bmatrix}^T$$

Using this definition, an expanded form of Equation (3.14) is presented, which demonstrates where coupling terms are applied between the two shafts:

$$\begin{bmatrix} \mathbf{M_R} & \mathbf{0} \\ \mathbf{0} & \mathbf{M_S} \end{bmatrix} \begin{bmatrix} \ddot{\mathbf{Q}}_\mathbf{R} \\ \ddot{\mathbf{Q}}_\mathbf{S} \end{bmatrix} - \begin{bmatrix} \Omega\mathbf{G} & \mathbf{0} \\ \mathbf{0} & \mathbf{0} \end{bmatrix} \begin{bmatrix} \dot{\mathbf{Q}}_\mathbf{R} \\ \dot{\mathbf{Q}}_\mathbf{S} \end{bmatrix} + \dots$$
$$\dots \begin{bmatrix} \mathbf{K_R} & 0 \\ 0 & \mathbf{K_S} \end{bmatrix} \begin{bmatrix} \mathbf{Q_R} \\ \mathbf{Q_S} \end{bmatrix} = \begin{bmatrix} \mathbf{F_R} \\ \mathbf{F_S} \end{bmatrix} + \begin{bmatrix} \mathbf{B_R} \\ \mathbf{B_S} \end{bmatrix} \mathbf{U} \quad (3.18)$$

where $\mathbf{U}$ contains magnetic bearing force components that are applied to the primary rotor and secondary shaft according to the distribution matrices $\mathbf{B_R}$ and $\mathbf{B_S}$. Note that due to its non-rotation, there is no gyroscopic term for the secondary shaft. When control is configured

to be spring-like, the equation becomes:

$$\begin{bmatrix} \mathbf{M_R} & \mathbf{0} \\ \mathbf{0} & \mathbf{M_S} \end{bmatrix} \begin{bmatrix} \ddot{\mathbf{Q}}_\mathbf{R} \\ \ddot{\mathbf{Q}}_\mathbf{S} \end{bmatrix} - \begin{bmatrix} \Omega\mathbf{G} & \mathbf{0} \\ \mathbf{0} & \mathbf{0} \end{bmatrix} \begin{bmatrix} \dot{\mathbf{Q}}_\mathbf{R} \\ \dot{\mathbf{Q}}_\mathbf{S} \end{bmatrix} + \dots$$
$$\dots \begin{bmatrix} \mathbf{K_R} + \mathbf{K_C} & -\mathbf{K_C} \\ -\mathbf{K_C} & \mathbf{K_S} + \mathbf{K_C} \end{bmatrix} \begin{bmatrix} \mathbf{Q_R} \\ \mathbf{Q_S} \end{bmatrix} = \begin{bmatrix} \mathbf{F_R} \\ \mathbf{F_S} \end{bmatrix} \quad (3.19)$$

The $\mathbf{K_C}$ terms in Equation (3.19) represent the stiffnesses of the magnetic couplings between the two shafts. However, due to the actively controlled nature of the magnetic bearings, it is possible to implement other forms of coupling. For instance, damping can be added by applying a control force proportional to the relative velocity, rather than the relative displacement, of the two shafts. This may be modelled by modifying the second matrix term in Equation (3.19) to

$$\begin{bmatrix} \Omega\mathbf{G} - \mathbf{C_C} & \mathbf{C_C} \\ \mathbf{C_C} & -\mathbf{C_C} \end{bmatrix}$$

where $\mathbf{C_C}$ includes a damping rate. For the present case however, the model is left as in Equation (3.19).

To achieve a frequency analysis of a rotor subject to any given forcing, one can take the Laplace transform of Equation (3.19), set $s = j\omega$, and rearrange into the form of

$$\mathbf{Q}(j\omega) = (-\mathbf{M}\omega^2 - j\omega\Omega\mathbf{G} + \mathbf{K})^{-1}\mathbf{F}(j\omega) \quad (3.20)$$

It can be seen that for a specific rotor with a specific out-of-balance mass, all the terms on the right hand side of Equation (3.20) are known, and thus the response in the various degrees of freedom may be calculated. Note that the large inverse bracket on the right hand side of the equation is sometimes known as the *receptance matrix*.

3.1.4 State Space Formulation

For certain elements of analysis, it is convenient to derive a state space formulation of the governing equation of motion. Taking Equation 3.14, state variables are defined as $\mathbf{Q}$ and $\dot{\mathbf{Q}}$, and thus a state space representation given as

$$\begin{bmatrix} \dot{\mathbf{Q}} \\ \ddot{\mathbf{Q}} \end{bmatrix} = \begin{bmatrix} \mathbf{0} & \mathbf{I} \\ -\mathbf{M^{-1}K} & \Omega\mathbf{M^{-1}G} \end{bmatrix} \begin{bmatrix} \mathbf{Q} \\ \dot{\mathbf{Q}} \end{bmatrix} + \begin{bmatrix} \mathbf{0} \\ \mathbf{M^{-1}} \end{bmatrix} \mathbf{F} \tag{3.21}$$

As usual the output can be defined to select any of the state variables - of most interest in the rotor analysis codes are the displacements in the x and y directions, which give a physical response shape of the system to the input $\mathbf{F}$. These values can be selected for output with appropriately placed 1s on the main diagonal of $\mathbf{C_1}$ as in

$$\vec{y} = \begin{bmatrix} \mathbf{C_1} & \mathbf{0} \end{bmatrix} \begin{bmatrix} \mathbf{Q} \\ \dot{\mathbf{Q}} \end{bmatrix} \tag{3.22}$$

3.2 Application to Novel Rotor System

The modelling techniques described above are used to assess the merit of the proposed rotor system of Section 2.5. An example geometry is introduced for the purposes of this analysis. The system consists of a hollow tube steel rotor carrying three rotationally symmetric discs. The key dimensions are illustrated in Figure 3.5, with further details on the disc properties in Table 3.1.

For the purposes of modelling, the rotor is divided into 20 evenly spaced elements; the secondary shaft has 22 elements. This number of elements is greater than what would be necessary for moderately accurate calculation, but has the advantage of allowing the plotting of smooth, realistic deflected beam shapes. The rolling element bearings supporting the rotor are modelled as having a stiffness of 1×10^9 N/m with negligible damping (negligible damping is a realistic assumption for rolling element bearings, see Kramer [57]). The supports for the secondary shaft are modelled as pinned joints also with a stiffness of 1×10^9 N/m, also initially with no damping. Both shafts are made from steel.

Table 3.1: Disc properties of modelled system

Disc	Mass (kg)	Diameter (m)	Thickness (m)
D1	75	0.7	0.12
D2	100	0.8	0.1
D3	150	0.9	0.15

As this model is merely a proof of concept, the details of the magnetic bearing are not considered in depth. For the purposes of the model, it is taken that it has a mass of 30 kg, and can (under

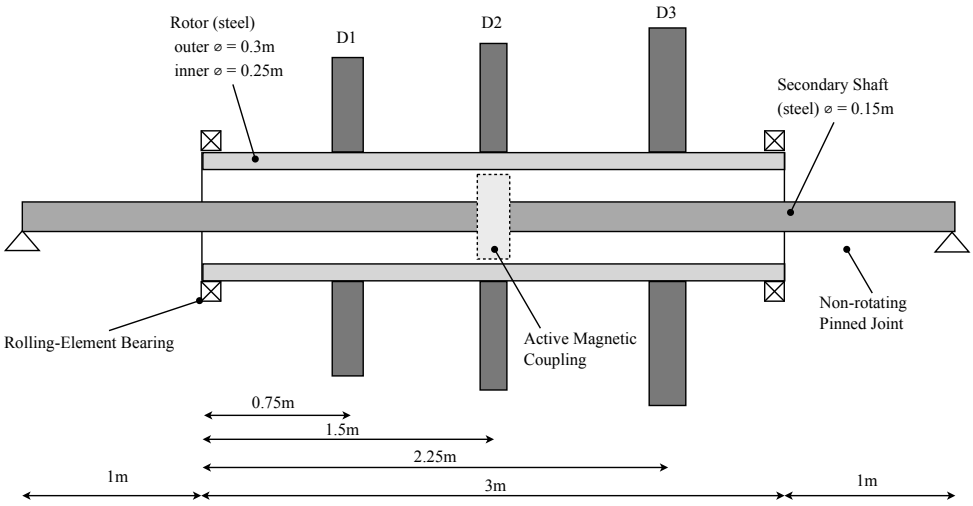

Figure 3.5: Geometry of an example rotor for illustrating the properties of the proposed vibration reduction method (not to scale)

appropriate control) effect a coupling stiffness of 5×10^7 N/m between the rotor and the secondary shaft.

A set of **M**, **G** and **K** matrices are created to describe the geometry presented, as per the preceding section. These are then combined in a state space representation, such that the system matrix **A** contains all information regarding the character of the rotor.

To prove the validity of the finite element model, the first three natural frequencies of each of the rotor and secondary shaft are calculated both numerically and analytically. Numerically, the natural frequencies are the imaginary parts of the eigenvalues of the system matrix. To enable the analytical calculations, the effects of the discs on the rotor and the mass of the magnetic bearing are ignored for this first calculation, and it is assumed the rotor is not rotating, i.e. can be treated as a beam. The equation for the analytical calculation is shown in Equation 3.23. This equation applies to beams with pinned ends, and can be found in any book on beam vibration, see for instance Meirovitch [58]. Table 3.2 presents these results.

Table 3.2: Natural frequencies of members of example rotor system calculated analytically and numerically. Discs and magnetic bearing effects excluded. Subscript $_a$ and $_n$ indicate analytical and numerical results respectively.

	ω_{a1}	ω_{n1}	ω_{a2}	ω_{n2}	ω_{a3}	ω_{n3}
	(Hz)					
Rotor	88	85	352	310	792	590
Secondary Shaft	12	12	49	49	110	109

The higher analytical values are to be expected, as the calculation assumes infinitely stiff

bearings / supports, whereas in the numerical model, values with more realistic stiffness are used. It is also expected that at higher modes, the finite stiffness of the supports will have a greater effect. The explanation of this difference is easily visualised in Figure 3.6. The figure shows the rotor mode shape associated with the third natural frequency (590 Hz) as predicted by the model, with each of flexible and rigid supports (stiffness of 1×10^{9} and 1×10^{15} respectively). Observe that the ends of the rotor are substantially displaced from the origin when flexible bearings are used. Conversely, the analytical calculation does not permit this behaviour, always forcing the rotor ends to remain undisplaced, which is associated with the higher natural frequency.

$$\omega_n = (n\pi)^2\sqrt{\frac{EI}{\mu l^4}} \tag{3.23}$$

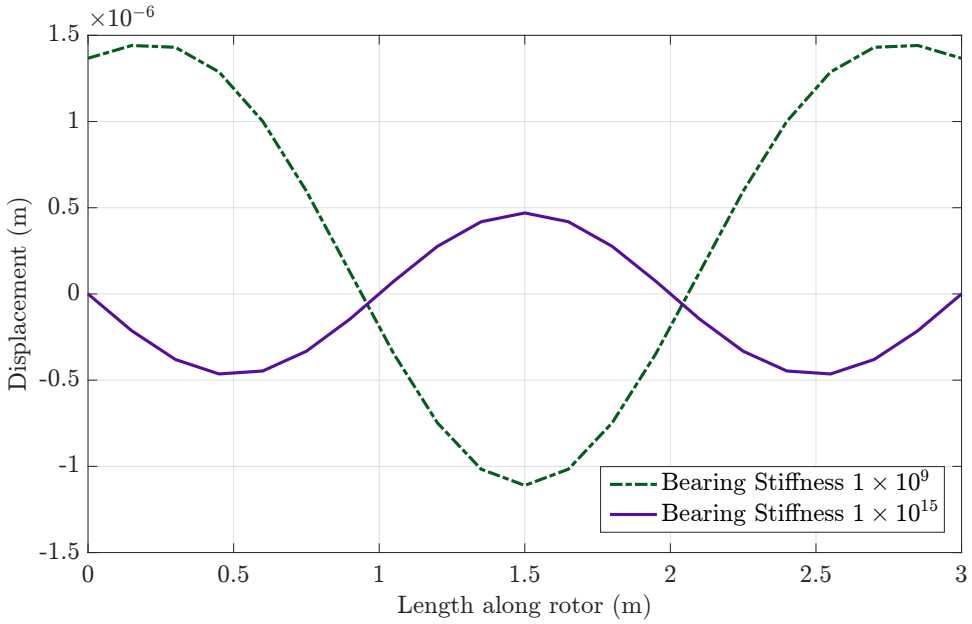

Figure 3.6: The effect of finite stiffness bearings on rotor third mode shape

With the numerical model shown to give results in agreement with analytical values, the eigenvalue analysis is repeated in the finite element model, but now with the discs and magnetic bearing included. The results are shown in Table 3.3. At this point, the magnetic bearing is still switched off, so that the two shafts effectively form two independent systems. It is observed that the magnetic bearing mass makes little difference to the natural frequencies of the secondary shaft, however the discs on the rotor substantially lower its natural frequencies.

Table 3.3: Numerically calculated natural frequencies of members of example rotor system, including discs and magnetic bearing

	ω_1	ω_2	ω_3
	(Hz)		
Rotor	62	234	465
Secondary Shaft	12	49	105

3.2.1 Singular Value Analysis

To assess the performance of a multi-degree-of-freedom system over a range of frequencies, it is useful to employ singular value analysis. This can be considered as an extension of a bode plot for a single degree of freedom system, whereby the influence of every input on every output is included in the analysis. As such a singular value frequency plot provides a very convenient way to assess the character of the system, and to see how certain operations change that character.

In particular, singular values are used in this project to compare the performance of the rotor when it rotates alone, as compared to when it rotates coupled to the secondary shafts by various control mechanisms.

A mathematical definition of singular values is shown in Equation 3.24. Here the matrix $\mathbf{A}$ is decomposed into a set of three matrices.

$$\mathbf{A} = \mathbf{U}\mathbf{\Sigma}\mathbf{V}^* \tag{3.24}$$

where the diagonal elements of Σ are the singular values. Such a tool is available through Matlab via the `svd` function.

To assess how useful the magnetic coupling may be, singular value analysis can be performed on each of i) the uncoupled system and ii) the coupled system. For the magnetic bearing/secondary shaft to be considered useful, the peaks of the coupled response must occur at different frequencies than the coupled response. The steps in the singular value decomposition are as follows:

1. form receptance matrix (as in Equation 3.20)
2. perform singular value decomposition
3. select largest singular value
4. loop through these steps at regular frequency intervals over range of interest
5. repeat with receptance matrix for both full system, and for rotor only to allow comparison

It is not actually necessary to use the entire receptance matrix, as the primary concern at this point is the behaviour of the rotor, while the repectance matrix contains data pertaining to the whole system, including both rotor and secondary shaft. Therefore only the top portion (the same number of rows as there are degrees of freedom in the rotor model) are analysed for singular values.

The result of performing this analysis on the system presented are shown in Figure 3.7. It is seen clearly that the coupled system exhibits a behaviour substantially different from the rotor alone. This indicates a good ability to alter the system characteristics through the activation of the magnetic bearing.

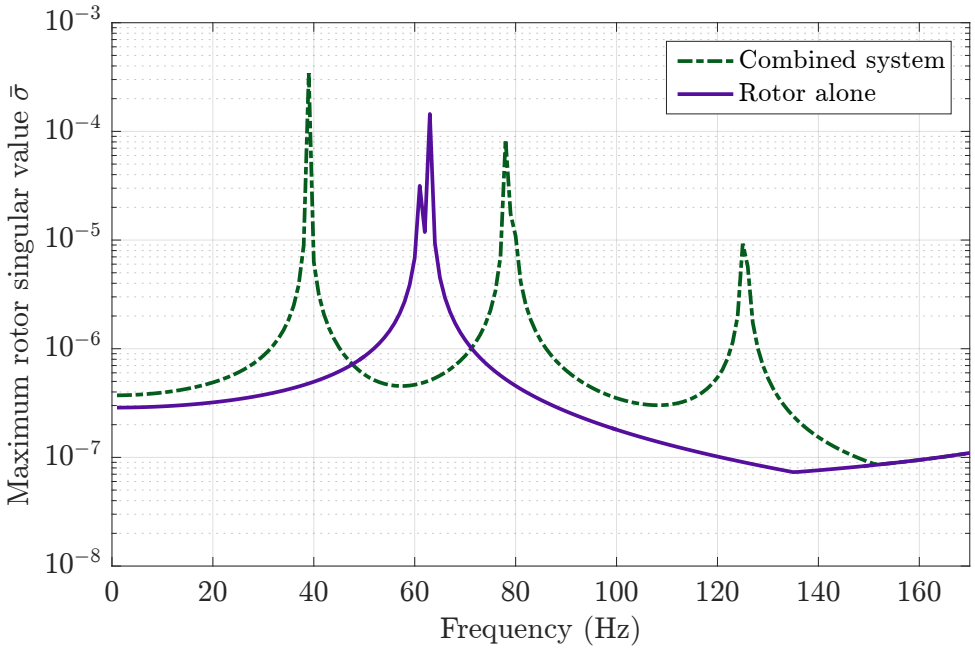

Figure 3.7: Results of singular value decomposition on rotor receptance matrix to evaluate the effect of activating the magnetic bearing

3.2.2 Out of Balance Response

Thus far the analysis has only looked at the system inherent character, but has not considered actual, real-world inputs and outputs. The final stage therefore is to simulate the response of the rotor to a specific out of balance mass over a range of rotational speeds. A value of mass of 1 kg is chosen and it is located at node 9 (out of 21). This node is chose because it will allow the excitation of at least the first three modes of vibration - a mass at the centre node, for instance, will not excite the second vibrational mode of the rotor, because the second mode of a symmetric rotor has a stationary point at this location. The response of the rotor - without any coupling to the secondary shaft - is shown as the solid line in Figure 3.8. The amplitude

shown is a root mean squared value of the amplitudes at each node. The plot represents the vibration in both the x and y planes, as the system is rotationally symmetric. As expected, a peak is seen around 62 Hz corresponding to the rotor first natural frequency.

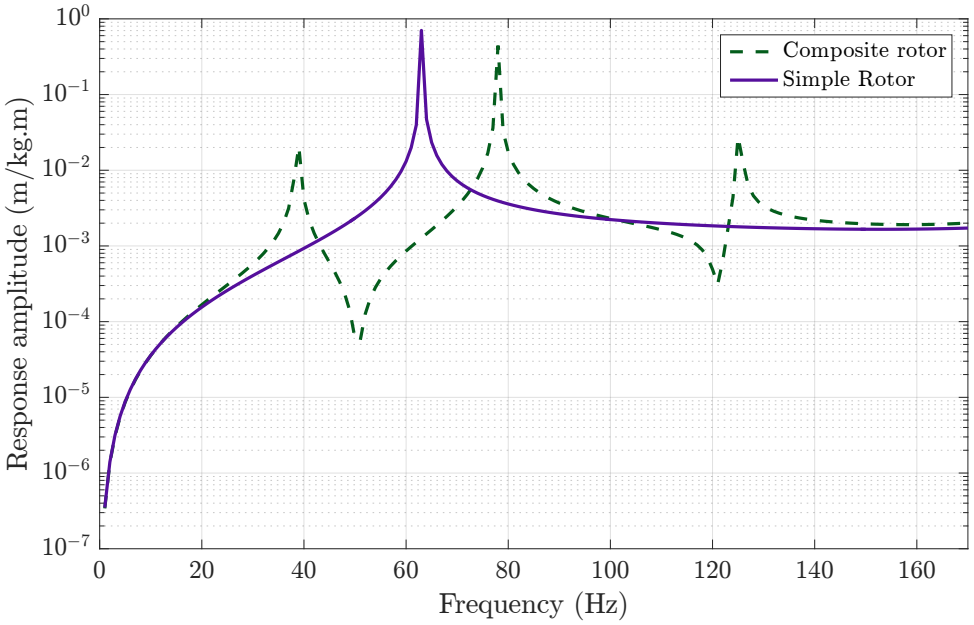

Figure 3.8: RMS response of the rotor in the example system both with and without coupling to the secondary shaft applied

A noteworthy difference is seen when comparing Figure 3.7 with Figure 3.8, specifically that the "Rotor alone" response in the former contains a split or double peak at the resonance, while the corresponding plot in the latter has only a single peak. As a singular value analysis, the data in Figure 3.7 represents information about the system characteristic, and the double peak illustrates that the rotor exhibits gyroscopic splitting - i.e. it has both a forward and a backward whirling mode. The two peaks occur at approximately 61 Hz and 63 Hz, either side of the 62 Hz first natural frequency of the non-rotating rotor. In contrast, the data of Figure 3.8 represents the system response to a specific forcing scenario (synchronous unbalance forcing). Under this particular forcing, only the forward whirling mode of the rotor is excited, and thus a peak is seen at 63 Hz, but not at 61 Hz.

The goal of coupling the rotor to the secondary shaft is to alter the character of the solid-line plot of Figure 3.8. Specifically, it is desirable to avoid the peak at 62 Hz. If this can be achieved, it should be possible by selectively turning on and off the active coupling(s) to switch between the two responses as the rotor speeds up in such a way as to avoid all vibration peaks.

In the model, therefore, a coupling is turned on at the mid-span location. The coupling is modelled with stiffness of 5×10^7 N/m. The out of balance response (with the same value and location as the above response) is simulated, and the result presented as the dashed line in

Figure 3.8. It can be seen that the peak of the rotor in the uncoupled situation is missed by the response when the coupling is activated. This is exactly what is required to allow the avoidance of the original peak, i.e. if the coupling is activated over the speed range of the original vibration peak, the amplitude of vibration seen in the rotor will now be greatly reduced. To illustrate the reduction, Figure 3.9 shows the response shape of the rotor both before and after the coupling is activated, together with the response of the secondary shaft when the coupling is active. The result presented is at a rotational speed of 62 Hz - at the first peak of the uncoupled rotor response. The slight lack of symmetry seen in the response is due to the out-of-balance mass being applied to an off-centre node.

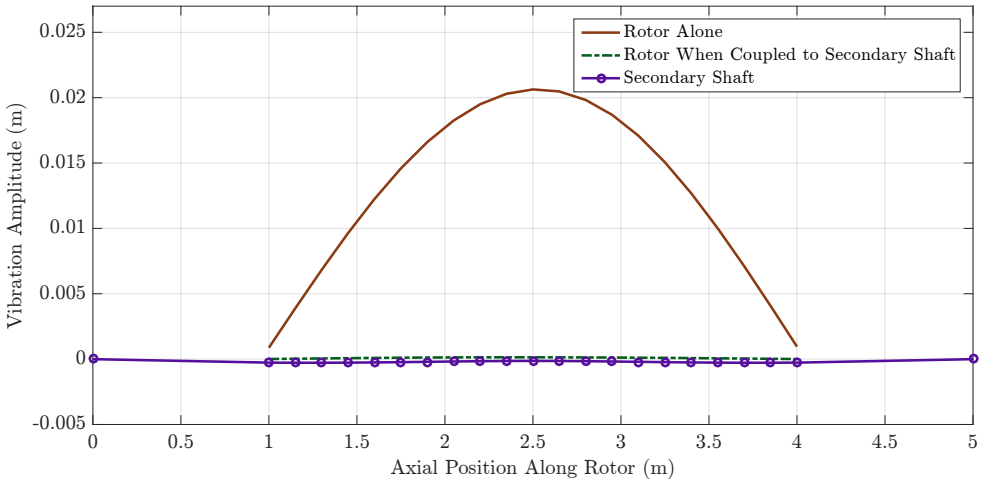

Figure 3.9: Response of "simple" and "composite" rotor to out of balance of 1 kg at 10 cm at off-centre node at 62 Hz rotational speed

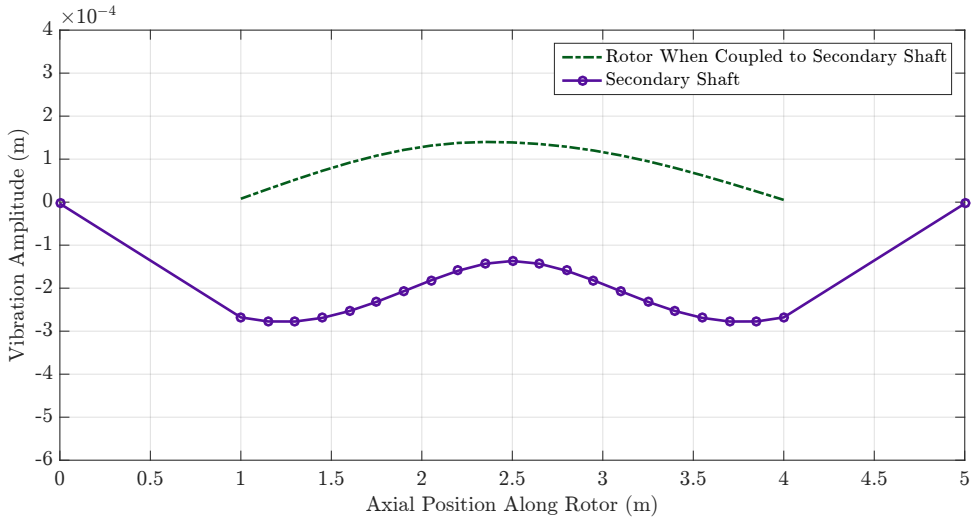

Figure 3.10: Close up of secondary shaft deflected shape as system response to 1kg out of balance at 10 cm at 62 Hz rotational speed

It is apparent that a reduction in vibration amplitude of an order of magnitude is achieved by the model with the coupling activated. The secondary shaft - plotted in close view in Figure 3.10 - is observed to be exhibiting a bending shape involving components of both first and third classic bending modes. Given that the excitation frequency is very close to the shaft's second natural frequency, and also given that it is impossible to excite the beam's second natural frequency due to the magnetic bearing being mounted at the centre, the combination of first and third mode shapes makes sense.

Closing Comments

This worked example has been used to illustrate that there is potential for successful vibration reduction through the introduction of a flexibly mounted magnetic bearing to a hollow shaft rotor.

It is highlighted here, however, that the control technique demonstrated in this example - i.e. coupling the shafts by means of a simple stiffness - is one of the most basic of a number of potential controllers that might be employed in such an application. Indeed it is demonstrated later in the thesis that other techniques have the potential to provide more capable and efficient vibration control, using the same system geometry, even with magnetic bearings capable only of much smaller forces.

Chapter 4

Test Rig Design and Construction

A TEST rig is required to practically verify the work of the theoretical modelling. The particular layout of this problem is highly specialised, and as such it was not possible to adapt an existing test rig to investigate the new layout. Instead, a completely new rig had to be designed and built from scratch. This process has formed a considerable part of the overall project, and this chapter details the development of such a rig.

Initially, an outline of the completed system is presented, as this helps give context can clarity to the more detailed consideration of the component parts that follows. The test rig details are then collected in three major sub-sections, respectively considering mechanical, electrical and software/computational components.

4.1 Introducing the Test Rig

4.1.1 Outline of Complete System

Before detailed attention is given to any aspect of the rotor system, an holistic overview of the entire test apparatus is provided. Figure 4.1 shows the main components of the overall system, and how they interact.

All the bespoke hardware addressed over the course of this chapter, including rotor, secondary shaft and magnetic couplings, are collected as a single unit labelled “Test Rig”. Inputs to the rig can be considered the currents delivered to the magnetic bearings. These are supplied from a bank of digital amplifiers. The rig outputs are displacement sensor readings, describing the motion of the components. Forming the link between these inputs and outputs is a dSPACE

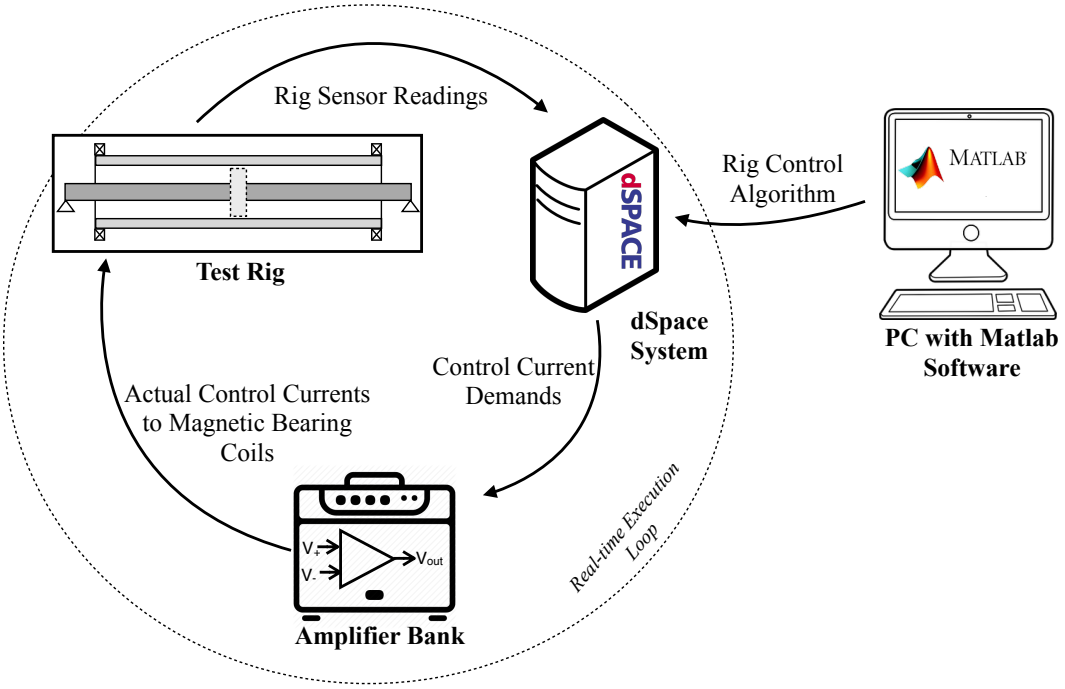

Figure 4.1: Holistic overview of key components of new rotor test rig

real-time processing unit. The dSPACE unit is running a programme designed on the PC, which includes all control logic for the rig and calibration data pertaining to the sensors and amplifiers. In accordance with the algorithms of this programme, the dSPACE system calculates a set of control currents to be enacted via the magnetic bearings in response to the inputted sensor signals.

4.1.2 Establishing Basic Rotor Geometry

As a starting point for designing a new test rig, some key constraints pertaining to the geometry and characteristics were identified:

- the whole rig must fit within a fairly compact footprint. A maximum overall length of 1.5 m was dictated by available lab space.
- the (hollow) rotor must have a sufficiently large inner diameter (ID) to accommodate a magnetic bearing capable of significant force output. Preliminary magnetic bearing calculations indicated a minimum ID around 80 mm
- the rotor must have sufficient wall thickness to avoid magnetic saturation under the applied fields
- the rotor must exhibit flexible behaviour at a relatively low rotational speed. It was

decided to limit the first critical speed to 5000 rpm, however a lower speed was highly desirable.

Clearly, a rotor such as the one in the case study presented in Section 3.2 is far too large to be practical in a small lab setting. Upon performing numerical modelling a variety of scaled-down rotors of similar basic geometry, it quickly became apparent that it would be difficult to design a single-piece rotor, of a diameter large enough to reasonably house a magnetic bearing, which could operate supercritically in a small-scale laboratory setup.

To overcome this difficulty it was proposed that a rotor could be designed to be fabricated out of multiple sections. As specified in the requirements, it is necessary for the rotor to contain at least one hollow section in which a magnetic bearing may be placed, however it is not necessary that the entire length of the rotor is of a uniform geometry. Working from this viewpoint, a design was conceived which consists of a rotor with a large hollow section at each end connected by a thinner, solid section in the centre. This centre section can be designed to give the overall rotor a far greater flexibility than if it had been constructed from a single large diameter tube.

Of course with such a design it is impossible to run a secondary shaft through the rotor as is done for a simple tube rotor. Instead, a modified design was conceived, incorporating two separate secondary shafts, one at each end of the rotor. Each secondary shaft is a clamped cantilever rather than a pinned beam, allowing the magnetic bearing to be inserted into a "blind" section of rotor. A generalised schematic of such a rotor system is presented in Figure 4.2.

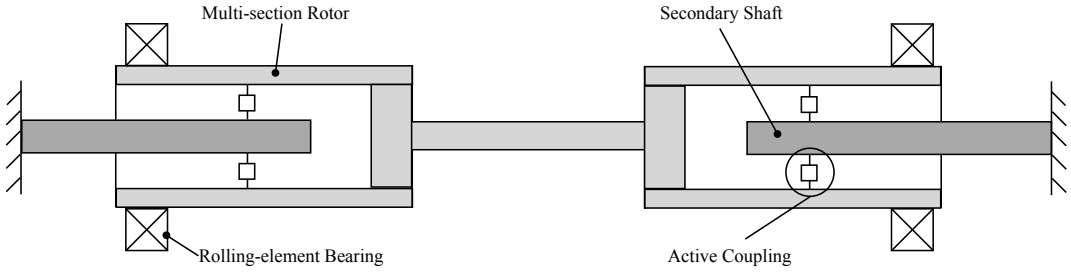

Figure 4.2: A multi-section rotor - the thin centre section of the rotor allows the system to have far lower natural frequencies than if the shaft was a single, large diameter tube

Once the general topology for the rig was established, numerical analysis - as presented in Section 3.1 - was used iteratively to inform the choice of the final dimensions. It was observed that the first critical speed of a rotor of this topology is almost exclusively dependent on the character of the central member, due to the fact that this member is greatly more flexible than the hollow tubes.

4.1.3 Completed Test Rig - A Preview

An outline of the final test rig constructed is shown in Figure 4.3. This preview is presented here to give context to the detailed discussion of the various components over the rest of this chapter.

As can be seen, the rotor is positioned in the centre of the bed plate, supported at either end by rolling-element bearings. The rotor has a multi-part construction, such that it is wide and hollow at its ends, with a thin, solid section in the centre. Mounted on this thin central section is an impulse turbine, which is used to drive the rotor from a compressed air supply.

Two secondary shaft sub-assemblies - one at each end of the rotor - support the magnetic bearings. In Figure 4.3 these are shown outside of the rotor for purposes of illustration, but in their normal position they are inserted into the hollow end sections of the rotor.

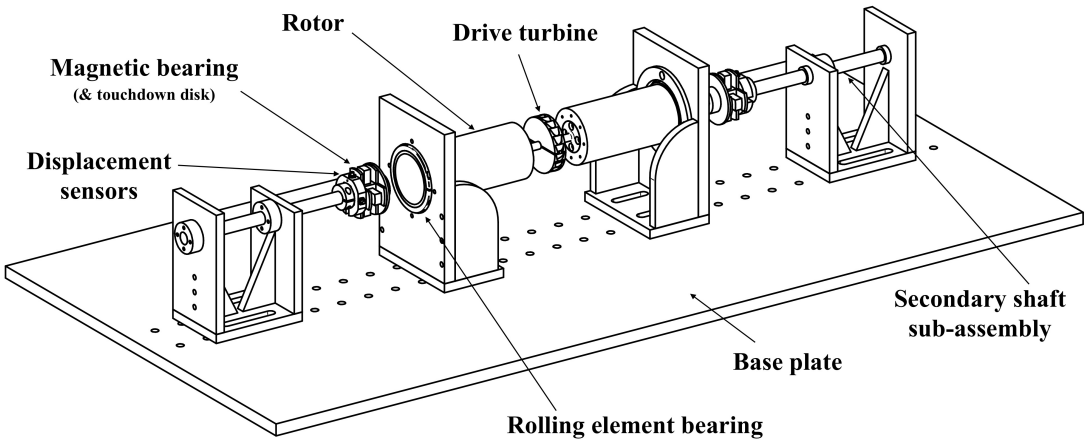

Figure 4.3: Outline view of complete test rig - note rig is symmetrical about turbine

The rest of this chapter presents more details on the design of the various parts of the system, including particular problems that were encountered and how they were solved.

Note that there were actually two separate rotors manufactured as part of this project - first and second generation designs. While both have the same key geometry, their construction details are substantially different, and so both generations are presented in the following material.

A Note on Notation

Over the rest of the thesis - particularly in later chapters where results are presented - many references are made to the ends and or axes of the rotor system. The system, as seen in Figure 4.3, clearly has two symmetric end, and these are termed End 1 and End 2. Which end is which was an arbitrary choice (they are nominally identical), but the names are applied

consistently and are a useful handle for identifying where a particular result or phenomenon was observed. Each end has sensors in each of the x and y directions. These are respectively horizontal and vertical in the usual Cartesian way. Sometimes, shorthand notation is used, e.g. a result may be said to have been observed in the "x1" axis. This indicates that the result comes from a measurement at "End 1" of the rotor in the horizontal plane. This notation is consistent throughout the thesis - axis x1 in Chapter 1 is axis x1 in Chapter 7 and so on.

4.2 Design Details - Mechanical

In this section, consideration is given the the main mechanical subsystems of the test rig. Specifically, focus is drawn in turn to each of the first and second generation rotor assemblies, and then to the secondary shaft arrangement. The material is designed to be explanatory in nature - fully dimensioned technical drawings of the components discussed may be found in Appendix B.

4.2.1 The First Generation Rotor

Figure 4.5 shows an exploded view of the first generation rotor for the test rig, and an associated parts list is given in Table 4.1; the right hand end of the rotor is left unlabelled, as these parts are a mirror image of the left hand end (parts (a) to (f)).

Table 4.1: Parts list for first generation rotor

Part	Name	Material
(a)	Rolling element bearing	Steel
(b)	Bearing mount block	Aluminium
(c)	Main rotor tube	Steel
(d)	Tube end cap	Aluminium
(e)	Alignment adjuster	Aluminium
(f)	Locking bush connecting tube to centre section	Steel
(g)	Locking bush for locating turbine	Steel
(h)	Turbine	Aluminium
(i)	Main rotor centre section	Steel

The main hollow sections (c) were constructed from welded steel tube with a 5 mm wall thickness - the thickness of this tube is chosen as a balance between being thick enough to avoid flux saturation from the magnetic bearings, while remaining thin enough to not be excessively heavy and thus induce a static bow in the rotor.

Figure 4.4: Parts list for first generation rotor

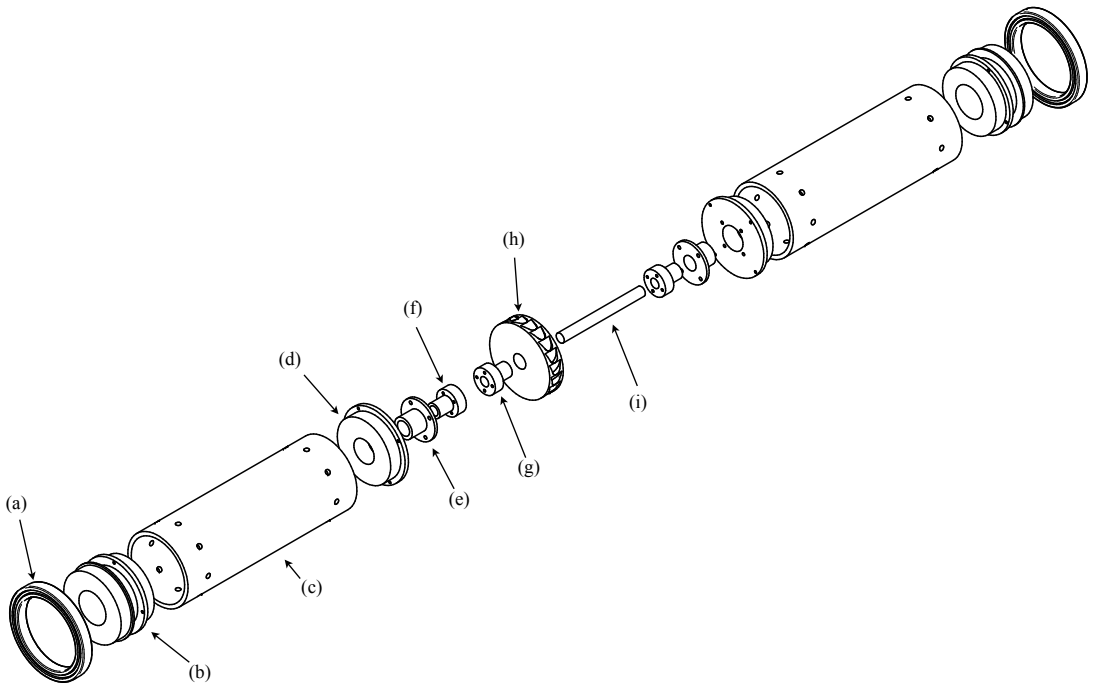

Figure 4.5: Exploded view of first generation rotor

The central section of the rotor (i) is formed from a solid steel bar with a 12 mm diameter. The thickness here is informed partly by the need for the rotor to be strong enough to support its own weight, and partly by the requirement of keeping the first critical speed as low as possible.

A combination of custom designed aluminium blocks (d and e) and off-the-shelf expanding locking bushes (f) are used to join these sections together. The turbine (h) is mounted via another expanding bush (g). The rolling element bearings (a) mount on the aluminium blocks (b) bolted to each end of the rotor.

Concerning Rolling Element Bearings

The rotor was designed to be fully supported on a pair of rolling element bearings, such that it can be operated entirely without the secondary shafts or magnetic bearings. The magnetic bearings were then to be used as a mechanism to alter the overall system characteristics. A substantial practical difficulty faced was to do with locating the rolling element bearings of the system. Initially it was desired that these bearings would be capable of being moved to different axial locations along the rotor. This would give the system substantial adjustability to be tested in a number of different topological arrangements with different natural frequencies.

However, the practical difficulties of designing such a bearing location system quickly proved to outweigh the advantages it might offer. A single pair of non-adjustable rolling-element bearing location points are still amply sufficient for testing the merit of the overall system design. It is logical to select locations at the very outer ends of the rotor as the bearings positions, as this gives the lowest critical speeds.

A pair of deep-groove ball bearings are selected for use in the rig. These offer good radial load and high speed capacity, as well as offering moderate axial load support, negating the need to include any further axial constraint on the rotor. Open (i.e. unsealed) bearings were chosen, as these offer far less rolling resistance than their sealed counterparts, meaning less torque is required to turn the rotor.

Consideration was given to mounting the bearings directly on the steel tube of the rotor, however, given the thin walled nature of the tube, it this was deemed to be unsatisfactory, and thus a bearing location block was designed. This is an aluminium block ((b) in Figure 4.5) which bolts onto the end of the rotor via a flange plate, and includes a machined surface and a retaining lip for location of the bearing. The bearing surface is machined to have an interference fit with the bearing inner race, and assembly is achieved with a manual press. The retaining lip ensures the bearing sits dead square to the block, and the alignment (or run-out) is checked after assembly with a Dial Test Indicator (DTI), and found to be within a 0.02 mm tolerance.

Shaft Alignment

Perhaps the single most difficult practical consideration of the test rig is achieving axial alignment of all the components. This includes both the set up to get the rotor to run true, and the locating of the secondary shafts to achieve the correct clearance between the magnetic bearings and the inner surface of the rotor.

The radial design clearance for the magnetic bearings is 0.7 mm, while the touchdown ring has a clearance of only 0.4 mm. With such fine tolerances, it is imperative that all components run with very good concentricity in order to avoid any contact between rotor and magnetic bearings. In a system of so many linked parts, this means each joint has to be very carefully considered to eliminate any play or slight misalignment.

The rotor is permitted a maximum of 0.1 mm eccentricity during low speed (i.e. rigid) rotation. To achieve this, a combination of shrink fits, flange joints and taper-lock bushes have been used.

The key to allowing precise alignment is to include capacity for fine adjustment in the design of the rotor. For this reason the flange joints which connect the large diameter tubes to the thin central section of the rotor, and the flange joints where the rolling element bearing blocks are connected to the tubes, are designed to have a clearance fit in the tubes, and the bolt holes in

the connectors are oversize. This allows the rotor to be assembled with the flange joints bolted only lightly, and then the joints can be gently tapped to reposition them.

To measure the alignment as adjustment is being performed, the rotor is supported in ground V-blocks on a flat marking-up table. A DTI gauge is then used to observe the run-out incurred by the joints in the rotor, and adjustments are made to compensate. It is important to work from one end of the rotor to another, such that all parts of the rotor are effectively aligned to the same datum.

The bearing stands were also skimmed to bring their heights into exact alignment, allowing the rotor to sit perfectly level. The same operation was performed on the stands which hold the secondary shafts, such that they can run exactly concentrically within the rotor. This ensures all parts must sit exactly vertically level. To align all components in the horizontal plane, and ensure none exhibit any twist, each of the four stands has one side skimmed, and a parallel tool is used to set each stand the exact correct distance and perfectly square to the machined edge of the bed plate.

Once all these operations were completed and all system components aligned in precisely the correct place, they were drilled and doweled to the bed plate. This allows for the system to be dismantled (which is necessary to include the magnetic bearing assembly), and then replaced in the exact same position with ease.

Rotor Drive Mechanism

Driving the rotor in this scenario is something of a challenge - in many rotor configurations, a motor is connected to one end of the shaft via a flexible coupling. With the rotor considered here, the ends of the shaft are largely inaccessible, due to the secondary shafts and their support brackets positioned at either end.

It would theoretically be possible to drive the rotor via a non-axially aligned coupling with a motor, for example via a belt drive or through gears. However these methods introduce significant complications, and possibly also implications for the rotor dynamic behaviour, especially when the rotor is vibrating significantly.

The final solution proposed therefore was to use an air-powered turbine wheel. This allows a contact free drive mechanism, and as there is no significant torque load on the rotor, does not require a particularly powerful air supply. A simple impulse type turbine was designed, based on a solid disc with dovetail cutouts around the circumference. This turbine was designed to mount at the axial centre of the rotor, on the thin section of shaft. The component is made from a single piece of aluminium, and can be seen in Figure 4.6.

In order to extract the maximum possible effect from a given airflow, a housing was designed to surround the turbine wheel and minimise the escape of air before it has done useful work.

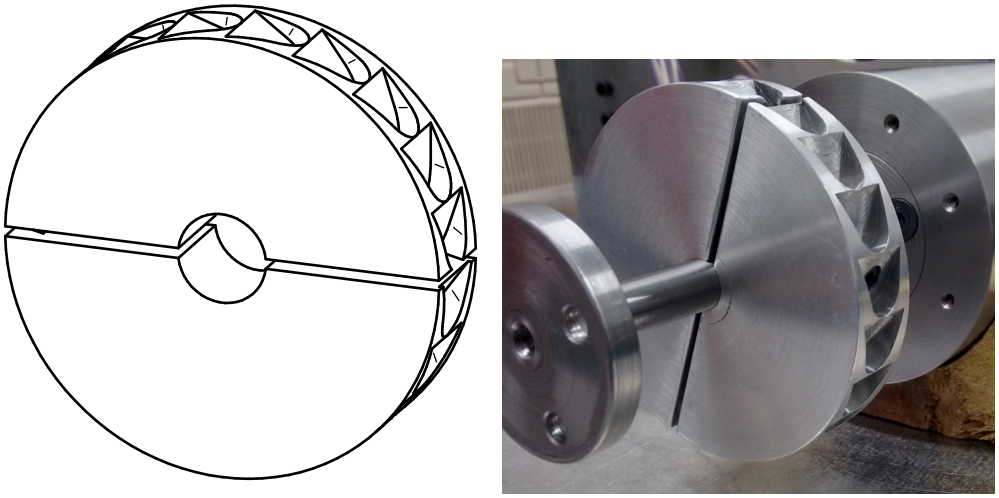

(a) (b)

Figure 4.6: Impulse turbine for driving the rotor. The turbine is split to facilitate assembly.

The housing was fabricated from aluminium, with acrylic side panels over the turbine chamber, complete with rubber seals. The exhaust gas exits through gaps left between the perspex side panels and the shaft of the rotor. The housing is illustrated in Figure 4.7.

The air supply is from a standard workshop air-line, operating at a pressure of 7 bar, which is easily capable of spinning the rotor to speeds well in excess of the first critical speed.

Running the First Generation Rotor

The first rotor constructed was very typical of a new design or prototype in the sense that the design evolved substantially during the course of construction, as various difficulties and problems arose and were addressed. A photograph of the final rig in the "First Generation" configuration is shown in Figure 4.8

During initial testing with the completed rotor, a number of issues were encountered which, when considered all together, motivated the complete redesign of the rotor construction. Particular points of concern were:

- it was discovered upon testing that results from the rotor had poor repeatability. Further investigation led to the discovery that the rotor had substantially non-uniform stiffness. This result is largely due to the tube used to construct the rotor - the welded tube is constructed from flat sheet which is rolled into shape and the seam welded. This process leaves significant stresses in the material, and the welding process leads to a seam of material of a stiffer, more brittle character.
- lack of fully-secure bearing constraint, leaving potential for the bearing inner race to slip

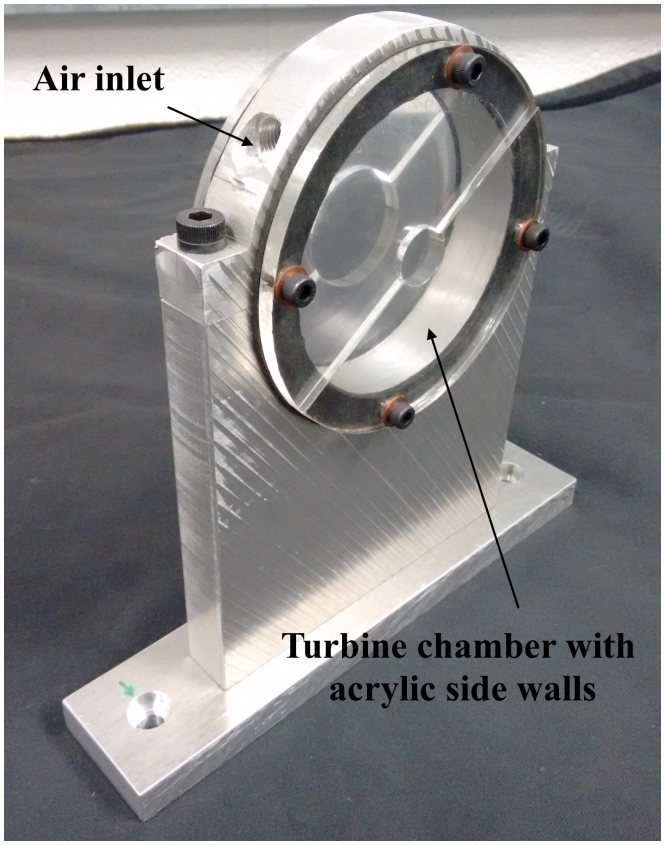

Figure 4.7: Housing for rotor drive turbine

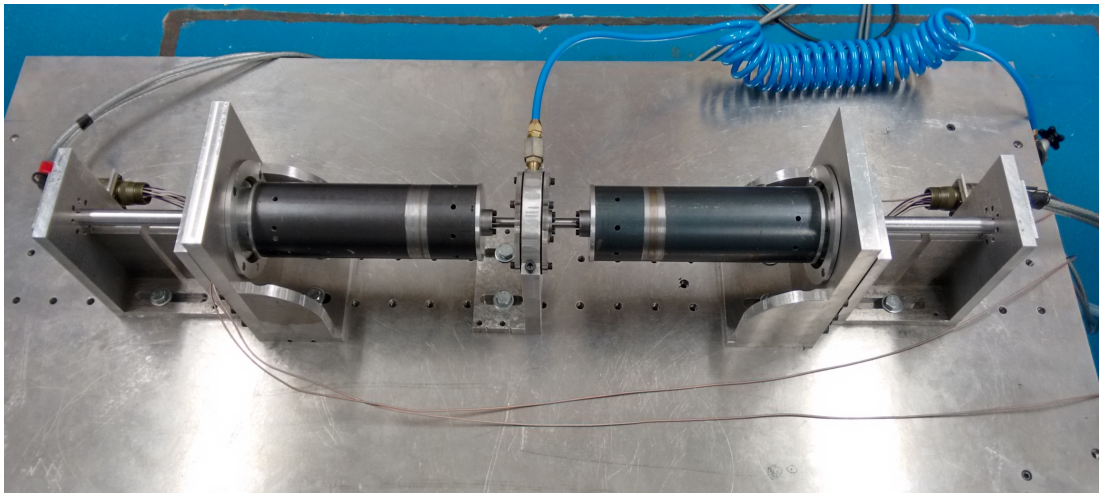

Figure 4.8: The completed first generation test rig

against the rotor

- as has already been described, aligning the many components of the rotor to all run with high concentricity was extremely difficult and time consuming. In addition to this, it was noticed that the vibration experienced by the rotor while running tests was sufficient to disturb the alignment, once achieved
- the use of the aluminium blocks at the ends of the rotor to mount the rolling element bearings made direct insertion of the magnetic bearings into the rotor impossible. Instead the rotor had to be partially dismantled for bearing insertion. This gave rise to two difficulties: firstly, the magnetic bearings are left virtually inaccessible once the rig is assembled, making visual inspection (e.e. during alignment set-up) impossible; secondly, it meant the axial alignment of the rotor assembly achieved on the marking-up table was lost, and had to be re-achieved with the rig in-situ - an awkward and cumbersome task.

4.2.2 The Second Generation Rotor

With much learnt from the construction of the first generation rotor, a new design was conceived. While maintaining the same overall geometry, the second generation rotor has a far simpler and more reliable construction. The exploded view shown in Figure 4.9 clearly illustrates a more streamlined rotor construction than the first generation. The main rotor is constructed from only three separate parts, which are all machined from solid billets of steel. The associated parts list is shown in Table 4.2.

Table 4.2: Parts list for second generation rotor

Part	Name	Material
(a)	Bearing retainer ring	Aluminium
(b)	Rolling element bearing	Steel
(c)	Main rotor tube	Steel
(d)	Turbine (split)	Aluminium
(e)	Main rotor centre section	Steel

Improvements over Mark I Rotor

The redesigned rotor includes a number of specific improvements which address the shortcomings of the first generation model.

Material

The rotor was fabricated from EN32 steel. Each of the three main sections is machined from

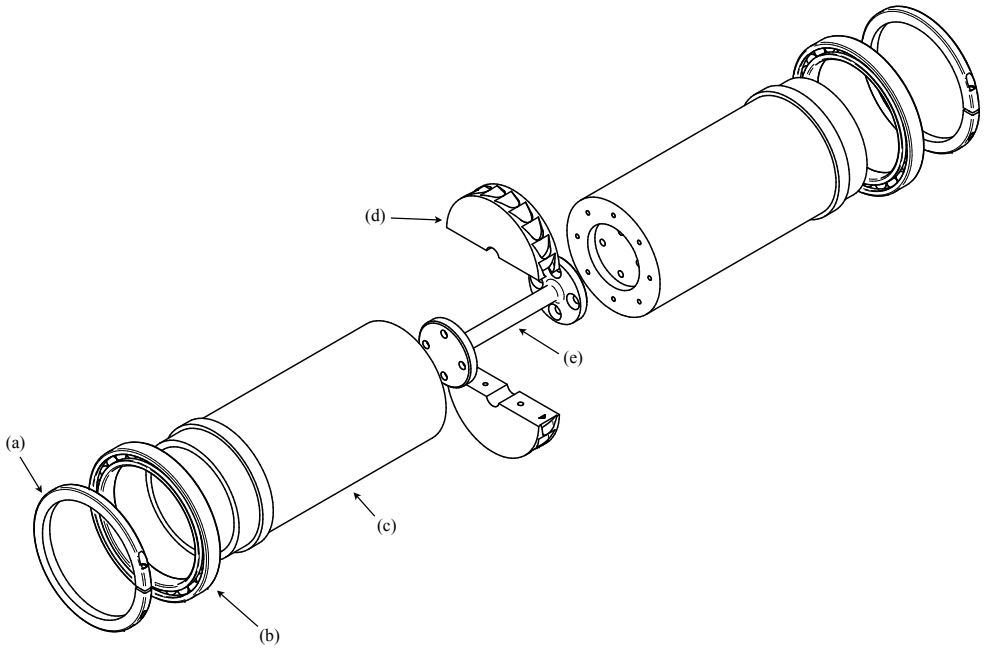

Figure 4.9: Exploded view of second generation rotor

a solid, normalised billet of material. This gives a huge advantage over the welded steel tube used in the first rotor, as the material has uniform properties and very little residual stress. This contrasts with the old tube, where the weld joint led to variable material properties and high internal stresses.

During manufacture, it was recognised that the machining to form the central thin section of the rotor may introduce some stresses due to the large step in diameter. For this reason, once the shape had been roughed-out, the piece was heat treated to alleviate any such stresses before the final geometry was machined.

Bearing Location

Two modifications to the mounting of the rolling element bearings have been implemented in the new design. Firstly, allowance was made to mount the bearings directly on the hollow steel sections of the rotor. This had not been possible previously as the tube used was too thin, and did not allow sufficient material for secure mounting. Therefore a slightly larger diameter bar was used for the new rotor, with the majority of the excess material machined away, but with suitable bearing mounting surfaces left.

This design eliminates the extra aluminium blocks used on the first generation rotor, and with them the possibility of introducing misalignment between the bearings and the rotor.

The second improvement to the bearing mounting mechanism is the inclusion of bearing retainer rings. These are simply split collars with a bolt to tighten them on the rotor. Given the

vibration expected during running of the rig, these collars prevent the possibility of the bearings becoming dislodged from from their location shoulder, and thus ensures that they will remain square.

Component Concentricity

The beauty of the new design is in its simplicity. Having only three components affords far less opportunity for alignment errors to occur. The key to allowing this simplicity was in fabricating each part from a solid billet (as opposed to starting with a tube). This allowed one end of each tube to be left closed, and into this remaining material a very accurate locating surface was machined.

In a similar way, instead of using a simple bar for the central rotor member, a much larger bar was used as the starting point, such that the ends could be left at a larger diameter, again to form an accurate locating surface, as seen in Figure 4.9.

Overall Assembly

Aside from the direct advantage of locating the bearings on the rotor itself, as outlined above, the elimination of the the aluminium mounting block used in the first generation design confers another considerable advantage. Specifically, the secondary shafts can now be directly inserted into the ends of the rotor without the rotor having to be disassembled in any way. Previously the process of inserting the secondary shafts was highly convoluted and, as it required partial disassembly of the rotor, was liable to upset the critical alignment of the various rotor components.

Illustrations

The second generation rotor constitutes the heart of the final test rig. The rig can be seen in Figure 4.10, and a 3D cutaway illustration showing a view of a magnetic bearing in its operational location is provided in Figure 4.11.

4.2.3 Secondary Shaft Sub-Assembly

The secondary shafts support and locate a number of components, in particular the magnetic bearings, the displacement sensors and the touchdown disks. The shafts are supported in their own dedicated brackets which are bolted independently to the bed plate. Each shaft is clamped at two locations via expanding locking collars to provide rigid support. An overview of the assembly that comprises the secondary shafts is illustrated in Figure 4.12 (parts list in Table 4.3), while a detailed, exploded view of the assembly arrangement of the components mounted on the shafts is shown in Figure 4.13; the eddy current sensors, supported in custom brackets, are closest to the clamped end of the shaft, and pass through clearance holes orthogonal to the

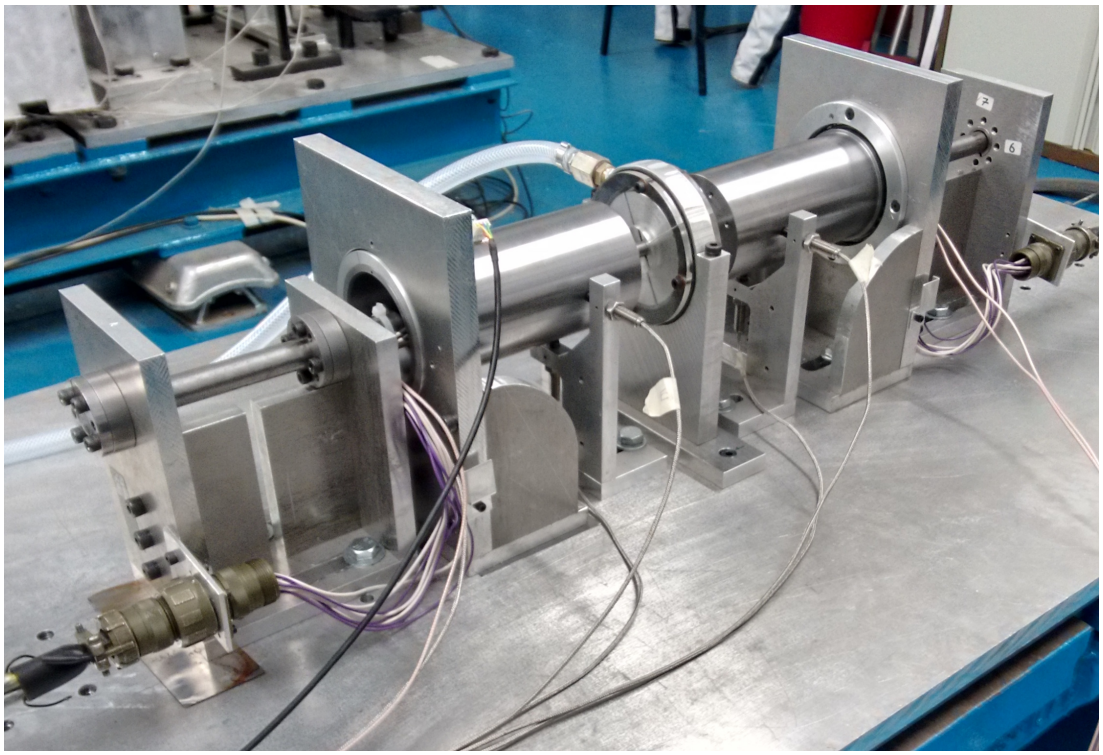

Figure 4.10: Photograph of the completed second generation rotor system

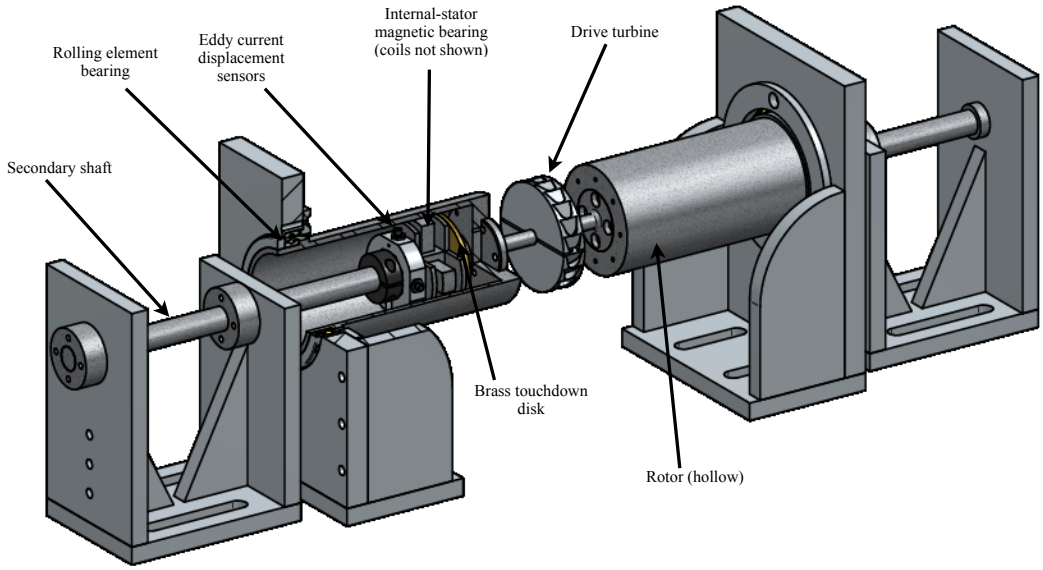

Figure 4.11: 3D CAD view showing key structure of the overall assembly of the final rig, including cut-away to see secondary shaft and magnetic bearing details

shaft axis, as shown in the fxigure. The location of these holes fixes the location of all the components mounted on the shaft, and as such the position is chosen in accordance with the results of the numerical modelling, to place the magnetic bearing at the desired distance from the clamped end. The magnetic bearing itself is the next component to be mounted, followed by the brass touchdown disk. This disk is 4 mm thick, and has a diameter 0.6 mm larger than the magnetic bearing. Its function is to protect the magnetic bearing from damage if a touchdown event with the rotor should occur.

The components are held in place axially between a pair of self-clamping friction shaft collars. In order to prevent the components rotating about the shaft, a small dowel is passed through the whole set of components, including the locking collars. As the collars are clamped tight and therefore unable to rotate, the magnetic bearing, sensors and touchdown disk are also prevented from rotating.

Table 4.3: Parts list for secondary shaft assembly

Part	Name	Material
(a)	Secondary shaft stand	Aluminium
(b)	Secondary shaft	Steel
(c)	Locking bush	(Steel)
(d)	Shaft friction collar	(Steel)
(e)	Sensor bracket (with sensors)	Aluminium
(f)	Magnetic bearing	SMC
(g)	Touchdown disk	Brass

Sensor Holders

In order to maintain the compact and clean design of the system, the sensors are located inside of the rotor, adjacent to the magnetic bearings. This presented a number of problems, both in terms of the physical design, and of the control.

The issues with control are based on the fact that, by mounting sensors on the secondary shaft, what you're actually measuring is the *relative* displacement of the rotor and the secondary shaft, not the *absolute* displacement of the rotor. The implications and solution of this issue are dealt with in Section 7.2.3.

From a system design point of view, the problem is one of location, i.e. how to physically install the sensors within the limited space available. The shortest-bodied eddy current sensors that could be found were longer than the inner radius of the rotor. This means they have to pass through the secondary shaft in order to fit. This called for holes through the secondary shaft,

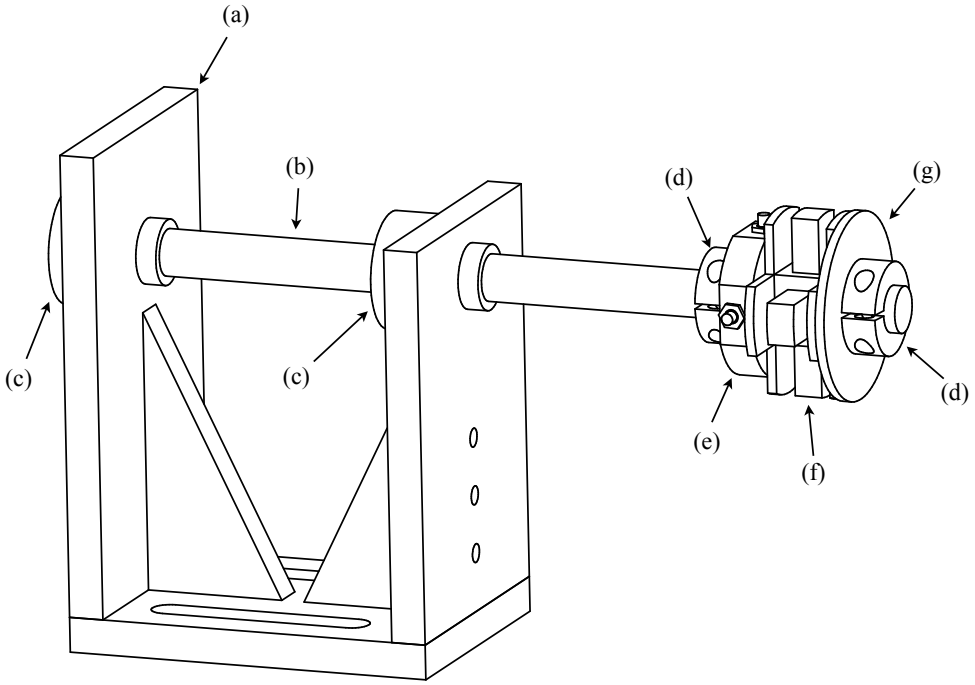

Figure 4.12: Overview of test rig secondary shaft

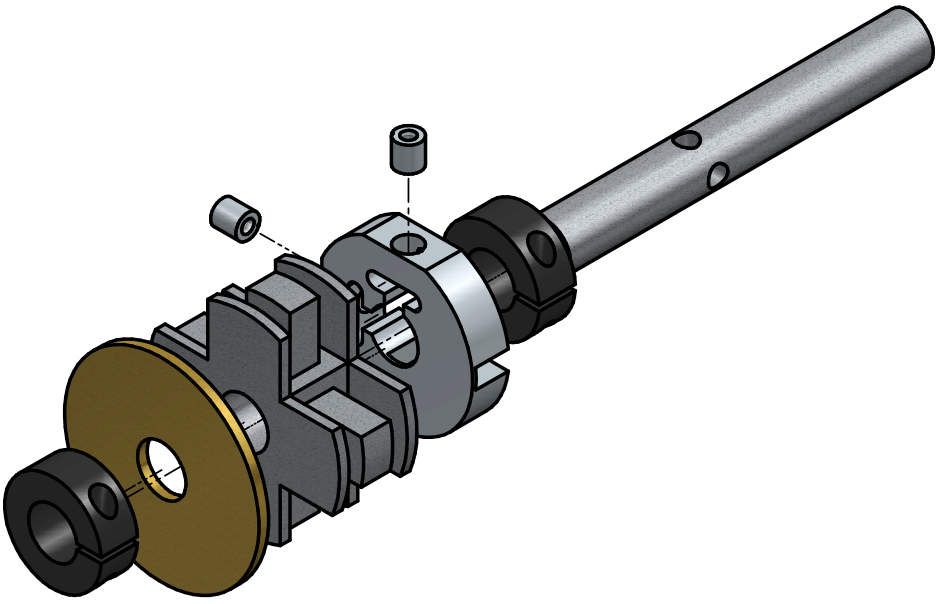

Figure 4.13: An exploded view of the components mounted on the secondary shaft. From left to right: outer lock ring, brass touchdown disc, magnetic bearing, sensor bracket, inner lock ring.

and specially designed brackets to hold the sensors in place. Figure 4.14 illustrates the solution used.

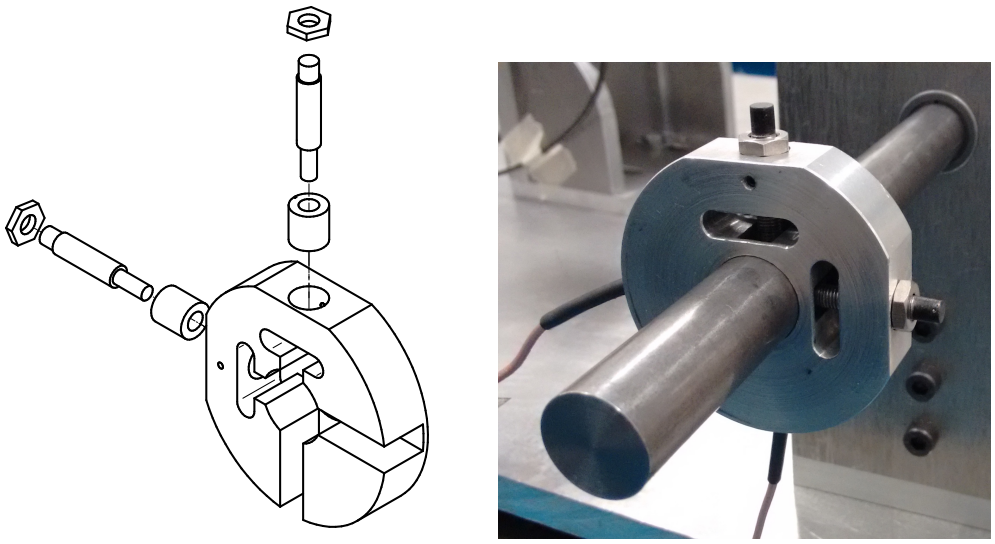

(a) (b)

Figure 4.14: Holding the sensors inside of the rotor requires a custom bracket and a hole through the supporting shaft

Note that, to facilitate easy insertion and removal of sensors, a removable sleeve is incorporated into the sensor bracket design, such that the sleeve may be screwed onto the body of the sensor, and then the unit may be slid directly into the accommodating space on the main sensor bracket. The sleeve is held in place with a grub screw.

Furthermore, for practical reasons the pair of sensors held in each bracket are not actually quite in-line with one another. This is necessary to prevent them interfering with each other in the centre of the bracket. Instead, they are offset by 3 mm, giving just enough room to pass one another, but without the offset being significant enough to effect accuracy of readings (which are assumed to be in a single plane for a given sensor pair).

4.3 Design Details - Electrical

Given the inherently mechatronic nature of magnetic bearing systems, all such plants must incorporate various electrical subsystems. The two main electrical subsystems are the amplifiers which drive the magnetic bearings, and the sensors which report the rotor position. Information about both of these is presented here, together with information about the design and implementation of an encoder to record rotor speed.

4.3.1 Amplifiers

Each of the two magnetic bearings of the system has four coils, each of which has its own amplifier. This gives a total of eight amplifiers. In order to be used to control system vibrations, it is important for the amplifiers to have faster dynamics than the plant they are controlling. This essentially means they must respond quickly and accurately to changes in the demand current provided by the controller.

For this rig, a set of Xenus XTL Digital Servo Drive units is used. These amplifiers were already available in the lab, and were amply sufficient for the needs of the magnetic bearings. If anything, these units (up to 4 kW, continuous current rating 12 A) were somewhat over specified for the job, but as they are software tuneable, it was possible to tune them to the very low loads of the magnetic bearing coils. The amplifiers were checked with their in-built scoping tool, and found (once tuned) to be matching with reasonable accuracy current demands of several amps up to at least 1 kHz. It is noted that their tracking performance, while good, was not outstanding, and this imperfection may have been a contributory factor to numerous cases of instability that were encountered while designing controller for the rig.

4.3.2 Displacement Sensors

The control of the rotor system relies on the instantaneous position of the rotor being known, and this data must be provided by sensors on the rig. A number of displacement sensors are potentially suitable for this application, and an overview of some of the different types available is provided in Table 4.4.

In this project, the use of eddy current displacement sensors was selected for a combination of reasons. They offer a good balance of high resolution, satisfactory interference rejection (depending on wiring) and low cost, and in addition a number of drive units for such sensors were already available in the lab, offering a substantial cost saving. An illustration of the basic working principle of eddy current sensors is provided in Figure 4.15.

Table 4.4: Various sensors that could be used to measure rotor position / displacement in a system with magnetic bearings

Sensor Type	**Description**
Optical	There are a number of sensing techniques employing optical technology, all of which involve emitting and then measuring beams of light. Strategies available include measurement of direct reflection from a target, intensity measurement based on occlusion effects, and interferomatic techniques, whereby phase changes between light beams covering different distances (one known, one target) are measured. Optical techniques in general are extremely capable, offering very high resolution and frequency of measurement and little or no susceptibility to interference. They do, however, generally have a higher cost than many other sensors, limiting them to applications where their higher performance is essential. For magnetic bearings systems, other, cheaper sensors are normally sufficient.
Hall Effect	A Hall Effect probe is capable of measuring the strength of a magnetic field. As a proximity sensor, it provides a source of a magnetic field, often a permanent magnet, and the strength of the resulting field will be dependent on the distance the sensor is from the target. A significant drawback of these sensors in a magnetic bearing system is that they are highly susceptible to interference from the magnetic fields of the bearings themselves, so may require to be located a significant distance away. This in turn amplifies possible problems of sensor non-colocation and resulting instability effects. Therefore, while they are low cost sensors and very useful in a variety of applications, there are better alternatives for magnetic bearing systems.

Eddy Current	Eddy current sensors contain a coil at the tip of the sensor which is fed an alternating current. This current generates a magnetic field, which induces small currents (eddy currents) in the target. These eddy currents generate their own small magnetic field, which acts to oppose the field of the probe. The interaction of these two magnetic fields is dependent on the distance between the probe and the target; the electronics in the sensor drive unit detects the interaction, and generates an output voltage proportional to the gap size. Eddy current sensors require a conductive target, and work best with ferromagnetic materials. They can be susceptible to noise interference, especially switching noise from digital amplifiers which are commonly used with magnetic bearings.They are best suited to small distance measurements of the order microns to millimetres.
Acoustic (ultrasonic)	Acoustic sensors work on the same principle as sonar or echo location - a pulse of sound (ultrasonic) is sent out, and then the returning wave reflected from the target is picked up. The time delay between the emission and the detection of the pulse allows calculation of distance. Acoustic sensors are something of a niche in applications of this kind - they tend to excel better in fields where larger displacements are to be measured, or where their particular characteristics provides some notable benefit in a certain application. For high resolution, high frequency measurement of small, sub-millimetre displacements of metallic targets, other sensors listed here are more appropriate.
Capacitive	In any arrangement with two conducting plates separated by a reasonably small non-conducting gap (often air), there exists a property known as capacitance. This property is a measure of how the system responds to a potential difference applied across the plates. For an arrangement where the area and material of the plates and the separating gap are constants, the capacitance varies only with the size of the gap between the plates. For capacitive sensing, the probe tip acts as one of the plates, while the target being measured is the other. The probe carries electronics to generate and measure an electric field between itself and the target, and thus (via calibration) provide a measurement of the gap size. Capacitive sensors are substantially similar to eddy current sensors, although their “working medium” is an electric field rather than a magnetic field. Capacitive sensors can offer higher resolution than eddy current sensors (down to nanometer level), but also come with a corresponding cost penalty.

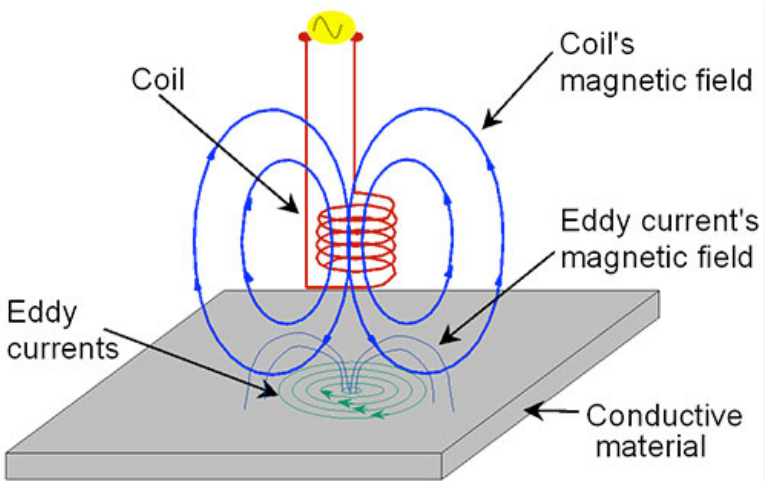

Figure 4.15: Fundamental principle of operation of eddy current sensors. *Image courtesy: http://www.analog-eetimes.com*

Sensor Calibration

The sensors output a voltage which corresponds to the distance they are from the surface being measured. The exact nature of the relationship between voltage and distance varies according to a number of parameters, including the target material, the geometry of the target (flat, curved etc) and angle of sensor with respect to target. Indeed, the units are so sensitive that even small differences in the manufacturing of each sensor will have an effect, meaning that no two sensors are guaranteed to give identical outputs in identical circumstances.

These factors mean each sensor must be individually calibrated in a situation simulating the conditions which will prevail in the sensor's final location. To do this, a custom target was made, taken from the same material the tubular section of the rotor is made from. The target also has the same curvature as is seen on the inside of the rotor. This target piece was mounted on the moving arm of a highly accurate digital micrometer, with the sensor being calibrated held pointing squarely at the target. The sensor is connected to the computer via dSPACE, such that its raw output voltage is displayed on screen. The micrometer arm is then used to slowly move the target rotor piece from touching the sensor away over a distance range of interest. At regular intervals, the reading on the micrometer and the corresponding voltage output of the sensor are recorded, and thus a custom calibration curve produced. The calibration characteristics for each of the sensors are then input to the computer, such that the program can display displacements in millimetres directly.

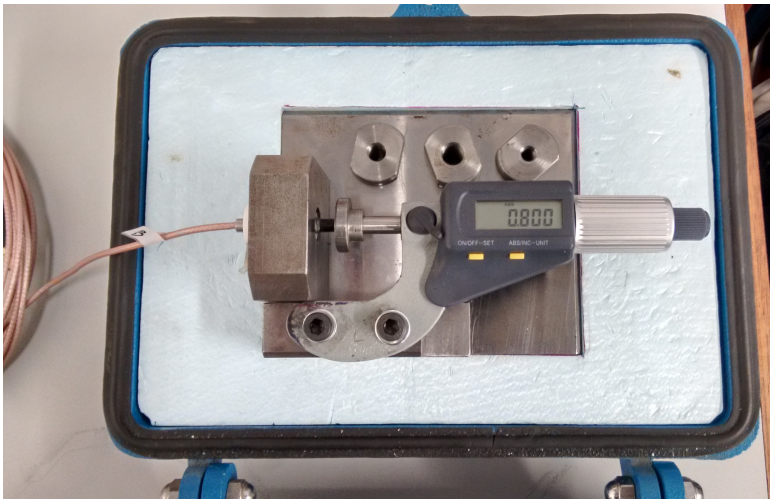

Figure 4.16: Arrangement for calibration of eddy current sensors

External Sensors

The test rig is designed such that it may be used with feedback provided only by sensors mounted on the secondary shafts, as presented above. However, for the purposes of proving the capabilities of the system, it is useful to be able to directly measure the motion of the rotor relative to the fixed base. For this purpose a second set of four eddy current sensors are employed. These are mounted on their own brackets bolted directly to the baseplate. It is stressed that these are not to be used for control of the rig in any way, but purely for data collection purposes.

4.3.3 Encoder

During early testing, the rotational speed of the rotor was only determined manually, with a hand-help optical tachometer. While this gives a good guide to the speed, it is useful to have the speed data collected and retained in the computer for later analysis. In addition it is more convenient to have this data constantly displayed on the rig computer interface instead of taking manual readings. For these reasons, an encoder was designed for the system.

A number of potential methods of passing the rotational speed to the dSPACE system were considered, including the use of an external eddy current sensor or hall effect sensor. In the end however, a simpler and cheaper, yet highly reliable solution was found making use of a slotted optical switch to record rotational speed during testing. A small pick-up is included at one end of the rotor to break the beam of the switch once per rotation. The switch is chosen due to its simple yet reliable operation, and lack of interference with any other part of the system.

A photograph of the encoder is included in Figure 4.17. The output signal is taken to the

dSPACE system to allow real time monitoring and recording of speed data which will correlate with vibration data collected.

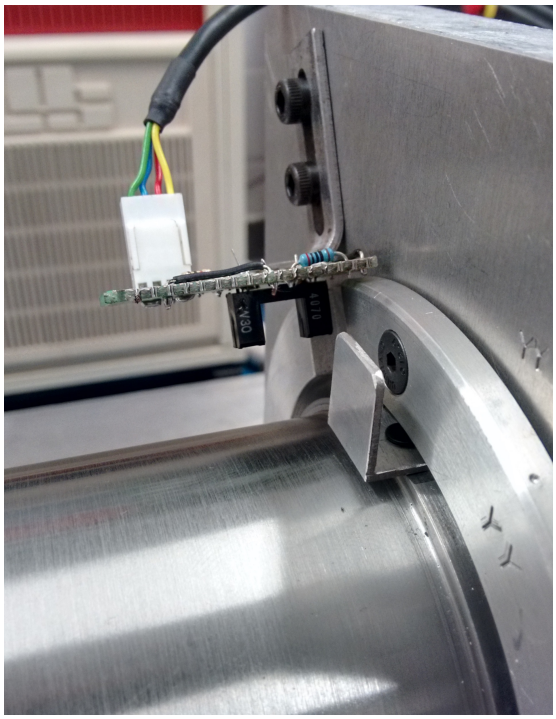

Figure 4.17: Slotted optical switch shown next to rotor-mounted pick-up, together forming a simple encoder

The encoder circuit outputs 0 V (nominally) when the optical switch beam is unbroken, and 5 V when the path is obstructed. In order to convert this series of pulses into a meaningful speed reading, the data is passed through a rinsing-edge counter, which is reset every half a second. The output of the counter is passed to a sample and hold block, which is triggered by the same 0.5 s signal which resets the counter. This gives an output that updates every 0.5 s, and between updates holds a value equal to the number of pulses counted in the preceding 0.5 s. This value is interpreted as "number of pulses in half a second", and from there is converted to a speed in hertz. The Simulink circuit to interpret the encoder signal is shown in Figure 4.18.

4.3.4 Obstacles and Considerations

Sensor Discrepancies

In making comparisons between the readings of the internal and external sensor sets, as well as between values predicted in simulation, it is important to bear in mind that they cannot be expected to be identical.

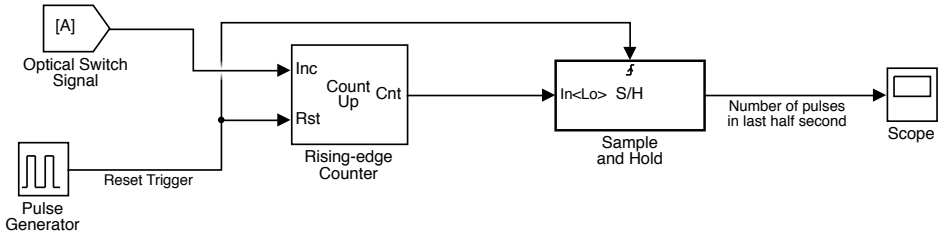

Figure 4.18: A rising edge counter used with the slotted optical switch to form an encoder. The count is reset by the pulse at a frequency of 2 Hz.

In particular, regarding the two separate sets of sensors (internally and externally mounted), there are two clear causes of expected discrepancy. The first has already been alluded to above, and it is related to the calibration of the sensors and their extremely high sensitivity. The internal sensors were calibrated against a concave surface to try and emulate the internal rotor surface they read in service. However, there was no convex calibration target available for use with the external sensors (which measure the convex external surface of the rotor in service). Therefore these sensors were calibrated against a flat target, which could lead to the sensors reporting a slightly larger-than-actual size for the gap when used on the rotor.

The second expected cause of inconsistency between internal vs. external sensors is due to their axial locations. Due to practical space considerations, the two sets of sensors are not mounted in exactly the same plane as each other. This is easily illustrated with a cross section of the rig from above, as shown in Figure 4.19. As can be seen, the externally mounted sensors are located slightly closer to the centre of the rotor than the internal set. As the rotor is constrained at its ends by the rolling element bearings, and almost all flexible behaviour is expected to occur in the thin central section of the shaft, the external sensors would be expected to return a larger reading than the internal sensors for a given rotor deflection.

While the second issue could easily be resolved by a simple geometric compensation factor, the calibration issue would still remain, and thus it is considered preferable to use empirically derived compensation factors. This essentially means mechanically causing a rotor deflection, recording the readings of the deflection by each of the sensors, and then calculating a scaling factor between equivalent external/internal sensor pairs. Values of external/internal scaling factor have been measured as:

None of the results presented later rely on an accurate direct comparison between internal and external sensor magnitudes, so this “problem” is not in any way troublesome. However it is highlighted here to explain why the external sensors often report a larger value than their internal counterparts when observing the same motion, and the scaling factors may be used if direct comparison is required at any point.

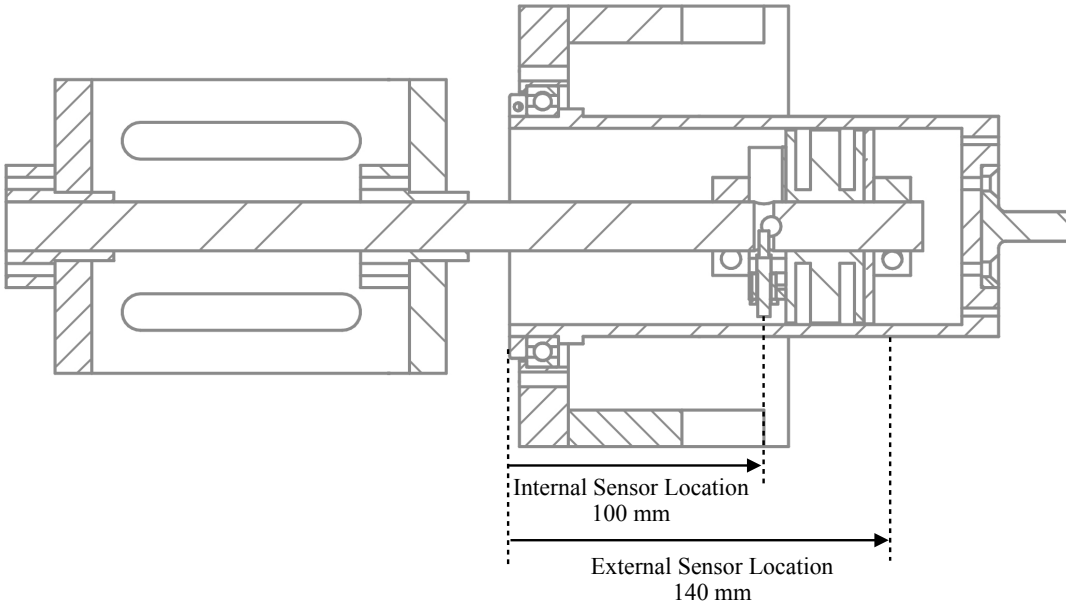

Figure 4.19: Internal and external sensors lie at different axial locations, causing them to give different readings for a given rotor displacement

Table 4.5: Empirically derived compensation factor between internal and external sensors in each test rig axis

Axis	Scaling Factor
x1	1.6
y1	1.7
x2	1.4
y2	1.4

Noise Interference

Some substantial issues were experienced with sensor signals being obscured - and in some cases effectively obliterated - by interference noise. A clear link was quickly established between the noise and the amplifier bank, i.e. when the amplifiers were activated, the noise was present in the signals. The switching circuits of digital amplifiers are known to generate substantial electromagnetic interference, and via probing the various components of the rig circuits, it was proved that the amplifiers were indeed broadcasting a very strong interference.

Given the strength of the noise, it was a little more difficult to ascertain exactly where in the rig circuits the noise was being picked up, and thus to find an appropriate solution. It was eventually discovered that the eddy current sensors themselves are well shielded, and were not susceptible to the noise of the amplifiers. In the original setup, the signals then proceeded from

the eddy current sensor drive unit via a serial cable to a breakout board, after which the signals were routed to a 50 pin sub-D connector, which carried them to the analogue-to-digital (AD) board of the dSPACE unit.

The serial cable was, in the first instance, identified as a weakness, leading to an altered set up where the outputs of each eddy current driver were taken via individual BNC cables to the breakout board. The BNCs provided a significant improvement over the original serial cable, due to their better shielding.

However, the noise issue was still present at unacceptable levels. Further investigation revealed that the 50 pin sub-D cable was actually picking up significant noise. As only a few of the 50 available channels were in use, it was decided to eliminate this cable, replacing it with a custom connector which allows the individual BNC cables carrying the sensor readings to connect directly to the sub-D input on the dSPACE AD board. The connector fabricated for this purpose can be seen in Figure 4.20. This further reduced to noise seen in the readings, this time to an acceptably small level.

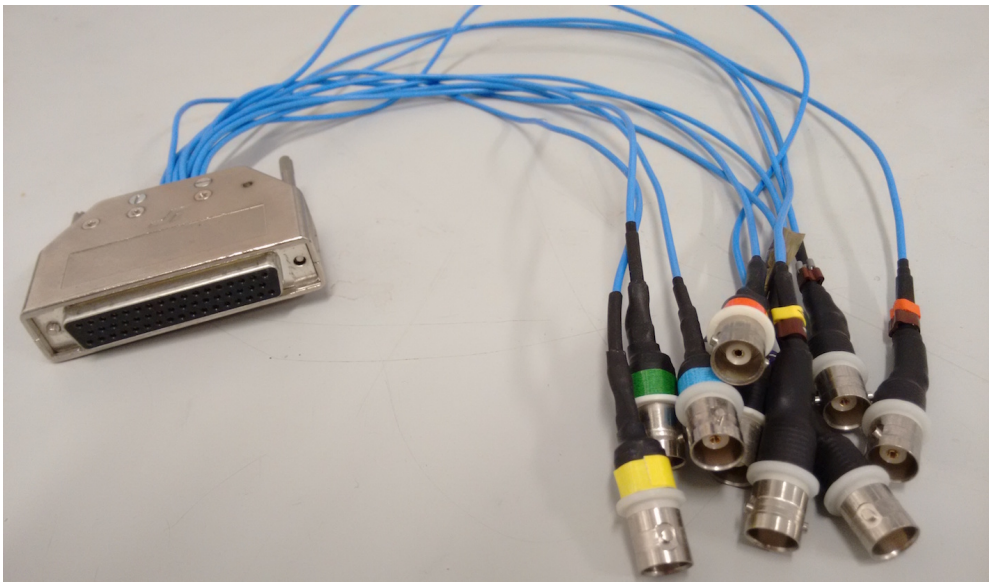

Figure 4.20: Custom connector to bring BNC cables directly to the dSPACE unit, enabling substantial signal noise reduction

4.4 Design Details - Software

In order to operate the rig, a bespoke software interface was created. The "technical" aspects of this software is built in Simulink, dealing with receiving sensor signals from the rig, and outputting amplifier demands to operate the bearings. Information on this aspect is presented in Section 7.1.

The "front end" for the Simulink model is then constructed in dSPACE ControlDesk. This is a traditional user interface with graphs, numerical readouts, buttons, sliders and so on for observing and controlling the signals of the underlying Simulink model. A screen shot of the interface designed is shown in Figure 4.21. The panels down the left-hand side are used for imposing open-loop signals on the rig. In the centre, the readings from the eddy current sensors are plotted, but in orbit form (x against y plots), as well as in individual time-series plots. On the right-hand side, activation of both the PID and H_∞ controllers is provided.

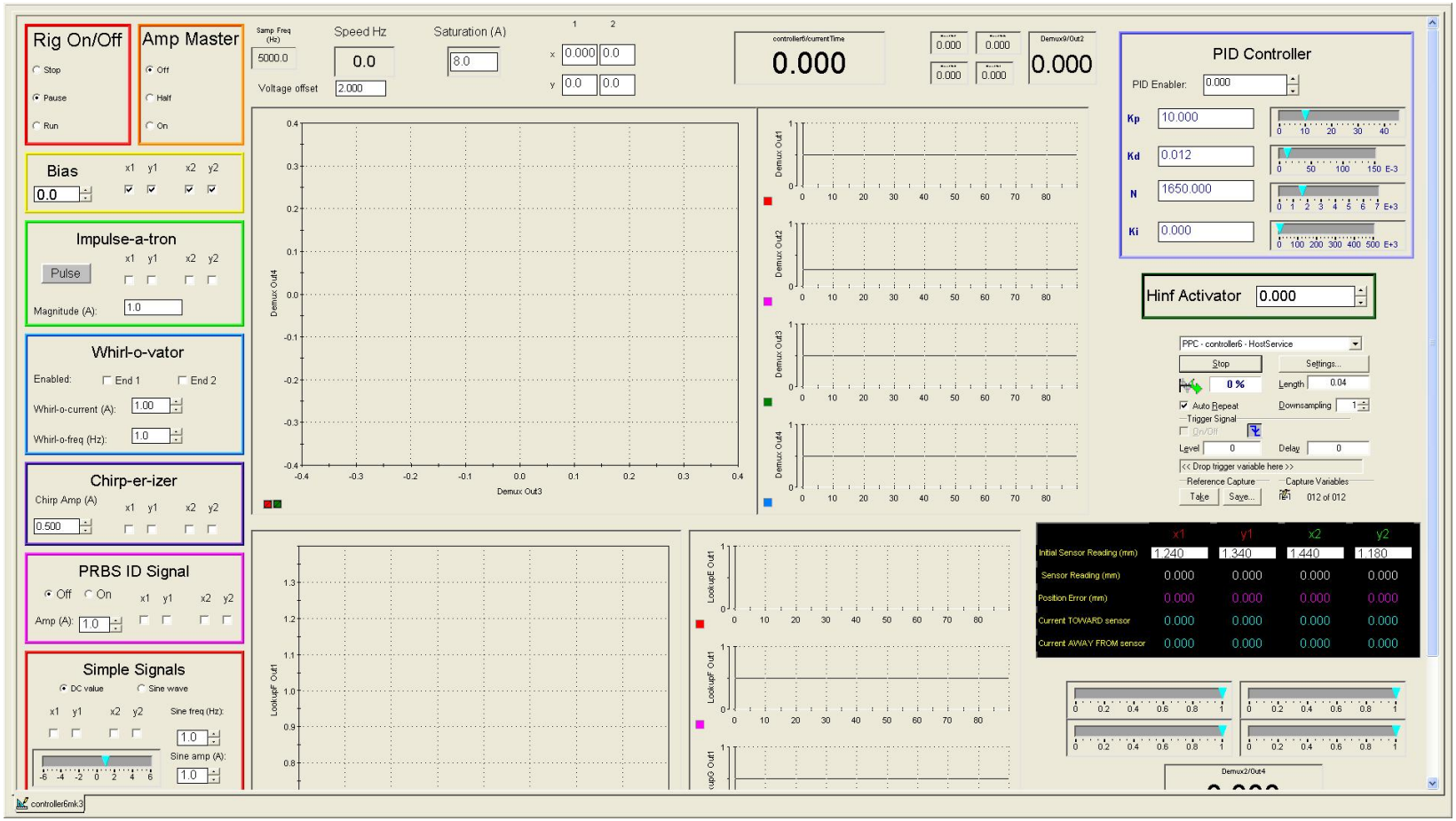

Figure 4.21: Software interface designed in dSPACE ControlDesk for operating test rig

Chapter 5

Magnetic Bearings - Theory, Design and Materials

THIS chapter give consideration to the test rig magnetic bearings, which will form the active couplings between the rotor and the secondary shafts. To begin with, the fundamental equations and principles behind electromagnetic levitation are presented, including basic physical considerations, as well as the control requirements for stable levitation.

A particular challenge with this project relates to geometry and construction of the magnetic bearings, given the tight space constraints locating the bearings *inside* the rotor entail. The question of how the geometry was designed, and how this led to the selection of a Soft Magnetic Composite (SMC) material are addressed next. This is followed by some experimental test results illustrating the satisfactory properties and performance of the SMC bearings.

5.1 A Mathematical Consideration of Magnetic Bearings

A mathematical treatment of magnetic bearings may begin with the analysis of a single "horseshoe" electromagnet attracting a ferromagnetic block - conceivably part of a rotor. With a knowledge of the physical properties of such a system, it is desired to calculate the attractive force between the magnet and the block, given a known flow of current in the coils of the electromagnet. A system of this kind is shown in Figure 5.1. For initial analysis, the system is considered as four distinct "units": the magnet, the block (or rotor), and two separate air gaps. Ampère's Law is then applied to the overall circuit.

$$\frac{B_1 l_1}{\mu_1} + \frac{B_2 l_2}{\mu_2} + \frac{B_{g1} l_{g1}}{\mu_{g1}} + \frac{B_{g2} l_{g2}}{\mu_{g2}} = NI \tag{5.1}$$

where B_x, l_x and μ_x are respectively the magnetic flux density, length of magnetic path and relative permeability of "component" x in the system. N is the number of turns of the coil on the electromagnet, and I is the current in the coil.

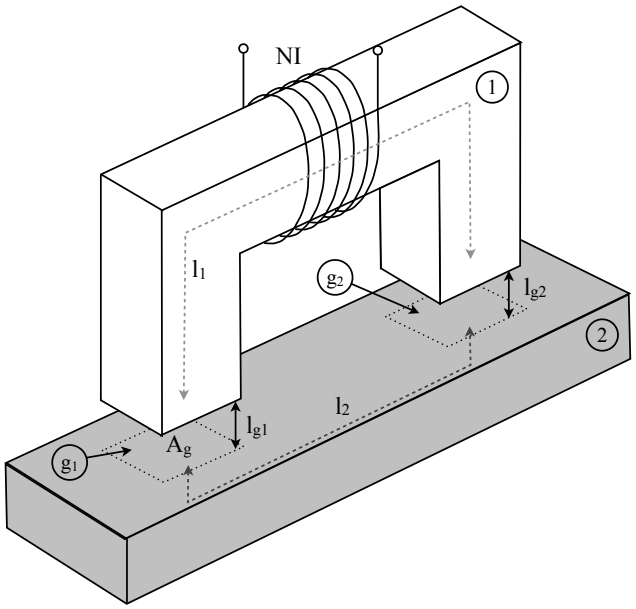

Figure 5.1: Key properties of the basic horseshoe electromagnet for force analysis

It is recognised that the relative permeability of the air gap will be far lower than that of either the rotor or the electromagnet core (by around nine orders of magnitude assuming both rotor and magnet are ferromagnetic), and thus the gap terms will dominate the equation. It is also noted that, assuming no flux leakage, all flux density terms B_x will be equal. Finally, it is observed that lengths of the air gaps are identical ($l_{g1} = l_{g2} = l_g$) and the value of the relative permeability of the air gaps is

$$\mu_{g1} = \mu_{g2} = \mu_0 = 4\pi \times 10^{-7} \text{ N/A}^2 \text{ - the permeability of free space}$$

These considerations allow the simplification of Equation (5.1) to

$$\frac{2Bl_g}{\mu_0} = NI \tag{5.2}$$

In general, the force acting on a body due to the magnetic field it is immersed in is approximated by

$$f = \frac{1}{2\mu_0} \sum_{i=1}^{n} B_i^2 A_i \tag{5.3}$$

This comes from consideration of Maxwell's stress tensor [55]. In this instance, the assumption of no flux leakage means there is only flux outside the ferromagnetic bodies in the air gaps, so Equation (5.3) becomes

$$f = 2 \times \frac{1}{2\mu_0} \times B^2 A_g = \frac{B^2 A_g}{\mu_0} \tag{5.4}$$

Now from Equation (5.2) it is seen that

$$B = \frac{NI\mu_0}{2l_g} \tag{5.5}$$

and this can then be substituted into Equation (5.4) to give

$$f = \frac{(NI)^2 A_g \mu_0}{4l_g^2} \tag{5.6}$$

This equation applies to a single horseshoe electromagnet. To extend the analysis to a typical magnetic bearing, a pair of such electromagnets are considered working opposite to each other, as in Figure 5.2. If the rotor is dead centred between the two magnets, then each has an air gap of g_0. If the rotor is displaced slightly, say in the direction towards electromagnet 1 by a distance y, the gap size for electromagnet 1 is $g_0 - y$, while the gap for electromagnet 2 becomes $g_0 + y$. In such a scenario, the overall force on the rotor towards actuator 2 is given in Equation (5.7).

$$f = \frac{N^2 A_g \mu_0}{4} \left(\frac{I_2^2}{(g_0 + y)^2} - \frac{I_1^2}{(g_0 - y)^2} \right) \tag{5.7}$$

This equation is a non-linear expression in terms of both current and gap length. From a control point of view, it is highly desirable to work with a linear equation, and so it is undertaken to linearise the expression about a working point.

To achieve this, the concept of a bias current is introduced. This is a current which is present in all coils of the magnetic bearing when the rotor is in the dead centre position. The overall current in a given coil then is the sum of the bias current i_b, and the demanded control current i_c:

$$I_1 = i_b - i_c \qquad I_2 = i_b + i_c \tag{5.8}$$

If a total current becomes less than zero, i.e. if $i_c > i_b$, the the current for that coil is set to zero, due to the fact that a "negative" current produces the same attractive force on a ferromagnetic body as the equivalent positive current.

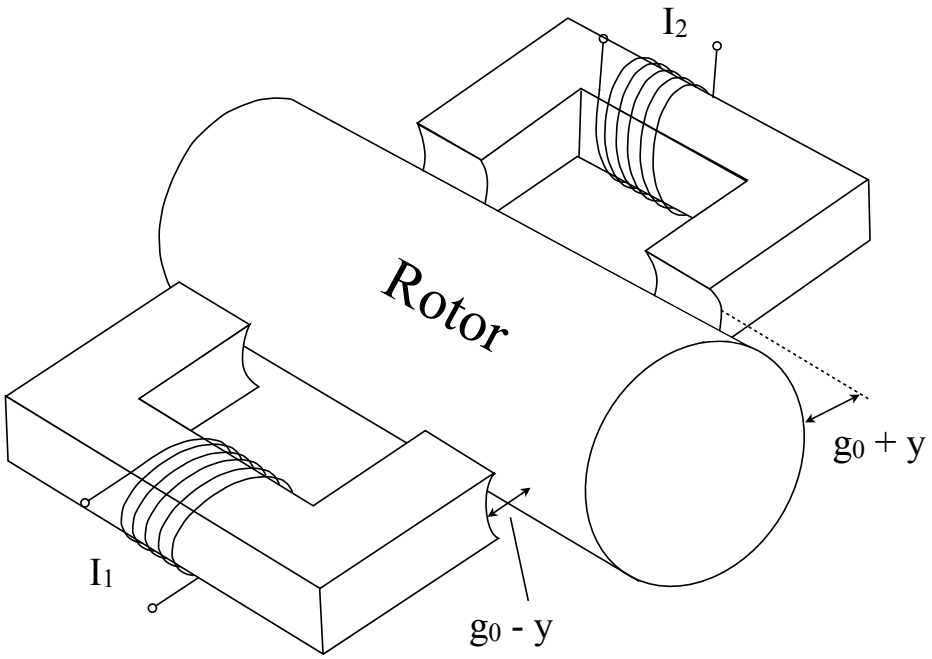

Figure 5.2: A pair of opposing horseshoe electromagnets acting on a rotor

Now applying this substitution to Equation (5.7), it is seen that the overall force on the rotor is

$$f = \frac{N^2 A_g \mu_0}{4} \left(\frac{(i_b + i_c)^2}{(g_0 + y)^2} - \frac{(i_b - i_c)^2}{(g_0 - y)^2} \right) \tag{5.9}$$

This can now be linearised for small changes about the bias current i_b and the equilibrium gap g_0 through use of the Taylor expansion:

$$f = f|_{y=y_0, i_c=i_{c0}} + \left.\frac{\partial f}{\partial i_c}\right|_{y=y_0, i_c=i_{c0}} (i_c - i_{c0}) + \left.\frac{\partial f}{\partial y}\right|_{y=y_0, i_c=i_{c0}} (y - y_0) + \ldots \textit{(higher order terms)} \tag{5.10}$$

At the linearisation point, $y_0 = 0$ and $i_{c0} = 0$, thus

$$f = f|_{y=0, i_c=0} + K_y y + K_i i_c \tag{5.11}$$

where

$$K_y = \left.\frac{\partial f}{\partial y}\right|_{y=0,i_c=0} = -\frac{N^2 A_g \mu_0}{g_0^3} i_b^2$$

which is the open loop (negative) stiffness of the system, and

$$K_i = \left.\frac{\partial f}{\partial i_c}\right|_{y=0,i_c=0} = \frac{N^2 A_g \mu_0}{g_0^2} i_b \tag{5.12}$$

which is the current or actuator gain.

5.1.1 Achieving Positive Stiffness

Magnetic fields naturally exhibit a negative stiffness characteristic. To use a magnetic actuator stably, however, it must be actively controlled such that it exhibits a positive stiffness. Consider the case shown in Figure 5.2; if the rotor moves towards actuator 1 by a distance y, it is desirable to apply a force away from actuator 1, to move the rotor back to the centre, i.e. a force proportional to -y is required.

Now consider the resultant force of the actuator pair, as expressed in Equation (5.7), only this time expressing the force towards actuator 1, rather than 2:

$$F = K\left[\frac{(i_b + i_c)^2}{(g_0 - y)^2} - \frac{(i_b - i_c)^2}{(g_0 + y)^2}\right] \tag{5.13}$$

where $K = \frac{N^2 A_g \mu_0}{4}$. Now a g_0^2 term is extracted from the denominator of each term, giving

$$F = \frac{K}{g^2}\left[\frac{(i_b + i_c)^2}{(1 - \frac{y}{g_0})^2} - \frac{(i_b - i_c)^2}{(1 + \frac{y}{g_0})^2}\right] \tag{5.14}$$

Multiplying the denominators leads to

$$(1 - \frac{y}{g_0})^2 \times (1 + \frac{y}{g_0})^2 = 1 - \frac{2y^2}{g_0^2} + \frac{y^4}{g_0^4} \tag{5.15}$$

However, as y is small, it is considered reasonable to neglect the latter two terms, and treat the result as unity. Thus equation 5.14 becomes

$$F = \frac{K}{g_0^2}\left[(i_b + i_c)^2(1 + \frac{y}{g_0})^2 - (i_b - i_c)^2(1 - \frac{y}{g_0})^2\right] \tag{5.16}$$

This may be expanded (once more neglecting terms in y^2) and collected to give

$$F = \frac{K}{g_0^2}\left(4i_b i_c + \frac{4(i_b^2 + i_c^2)}{g_0}y\right) \tag{5.17}$$

As above, in order for the system to exhibit positive stiffness, it is required that the force is proportional to $-xy$. If i_c is set to zero (only a bias current is used in the bearing), it is clear that $F \propto y$, i.e. the system has negative stiffness. This is an inherent characteristic of a non-controlled magnetic field. It is equally clear that if i_b is zero, no matter the value of i_c, the relationship $F \propto y$ will always hold, due to the i_c^2 term. Therefore for positive stiffness characteristic, we set $i_c = -k_p y$, where k_p is a controller gain, and require $k_p > \frac{i_b}{g_0}$. This leads to $F \propto -y$, which represents a positive stiffness.

5.2 Bearing Design / Geometry

In addition to the new ideas regarding rotor topology presented in earlier chapters, significant consideration is given to the magnetic bearings that are to form the active coupling elements. In the vast majority of magnetic bearing systems used today, the stator of the bearing is outside of the rotor. This arrangement is chosen because it removes size constraints from the design of the stator allowing higher capacity bearings to be designed. Also, it is clearly infeasible to use internal stator bearings on either solid shafts or very thin shafts. However, the external stator does have disadvantages. It takes up significant space along the rotor's length that may otherwise be either used for mounting other components. Furthermore, in certain applications there may not be space in the vicinity of the shaft to use an external stator bearing. The design presented here uses custom designed internal stator magnetic bearings.

A fundamental choice exists when designing a magnetic bearing between a heteropolar or a homopolar layout. By far the most common choice is the heteropolar. The chief advantage of this design is the simplicity of construction from laminations. The disadvantage is that a heteropolar bearing will tend to induce substantially greater losses in the rotor, due to the high frequency changing magnetic field the rotor experiences, building up eddy currents. Kasarda et al [59] have presented work illustrating these differences. This issue is traditionally mitigated by fitting a laminated collar on the rotor.

In this project, however, internal stator bearings are envisaged. This leads to a complication in terms of space limitation. For a given diameter of rotor, there is only a certain space available within it to fit the magnetic bearing. If part of this space is taken up with an internal laminated collar, there is then less space for the bearing, which leads to a lower force capacity bearing.

For this reason, the proposal is to use a homopolar bearing design. With homopolar bearings, the rotor experiences far less variance in magnetic field, and thus eddy currents are reduced

significantly. This eliminates the need for a laminated collar. This choice does, however, have implications in terms of the material choice for the bearing core.

5.3 Stator Core Material

It is almost universal practice in magnetic bearing design to construct the cores out of laminated electrical steel. This provides a high level of magnetic permeability and good saturation strength, while reducing energy losses due to eddy current build up. However, design geometry possibilities are considerably limited when working with laminated steel. In particular, to facilitate manufacture it is desirable for the design to be prismatic in the stacking direction. It is well documented that this requirement makes the manufacture of homopolar magnetic bearings more complex and costly than heteropolar designs.

To overcome this trade off, it is proposed that laminated steel is replaced with a powder metal based Soft Magnetic Composite (SMC) as the core material for a magnetic bearing. SMC offers some clear advantages over laminated steel:

- it has effectively isotropic lamination and is thus capable of supporting alternating magnetic flux in any direction without significant eddy current build up
- it has the ability to be formed into complex 3D shapes

A quantity of literature has been published discussing the use of SMC, although work focusing on using the material specifically in magnetic bearing application is limited. A general review of the use of SMCs replacing traditional laminated steel components is presented by Shokrollahi and Janghorban [60]. They particularly highlight the advantages of reduced losses (especially eddy current losses) in medium to high frequency AC applications, and the increased flexibility of design afforded by the material.

In a more specific example, Fleischer and Hofmann have presented work [61] considering the use of SMC material for the rotor itself in a magnetic bearing situation. Particularly they prove via 3D-FEM analysis that there is considerable potential for increased efficiency using SMC material due to reductions in eddy current losses. In a later paper [62], the same authors develop a combined radial and axial magnetic bearing stator fabricated from SMC. This is one of very few explorations of SMC in magnetic bearing stators in the literature - no examples of a homopolar internal-stator design such as is used in this project have been seen.

Another interesting study involving SMCs in a magnetic bearing scenario is the construction of an energy storage flywheel by Howe et al [63]. Once again, it is the rotor that is constructed with SMC here, but another point of considerable relevance to the present project is included in this paper, namely that the flywheels being designed are levitated by magnetic bearings located *inside* the rotor. Few applications with this arrangement have been seen, with the more usual arrangement levitating the rotor from without; however, Howe et al omit to elaborate on any

details of the design of these bearings in this paper, which may face substantial difficulties relating to limited space.

The adoption of SMC allows the magnetic bearings to use a compact, single piece homopolar design similar to that shown in Figure 5.3. A photograph of a completed bearing to this design is shown in Figure 5.4. Fabricating this design directly from laminated steel in an analogous way to heteropolar bearings would incur greater eddy current losses than an SMC core as not all directions are insulated in the steel. This can be seen in Figure 5.5, which represents a cross-section of one of the poles of the proposed homopolar geometry. The lamination in the shaded area marked "A" is in the correct orientation to retard the formation of eddy currents, whereas in the perpendicular field highlighted in area "B", the laminations are not oriented in the optimum direction.

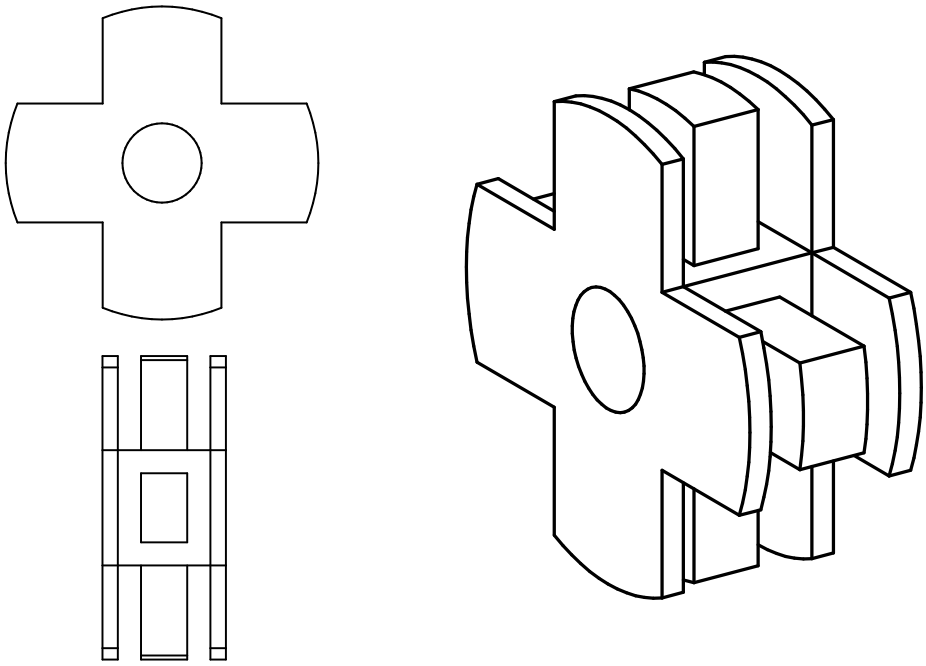

Figure 5.3: An internal-stator homopolar bearing core design

In general, the SMC is fabricated from iron powder, chemically treated to leave each individual grain with a thin layer of electrically insulating material around the outside. The powder is then compressed in a mould to form the final shape of the component required. Post forming heat treatments are also applied to relieve stress from the compaction process.

Of course, the compaction-forming of powder-metal components is generally only financially viable on production-scale runs. For this reason, prefabricated discs of a version of the SMC material specially treated to have good machinability properties were used. It is noteworthy that in altering the material to give good machinability, the magnetic properties of the SMC are slightly adversely affected. A pair of microscope images (optical and electron) of the structure

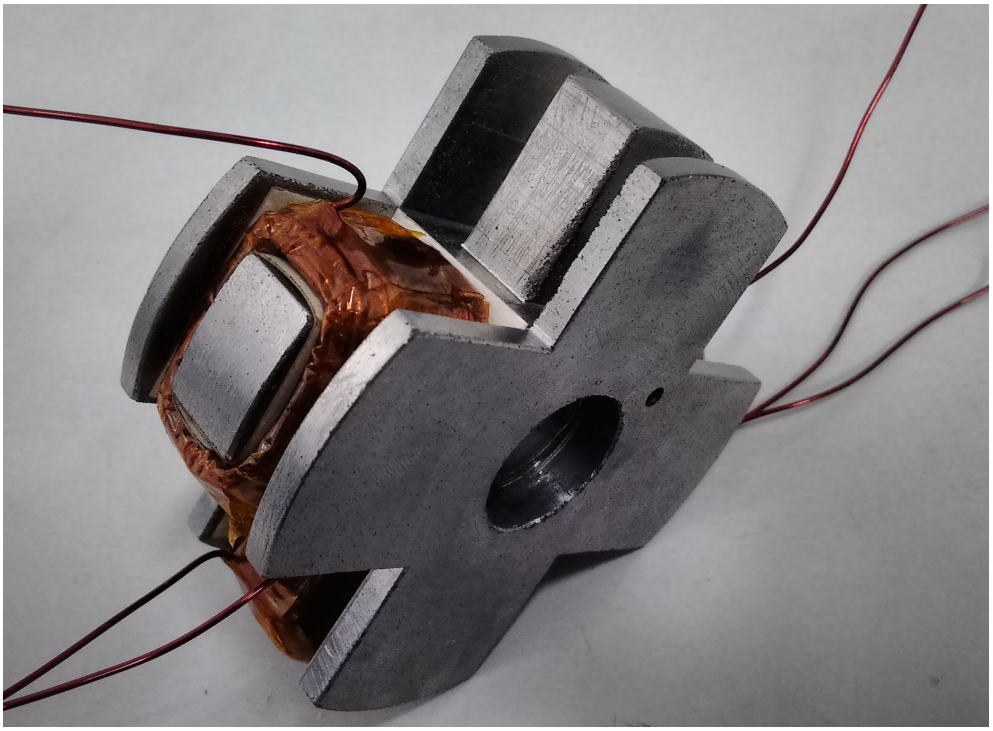

Figure 5.4: An SMC homopolar magnetic bearing. This geometry would be very difficult to fabricate with laminated steel sheets. Note that one coil is removed for illustration purposes

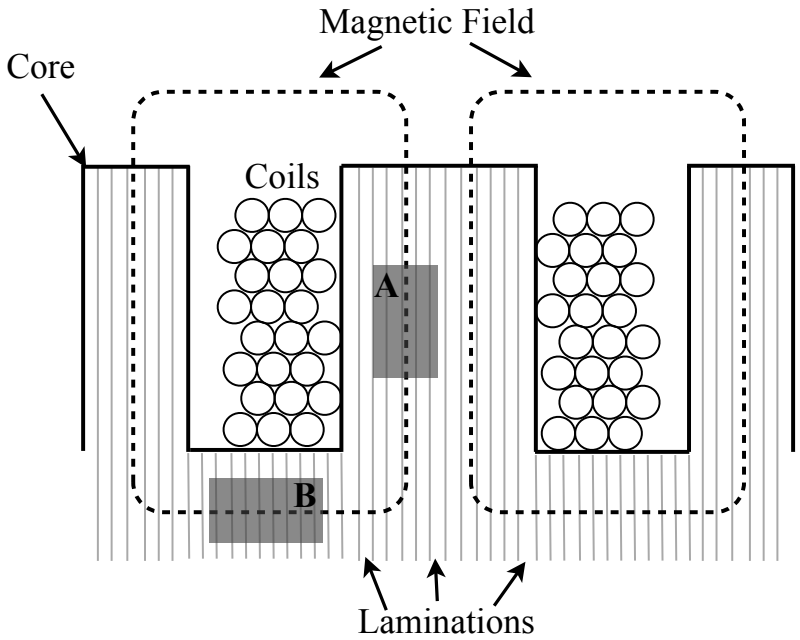

Figure 5.5: In a homopolar bearing, uniform laminations cannot optimally block eddy current formation in all directions

of the material is shown in Figure 5.6.

Of course, there are still the issues of space limitation when designing an internal-stator magnetic bearing. In general this means one is limited by the load capacity of the bearing. This is, however, by no means a prohibitive difficulty in this design, owing to the fact that the bearings are not required to support the mass of the rotor, which is dealt with by external rolling element bearings.

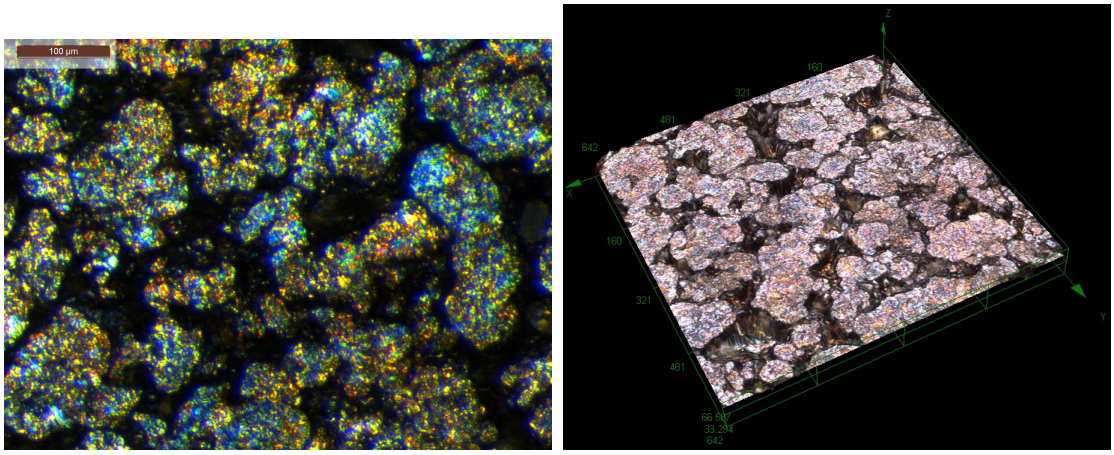

(a) (b)

Figure 5.6: Optical (a) and electron (b) microscope image showing the micro-structure of the SMC. Individual "grains" of iron (lighter areas) are seen to be isolated from one another, preventing eddy current build up.

5.4 SMC Performance

In using a new material for the bearing core, it is naturally important to examine its performance against the traditional material used in the application, in this case laminated steel. Two performance criteria in particular are of interest to the majority of magnetic bearing designers, and those are force capability and thermal characteristics. To facilitate testing of these properties, two magnetic bearings were fabricated of identical geometry, but with differing core materials. One uses 0.3 mm steel laminations, while the other uses a Soft Magnetic Composite. Note that these bearings are distinct from the bearings to be used on the main rotor test rig. These bearings are of internal-stator, heteropolar design, owing to the difficulty already described in manufacturing a compact homopolar bearing from laminations, and are shown in Figure 5.7.

A test rig was constructed to allow the measurement of the forces exerted by a pole pair of these bearings over various frequencies of coil excitation. It allows for the rigid mounting of a magnetic bearing directly above a load cell. The top of the load cell carries a curved block of

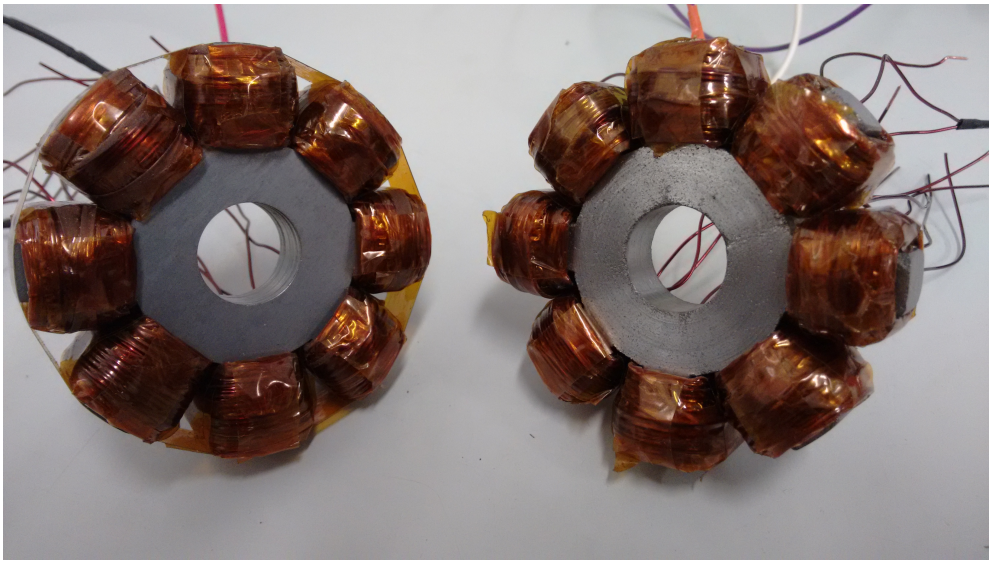

Figure 5.7: Two internal-stator heteropolar bearings for comparison between laminated steel (left) and SMC (right) cores

SMC to recieve the magnetic field. The arrangement can be seen in Figure 5.8. The coils of the bearing are powered by a digital amplifier, which is fed by a computer generated demand.

Tests were performed by feeding the coils with a fixed amplitude chirp signal, varying in frequency from 100 to 1500 Hz. Note that the current is offset to always be of positive magnitude, with a peak amplitude of 5 A, as in

$$I = 2.5(1 + \cos(\omega t)) \text{ A}$$

This is to avoid the circumstance when a non-offset current is used which would lead to the force frequency seen by the load cell being twice the current frequency.

The results of this testing are seen in Figure 5.9. The force characteristics are very similar between the two bearings. Note that the peak in the force measurement seen at around 400 Hz is due to internal load cell dynamics (resonance effect), rather than being a property of the bearing itself. Hence the force measured is that transmitted to the base. Nonetheless the important point is the parity between the two bearings of different materials.

The power losses from magnetic bearing stators also manifest themselves through heat generation. Therefore excess losses not only reduce system efficiency, but also have the potential to cause thermal damage, particularly to insulating coatings on the copper wires, and on sheet / grain laminations. Thus it is of interest to ensure that an SMC core does not incur greater thermal losses than a laminated one, which may be considered the benchmark.

In theory, there should be lower losses in an SMC core, as there should be less eddy current

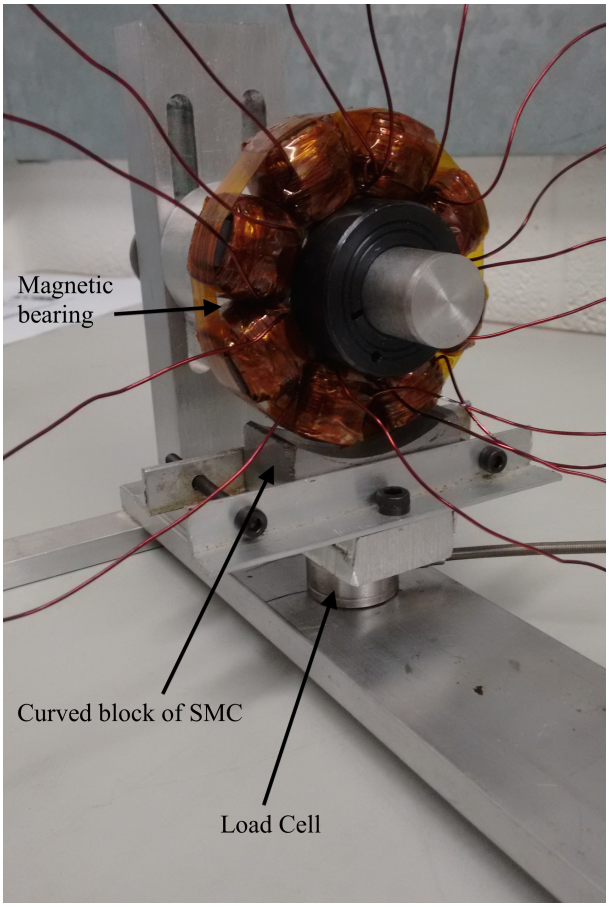

Figure 5.8: Load cell rig for testing magnetic bearing force capacity

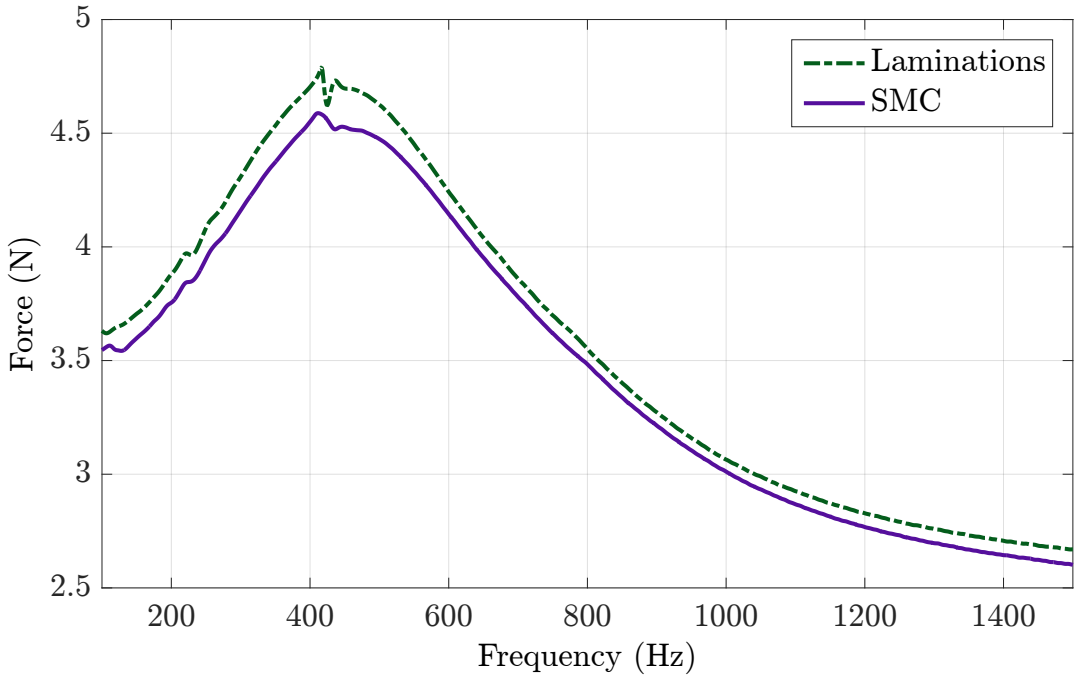

Figure 5.9: Force test data comparing traditional laminated core with SMC core

build up. In order to assess the core thermal characteristics, a test was performed whereby a single pole pair of each bearing was fed a 6 A (peak) AC current at 1000 Hz. The temperature of the cores was recorded over time with a digital thermometer. A heat transfer compound paste was used to couple the bearing core to the the probe of the thermometer for accurate results. The results from the two different core materials are shown in Figure 5.10. The results show very similar thermal characteristics between laminated and SMC core materials, with temperature rise being predominantly attributed to heating in the copper coils, rather than core effects. It is expected that at higher current frequencies, eddy current effects would be more significant, although such frequencies are not generally required in AMB systems.

These results therefore confirm that SMC offers equal performance to the laminated version, but with the considerable advantage of increased design possibilities resulting from its isotropically "laminated" quality, and resulting 3D geometry freedom.

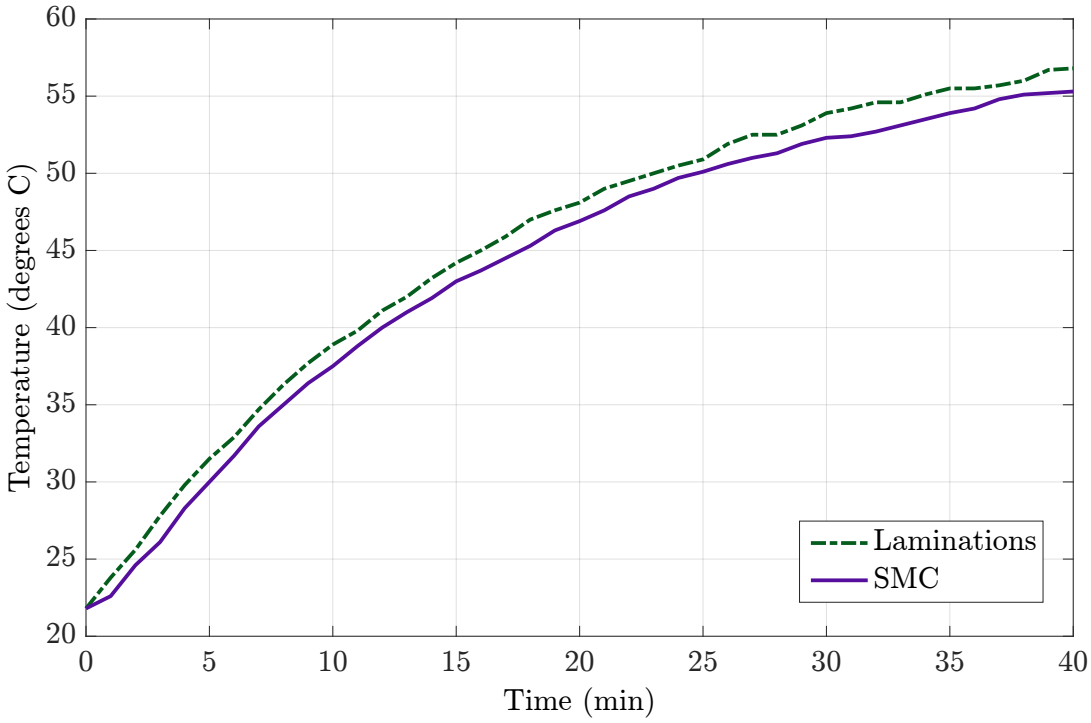

Figure 5.10: Core heating characteristics

Chapter 6

Model Tuning and System Identification

After the completion of the design and construction of the test rig, a substantial amount of work went into bringing it on-line. This chapter begins by presenting a specific details of a numerical model of the rig, based on the theory of Chapter 3. The concept of model *order reduction* is then introduced and applied to the model as a prerequisite to simulation and, later, control.

With a reduced order model in-hand, a parameter identification is then undertaken. In essence, this is a process of tuning a variety of the model variables (e.g. support structure stiffnesses) to ensure the model behaviour closely follows the behaviour of the physical rig.

Later in the chapter, the necessary preparatory tests which precede actual rotating tests of the rig are presented. These include rotor balancing and bias current selection.

6.1 Numerical Analysis of Rig Rotor

As part of the design process of the test rig rotor, it was subject to numerical analysis, to ensure that its behaviour would allow demonstration of the required principle. Here, the details of the structure of the model representing the final version of the test rig are provided.

The rotor system is broken down into finite elements as shown in Figure 6.1. The illustration is to scale, with the background grid representing one centimetre squares. The nodes of each of the rotor and the secondary shaft are indicated by "R#" and "S#" respectively. Note the alignment between R3 and S5, and R4 and S6 - the first pair are the location where the internal sensor is modelled as acting, while the second pair are where the force from the

Table 6.1: Location and purpose of discs added to rotor system finite element model

Node	Representing
S6	Magnetic bearing and ancillary equipment
R5	Solid, closed end of the rotor tube
R7	Drive turbine

magnetic bearing is modelled to act. In terms of fixed support locations, the rotor is supported at R1, while the secondary shaft is supported at S1 and S3. Both rotor and secondary shaft supports are modelled as a combination of lateral and torsional stiffness, with greater torsional stiffness for the secondary shaft supports due to the nature of the clamping collars used at these locations. The illustration in the figure shows exactly half the axial length of the rig - the model is symmetrical about node R7. The model has extra masses (discs) added at the locations specified in Table 6.1.

Whilst there are more nodes in this model than would strictly be necessary to represent the system and locate all salient features, the additional nodes allow for the generation of reasonably accurate plots of the deflected shape of the structure during simulation, which can be helpful in analysing the system behaviour.

The overall system matrices (i.e. the **M**, **K** and **G** matrices) are assembled as indicated in Figure 6.2. These include matrices for the rotor, and for each of the two secondary shafts.

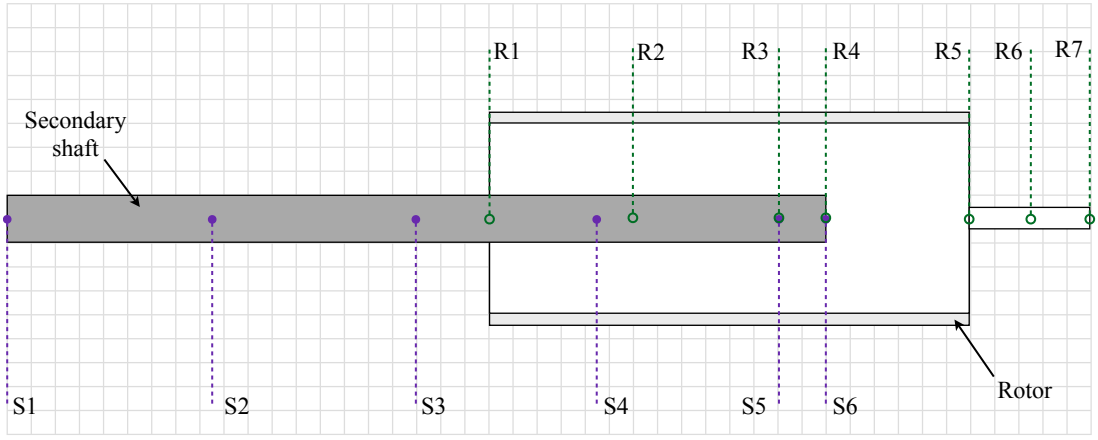

Figure 6.1: Illustration of finite element breakdown of test rig rotor and secondary shaft for modelling and simulation

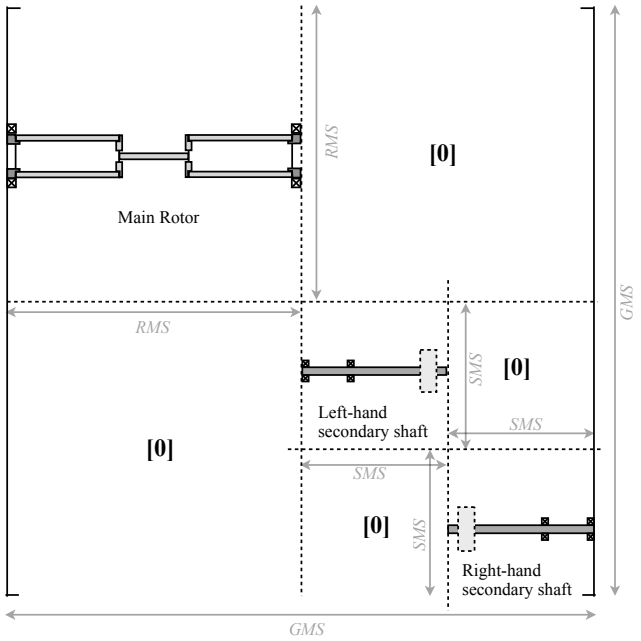

Figure 6.2: Pictorial overview showing layout of system components when constructing finite element global matrices (i.e. **M**, **K** and **G** matrices). RMS, SMS and GMS stand for Rotor Matrix Size, Shaft Matrix Size and Global Matrix Size respectively, and are useful handles for keeping track to the positions of various degrees of freedom in the model.

6.2 Generating a Reduced Order Model

The model generated by the finite element process in the previous section is, mathematically speaking, relatively complex. It is said to be of "high order". The term "order" here is a measure of the number of states, or degrees-of-freedom, contained in the model. In the test rig model, the rotor has 13 nodes, and each secondary shaft has six nodes. Each node is assigned four degrees-of-freedom (two translational and two rotational displacements), and the final state space model states consist of this set of displacements together with corresponding velocities. Thus the complete model has an order of:

$$2 \times 4 \times (13 + [2 \times 6]) = 200 \quad \text{states}$$

The problem with high order models is that they require large computational resources and are very slow to work with. Specifically, for use in either simulation or as part of a real time controller, a much lower order system is required.

Reducing the order of a model involves deleting some of the information about the system, and naturally this leads to less accurate simulation. However, if one is selective about the information removed, the new, reduced-order model can be tailored to have behaviour which

very closely reflects the full-order model *within a certain set of operating conditions of interest*.

In particular, a large order model will contain information about a system's behaviour up to a very high frequencies. This high frequency data can be safely disregarded for two reasons: firstly, beyond the systems first few natural frequencies, even the full order model cannot be expected to be giving accurate information, as higher frequency behaviour will contravene the fundamental assumptions underlying the model; secondly, within all conceivable operating conditions, the system behaviour will be dominated by its low frequency characteristics in any case.

Therefore, the goal is to generate a second model of much lower order than the first one, which accurately represents the characteristics of the full-order model *at low frequencies*. This low-order model can then be used in simulation and real-time control loops due to its much lower computational requirements.

The following logic allows for the generation of a reduced order model which has this desired characteristic.

We first assume the existence of the "full" order state space representation of the system. "Full" order here means the size of the system generated by the finite element model,

$$\begin{aligned} \dot{\mathbf{x}} &= \mathbf{A}\mathbf{x} + \mathbf{B}\mathbf{u} \\ \mathbf{y} &= \mathbf{C}\mathbf{x} + \mathbf{D}\mathbf{u} \end{aligned} \tag{6.1}$$

This system has eigenvalues $\mathbf{\Lambda}$ and eigenvectors $\mathbf{V}$ which satisfy the equation:

$$\mathbf{A}\mathbf{V} = \mathbf{V}\mathbf{\Lambda} \tag{6.2}$$

In practice, when these values are generated in Matlab they will not necessarily occur in any specific order, however they can then be "manually" sorted such that the eigenvalues are in ascending order (in terms of their imaginary parts, i.e. frequency), and the eigenvectors are arranged to correspond.

If one then takes a modal transform according to $\mathbf{x} = \mathbf{V}\mathbf{p}$, and its derivative $\dot{\mathbf{x}} = \mathbf{V}\dot{\mathbf{p}}$, these substitute into Equations (6.1) and (6.2) to give:

$$\begin{aligned} \mathbf{V}\dot{\mathbf{p}} &= \mathbf{A}\mathbf{V}\mathbf{p} + \mathbf{B}\mathbf{u} \\ &= \mathbf{V}\mathbf{\Lambda}\mathbf{p} + \mathbf{B}\mathbf{u} \end{aligned} \tag{6.3}$$

and then, finally:

$$\begin{aligned} \dot{\mathbf{p}} &= \mathbf{\Lambda p} + \mathbf{V^{-1}Bu} \\ \mathbf{y} &= \mathbf{CVp} + \mathbf{Du} \end{aligned} \tag{6.4}$$

Equation (6.4) can be written in an expanded form, taking account of the fact that the terms are in ascending order of frequency, and can thus be divided at any nominated cut-off point into low (l) and high (h) frequency components:

$$\begin{bmatrix} \dot{\mathbf{p}}_l \\ \dot{\mathbf{p}}_h \end{bmatrix} = \begin{bmatrix} \mathbf{\Lambda}_l & \mathbf{0} \\ \mathbf{0} & \mathbf{\Lambda}_h \end{bmatrix} \begin{bmatrix} \mathbf{p}_l \\ \mathbf{p}_h \end{bmatrix} + \begin{bmatrix} \hat{\mathbf{B}}_l \\ \hat{\mathbf{B}}_h \end{bmatrix} \mathbf{u} \tag{6.5}$$

$$\begin{bmatrix} \mathbf{y}_l \\ \mathbf{y}_h \end{bmatrix} = \begin{bmatrix} \mathbf{CV}_l & \mathbf{CV}_h \end{bmatrix} \begin{bmatrix} \mathbf{p}_l \\ \mathbf{p}_h \end{bmatrix} + \mathbf{Du} \tag{6.6}$$

where:

$$\begin{bmatrix} \hat{\mathbf{B}}_l \\ \hat{\mathbf{B}}_h \end{bmatrix} = \mathbf{V^{-1}B} \tag{6.7}$$

As stated above, the motivation for implementing a reduced order model is to define a system which matches the output of the full order system at low frequencies (i.e. matches "$\mathbf{y}_l$"). Thus we can essentially just ignore the "high" frequency part of the system equations, and define our new system as:

$$\begin{aligned} \dot{\mathbf{p}}_l &= \mathbf{\Lambda}_l \mathbf{p}_l + \hat{\mathbf{B}}_l \mathbf{u} \\ \mathbf{y_r} &= \mathbf{CV}_l \mathbf{p}_l + \mathbf{Du} \end{aligned} \tag{6.8}$$

One notable problem with this technique stands out, and that is the steady state response of the reduced order system is missing terms from the full order system, thus will be inaccurate here. For the full order system, the steady state output for $\mathbf{y_l}$ is:

$$\mathbf{y_l} = -\mathbf{CV}_l {\mathbf{\Lambda}_l}^{\mathbf{-1}} \hat{\mathbf{B}}_l \mathbf{u} - \mathbf{CV}_h {\mathbf{\Lambda}_h}^{\mathbf{-1}} \hat{\mathbf{B}}_h \mathbf{u} + \mathbf{Du} \tag{6.9}$$

By contrast, the steady state output of the reduced order system derived thus far is:

$$\mathbf{y_r} = -\mathbf{CV}_l {\mathbf{\Lambda}_l}^{\mathbf{-1}} \hat{\mathbf{B}}_l \mathbf{u} + \mathbf{Du} \tag{6.10}$$

This response is clearly missing the second term of the steady state response of the full order model. To remedy this incongruity, one may simply redefine the $\mathbf{D}$ term of the reduced order system, such that:

$$\hat{\mathbf{D}} = \mathbf{D} - \mathbf{C}\mathbf{V}_h {\boldsymbol{\Lambda}_h}^{-\mathbf{1}} \hat{\mathbf{B}}_h \tag{6.11}$$

which then gives the final reduced order system as:

$$\begin{aligned} \dot{\mathbf{p}}_l &= \boldsymbol{\Lambda}_l \mathbf{p}_l + \hat{\mathbf{B}}_l \mathbf{u} \\ \mathbf{y_r} &= \mathbf{C}\mathbf{V}_l \mathbf{p}_l + \hat{\mathbf{D}}\mathbf{u} \end{aligned} \tag{6.12}$$

These equations now represents a system of far lower order than the original system, but maintaining very similar low frequency behaviour. Two more steps are taken before the system is practically implemented in Matlab. Firstly, in order to supply the state space representation in Matlab with real forms only (in general the terms of Equation (6.12) will be complex), the terms are separated into real and imaginary components in the following way:

$$\mathbf{p}_l = [p_{R1} + ip_{I1}, p_{R2} + ip_{I2}, ..., p_{Rn} + ip_{In}]^T = \mathbf{p}_{Rl} + i\mathbf{p}_{Il} \tag{6.13}$$

and then a new state vector $\mathbf{q_l}$ is defined as

$$\mathbf{q}_l = [p_{R1}, p_{R2}, ..., p_{Rn}; p_{I1}, p_{I2}, ..., p_{In}]^T = \begin{bmatrix} \mathbf{p}_{Rl} \\ \\ \mathbf{p}_{Il} \end{bmatrix} \tag{6.14}$$

A new system can then be defined, which is mathematically the same as that in Equation (6.12), but has purely real system matrices.

$$\begin{aligned} \dot{\mathbf{q}}_l &= \mathbf{A}_l \mathbf{q}_l + \mathbf{B}_l \mathbf{u} \\ \mathbf{y_r} &= \mathbf{C}_l \mathbf{q}_l + \mathbf{D}\mathbf{u} \end{aligned} \tag{6.15}$$

where the system matrices are defined as

$$\mathbf{A}_l = \begin{bmatrix} \boldsymbol{\Lambda}_{Rl} & -\boldsymbol{\Lambda}_{Il} \\ \\ \boldsymbol{\Lambda}_{Il} & \boldsymbol{\Lambda}_{Rl} \end{bmatrix}, \qquad \mathbf{B}_l = \begin{bmatrix} \hat{\mathbf{B}}_{Rl} \\ \\ \hat{\mathbf{B}}_{Il} \end{bmatrix}$$

$$\mathbf{C}_l = \mathbf{C}[\mathbf{V}_{Rl} \quad -\mathbf{V}_{Il}], \qquad \mathbf{D}_l = \mathbf{D} - \mathbf{C}\mathrm{Re}(\mathbf{V}_h \boldsymbol{\Lambda}_h^{-1} \hat{\mathbf{B}}_h)$$

The final adjustment to be made is as a result of the fact that, in separating the real and imaginary parts of the eigenvalue and eigenvector matrices, the reduced order system matrices end up double the size they were before separation. That is to say that the system of Equation (6.15) is twice the order of the system of Equation (6.12). However, there are no extra data in the system of (6.15), rather all the data from (6.12) appear twice. Thus by judiciously cropping system 6.15, the equations can be reduced to the original order achieved in 6.12. This duplication and subsequent cropping can be seen by considering the following explanation.

When the eigenvalues and eigenvectors of the system are calculated, they generally come out in complex conjugate pairs. This means the same data is presented twice, and it is unnecessary to keep the duplicates, which are effectively doubling the system size. This is illustrated by expanding the matrices that constitute $\mathbf{A}_l$. Here it is taken that the system has first and second eigenvalues of $(\alpha \pm j\sigma)$ and $(\beta \pm j\tau)$

$$\Lambda_{Rl} = \begin{pmatrix} \alpha & & & & \\ & \alpha & & & \\ & & \beta & & \\ & & & \beta & \\ & & & & \ddots \end{pmatrix}, \Lambda_{Il} = \begin{pmatrix} \sigma & & & & \\ & -\sigma & & & \\ & & \tau & & \\ & & & -\tau & \\ & & & & \ddots \end{pmatrix}$$

Examining these matrices, it is seen that striking out every second row and column will not actually lose any data. The same is true of the eigenvectors in $\mathbf{V}$ - every other column may be deleted as there is a complex conjugate pair of eigenvectors associated with every complex conjugate pair of eigenvalues.

Removing these data strips the system equation back down to the size it was before the complex numbers were separated into their real and imaginary parts. A small caveat applies when applying this cropping to the output $\mathbf{C}_l$ matrix. It is necessary that the system response $\mathbf{y}$ is the same both before and after the $\mathbf{C}_l$ matrix is modified. This means one has to be careful to not *only* delete data from it (which must be done to bring its size in line with the size of the modified $\mathbf{A}_l$ and $\mathbf{B}_l$ matrices), but to also modify the remaining data to reform the same output $\mathbf{y}$.

Given that the eigenvectors are arranged column-wise in complex conjugate pairs (associated with the complex conjugate eigenvalue pairs), when alternate columns are deleted, the output ($\mathbf{y}$) values are effectively halved. Thus, after the alteration, the new $\mathbf{C}$ matrix must be doubled to maintain the correct output values.

6.2.1 A Modified Formulation

It is noted that Equation (6.4) can be expressed in a slightly different way, which is made use of during parameter identification. In the above derivation, $\mathbf{V}$ is defined as the eigenvectors of the system matrix $\mathbf{A}$. Technically, these are the *right*-eigenvectors. These may be denoted as $\mathbf{V}_r$, the $_r$ signifying "right". It is also possible to define *left*-eigenvectors, $\mathbf{V}_l$ such that

$$\mathbf{V}_l^T = \mathbf{V}_r^{-1} \tag{6.16}$$

Using these left- and right-eigenvectors, Equation (6.4) is then written as:

$$\begin{aligned} \dot{\mathbf{p}} &= \mathbf{V_l^T A V_r p} + \mathbf{V_l^T B u} \\ \mathbf{y} &= \mathbf{C V_r p} + \mathbf{D u} \end{aligned} \tag{6.17}$$

6.2.2 Validating Reduced Order Model

Using this reduction technique, the original finite element model of 200 states was reduced to a model of only 12 states. This value of 12 is chosen to allow a cut-off frequency of 1 kHz, i.e. the states of the full order model with eigenvalues of 1 kHz or less were retained for the reduced order model. All higher frequency information is sacrificed. The 1 kHz value is chosen to be several times higher than frequencies of phenomenon we're actually interested in modelling, which is perhaps up to 150 - 200 Hz.

Once a reduced order model has been generated, it is important to assess the resulting system to ensure it is a suitably accurate representation of the full order system. In general, a reduced order system is required to exhibit the same behaviour as the full order system at low frequencies, but allowed to deviate at higher frequencies beyond a cut-off point. This is the present case the reduced order model is required to be accurate up to around 200 Hz, such that it includes both the rotor and secondary shaft first bending modes. Given that these first modes will dominate the system behaviour in all tests to be done, higher frequency information is not necessary.

A good way to compare the performance of the full- and reduced-order systems is to generate singular value plots of both systems. Such a comparison is presented in Figure 6.3. It is seen that there are clearly two distinct groupings of the singular values - owing to the logarithmic scale, the lower grouping have extremely low values, and as such correlation between the two systems in these series is not required. In the main grouping, with the larger singular values, it is seen that the two systems have extremely similar performance up to around 500 Hz or so. After this, it is observed that the singular values of the full-order plot contain some response detail not present in the reduced-order data. This is as expected, and the discrepancies at these high frequencies should not negatively influence the value of the reduced-order model.

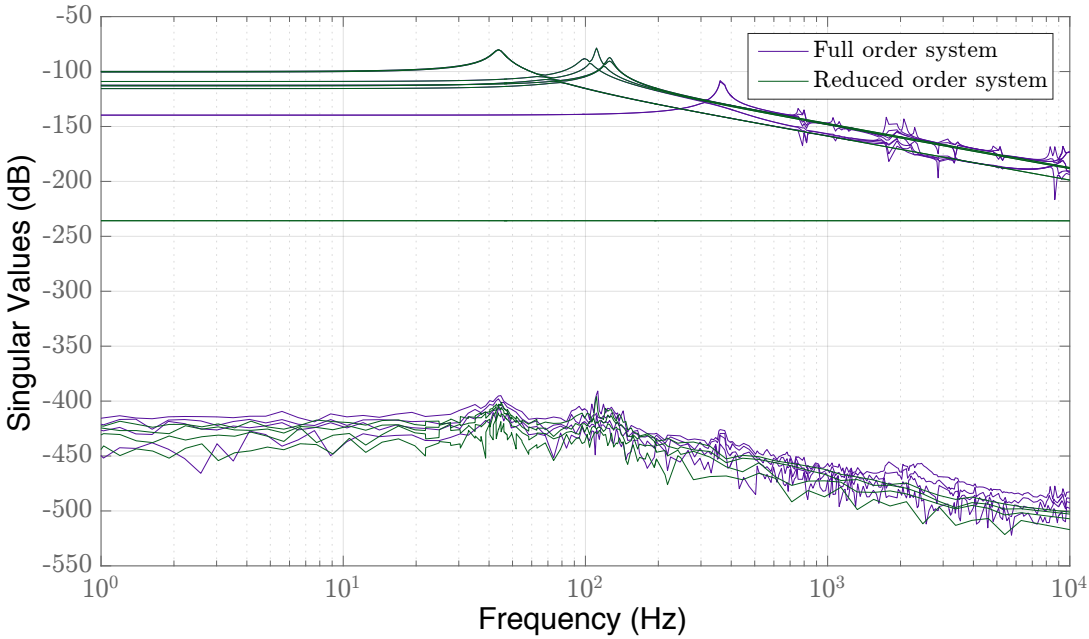

Figure 6.3: A comparison of the singular values of the full and reduced order system models. As required, good agreement between the models is seen at low frequencies.

By way of a further verification of the reduced-order model, a simulation was run whereby both reduced and full-order models were subject to a step force input in one of the four control axes of the system. The time response of the three measurements of interest in the excitation axis (rotor absolute motion, secondary shaft absolute motion and relative motion between the two bodies) were captured for each system. Figure 6.4 presents plots of each systems' response. It is observed that they are nearly identical, however it can be illustrated that subtle differences do occur from the data in Figure 6.5. This figure overlays the relative displacement measurement from each of the systems, and zooms in on a small section of this data.

These results confirm that the model order reduction has been successful, and allow for the reduced order model to be taken forward for use in simulation and control.

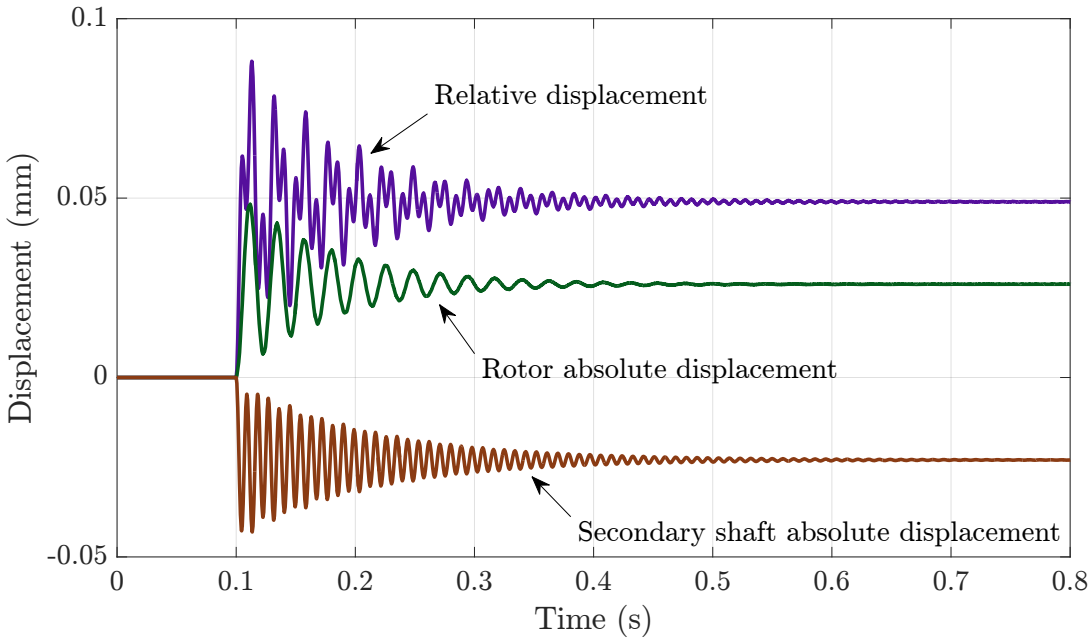

(a)

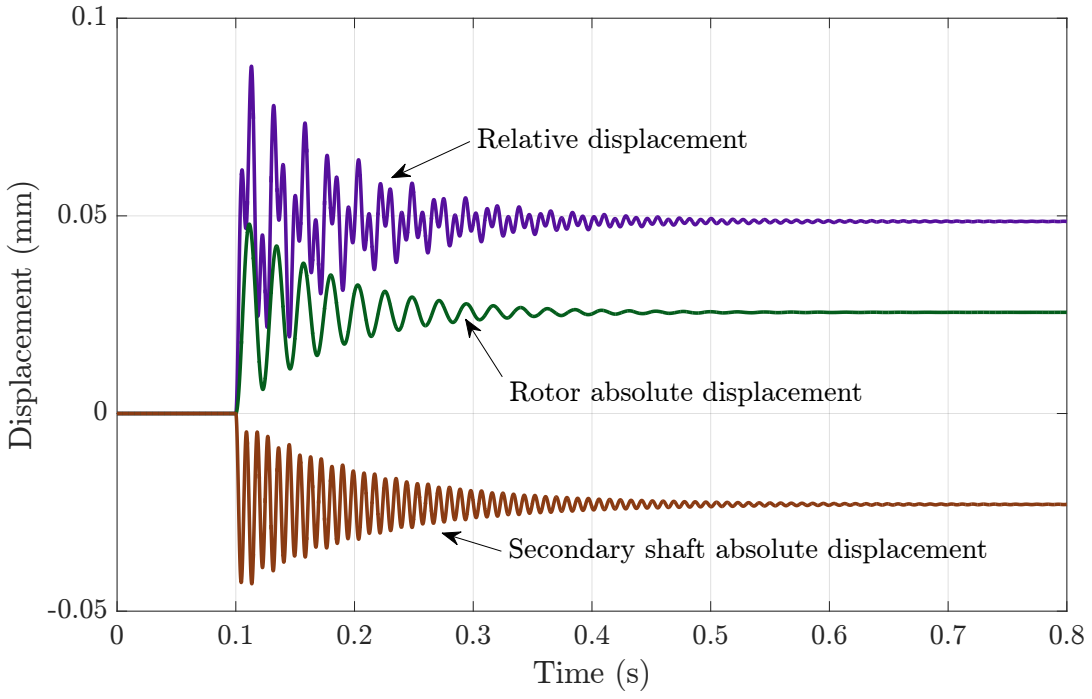

(b)

Figure 6.4: Response of each of the full order model (a) and reduced order model (b) to a step input. Extremely similar responses are seen.

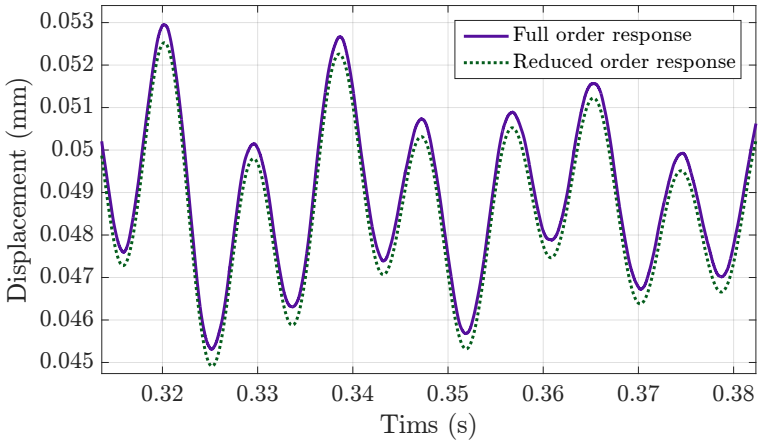

Figure 6.5: Narrow window view comparing the relative displacement signal produced in response to a step input to each of the full and reduced order models

6.3 Parameter Identification

For modelling all but the simplest systems, it is apposite to expect the model behaviour to deviate somewhat from the behaviour of the real system, at least with the first-generation, purely theoretical model. Consider that the physical test rig unavoidably includes many non-ideal joints, couplings and interfaces which it is futile to try and model as their nature is, by definition, unknown. Examples of specific features which may contribute to behaviour unpredicted by the model are:

- the dynamics of the rolling element bearings
- the clamping qualities of the secondary shaft which may have some minute play leading to a non-linear behaviour
- the (non-uniform) flexibility of the aluminium stands supporting both the rotor and the secondary shafts
- the flexible behaviour from the rig base plate
- aerodynamic forces associated with the turbine behaviour

One particular concern pertains to the magnetic bearings. Ideally, these should be perfectly concentric with the bore of the rotor, with an exactly equal gap between each pole and the surface of the rotor. In practical terms, it is virtually impossible to ensure an *exact* alignment. In addition to this there is a certain run-out of the rotor (due to assembly imperfections), so that even if the magnetic bearings could be exactly centralised according to any given rotor position, as the rotor is slowly rotated, the perfect alignment with the magnetic bearing will be lost. The results of this is that, for a given opposing coil pair, the same current in each coil (e.g. the bias current) will produce unequal forces on the rotor.

However, if a model is sufficiently close in character to the real system, it is generally possible to mitigate against these sorts of effect by "tuning" one or more parameters of the model in order to bring the model response closer to the physical system response, helping to remedy any inaccuracies in the initial model. This process is termed "parameter identification", which is a sub-branch of the more general field of system identification.

System identification is a topic of some considerable scope, and the associated literature comprises a correspondingly vast body of work. The techniques transgress traditional discipline boundaries, finding applications in fields varying from engineering to economics.

The basic principle of system identification is to give a system a known input, and measure the output. One then builds or modifies a model of the system to give the same output to the same input. The choice of input signal can significantly effect how well the derived model represents the real system. The most important consideration in this vein is that the input signal contains excitation at all frequencies at which it is required for the model to be accurate. Possible input signals may be:

- impuse
- swept sinusoid
- pseudo-random binary sequence
- Schroeder phased harmonic sequence

Well-known, comprehensive texts covering these and other fundamental considerations of the field are provided by Söderströdm and Stoica [64], and Ljung [65].

There again, many classic techniques are designed for use with open-loop systems, and are inappropriate for use with systems needing to be identified under closed loop operation, and potentially open-loop unstable. Consideration to this aspect, with particular reference to magnetic bearing systems, is given by Gahler et al. [66], who also propose their own identification algorithm for such cases. It is reported by Vázquez et al.[67] that this method is not universally successful however.

Work on using a Schroeder phased harmonic sequence [68] for identification associated with multi-frequency vibration control within a magnetic bearing systems has been presented by Sahinkaya et al. [69].

The technique used in this work is based on a method recently presented by Lauridsen et al. [70]. It has been used by Niemann et al. for the estimation of parametric faults [71, 72], and is founded on a linear fractional transformation (LFT) approach presented by Wolodkin et al. [73] .

Conceptually, the technique involves the following steps:

- build an initial nominal model of the system which captures the key characteristics/dynamics of the plant. The system matrix of this model is $\mathbf{A}_{\text{nom}}$. Note that for large models such as the rotor model in this project, a reduced order model should be used, owing to the need for many simulations to be run.
- select parameters in the model which may need to be adjusted to get a realistic response. In general these will be inertia, stiffness and damping qualities. Any number of parameters may be chosen for identification, and judicious choice of parameters informed by physical insight to the system will contribute to a better final model.
- for a system with n parameters to be identified, n versions of the system matrix are generated, each one generated from a model identical to the nominal system, except for having an arbitrary change in one of the parameters (e.g. double the parameter value from the nominal value). This results in a series of systems $\mathbf{A}_1 \ldots \mathbf{A}_{\text{n}}$
- a series of "delta systems" is constructed by subtracting each of the systems associated with the parameter changes ($\mathbf{A}_1 \ldots \mathbf{A}_{\text{n}}$) from the nominal system ($\mathbf{A}_{\text{nom}}$), as show in Equation (6.18).
- a single "test system" is constructed as shown in Equation (6.19). Each θ value is a constant which will be made available to the optimisation algorithm for tuning.
- the simulation of the test system is then run, and the output compared with experimental response to the same excitation. The difference between the model output and the real system results are expressed as a cost function.
- an optimisation algorithm is used to minimise the cost function by tuning the values of θ. A number of such algorithms are possible - in this case a non-linear least squares routine was chosen (`lsqnonlin`) for rapid convergence.

$$\mathrm{d}\mathbf{A}_i = \mathbf{A}_{\text{nom}} - \mathbf{A}_i \qquad\qquad i = 1 \text{ to } n \tag{6.18}$$

$$\mathbf{A}_{\text{test}} = \mathbf{A}_{\text{nom}} + \mathrm{d}\mathbf{A}_1\theta_1 + \mathrm{d}\mathbf{A}_2\theta_2 + \cdots + \mathrm{d}\mathbf{A}_n\theta_n \tag{6.19}$$

A wide range of input signals to run through the system for identification exists. A key requirement for the identification signal is that it contains all frequencies over which one requires the model to give an accurate response. Examples of possible inputs include impulses, steps and frequency swept sine waves. For different systems it may be found that different inputs lead to better or worse tuned models. In this scenario, it was found a pseudo-random binary sequence (PRBS) containing a frequency range of 0 - 400 Hz (weighted towards lower frequencies) leads to a good convergence of the optimisation algorithm and a well tuned system model. The power spectral density of the PRBS signal used on the rig is shown in Figure 6.6.

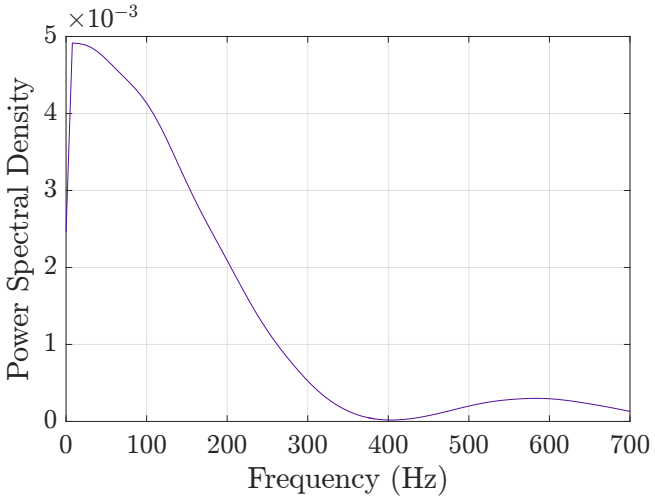

Figure 6.6: Power spectral density of pseudo-random binary sequence used in rig identification

For the rotor system, around twenty parameters were made available to the optimisation algorithm for identification. They were chosen because they were recognised as those with substantial uncertainty and the capability to cause significant alterations in the model response. The identified parameters were:

1. magnetic bearing negative stiffness
2. magnetic bearing current gain
3. damping of rotor
4. damping of secondary shafts
5. stiffness of rolling element bearings (lateral)
6. stiffness at secondary shaft clamping locations (lateral and torsional)

A number of these parameters were allowed to be optimised individually in different axes (x and y directions), as well as differently at each end of the rotor, in recognition of such variations having been already observed on the real rig.

Figures 6.7 and 6.8 illustrate the comparison between the simulated and experimental responses to a PRBS input before and after the model parameters are optimised, from the point of view of the internal sensors. Note that in the background of these plots a scaled representation of the excitation signal is shown for reference.

To ensure that the identification remains accurate to the individual characters of both the rotor and the secondary shaft (and not just their combined behaviour), the signals from the external sensors measuring only the rotor are included in the identification, and an example results from one of these sensors is shown in Figure 6.9.

The nominal model treats the rotor as symmetric between the ends - i.e. end one has the same properties as end two. However, it can be seen from the experimental results, most obviously by comparing the x1 and x2 axes, that in reality the two ends have similar but distinctly different behaviours. This can be attributed to a number of "reality factors" which naturally occur during the manufacturing and assembly process. This means that the identification process must be permitted to treat the ends differently as well - it is not possible to fit a single set of parameters to two differing sets of data. This capability was therefore built into the model prior to identification.

It is important to bear in mind when using such an optimisation process that physical realism should be preserved. The optimisation algorithm is purely mathematical, and as such it may suggest solutions using values which clearly have no physical meaning (for example, giving a joint negative stiffness) if this leads to a better optimisation. In general, the more complex a system is, the more likely such a solution is to occur. To counteract this, the optimisation is done in stages, and at each stage, the algorithm is only permitted to make changes up to $\pm$ 20% on the nominal parameter values. If the optimised solution reaches that limit on any given parameter, then a decision is taken as to whether allowing that particular parameter more flexibility can be physically justified. This process is iterated to find a final model which has a good fit to the experimental data, but maintains realistic parameter values.

It is further noted that the optimised solution is - in a complex model - almost certain not to be unique. For example, considering a beam/rotor support location which is characterised by both lateral and torsional stiffness, it is likely that one could play these values off against each other (increasing torsional stiffness while decreasing lateral stiffness, say), without significantly altering the goodness-of-fit of the model to the experimental data. This characteristic is further complicated by the fact that the response of the real system will be influenced by more than just the parameters available for optimisation. For example in the test rig here, the rig base plate is not entirely rigid, and thus its behaviour will have an influence on the experimental results. However, the plate is not included in the model, and thus the optimisation process will attempt to account for this influence by altering the available parameters across the rest of the rig. This may reduce the realism of the values produced, although it may result in a better overall model in terms of reproducing realistic behaviour.

The main point to bear in mind is that the model is simply a tool, and the identification process is merely trying to improve that tool according to a certain set of criteria, but but a perfect or ideal model will never be achieved for any but the simplest of systems.

In any case, the results of the parameter identification here identify the achievement of realistic model behaviour, and so give confidence in the further use of the model, for instance in controller design.

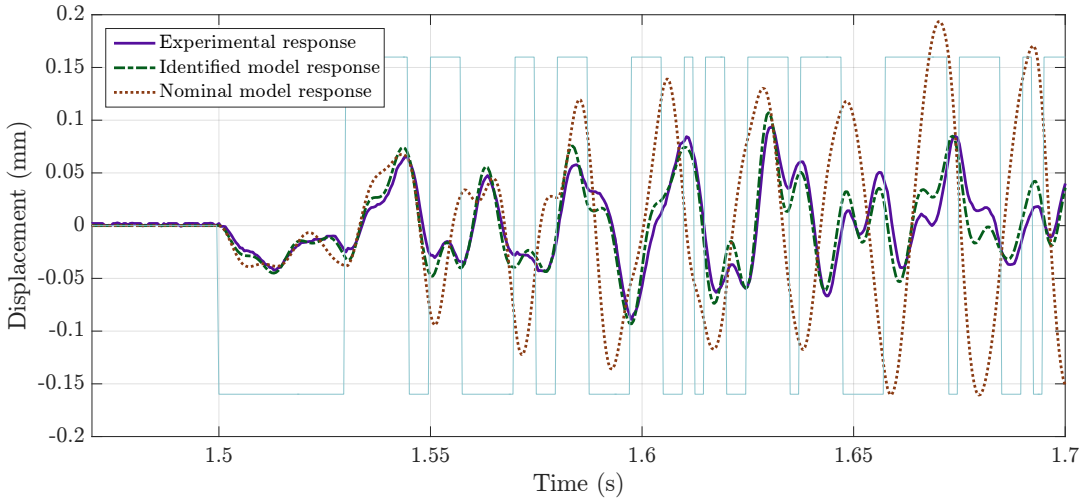

(a)

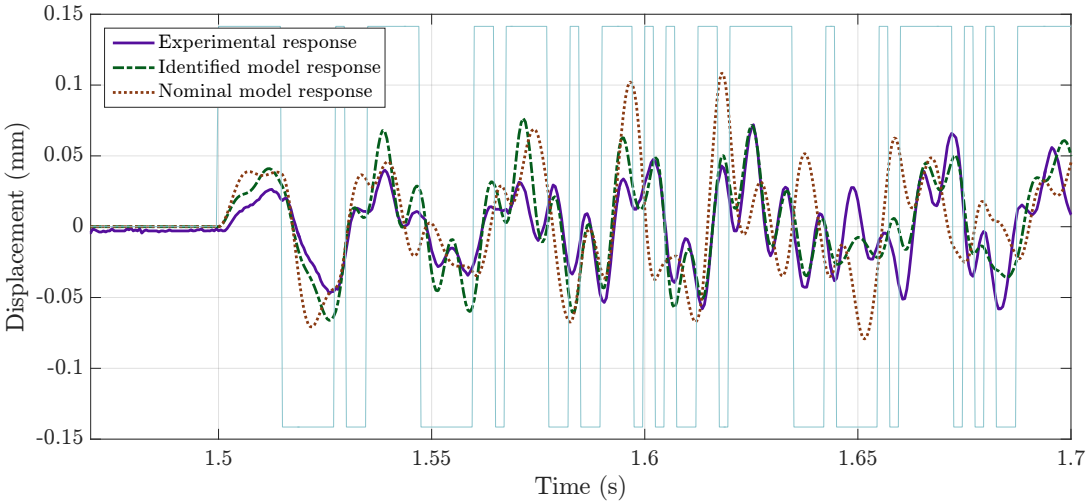

(b)

Figure 6.7: Comparison of the response seen at end 1 of the system to PRBS input for each of: i) experimental plant, ii) model with nominal parameters and iii) model with identified parameters. Plot (a) shows readings in the x1 direction, (b) shows the y1 direction

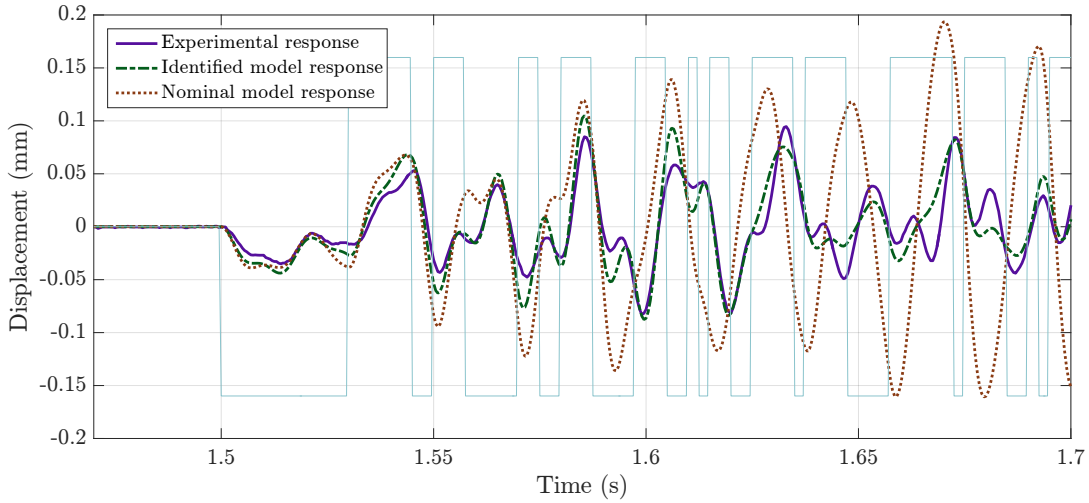

(a)

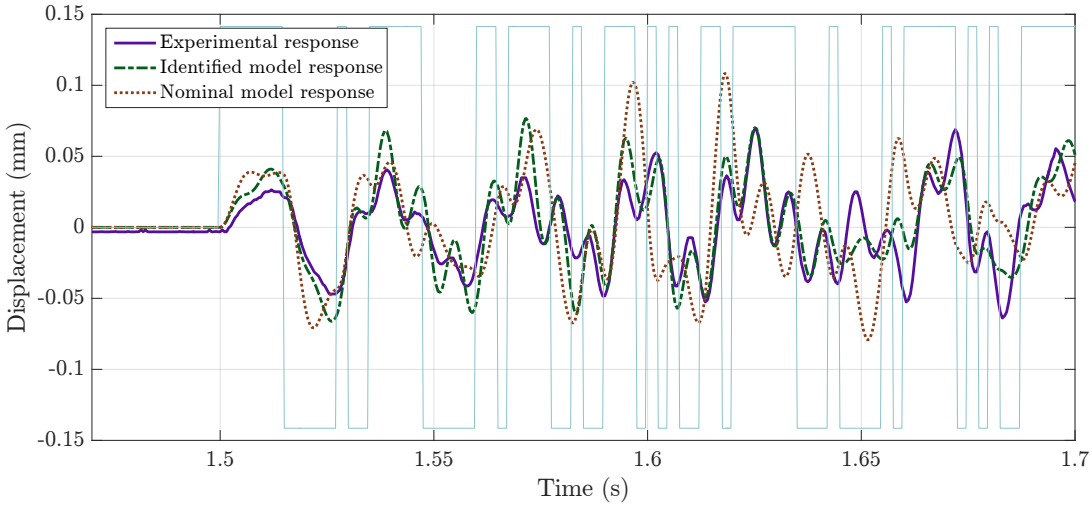

(b)

Figure 6.8: Comparison of the response seen at end 2 of the system to PRBS input for each of: i) experimental plant, ii) model with nominal parameters and iii) model with identified parameters. Plot (a) shows readings in the x2 direction, (b) shows the y2 direction

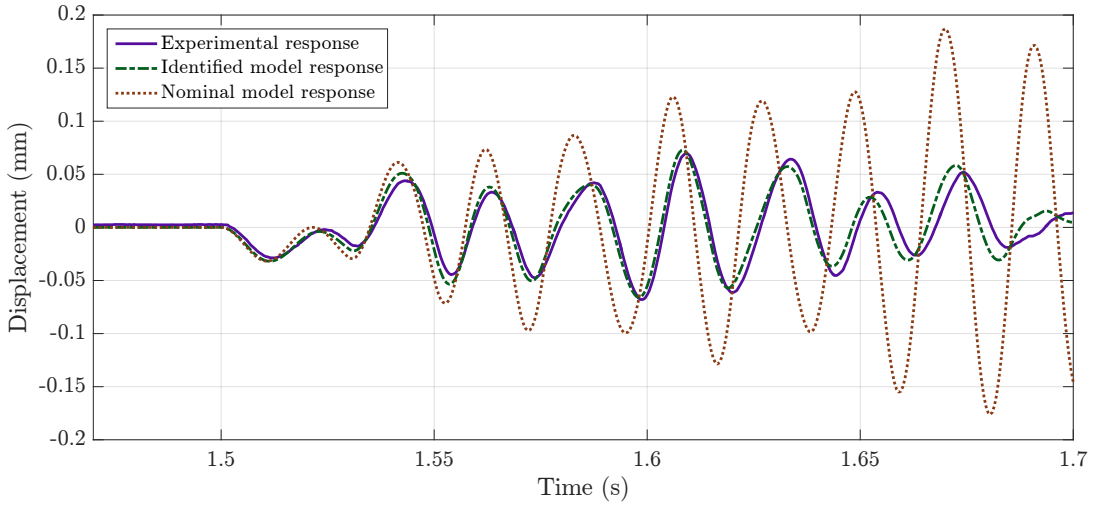

Figure 6.9: Comparison of the response of just the rotor seen at end 1 of the system given a PRBS input for each of: i) experimental plant, ii) model with nominal parameters and iii) model with identified parameters

6.4 Final Model Characteristics

To review briefly then, so far this chapter has described the formation of a finite element model to fit the geometry of the test rig constructed. It has been seen how such a model can be reduced in order to allow for much faster computation of simulations and controllers while maintaining accurate performance, and finally a process for tuning the model parameters to account for unmodelled effects and bring the model performance closer to the behaviour of the real test rig has been presented.

Now, a few results from this final model are given to indicate key characteristics of the test rig.

Natural frequencies (ω) - based on eigenvalue analysis - for each of the rotor and the two secondary shafts are indicated in Table 6.2. The table includes first and second natural frequencies for each member, in each of the x and y directions. It is seen that there is a noticeable difference between the x direction natural frequencies of the two secondary shafts, and also that each secondary shaft exhibits a significant difference between its x and y direction natural frequencies. Such characteristics are certainly evident when running the test rig, and results from "real effects" such a non-uniform stiffness in support structures, assembly discrepancies etc. The model's ability to reflect these realistic phenomena is a result of the parameter identification process.

In a similar way to the worked example presented in Section 3.2 a plot of the maximum singular values of the system receptance matrix can be produced to give an overall guide to system resonances. The maximum singular value plot is presented in Figure 6.10. Values for two

Table 6.2: Test rig component natural frequencies from identified model (frequencies in Hz)

	Rotor	Secondary Shaft 1	Secondary Shaft 2
ω_{1x}	46.8	103	114
ω_{1y}	46.8	129	129
ω_{2x}	366	760	774
ω_{2y}	367	805	805

systems are plotted - one for the rotor alone, and one for the complete system. When the complete system is modelled for this plot, a coupling is included between the rotor and the secondary shafts; at present this coupling is represented as a simple stiffness, whose magnitude is equal to the identified value of magnetic bearing negative stiffness. While this is only an estimate here, it is common in magnetic bearing design to tune a feedback controller to give positive stiffness of the same order of magnitude as the magnetic bearing negative stiffness. Thus it serves as a reasonable guide here.

It is seen that the peak representing the rotor first critical speed (around 40 - 50 Hz) exhibits a gyroscopic splitting effect, as the receptance matrix is a function of rotational speed. The peaks in the "combined system" plot between 100 and 140 Hz however are not associated with gyroscopic effects. These peaks represent the behaviour of the secondary shafts, which are non-rotating, and the "splitting" is simply a reflection of the different stiffnesses in the x and y directions, and between the two different shafts (as seen in Table 6.2).

A further feature in Figure 6.10 worthy of note is connected to the comparison between the series representing respectively the rotor alone, and the combined system. Specifically, the peak around 46 Hz in the plot for just the rotor is only increased by perhaps 5 Hz by introducing the secondary shaft. Ideally, there should be a noticeable separation between these peaks, which would require the coupling between the rotor and the secondary shafts to have a higher stiffness. The effects and implications of this observation are explored in Chapter 7.

By way of a graphical representation of the expected deflection of the test rig members during coupled operation, the first mode shape of the rig when running under PID control is seen in Figure 6.11. This figure was generated subsequent to doing some of the running tests of Chapter 7, and thus uses the PID gains actually used on the real rig. The mode shape is associated with an eigenvalue at approximately 51 Hz. It is seen that both the rotor and the secondary shafts adopt typical first bending mode shapes for their respective beam types. It is also seen clearly how all the bending in the rotor occurs in the central section where the rotor is thinnest. The hollow end sections remain rigid, as expected during the design.

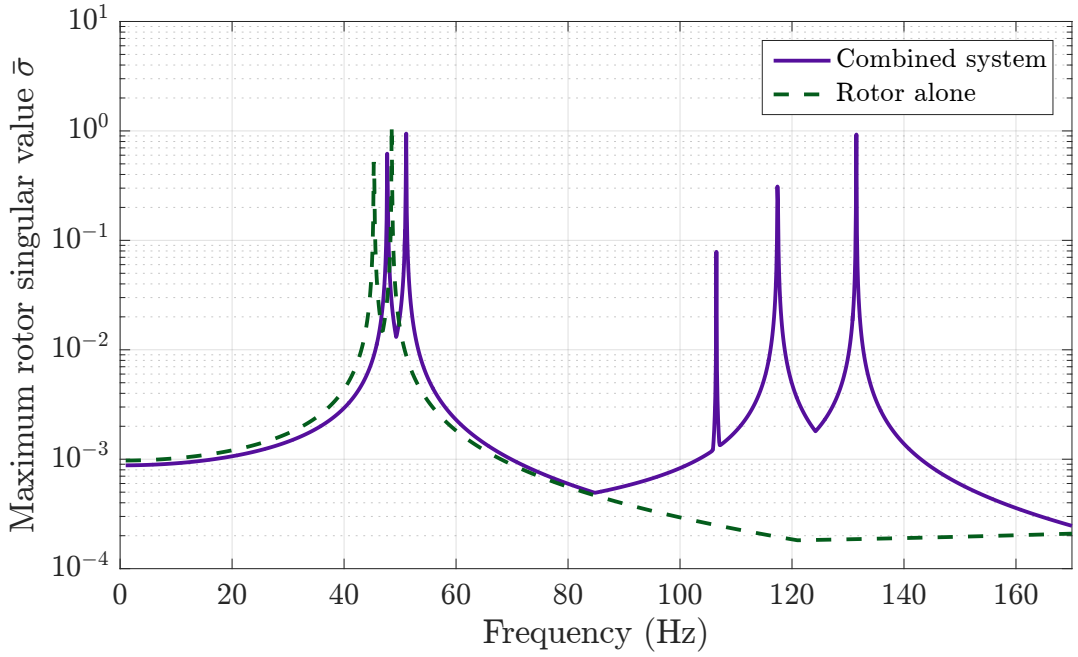

Figure 6.10: Singular value plots of system model showing both the rotor alone, and the whole system when the magnetic bearings are activated

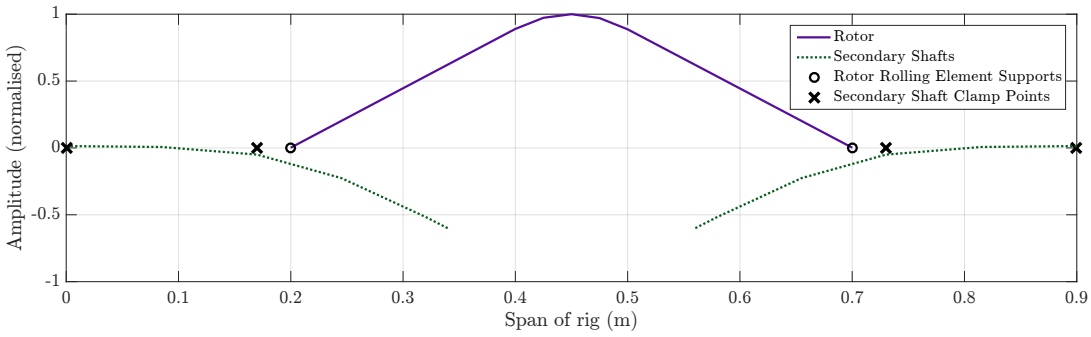

Figure 6.11: System mode shape under PID control, associated with 51 Hz natural frequency

6.5 Physical Rig Pre-Run Setup

Before actually running the test rig - the subject of the next chapter - it was necessary to undertake a couple of preliminary tasks. Firstly, an appropriate bias current for the magnetic bearings for use in testing had to be chosen, and secondly the unbalance of the rotor had to be considered. These two issues are addressed below.

6.5.1 Effect of Bias Current

It is of interest to understand how the presence of a bias current - and the magnitude of that current - influences the system characteristics. A series of impulse test were therefore performed on the rig with varying levels of bias current. Some key characteristics can be seen from time-series plots of these impulse responses, and as such these are presented in Figure 6.12. In particular it can be seen that a reduction in frequency of response accompanies increasing bias current, as well as a substantial increase in damping. The frequency reduction reflects the fundamental nature of the uncontrolled magnetic field, i.e. the negative stiffness effect. In order to quantify this change in frequency, Fourier analysis was applied to the sensor readings, and the results are summarised in Table 6.3. It is noted that, owing to the significant increase in damping at higher bias currents (especially 5 A), there is substantially less response data for the Fourier analysis to work with, and consequently the frequencies derived for the higher biases have a higher uncertainty.

Considering these results, for all running test to be conducted on the rig, a bias current of 3 A was chosen. This value represents a balance of considerations: on the one hand, a higher bias current is desirable, as it permits the implementation of a more "forceful" controller. This is owing to the fact that no control current may ever exceed the bias current (and indeed, to maintain approximate linearity, should remain somewhat lower), so the higher the bias used, the higher potential control forces are available. On the other hand, due to the inevitably imperfect concentricity between the rotor and the magnetic bearings, higher current values tend to move the system closer to instability - increasingly so as the current value rises due to the square relationship between current and magnetic force. There are also current constraints based on thermal considerations, amplifier slew rates and eventually magnetic saturation. Thus 3 A is selected as a reasonable balance of these considerations.

6.5.2 Balancing the Rotor

Upon completion of the manufacturing and installation of the test rig, one of the first tasks was to assess the balance of the rotor. Whilst the purpose of the rig is to allow vibration reduction even in the presence of rotor unbalance, there are testing situations which require the rotor to run freely without the magnetic bearings being used. In these cases, it is important that the

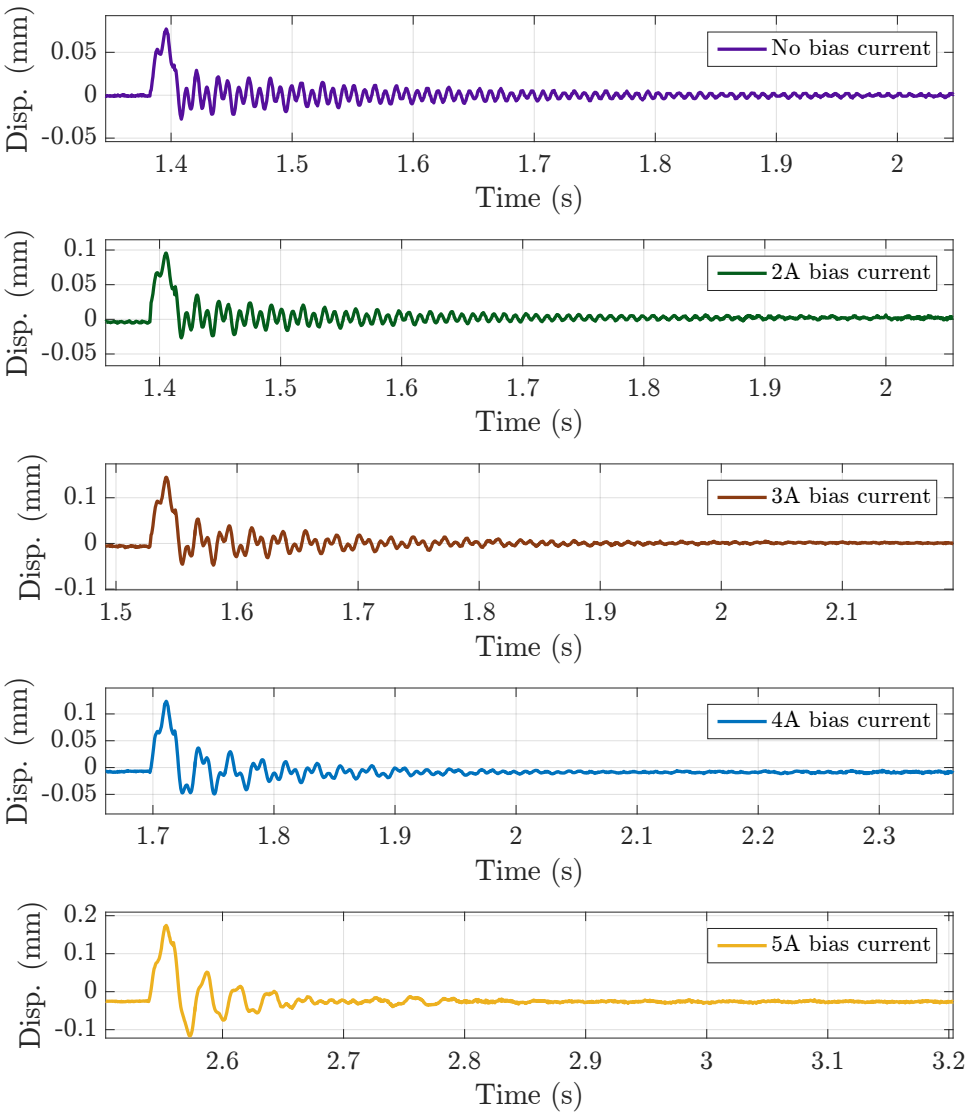

Figure 6.12: System response to impulse with varying levels of bias current

Table 6.3: Effect of bias current on system natural frequencies

Bias Current (A)	Rotor Natural Frequency (Hz)	Secondary Shaft Natural Frequency (Hz)
No Bias	47.7	114.8
2	47.0	114.5
3	44.1	111.9
4	41.0	109.2
5	34.7	108.5

rotor is sufficiently balanced to avoid vibration amplitudes that may cause contact with the (inactive) magnetic bearings. As such, the rotor is approximately balanced before testing is undertaken.

The rotor is designed with a series of threaded holes in each of two planes, specifically for the purpose of adding masses to alter the rotor's out-of-balance condition. These planes are located at the shoulders where the rotor steps down from the large hollow tube to the thin solid central span.

The process of balancing can be approached either from a mathematical viewpoint if fine-tuned balance is required, or else from an experimental angle, which is more straightforward for approximate balancing, but difficult to achieve precision with.

The mathematical technique first involves running the rotor at sub-critical speeds under a couple of trial conditions, before calculating the required position and mass of a balancing mass to minimise the vibration seen. The trial conditions used are:

- running the rotor "as-is" without any extra masses
- running the rotor with an arbitrary mass at an arbitrary location in one of the balancing planes

Calculation of a "correction mass" is then approached as follows, with reference to Figure 6.13.

Consider the situation for a stationary rotor (t = 0), with the potential to have an unbalanced mass in each of the x and y directions. At some time t later, the system has rotated, and the axes are momentarily in a new position, being a shift of Ωt from the starting position.

The unbalance in each of the x and y directions due to each of the masses m_x and m_y at time t may be written as:

$$\left.\begin{aligned} u_x &= m_x \cos(\Omega t) \\ u_y &= m_x \sin(\Omega t) \end{aligned}\right\} \quad \text{due to } m_x \tag{6.20}$$

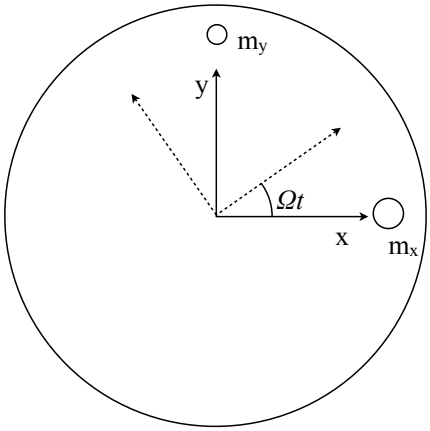

Figure 6.13: Out of balance masses on a rotor

$$\left.\begin{aligned} u_x &= -m_y \sin(\Omega t) \\ u_y &= m_y \cos(\Omega t) \end{aligned}\right\} \quad \text{due to } m_y \tag{6.21}$$

Therefore the total unbalance in x is given by:

$$u_x = m_x \cos(\Omega t) - m_y \sin(\Omega t) \tag{6.22}$$

By Euler's Formula this can be expressed as:

$$u_x = m_x \left(\frac{e^{j\Omega t} + e^{-j\Omega t}}{2} \right) - m_y \left(\frac{e^{j\Omega t} - e^{-j\Omega t}}{2j} \right) \tag{6.23}$$

which collects to give:

$$u_x = \underbrace{\left(\frac{m_x + jm_y}{2} \right)}_{U_c} e^{j\Omega t} + \underbrace{\left(\frac{m_x - jm_y}{2} \right)}_{\bar{U}_c} e^{-j\Omega t} \tag{6.24}$$

As a forced response to an harmonic excitation, the displacement of the rotor due to the out of balance mass can be expressed as:

$$x = X \cos(\Omega t + \phi) = \frac{X}{2} (e^{j(\Omega t + \phi)} + e^{-j(\Omega t + \phi)}) \tag{6.25}$$

which can be written in the same form as the unbalance as:

$$x = \underbrace{\left(\frac{X}{2}e^{j\phi}\right)}_{X_c} e^{j\Omega t} + \underbrace{\left(\frac{X}{2}e^{-j\phi}\right)}_{\bar{X}_c} e^{-j\Omega t} \tag{6.26}$$

The relationship between the unbalance and the response can then be expressed as:

$$X_c = A_x U_c \tag{6.27}$$

Similar working for the behaviour in the y-direction results in a comparable equation to Equation (6.27), and the two results are combined to give:

$$\begin{bmatrix} X_c \\ Y_c \end{bmatrix} = \begin{bmatrix} A_{xx} & A_{xy} \\ A_{yx} & A_{yy} \end{bmatrix} \begin{bmatrix} U_c \\ V_c \end{bmatrix} \tag{6.28}$$

With the known trial mass and measured response, it is then possible to calculate the values of A_{xx} etc. This calculated $\mathbf{A}$ matrix can then be used with the data from the run of the rotor in its original condition to ascertain what unbalance caused that result, i.e. what the rotor's natural unbalance is. It is then a simple matter of adding an equal "correction mass" 180° from the natural unbalance to cancel out its effect.

In this project however, it is not necessary - or indeed desirable - to balance the rotor with great precision. It is desirable to have at least some level of unbalance present to be able to evaluate the capabilities of the test rig to negate its effect. Therefore a simple experimental technique is employed to achieve an approximate balancing.

The technique requires an educated guess at a level of balancing mass to use, and then making a few trial runs (at a set speed) with the mass in different locations around the shaft and comparing the orbits seen.

The results of such an experimental balancing scheme are readily illustrated graphically; Figure 6.14 shows how the rotor orbit at a speed of 39 Hz is altered by the addition of a 5 g mass at several different locations. It is clear that when the mass is added at an angle of 240° (relative to an arbitrary starting point), a substantial reduction in orbit size is achieved. The orbit becomes significantly less round as it reduces size, which is a result of the rotor runout having greater influence on smaller orbits.

It will be seen in Chapter 7 that the reduced level of unbalance achieved this way affords the ideal conditions for testing the rig's capability - this unbalance is still large enough to prevent the rotor passing its critical speed without vibrating excessively, but small enough that orbits are not driven too large at lower speeds. If the balancing was "too good", the rotor may become able to pass its first critical speed without the use of the magnetic bearings, making it difficult

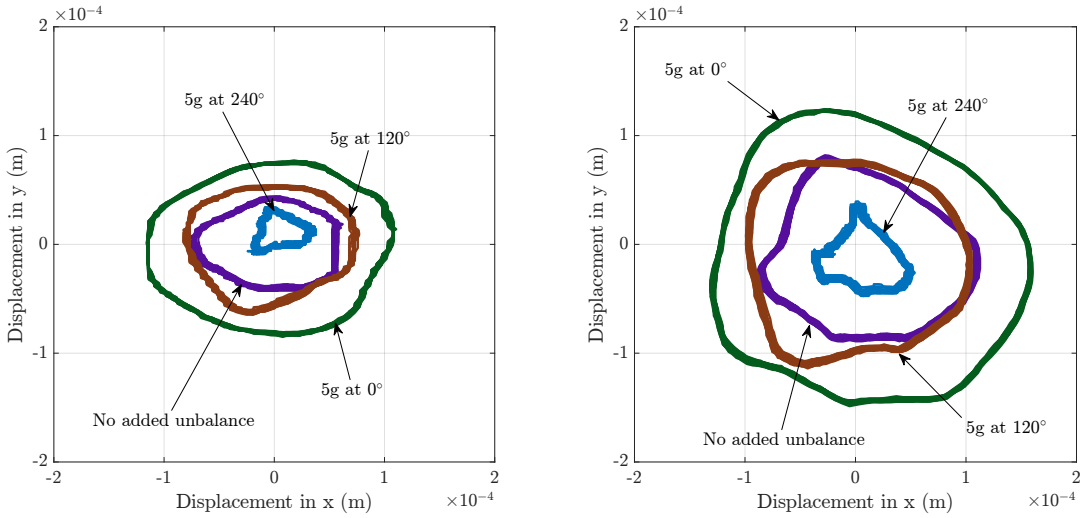

Figure 6.14: Rotor obits at end 1 (left) and end 2 (right) at 39 Hz (2340 rpm) with trial mass add various stations

to prove their performance.

Chapter 7

Demonstrating Vibration Control

The project thus far has involved the design, modelling, manufacture and identification of a test rig employing flexibly mounted magnetic bearings for vibration reduction in a flexible rotor. This chapter is concerned with actually demonstrating the fulfilment of the key project goal - illustrating the capability of the designed system to perform its proposed purpose.

Naturally, this means instituting an active control system to engage the magnetic bearings, and thus alter the rotor dynamics of the plant. A variety of control schemes are possible for such a target, and in this project, two alternatives are examined. In the first instance, a traditional PID controller is employed. Such controllers are extremely common in industrial systems of all kinds - including magnetic bearing systems - due to their simple concept, ease of application and reliable performance. Up until now, all simulations in the project of the test rig involving coupling the rotor to the secondary shaft have essentially assumed PID control (chiefly using the proportional control to provide a coupling stiffness).

The simplicity of the PID controller is, however, also one of its key drawbacks. The PID scheme works based on very small amount of data (a few sensor readings), and has very limited adjustable parameters; as such it gives the control designer limited capacity to alter how the system behaves. Therefore, to further explore what may be possible using this system topology, a second control technique is considered, namely a model-based H_∞ controller. While this is somewhat more complex to understand and design than a PID controller, it has the great advantage of affording far greater opportunity for the designer to choose how the controlled system behaves - one can effectively specify performance goals and costs, and calculate the controller which works within these parameters.

Thus this chapter presents the design of each of these two controllers, together with key re-

sults which illustrate the performance of the system under each control system. It is clearly demonstrated that - with a rotor which is unable to pass its first critical speed without the magnetic beatings active due to the occurrence of touchdown - appropriate control of the magnetic bearings can comfortably permit the rotor to reach supercritical speeds.

7.1 Practicalities of Implementing Control

As indicated in Section 4.1.1, all "active" aspects of the test rig are governed by software running on a dSPACE real-time processing system. Technically, the dSPACE system runs a code in the programming language C. However, all the actual construction and logic of the software is undertaken in a Simulink model, with the C code being automatically generated from that model. This section therefore gives an overview of the Simulink model which lies behind all active running of the rig.

An outline of the whole Simulink system is shown in Figure 7.1. For reference purposes, four "zones" (A - D) have been identified on the diagram.

An explanation of the function of the model begins in Zone A. Here, the system takes as inputs all sensor readings arriving from the rig. These readings are provided to the dSPACE analogue to digital (AD) board as simple voltages. The rig employs two types of sensor: the eddy current displacement sensors, and the slotted optical switch which functions as an encoder. The optical switch provides a binary output, so its signal may be used immediately in the encoder subsystem (see Section 4.3.3), but the displacement sensor readings must pass through a calibration to give a physically meaningful displacement value before use. For details on the sensor calibration process, see Section 4.3.2.

After calibration, the signals from the *external* sensors can then be left without modification - they are only used for monitoring purposes. However, the internal sensors are used for control, and the variable of interest to the controller is the *error* signal (or change in displacement), rather than the absolute value of the sensor reading. Therefore the instantaneous sensor readings are deducted from the initial readings, which is to say the readings the sensors produce when the system is first turned on, before any control or motion is applied.

These error signals are then available as inputs for any control action. Two controllers are implemented here - the upper path at the right-hand end in Zone A contains the PID controller, while the lower path contains the H_∞ controller. Each path then outputs four control currents - one for each of the control axes of the magnetic bearings.

Zone B is the home of a variety of open-loop current demand subsystems. These work entirely independently of any sensor signals, and are mostly designed to allow various set-up and identification processes to be carried out through the magnetic bearings. Such signals as impulses, steps, steady DC values, frequency swept sine-waves and a rotating circular force are available

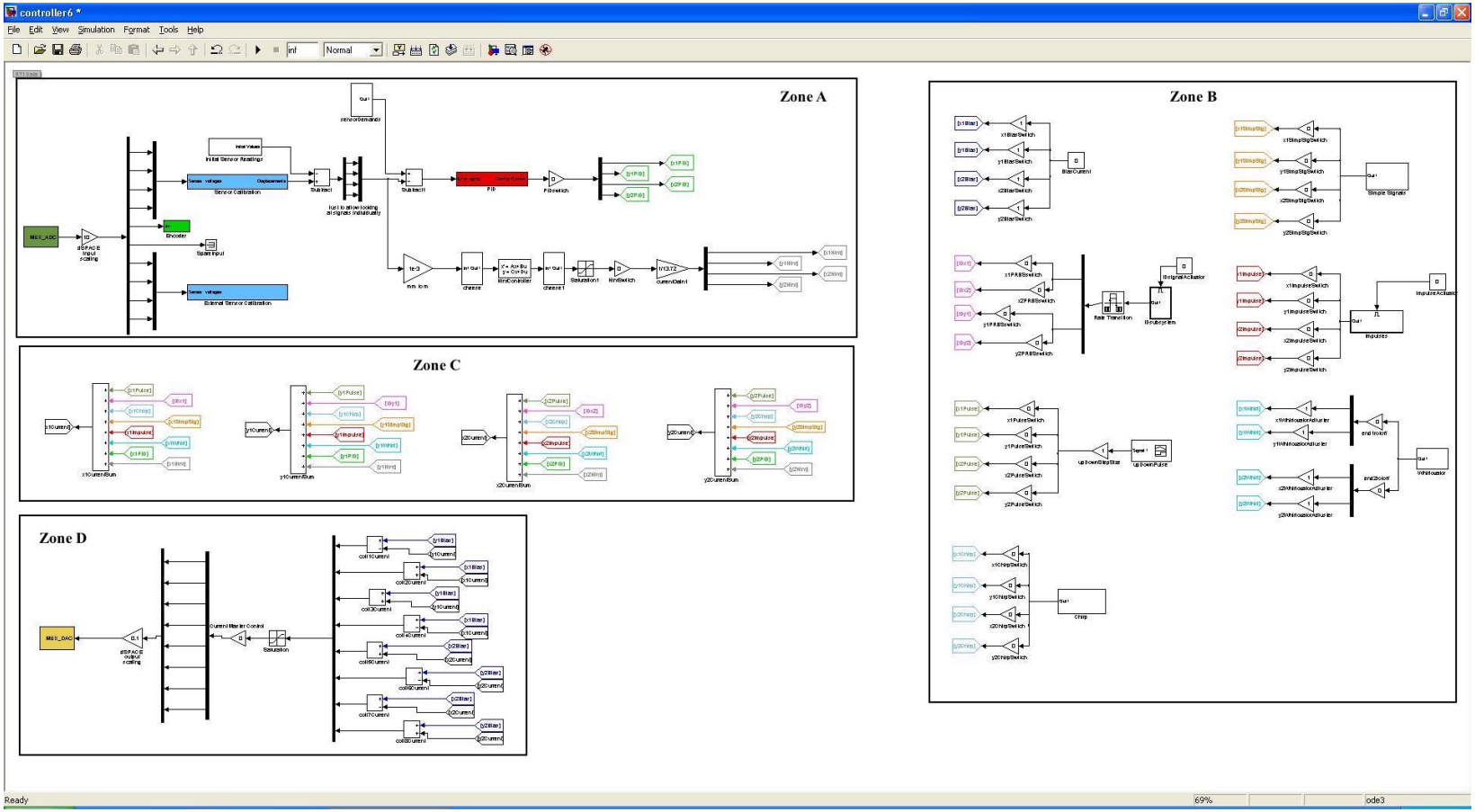

Figure 7.1: Overview of Simulink model which coordinates all “active” aspects of the test rig

from these subsystems. Each system outputs four separate current demands - again one for each axis of the magnetic bearings.

In Zone C, all demanded currents - including those associated with either of the control algorithms, and and open-loop demands - are summed for each of the four axes.

Finally, Zone D is concerned with outputting current demands to the amplifiers. While there are only four control axes, each axis uses two independently driven coils, and thus there are eight total coils, powered by eight actuators. In each axis, the two coils are driven as a linearised pair (see Section 5.1), i.e. one coil outputs $(i_b + i_d)$, while the other outputs $(i_b - i_d)$ where i_b is the bias current and i_d is the demanded current from Zone C. This is seen implemented in the right-hand end of Zone D, after which the currents are outputted (via a saturation limit for safety) to the dSPACE digital to analogue (DA) board.

7.2 Controller Theory and Design

This section covers the design / tuning of each of the PID and H_∞ controllers, together with appropriate theory.

7.2.1 An Initial Control Strategy - PID

As probably the single most commonly employed form of algorithm in feedback control systems, the PID controller needs little introduction. Its advantages lie in its simple and intuitive application, as well as its reliable and predictable performance, and general effectiveness across the majority of applications.

Designing a PID controller is really just an exercise in tuning, as the structure is predetermined. The designer may choose values for each of the proportional, integral and derivative gains, and usually also a filter coefficient for the derivative action.

Stub Shaft PID Experiments

By way of a"stepping stone" towards controlling the final rotor system, earlier in the project, a simpler mini-rig was assembled to perform some tests on the fundamental capabilities of the magnetic bearings and of their control system. The arrangement consisted of a short section of the same steel tube that the first generation rotor was made from supported on a single rolling element bearing, together with one of the "seconary shaft" assemblies from the main rotor system. A picture of this arrangement is shown in Figure 7.2.

In the first instance, even just assembling this mini arrangement provides encouraging reassurance, inasmuch as it illustrates that the manufacturing and assembly of these components is of

sufficient accuracy to allow them to interact correctly without interference. This is not a trivial result given the clearance of 0.4 mm between the inner surface of the rotor and the touchdown disk protecting the magnetic bearing.

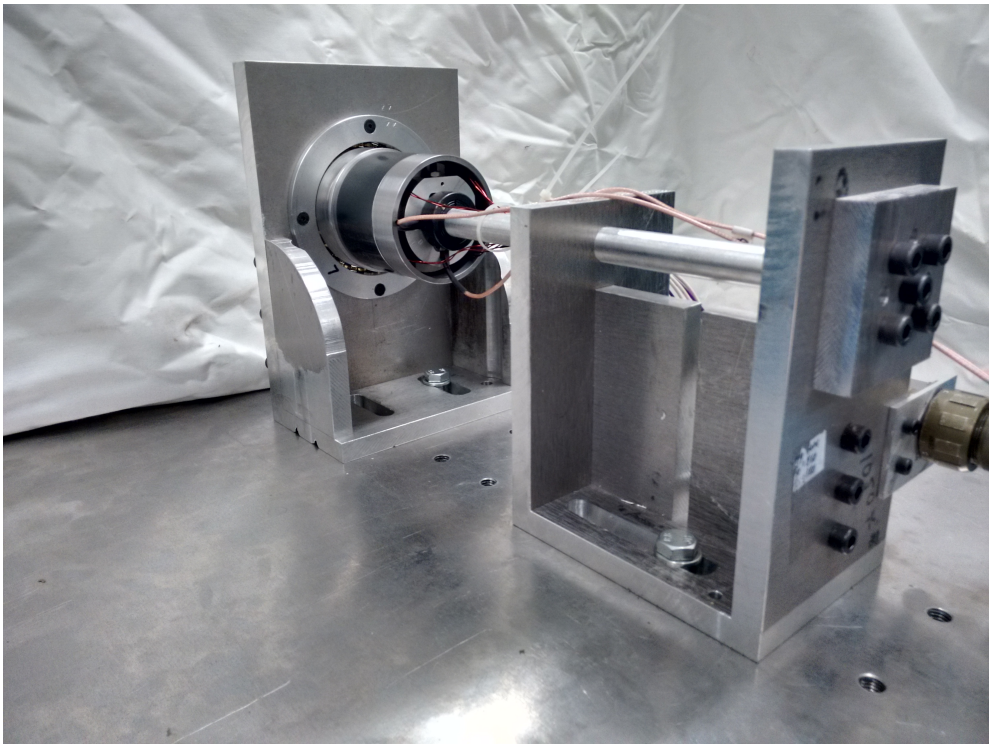

Figure 7.2: The stub shaft mini-rig arrangement

With the components in place, it was possible to check the mapping of which sensors aligned with which coils, and particularly which amplifiers needed to be activated to energise the correct coil for a given rotor displacement. Once these basic characteristics were verified a PID controller was applied to assess how the system responded to demands.

Firstly, a reasonable baseline of controller gains was experimentally determined, and then each of the PID gains was varied in turn to assess the behaviour of the system.

It is notable that the task using this mini-rig was to statically control the position of the stub shaft within the natural "float" of the rolling element bearing, i.e. the slight angular motion possible between the inner and outer race of the bearing. The stub shaft was not rotated. Due to the incredibly low stiffness of the bearing float, it is inevitable that substantial overshoot will occur when lifting the stub shaft with the magnetic bearing, regardless of controller gains.

As a basic test, the response of the system to a step demand, was assessed under each of PID, PD and PI control, to check whether expected characteristics were observed. The results of this comparison are shown in Figure 7.3. Note that the demand was set to a displacement of 1.85 mm. Also the difference in the starting time of each response is due to the controller being

manually activated, so for each experiment this was at a slightly different point in time.

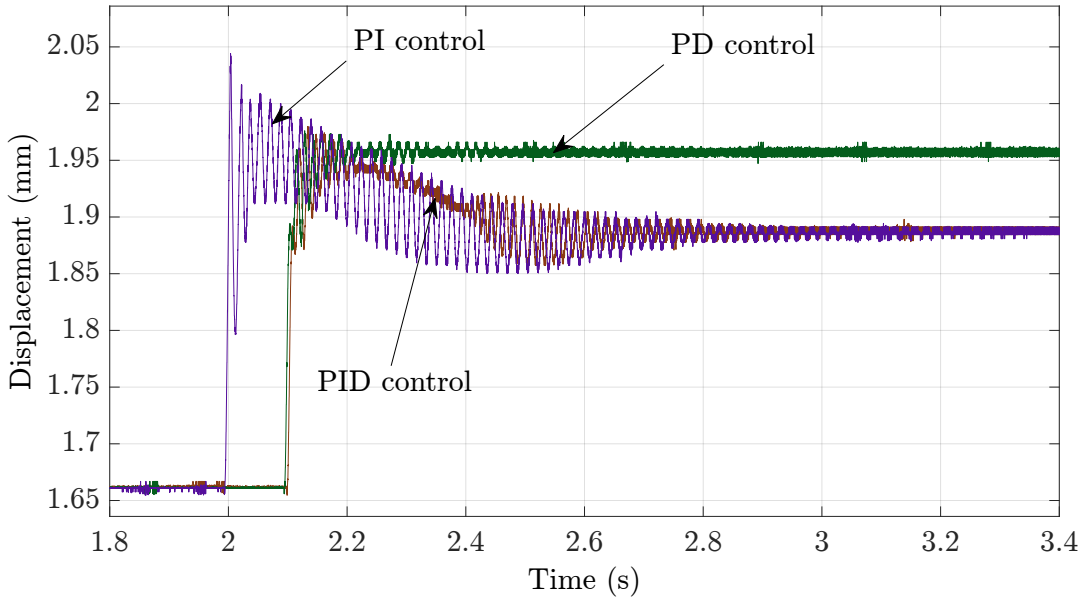

Figure 7.3: The response of the stub shaft system to a demand of 1.85 mm under each of PID, PD and PI control

The results show largely what would be expected of any system under such control schemes: PD control results in a notable steady state error due to the lack of integral control, PI control results in excessive oscillation due to a lack of damping, while PID control offers a good combination of both oscillation and steady state error characteristics. This is a good indicator that both the controller and the hardware are operating as designed.

Tuning PID Controller for Main Rig

In the first case, it is noteworthy that in this application, the integral action of a PID controller is unnecessary; integral control is used to eliminate steady state errors in a plant's performance, however, with the rotor system here, the desired set-point (i.e. bearings centred within the rotor) is already achieved by the rig set up, and thus does not need controlling. For an application where the rotor was levitated on the magnetic bearings then integral control would most likely be employed to achieve the desired levitation equilibrium point, but such is not the case in this project. Thus only PD control is used for vibration management, and in recognition of this, from here on this controller is generally just referred to as "the PD controller".

In terms of tuning the controller gains, while there do exist automated PID tuning codes and algorithms such as Ziegler-Nichols, it is recognised that these techniques use a purely mathematical logic to choose controller gains, and do not account for the nuances of the physical system, frequently resulting in poor or unstable performance. As such a manual tuning was

Table 7.1: Tuned PD controller coefficient values

Coefficient	Value
P	10 N/mm
D	0.012 Ns/mm
N	1650 rad/s

undertaken.

The general goal was to achieve a controller as stiff as possible without causing instability. This should allow the greatest effect on the rotor natural frequency, and therefore the best performance.

For the proportional gain, it was chosen initially to aim for a control force of around 10 N in response to an error of 0.1 mm. From this starting point, a stabilising value of derivative control was established, and these two parameters (together with the derivative filter coefficient) were experimentally adjusted until approximately the highest value of proportional gain that could still be reliably stabilised was found. Final gain values used to run the rig and generate results are shown in Table 7.1.

Results using this controller are found in Section 7.3.3.

7.2.2 H_∞ Control

PID control is the industrial standard in many applications, and while being straightforward and easy to apply, it has certain limitations. These include:

- the controller works with a limited amount of data - it has data from the sensor measurements, but it has no "knowledge" of the rest of the system dynamics. As far as the PID controller is concerned absolutely anything could be happening in the rest of the system outside its measurement points.
- there is limited capacity for tuning the response of a complex system. The PID method basically only gives three adjustable gain values, which are not sufficient for detailed control of a multi-degree-of-freedom system, and are not substantially frequency dependent.
- with the PID controller, one does not have the ability to impose "design goals" on the system, for example the goal that the rotor vibration amplitude be minimised while the secondary shaft is allowed to vibrate within a specified range of movement.

A number of more modern control techniques are available to address these issues. In this project, H_∞ control is selected as the most suitable technique - it not only offers solutions

to the above points, but also allows a robust controller to be generated, which is tolerant of modelling inaccuracies and external disturbances.

H_∞ control is somewhat unintuitive, and is significantly less widely understood and used across industry than PID control. Thus it is appropriate here to give a brief overview of the fundamentals of this method, before demonstrating its application to the composite rotor topology.

H_∞ Fundamentals

H_∞ control is a relatively new technique in the control field. It emerged towards the end of the 1970s, with key works presented by Zames [74], Helton [75] and Tannenbaum [76].

At its heart, the technique is a species of mathematical optimisation problem; the optimisation itself, however, is not of significant interest in an engineering context - the engineering challenge is in defining the variable/model *to be optimised*. The following material outlines how this may be undertaken.

Problem Formulation

The standard formulation for H_∞ control problems is shown in Figure 7.4. Here, $\mathbf{P}(s)$ is the plant to be controlled, and $\mathbf{K}(s)$ is the controller. The input $\mathbf{w}$ contains all external signals acting on the plant, which may include demand signals and disturbances. The output $\mathbf{z}$ contains the output variables which are regulated by the controller. The signals $\mathbf{y}$ and $\mathbf{u}$ are internal to the overall system, and contain respectively the measured values used by the controller and the control inputs provided to the plant.

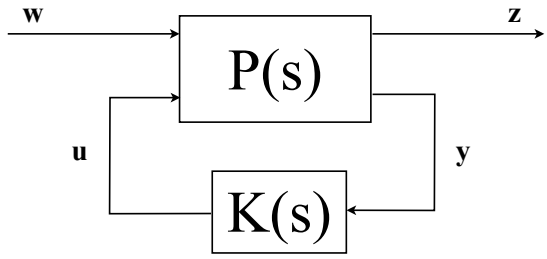

Figure 7.4: General structure of augmented plant for H_∞ controller design

The plant has two inputs and two outputs, and can therefore be considered as a collection of four transfer functions, relating each input to each output:

$$\begin{bmatrix} \mathbf{z} \\ \mathbf{y} \end{bmatrix} = \begin{bmatrix} \mathbf{P}_{11} & \mathbf{P}_{12} \\ \mathbf{P}_{21} & \mathbf{P}_{22} \end{bmatrix} \begin{bmatrix} \mathbf{w} \\ \mathbf{u} \end{bmatrix}$$

Of particular interest is the relationship between the exogenous inputs, $\mathbf{w}$, and the controlled

outputs, **z**. This relationship is denoted T_{zw} and termed the "lower linear fractional transformation", $F_l(\mathbf{P},\mathbf{x})$.

$$\mathbf{T}_{zw} = \mathbf{P}_{11} + \mathbf{P}_{12}\mathbf{K}(\mathbf{I} - \mathbf{P}_{22}\mathbf{K})^{-1}\mathbf{P}_{21} \tag{7.1}$$

The goal of the H_∞ control problem is then to minimise a quantity termed the "infinity norm" of this transfer function through the choice of the controller $\mathbf{K}(s)$. In mathematical terms, the infinity norm may be defined as follows.

For the generally complex matrix $\mathbf{Q}$, the positive square root of the eigenvalues of $\mathbf{Q}^H\mathbf{Q}$ are termed the singular values of $\mathbf{Q}$ ($\sigma(\mathbf{Q})$), where $\mathbf{Q}^H$ is the conjugate transpose of $\mathbf{Q}$. The largest such value is denoted $\bar{\sigma}(\mathbf{Q})$.

Now, if instead of a static matrix, one has a function of frequency - that is to say $\mathbf{Q}$ is replaced by $\mathbf{R}(j\omega)$ - then the spectral norm of $\mathbf{R}(j\omega)$ can be defined as the frequency-dependent largest singular value:

$$\|\mathbf{R}(j\omega)\|_s = \bar{\sigma}(\mathbf{R}(j\omega)) \tag{7.2}$$

The H_∞ norm is then defined by taking the maximum singular value over all frequencies:

$$\|\mathbf{R}(j\omega)\|_\infty = \sup_{\omega}(\mathbf{R}(j\omega)) \tag{7.3}$$

From the point of view of an "intuitive understanding", the H_∞ norm can be though of as an upper bound on the frequency response of a multi-input, multi-output system.

Generating H_∞ Controllers

As a matter of fact, a detailed understanding of the mathematical definition of the H_∞ norm and techniques to optimise it are not strictly necessary - as alluded to above, built in Matlab functions are generally used for this. In this project, two different algorithms are used: `hinfsyn` and `mixsyn`. Both of these algorithms take as inputs a model of the plant, and output a controller which minimises the H_∞ norm of the closed loop transfer function T_{zw}. The important consideration from an engineering standpoint, therefore, is the formulation of the model of the plant, which is passed to these Matlab functions to generate the controller.

Now an important distinction in notation is highlighted - the "fundamental" model of the plant (for example, resulting from finite element modelling) is denoted $\mathbf{G}(s)$. However, this is not the same as $\mathbf{P}(s)$ - the plant model on which the controller is built. $\mathbf{P}(s)$ is *based* on $\mathbf{G}(s)$, but in order to specify desired performance characteristics of the system, the plant model $\mathbf{G}(s)$ is augmented with one or more weighting functions. These are frequency dependent functions (commonly first or second order transfer functions) which multiply various plant input and

output signals, in order to cause the controller generated to give a greater or lesser emphasis to a particular part of the input or output over a particular frequency range. This new plant is $\mathbf{P}(s)$ - it is the fundamental model $\mathbf{G}(s)$ combined with the weighting functions. $\mathbf{P}(s)$ is known as the augmented plant, and this is what is passed to the controller design algorithm.

The real art, therefore, in H_∞ controller design lies in the choice of the plant augmentation weighting functions.

7.2.3 A Tale of Two Controllers

Over the course of the project, two separate methods for forming an H_∞ controller have been explored. The key conceptual different between the two formulations lies in their approaches to solving what may be termed the "relative displacement problem".

Recall that the test rig has two sets of sensors - one set mounted on-board the secondary shafts inside the rotor, and one set rigidly mounted to the rig base plate outside the rotor. As mentioned earlier, only the internal sensors are part of the system design - the external set being present purely for purposes of observation. Thus the only sensor readings available to any controller are those from the internal sensor set, which measure the *relative* displacement of the rotor to the secondary shaft.

Now consider that the design objective of the system is to minimise the *absolute* displacement of the rotor, and not necessarily the *relative* displacement value as provided by the sensors. This is the "relative displacement problem".

Over the following pages, each of the two approaches explored to solve this problem and generate an H_∞ controller are explained.

Imperfect Models

Model based controllers assume as a prerequisite a reasonably accurate model of the plant they are designed to control. For the test rig, a satisfactorily accurate model of the beam elements has been achieved via finite element modelling and parameter identification. However, models of the magnetic bearings, amplifier and sensors have not been developed. These item are therefore, by default, assumed by the model to be "perfect" - effectively all exhibiting a gain of 1 and a phase of 0 between all relevant inputs/outputs over all frequencies. Provided all these components have substantially faster dynamics than the main beam elements, this assumption should suffice. However it is recognised that a modicum of trial-and-improvement may be necessary to achieve a stable controller in light of these assumptions.

H_∞ Controller 1

The first avenue explored in the H_∞ arena builds a controller around the assumption that values of absolute rotor displacement *are* provided. Then, given that these values are not actually available from the rig, a traditional Luenberger Observer was designed to provide estimates of the absolute rotor motion, and these - together with the actual sensor measurements of the relative displacement - were provided to the controller.

Thus two systems must be built - first the controller, and separately the observer. As the controller was built on the assumption that both relative and absolute displacement values are readily available, it was possible to use a well-known formulation to design the controller know as the *mixed sensitivity* formulation. The key points of this technique, as well as notes on the observer design follow.

The Mixed Sensitivity Formulation

One relatively common way to generate an augmented plant is by using a formulation known as the mixed sensitivity problem. In this type of H_∞ problem, there is a pre-determined structure for the augmented plant, which can simplify the job of the control designer. The structure allows for weightings to be placed on three specific signals, and the block diagram for such a system is illustrated in Figure 7.5. The weighting functions are generally labelled $\mathbf{W}_1$, $\mathbf{W}_2$ and $\mathbf{W}_3$, as shown in the figure; a qualitative interpretation of the role of each weighting is provided as follows:

Table 7.2: Roles of plant-augmenting weighting functions

Weighting Function	Role
$\mathbf{W}_1$	Weights the closed loop sensitivity function of the system
$\mathbf{W}_2$	Used to limit the magnitude and frequency of control action that may be demanded, which can be used to prevent actuator saturation
$\mathbf{W}_3$	Weights the closed loop complementary sensitivity of the system

Generally $\mathbf{W}_1$ takes small values in the frequency range where good disturbance rejection is important, whereas $\mathbf{W}_3$ is best kept small in frequencies outside of the control bandwidth, to avoid potential instability issues.

The Matlab algorithm used in this case is `mixsyn`, which is specifically designed for the mixed sensitivity problem formulation. The function can either be passed the complete augmented plant $\mathbf{P}(s)$, or the fundamental plant $\mathbf{G}(s)$, together with values for $\mathbf{W}_1$, $\mathbf{W}_2$ and $\mathbf{W}_3$, which

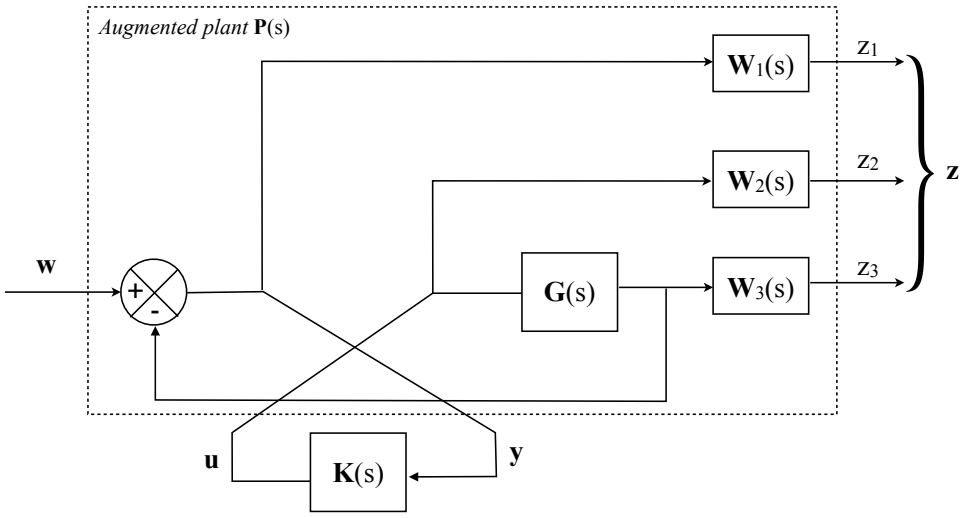

Figure 7.5: Illustration of the structure of the augmented plant for a mixed sensitivity problem showing placement of weighting functions

it will automatically assemble into an augmented plant. The two inputs are equivalent, and either will result in the output of the same H_∞ controller.

Observer Design

To provide the values of absolute rotor displacement that the controller is expecting, an observer is designed. An observer is essentially a model of a system which can - given a limited number of measurements from a system, and the knowledge of what forces are acting on the system - provide estimates of what is happening in other, non-measured, parts of the system.

The observer is given two sets of inputs: the first is the forces which are being applied to the real system, and the second is a set of measurement of the system response at certain locations (i.e. from sensors). If the observer is a *perfect* model of the real plant, then it could, in theory, make its estimates without the second input at all, just knowing the forces applied to the system. In reality, a perfect model is not achievable, and thus a technique is required to ensure the outputs of the observer match those of the real plant. This is done by comparing the known, measured, system response from the plant sensors to the values the observer is estimating for these measurements, and causing the observer to adjust its output until any difference in these values is removed. A practical, mathematical method of achieving this is now described.

Consider the existence of a plant with inputs $\mathbf{u}$ and measurements $\mathbf{y}_1$. The states of the plant are $\mathbf{x}$, such that

$$\begin{aligned} \dot{\mathbf{x}} &= \mathbf{A}\mathbf{x} + \mathbf{B}\mathbf{u} \\ \mathbf{y_1} &= \mathbf{C}\mathbf{x} + \mathbf{D}\mathbf{u} \end{aligned} \tag{7.4}$$

These measurements are not a complete description of the response of the plant, but a "snapshot" of the response of certain degrees of freedom (i.e. sensor readings).

Now consider that it is required to know the response of the plant in some degrees of freedom which are not directly measured. This can be viewed as a second set of responses, $\mathbf{y_2}$. One can define a model of the plant as

$$\begin{aligned} \dot{\hat{\mathbf{x}}} &= \mathbf{A}\hat{\mathbf{x}} + \mathbf{B}\mathbf{u} + \mathbf{T}(\mathbf{y_1} - \hat{\mathbf{y}}_\mathbf{1}) \\ \hat{\mathbf{y}} = \mathbf{C}\hat{\mathbf{x}} + \mathbf{D}\mathbf{u}, &\qquad \hat{\mathbf{y}} = [\hat{\mathbf{y}}_\mathbf{1} \quad \hat{\mathbf{y}}_\mathbf{2}]^T \end{aligned} \tag{7.5}$$

The $\hat{}$ in the equations describing the model are in recognition of the fact that the model will not have states and outputs which exactly match with the real states and outputs of the physical plant. They are estimates. Note also that this model has an extra input term: ($\mathbf{y}_1$ - $\hat{\mathbf{y}}_1$) - the difference between the measured outputs and the estimates of those outputs. This input is multiplied by the matrix $\mathbf{T}$, which is to be chosen by the model designer. The goal in choosing $\mathbf{T}$ is to cause any difference between the plant states $\mathbf{x}$ and the estimated states $\hat{\mathbf{x}}$ to rapidly decay to zero.

In pursuit of this goal, the state equations of the model and plant are subtracted as follows

$$\dot{\hat{\mathbf{x}}} - \dot{\mathbf{x}} = \mathbf{A}\hat{\mathbf{x}} - \mathbf{A}\mathbf{x} + \mathbf{B}\mathbf{u} - \mathbf{B}\mathbf{u} + \mathbf{T}(\mathbf{y_1} - \hat{\mathbf{y}}_\mathbf{1}) \tag{7.6}$$

and substitutions for $\mathbf{y}_1$ and $\hat{\mathbf{y}}_1$ are made

$$\begin{aligned} \dot{\hat{\mathbf{x}}} - \dot{\mathbf{x}} &= \mathbf{A}\hat{\mathbf{x}} - \mathbf{A}\mathbf{x} + \mathbf{B}\mathbf{u} - \mathbf{B}\mathbf{u} + \mathbf{T}\mathbf{C_1}\mathbf{x} + \mathbf{T}\mathbf{D_{11}}\mathbf{u} - \mathbf{T}\mathbf{C_1}\hat{\mathbf{x}} - \mathbf{T}\mathbf{D_{11}}\mathbf{u} \\ &= (\mathbf{A} - \mathbf{T}\mathbf{C_1})(\hat{\mathbf{x}} - \mathbf{x}) \end{aligned} \tag{7.7}$$

It is now clearly seen that if $\mathbf{T}$ is chosen such that its eigenvalues of ($\mathbf{A}$-$\mathbf{TC}_1$) have large negative real parts, any discrepancy between the real and estimated states will rapidly decay. As a general rule, $\mathbf{T}$ is chosen to give ($\mathbf{A}$-$\mathbf{TC}_1$) dynamics five to 10 times faster than the dominant plant dynamics.

The observer as derived thus far is suitable for most purposes, but an error is encountered when trying to implement such a system in a real-time controller. This is due to the feedback loop where the estimated states $\hat{\mathbf{y}}_1$ (an observer output) are looped back to become part of one of the observer inputs. This effectively creates an algebraic loop, which is not permissible in a real-time situation. To overcome this, a modified form of the observer can be generated whereby the algebraic loop has been manually eliminated.

Consider now the system defined in the following way:

$$\begin{aligned}\dot{\mathbf{x}} &= \mathbf{A}\mathbf{x} + \mathbf{B_1}\mathbf{u_1} + \mathbf{B_2}\mathbf{u_2} \\ \mathbf{y_1} &= \mathbf{C_1}\mathbf{x} + \mathbf{D_{11}}\mathbf{u_1} + \mathbf{D_{12}}\mathbf{u_2} \\ \mathbf{y_2} &= \mathbf{C_2}\mathbf{x} + \mathbf{D_{21}}\mathbf{u_1} + \mathbf{D_{22}}\mathbf{u_2}\end{aligned} \tag{7.8}$$

In the observer as it stands, input $\mathbf{u}_2$ is defined as

$$\begin{aligned}\mathbf{u_2} &= \mathbf{y_{1m}} - \mathbf{y_1} \\ &= \mathbf{y_{1m}} - \mathbf{C_1}\mathbf{x} - \mathbf{D_{11}}\mathbf{u_1} - \mathbf{D_{12}}\mathbf{u_2}\end{aligned} \tag{7.9}$$

where $\mathbf{y}_{1m}$ is the measured outputs $\mathbf{y}_1$. The algebraic loop is clearly seen here, as $\mathbf{u}_2$ lies on both sides of the equation. Rearranging, however, gives

$$\mathbf{u_2} = (\mathbf{I} + \mathbf{D_{12}})^{-\mathbf{1}}(\mathbf{y_{1m}} - \mathbf{C_1}\mathbf{x} - \mathbf{D_{11}}\mathbf{u_1}) \tag{7.10}$$

If this definition of u_2 is then substituted into the system equations, a new model can be defined as:

$$\begin{aligned}\dot{\mathbf{x}} &= \bar{\mathbf{A}}\mathbf{x} + \bar{\mathbf{B}}_\mathbf{1}\mathbf{u_1} + \bar{\mathbf{B}}_\mathbf{2}\mathbf{y_{1m}} \\ \mathbf{y_1} &= \bar{\mathbf{C}}_\mathbf{1}\mathbf{x} + \bar{\mathbf{D}}_{\mathbf{11}}\mathbf{u_1} + \bar{\mathbf{D}}_{\mathbf{12}}\mathbf{y_{1m}} \\ \mathbf{y_2} &= \bar{\mathbf{C}}_\mathbf{2}\mathbf{x} + \bar{\mathbf{D}}_{\mathbf{21}}\mathbf{u_1} + \bar{\mathbf{D}}_{\mathbf{22}}\mathbf{y_{1m}}\end{aligned} \tag{7.11}$$

where

$$\begin{aligned}\bar{\mathbf{A}} &= \mathbf{A} - \mathbf{B_2}(\mathbf{I} + \mathbf{D_{12}})^{-\mathbf{1}}\mathbf{C_1} \\ \bar{\mathbf{B}}_\mathbf{1} &= \mathbf{B_1} - \mathbf{B_2}(\mathbf{I} + \mathbf{D_{12}})^{-\mathbf{1}}\mathbf{D_{11}} \\ \bar{\mathbf{B}}_\mathbf{2} &= \mathbf{B_2}(\mathbf{I} + \mathbf{D_{12}})^{-\mathbf{1}} \\ \bar{\mathbf{C}}_\mathbf{1} &= \mathbf{C_1} - \mathbf{D_{12}}(\mathbf{I} + \mathbf{D_{12}})^{-\mathbf{1}}\mathbf{C_1} \\ \bar{\mathbf{C}}_\mathbf{1} &= \mathbf{C_2} - \mathbf{D_{22}}(\mathbf{I} + \mathbf{D_{12}})^{-\mathbf{1}}\mathbf{C_1}\end{aligned} \qquad \begin{aligned}\bar{\mathbf{D}}_{\mathbf{11}} &= \mathbf{D_{11}} - \mathbf{D_{12}}(\mathbf{I} + \mathbf{D_{12}})^{-\mathbf{1}}\mathbf{D_{11}} \\ \bar{\mathbf{D}}_{\mathbf{12}} &= \mathbf{D_{12}}(\mathbf{I} + \mathbf{D_{12}})^{-\mathbf{1}} \\ \bar{\mathbf{D}}_{\mathbf{21}} &= \mathbf{D_{21}} - \mathbf{D_{22}}(\mathbf{I} + \mathbf{D_{12}})^{-\mathbf{1}}\mathbf{D_{11}} \\ \bar{\mathbf{D}}_{\mathbf{22}} &= \mathbf{D_{22}}(\mathbf{I} + \mathbf{D_{12}})^{-\mathbf{1}}\end{aligned}$$

The second plant input is now just y_{1m}, so does not include the observer output. This model is then suitable for use in a real-time system.

Running with $\mathbf{H}_\infty$ Controller 1

Many attempts were made at running this controller on the rig with various values of weightings and observer properties. However, while it was often possible to simulate this controller stably, a number of problems were experienced while attempting to practically implement it. In particular, getting the observer to give a realistic and stable output in the presence of the

unmodelled rotor run-out proved very difficult. In addition, the dSPACE system used to implement the control in real time has a limit to the order of systems it can run in real time - as both the observer and the controller contribute additional states to the overall system, in some cases it was found that an unrealisable system was generated.

As a result, it was strongly desirable to find a way of avoiding using the observer.

H_∞ Controller 2

The problem with using the mixed sensitivity formulation is that it has a pre-defined structure. Specifically, it assumes that all outputs from the fundamental plant model $\mathbf{G}(s)$ are available for feedback, and makes no provision for placing weightings on unmeasured outputs.

After some consideration, therefore, a different problem formulation was conceived. In theory, due to the fact that the H_∞ controller is model-based, it should be possible to impose design objectives on *any* model output, even if that output is not actually provided as a measurement to the controller. In this scenario, the controller itself is acting as a sort of observer. Therefore a more general formulation of the augmented plant was devised, based on a slightly more "first principles" approach. The arrangement devised for this problem is shown in Figure 7.6.

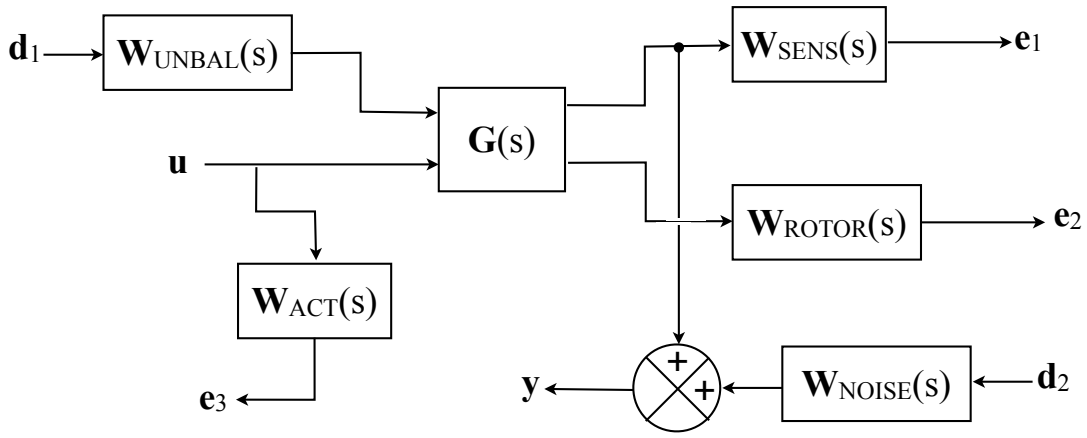

Figure 7.6: Layout of augmented plant for the second H_∞ controller design iteration

From this plant, a controller is designed to minimise the "errors" ($\mathbf{e}_1$, $\mathbf{e}_2$ and $\mathbf{e}_3$) subject to the disturbances $\mathbf{d}_1$ and $\mathbf{d}_2$. The controller will take as an input the signal **y,** and output control forces **u**.

The key feature which makes this structure particularly suited to this control problem is that the rotor motion (the second output of the plant $\mathbf{G}(s)$) can be given a performance weight, ($\mathbf{W}_{\mathrm{ROTOR}}(s)$) even though this signal is not fed back to the controller (i.e. the actual value is unmeasured).

With regards to the weighting functions, the purpose and actual transfer function used for each are described in the following sections.

Absolute Rotor Motion Weighting - $\mathbf{W_{ROTOR}}$

In order to design *weighting* for the absolute motion of the rotor, first a *target* for this performance was designed. The first step in this process is to examine the open loop plant performance, and identify where this is not satisfactory, and thus how the target closed loop performance should differ.

For the plant $\mathbf{G}(s)$ the frequency response between a disturbance $\mathbf{d}_1(1)$ and the rotor response $\mathbf{e}_2(1)$ can be plotted. This response is shown as the "open loop performance" in the bode plot of Figure 7.7. It is immediately obvious that the large peak just under 50 Hz - associated with the rotor first critical speed - is undesirable. Therefore, a "closed loop target" is specified as shown in the same figure, which matches the open loop performance most of the time, but does not include the resonance.

The transfer function for this target is shown in Equation (7.12).

$$\text{Rotor performance target:} \qquad 1.73 \times 10^{-7} \frac{s + 900}{s + 60} \tag{7.12}$$

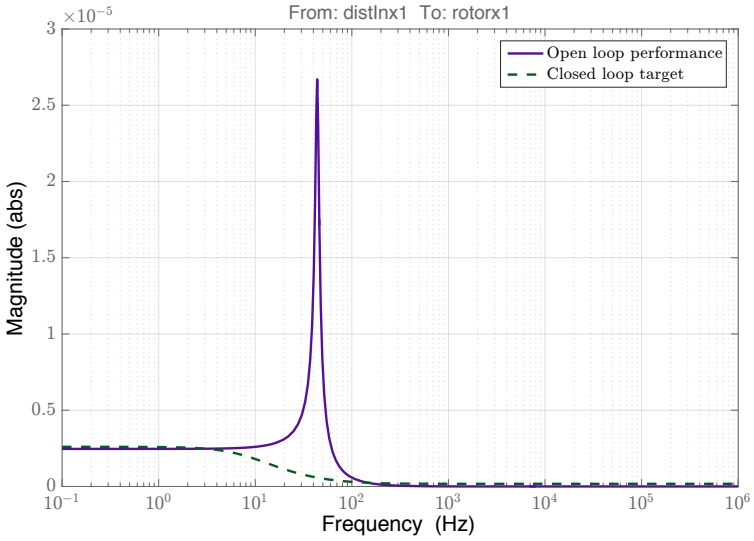

Figure 7.7: Bode plots of rotor open-loop performance and closed-loop target

The rotor performance *weighting* is now expressed as the reciprocal of this *target*.

With regard to each of the other weighting functions in Figure 7.6, their forms and functions are set out in Table 7.3.

Table 7.3: Roles of plant-augmenting weighting functions for H_∞ 2 controller

Weighting Function	Value	Description
$\mathbf{W}_{\text{SENS}}$	3.7×10^3	This weighting is set to be the reciprocal of the maximum permitted relative motion. This is to express the design goal that any displacement above this level must be penalised, regardless of frequency. Through experimentation, it is seen that touchdown occurs roughly when the relative sensor readings are about 0.2 mm. To build in a safety margin, a value of 0.15 mm is chosen as the maximum permitted level, hence the weighting.
$\mathbf{W}_{\text{ACT}}$	$100\frac{s+7}{s+7000}$	The function of the actuator weighting is to limit the control forces the controller may demand, specifically to avoid demands of forces of too high a magnitude, or to high a frequency, both of which would be unrealisable. Accordingly, the weighting has a high-pass shape, heavily penalising signals in and above the kHz zone.
$\mathbf{W}_{\text{UBAL}}$	$1 \times 10^{-4}\frac{s^2}{(\frac{s}{100}+1)^2}$	This weighting describing the expected unbalance force the rotor may experience. As this force is proportional to rotational speed squared, a second order transfer function is used.
$\mathbf{W}_{\text{NOISE}}$	$\frac{1}{s+1\times10^5} + 1 \times 10^{-5}$	This weighting describing the potential sensor noise which may effect the signals provided to the controller. An expected disturbance on signals of 10 μm amplitude is indicated, coupled with the potential for for a further 10 μm of DC offset due to the rotor runout.

Testing and Modifying H_∞ Controller 2

The weighting functions indicated above are the final values used to generate the controller responsible for the results presented later in this chapter. No secret is made of the fact that this is actually the 22nd such controller to be tested on the rig, and as such a good deal of trial-and-improvement has gone into these weightings. Space considerations preclude detailing all previous controllers and their various flaws, so just a couple of examples of the problems encountered and solutions implemented are provided.

Early attempts to run the controller were plagued with instability issues, and it was soon noticed that a discrepancy was observable when running the controller in simulation. Specifically, if a variable time-step solver was used, the system compiled and simulated without issue. However, when a fixed time-step was used, it was found to be necessary to use a very short time step (too short to be used on the dSPACE system) in order to achieve a stable simulation.

The problem was traced to the inclusion of several very fast poles in the controller, as generated by the `hinfsyn` algorithm. It is a known modelling phenomenon for high frequency model dynamics to sometimes cause stability issues in simulation or execution. To combat this, a frequency separation was used to split the controller into a high- and a low-frequency component. This was done via the Matlab command `freqsep`. It was found that the low frequency component resulting from this operation (including only frequencies up to 1×10^4 rad/s) ran stably with fixed time steps of suitably low frequency for real time implementation, and that the removal of the high frequency component had negligible effect on the performance.

Once the stability issue was resolved, the performance of the controller under rotating operation could begin to be assessed. One particular flaw that became apparent was an unhealthy enthusiasm on the part of the controller to exaggerate the rotor run-out profile during low speed operation. The rig's run-out profile is relatively large, being of the same order of magnitude as the unbalance response. This makes it difficult to design the controller to reject the phenomenon as a disturbance, without reducing the capacity to manage vibration behaviour as well. A number of adjustments to the weightings were trialled, but eventually, the best solution found was to multiply the entire controller by a high-pass transfer function. This was designed to scale back low frequency control action, but leave high frequency control free to act. Thus the controller generated by `hinfsyn` is multiplied by:

$$0.7\frac{s+50}{s+80} \tag{7.13}$$

This does not provided a perfect solution; the controller still has a notable tendency to pick up on low speed run-out, but the phenomenon is greatly reduced, and the performance now considered acceptable.

7.3 Testing and Results

7.3.1 Overview of Tests Performed

In order to investigate the controlled behaviour of the test rig and provide a convincing demonstration of its vibration-control capabilities, a series of test are performed, and associated results presented, for each of the following scenarios:

- test rig not using any form or control
- test rig under PD control
- test rig under H_∞ control

The key test used are as follows:

- an impulse response test
- non-rotating forced vibration response
- rotating unbalance response

The purpose and methodology associated with each of these tests are set out below, so as to avoid the need to include such details each time results are presented in the remainder of the chapter.

Note: it is important to remember when considering all results that the test rig has two "sets" of displacement sensors as follows:

- the first set of sensors are those mounted onboard the secondary shafts adjacent to the magnetic bearings. These therefore measure the *relative* displacement between the rotor and the secondary shaft, and their outputs are accordingly influenced by the properties of both bodies. In total there are four of these sensors, arranged in x/y pairs at each end of the rotor, and these are the sensors which are used for feedback control.
- the second set of sensors are those mounted rigidly to the rig base-plate, and these measure the displacement of the rotor only. These sensors are purely for observation, and are not used for feedback control; their output, however, is still of the first importance, and the fundamental objective of the project is to reduce the *rotor* vibration amplitude, and this sensor set provides the direct measurement of this effect.

Therefore, in many cases where results are presented, separate plots of a given result are presented, as seen from each of the two perspectives - relative displacement and absolute rotor displacement. For convenience, such results are often referred to by the terms *internal* and *external* respectively, in reference to where the sensors are mounted relative to the rotor.

Furthermore, as the two ends of the rotor are nominally identical, in a number of cases it is not necessary to present readings from both ends of the system for a given test, as they are generally near-duplicates. Therefore in the interests of concision often only readings from a single end are presented, and for uniformity this is kept as the same end - end 2 (arbitrary choice).

Impulse Responses

Impulse responses are a very simple and common technique to gain a good basic insight into the frequency characteristics of a system.

In this case, the impulse is delivered by means of the magnetic bearings - a very short "burst" of current is applied in the axis of interest, and the resulting vibration is recorded. There are two advantages to using the magnetic bearings for this purpose (as opposed, for instance, to an impulse delivered mechanically by tapping the rig): firstly, the impulse will always be the same magnitude across different tests; and secondly, the impulse equally excites both the rotor and the secondary shaft, allowing the combined response of the whole system to be examined.

With time series data of the system response to the impulse captured, it is a simple matter to perform a Fourier Analysis on the data, and plot a frequency response. This naturally indicates at which frequencies of excitation the system will give the greatest response (i.e. natural frequencies).

Non-Rotating Forced Vibration Response

One useful and informative way to assess the system performance - and how a given controller influences that performance - is to perform a frequency response. Here, the term frequency response is used to mean imposing a forced vibration on the system at a set frequency, and then calculating a gain between the forcing term and the measured response. This is repeated over a range of frequencies of interest, and the calculated gains plotted against frequency to give an overall picture of the system behaviour. A description of the execution and analysis of these tests follows.

Imposing Forced Vibration

The magnetic bearings are used to impose the forced vibration on the system. A sub-system is set up in Simulink to output an open-loop, sinusoidal current to each of the four coils of a magnetic bearing. The sinusoids provided to each coil are offset by 90° from one another in such a way as to generate a net rotating circular force, which naturally applies in an equal and opposite manner to each of the rotor and the secondary shaft. These forcing currents are added to a bias current to give a linearised force. Note that for these tests, the two ends of the rotor are treated separately, i.e. the process described is applied at one end while the magnetic

bearing at the other end is switched off, and then a second test series is performed with the second end active, and the first magnetic bearing off.

In terms of the forcing frequencies used, a range from 1 to 150 Hz is chosen as covering all potential operating speeds of interest, spanning both the rotor and the secondary shaft first natural frequencies. For the low frequencies ($\leqslant$ 30 Hz) tests are performed at 5 Hz intervals. From 31 to 150 Hz, tests are performed at 1 Hz intervals. A bias current of 3 A is used, with a forcing current amplitude of 0.35 A. At each test frequency, 2 s of data is captured.

Converting Experimental to Analytical Results

From the rig, experimental values of both the forcing current and the displacement response are recorded in each of the x and y axes as time series data. A custom automated script is then run to fit an analytical sine wave to each signal at each test frequency. The analytical sine wave takes the form $A\sin(\omega t + \phi)$. As the response is a steady state forced response, for each run the value of ω is already known - it's simply the forcing frequency. The amplitude (A) and phase (ϕ) can be worked out by determining peak and/or zero crossing locations in the time-series data. As an illustration of the effectiveness of this procedure, a plot of a sensor reading from such a forced vibration together with the automatically determined sine wave is provided in Figure 7.8.

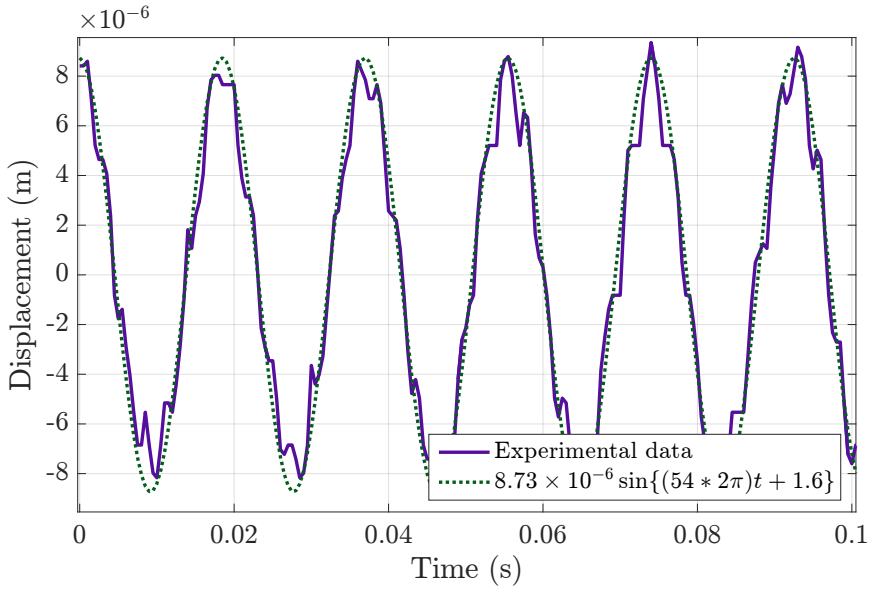

Figure 7.8: A comparison of experimental response to forced vibration with automatically fitted analytical sine wave, used in processing forced vibration responses

Once analytical fits have been performed on all data, this is presented as amplitude/frequency plots.

Rotating Unbalance Response

These tests may be considered as the "ultimate proof" of the capabilities of the rotor system design. Here to rotor, operating with an arbitrary unbalance, is spun over a range of speeds. As expected, the unbalance causes vibration in the rotor, and the effectiveness of the magnetic bearings / secondary shafts to reduce this vibration can be directly measured.

It is possible to present a number of results from test such as this. One of the most visually informative plots is a 3D depiction of rotor orbit against rotational speed. Note that while all such plots presented in this chapter are presented with a colour gradient applied, the colour is not technically meaningful, it is simply a visual aid to make the plots clearer and features easier to identify.

In addition to this, direct time-series data is presented from the same runs, which allows side-by-side viewing of internal displacement, external displacement, control current and running speed. These help provide further insight into the rig behaviour.

7.3.2 Uncontrolled Rig Behaviour

The first step towards appraising the test rig's ability to improve the vibration behaviour of the rotor is to record its behaviour without activating the magnetic bearings - effectively to establish a base line, against which progress can be measured. In this section, plots resulting from running the key tests described in Section 7.3.1 on the uncontrolled rig are presented, with salient features described, and targeted characteristics to be improved by the use of the magnetic bearings / secondary shafts highlighted.

Impulse Response

In the first instance, the result of the impulse test is presented in Figure 7.9.

This figure has four series, being the responses seen by each of the x and y direction sensors at each of the two ends of the rotor. In theory all four series would be identical, but it can be seen that practical, unmodelled effects from manufacturing and assembly have introduce some variation between the axes. Nonetheless, it is clearly seen that two dominant frequencies are present in each response - one around 50 Hz, and the other around 120 Hz. These frequencies correspond to the natural frequencies of the rotor and secondary shaft respectively, both of which are excited by the impulse. This is verified by considering the equivalent results as seen by the externally mounted sensors, displayed in Figure 7.10. These observe only the rotor motion, and are entirely unaffected by the motion of the secondary shaft. As expected then, these results show only the resonance around 50 Hz.

One apparent anomaly is identified in Figure 7.9, and that is the extremely low peak seen around 100 Hz in the response in the x2 direction. As a matter of fact - as will be illustrated in

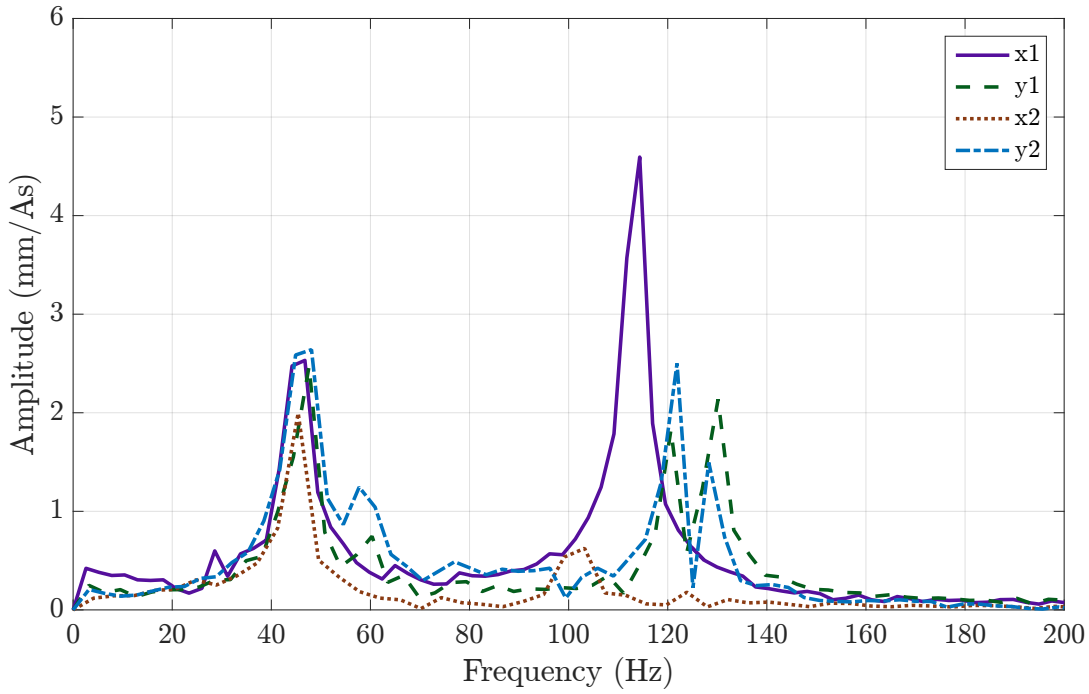

Figure 7.9: Frequency spectrum of impulse response of uncontrolled rig from internal sensors

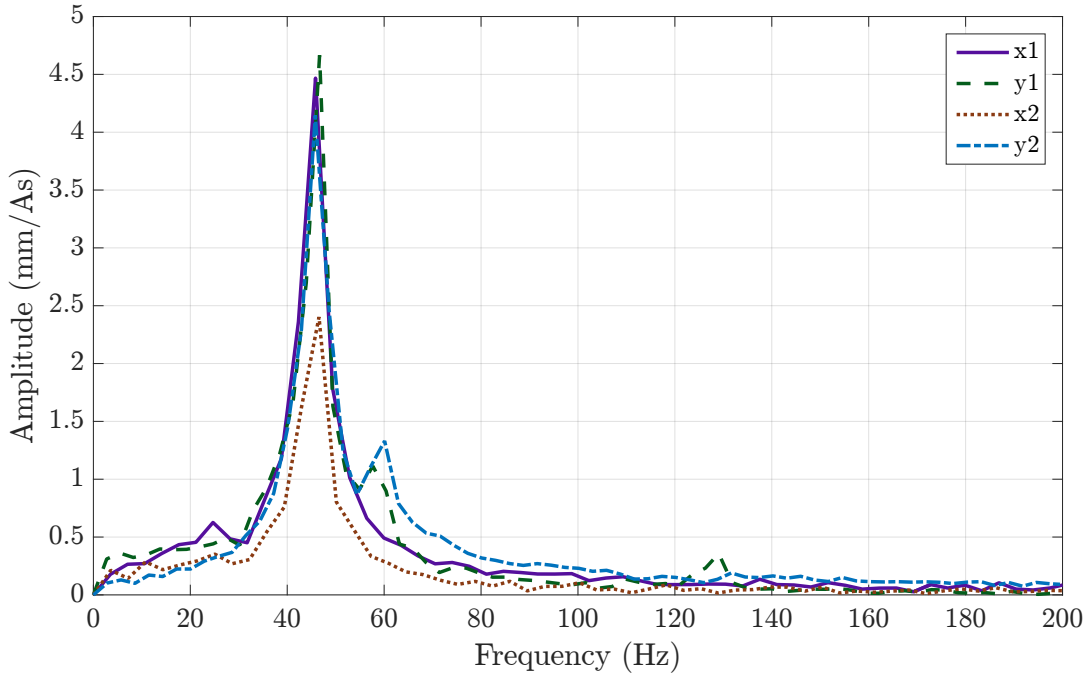

Figure 7.10: Frequency spectrum of impulse response of uncontrolled rig from external sensors

the next section - the x2 direction does have a resonance here comparable to that seen in the x1 direction. The lack of a clear peak in Figure 7.9 is really a result of the limitations of impulse testing - while generally a good tool for basic insight into system characteristics, the very small amount of data (and typically small amplitudes) being worked with does leave the technique open to sometimes producing slightly misleading results. In this case it could be conjectured that some local, possibly non-linear, damping effect in the clamping of this secondary shaft led to the suppressed peak.

From these results, it can be stated that the objective of activating the magnetic bearings is to significantly alter the first peak, around 50 Hz, in such a way as to allow the rotor to pass this pass this speed with a minimum of vibration.

Forced Vibration Response

Going a little deeper than the impulse response, the results of the force vibration tests give a more nuanced insight into the system character. An intuitive understanding of the results of these tests is gained from the plots in Figure 7.11, which show the displacement "orbits" resulting from the forcing as the forcing frequency varies, from both the relative (internal sensors) and absolute (external sensors) points of view.

The plots shown in Figures 7.12 and 7.13 are the more technical plots resulting from the analysis of the data in Figure 7.11, which illustrate well the same key data as provided by the impulse responses, as well as giving further insight into the various differences seen between the x and y directions, as well as between the two ends of the rotor. These differences are all due to unmodelled effects, and as such are not specifically predicted by the numerical simulations. One particular cause identified as affecting the system behaviour is actually the plate on which the rig is mounted. This is an aluminium plate 20 mm thick and measuring 1.5 x 0.75 m. Such a plate exhibits significant flexibility, and this will necessarily influence the apparatus mounted on it. Such effects, however, are in no way deleterious to the objectives of the project; all real system are influenced by disturbances and unmodelled effects, and it's important to demonstrate that the test rig can perform its designed function in spite of these discrepancies.

Note that in Figure 7.12b the secondary shaft resonance in the x2 direction at approximately 100 Hz is clearly visible, and is comparable to the x1 direction secondary shaft resonance shown in Figure 7.12b. This is the resonance that appeared to be "missing" in the impulse responses above; as is seen, a forced response is far less susceptible to misrepresenting system characteristics.

Unbalance Testing

For this test, the rotor was spun up by means of the drive turbine. At low speeds, a noticeable displacement is evident, however this is not a vibration effect but a simple rotor run-out effect. All rotors experience such a phenomenon to a degree. At a speed of around 40 Hz, the amplitude is observed to begin subtantially increasing - this is in response to the force caused by the rotor

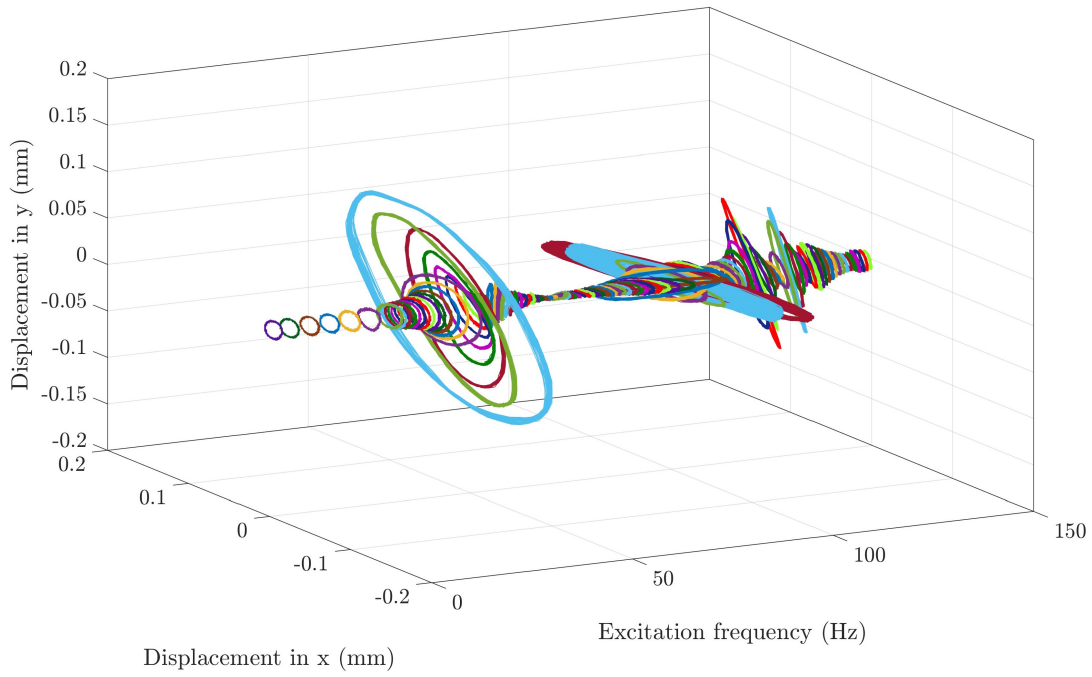

(a)

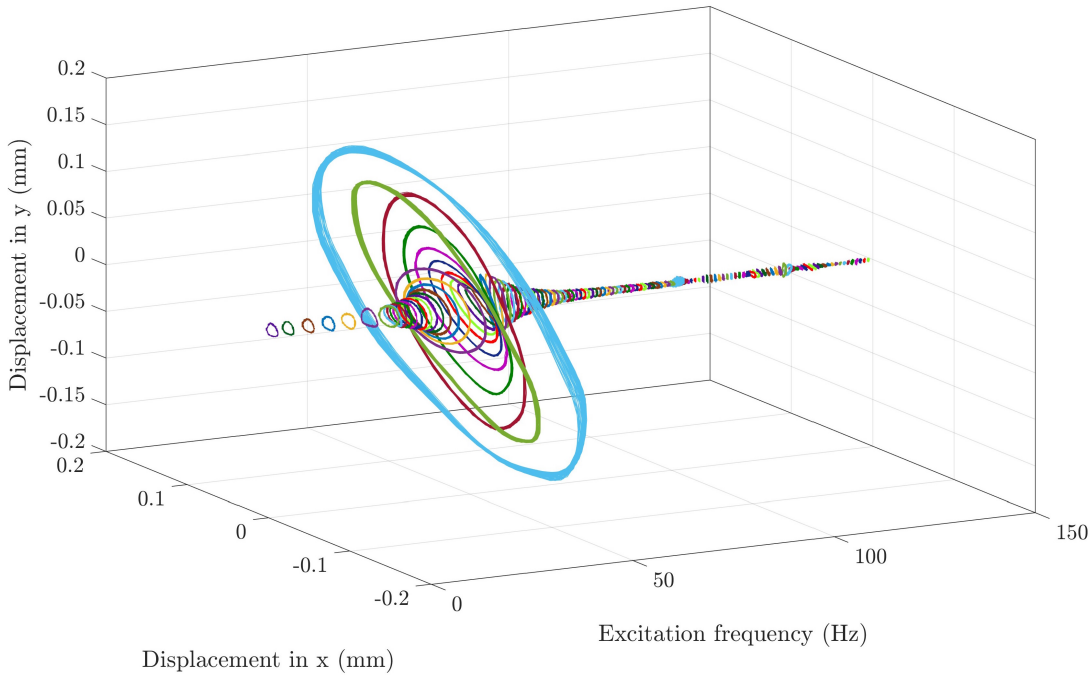

(b)

Figure 7.11: Forced orbits against forcing frequency at End 2 of the rotor. Orbits seen with internal sensors in plot (a), and with external sensors in plot (b)

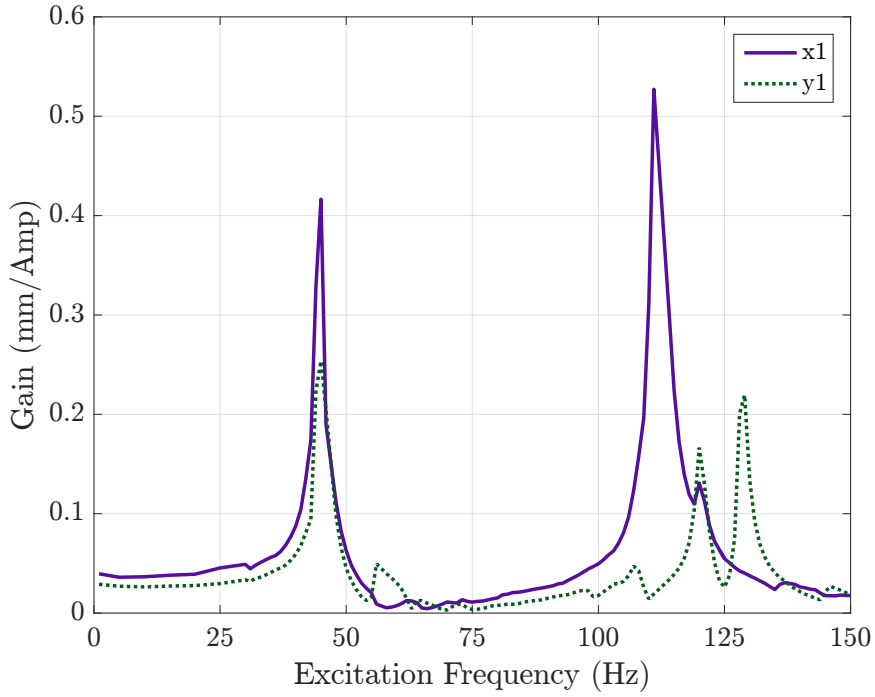

(a)

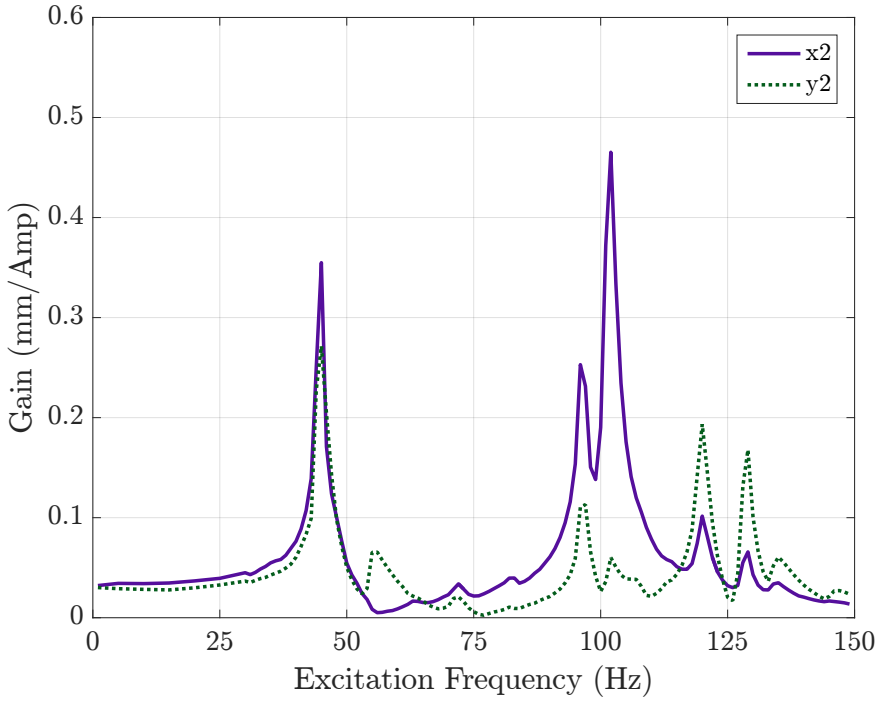

(b)

Figure 7.12: Current/displacement amplitude gain as seen by secondary shaft mounted sensors at End 1 (a) and End 2 (b) of the rig

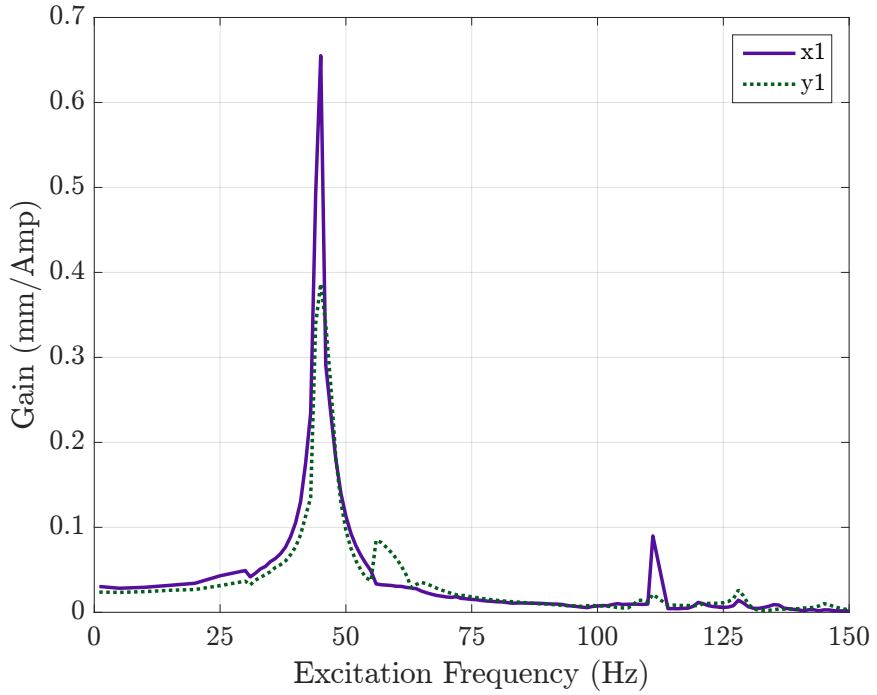

(a)

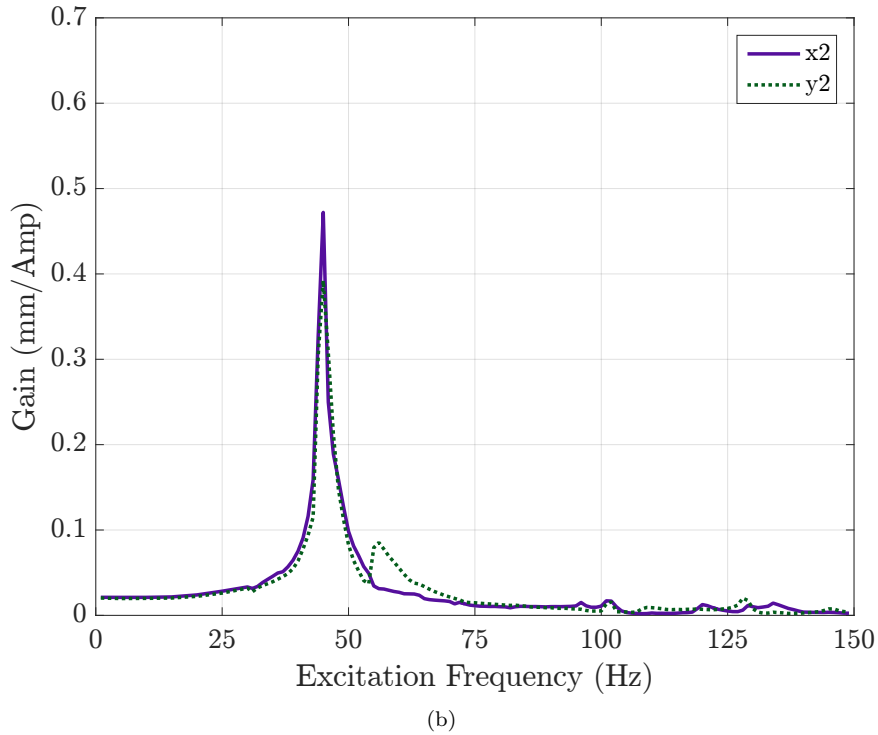

(b)

Figure 7.13: Current/displacement amplitude gain as seen by externally mounted sensors at End 1 (a) and End 2 (b) of the rig

unbalance. At a speed of approximately 52 Hz, the amplitude of the vibration was sufficiently large to cause the rotor to make contact with at least one of the touchdown disks protecting the magnetic bearings. As soon as this occurred, the gas supply to the drive turbine was turned off, and the rotor allowed to spin down again. The results presented here are taken from the data recorded as the rotor spun down.

Figure 7.15 is a 3D representation of the rotor orbit against rotational speed. As mentioned previously, the colours shown are purely as a visual aid, with no particular meaning. The plot provides a very easy to interpret overview of the key points of the system behaviour. At low speeds, below around 35 Hz, the orbit is more-or-less uniform in shape and size - this is the run-out. There are two notable diversions for this uniformity, which are the larger orbits at around 16 and 24 Hz. These represent the excitation of sub-synchronous vibration modes of the rotor, and are located at approximately $\omega_n/3$ and $\omega_n/2$ respectively. Such "mini-resonances" are relatively common in rotor systems, and generally not problematic. For interest, the orbit shapes of these modes are presented separately in Figure 7.14; notice that the orbit in plot (a) at a rotational speed of $\omega_n/2$ Hz has two clear loops, while the orbit at $\omega_n/3$ Hz in plot (b) has three loops. Occurances such as these can generally be attributed to non-linear effects in the system. It is common for these effects to be a feature of the rotor base / support structure rather than of the rotor itself. Analysis and discussion of such phenomenon has been presented in the literature, for instance by Bently [77] and Childs [78]. In this particular system, it is easy to envisage non-linear stiffness effects which may cause such excitations being caused by the rolling element bearings (specifically their fit into their housing) and also by the bolted assembly of the supporting structures, where even minor discrepancies in manufacture and assembly would lead to non-linear characteristics.

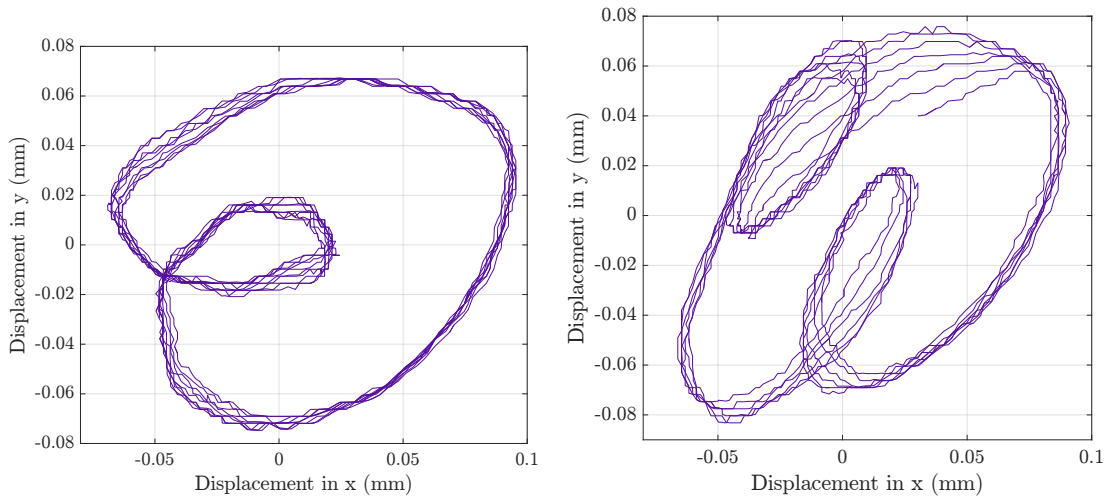

Figure 7.14: Sub-synchronous rotor orbits seen during uncontrolled run-down. The orbit in plot (a) is seen at 24 Hz and in plot (b) at 16 Hz, representing values of $\omega_n/2$ and $\omega_n/3$ respectively

At rotor speed above 40 Hz or so, the build up to the main resonance at the first critical speed is apparent, culminating in the chaotic orbits at the highest-reached speed of around 52 Hz. This motion is caused by a combination of a very large unbalance-driven orbit, combined with bouncing of the rotor on the magnetic bearing touchdown disk.

It is also possible to make out a "twisting" component in the orbit shape as it changes through the higher speeds - this is essentially a phase change between the driving force (unbalance) and the response, such as would be expected in all systems as they approach resonance, when the vibration occurs at 90° to the driving force. If touchdown did not occur, and therefore the rotational speed could be increased further, this phase change (or "twist") would be expected to continue until the vibration occurred at 180° to the forcing.

A slightly more detailed insight into the system behaviour while running down can be gained from the plots in Figure 7.16. This figure concentrates on the data from a single axis, which in this case is the x axis direction at End 2 of the rotor. This is effectively looking directly down from above with reference to the 3D plot of Figure 7.15. The four sub-plots of Figure 7.16 show relative displacement (internal sensor data), absolute rotor displacement (external sensor data), control current used and rotational speed. Naturally for this test, which is not using the magnetic bearings, the control current is zero, and the internal and external sensors show much the same data. Note that the difference in magnitudes between the data from the internal and external sensors (top two subplots) is, as mentioned in the rig design & construction chapter, a result partly of calibration considerations, and partly to do with non-alignment of the internal and external sensor sets.

In later, controlled, tests against which this plot may be compared, details such as the exact speed at which particular phenomena occur, how an motion is split between the rotor and the secondary shafts, and how much and how effectiverundownly any control current is used to achieve improved behaviour can be seen.

From the particular data of Figrue 7.16, one important detail is highlighted: an enlargement of the first few seconds of data from the second subplot is shown in Figure 7.17. Here it is clearly seen that, on top of the displacement due to the rotor whirl, a second, low frequency effect is superimposed. This is the touchdown, or "bouncing" of the rotor on one of the touchdown disks. This is what prevents running the rotor any faster without control, and what must be avoided through the use of the magnetic bearings and secondary shafts.

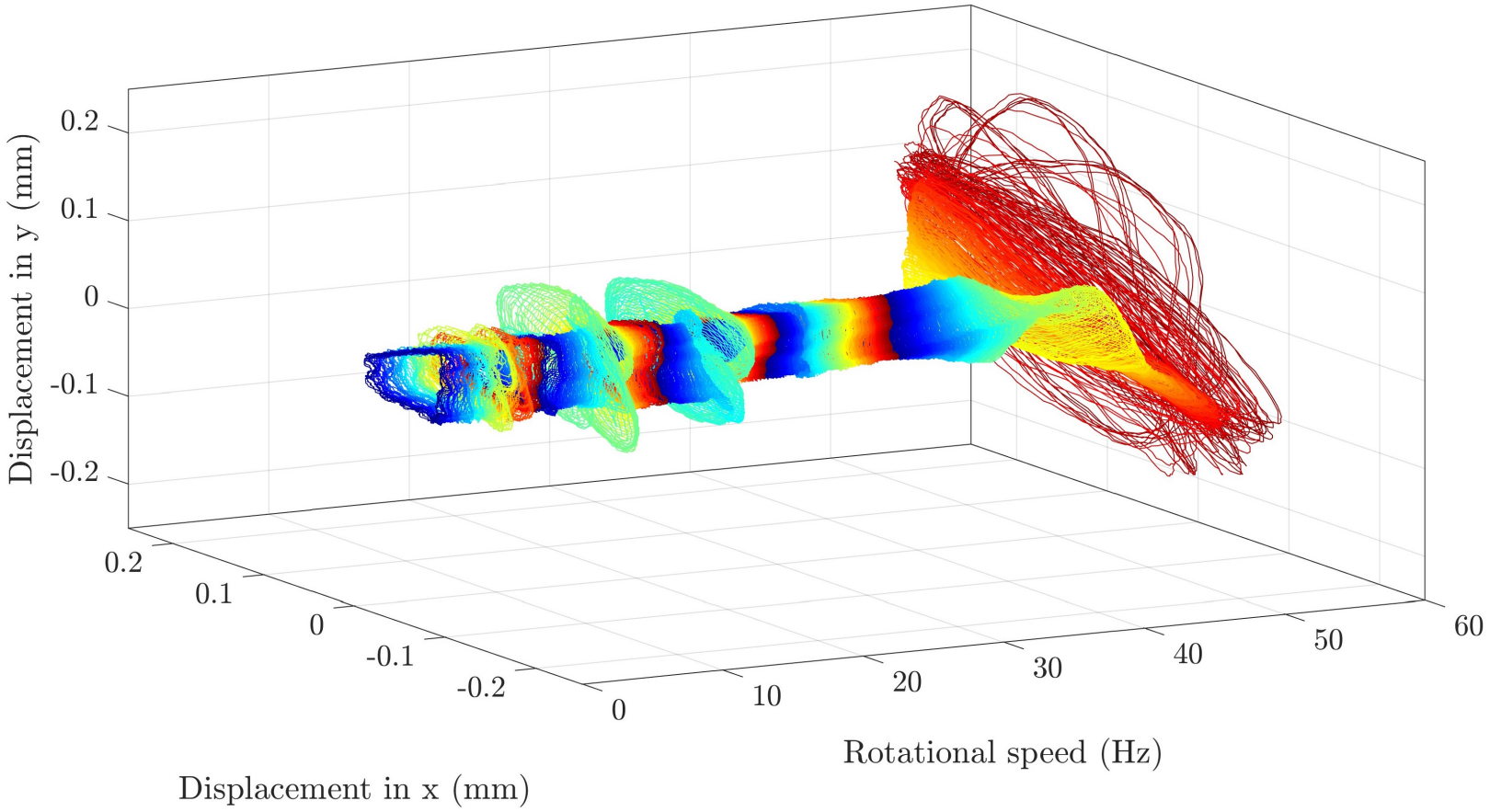

Figure 7.15: Rotor run-down without magnetic bearings active, as observed by internal sensors

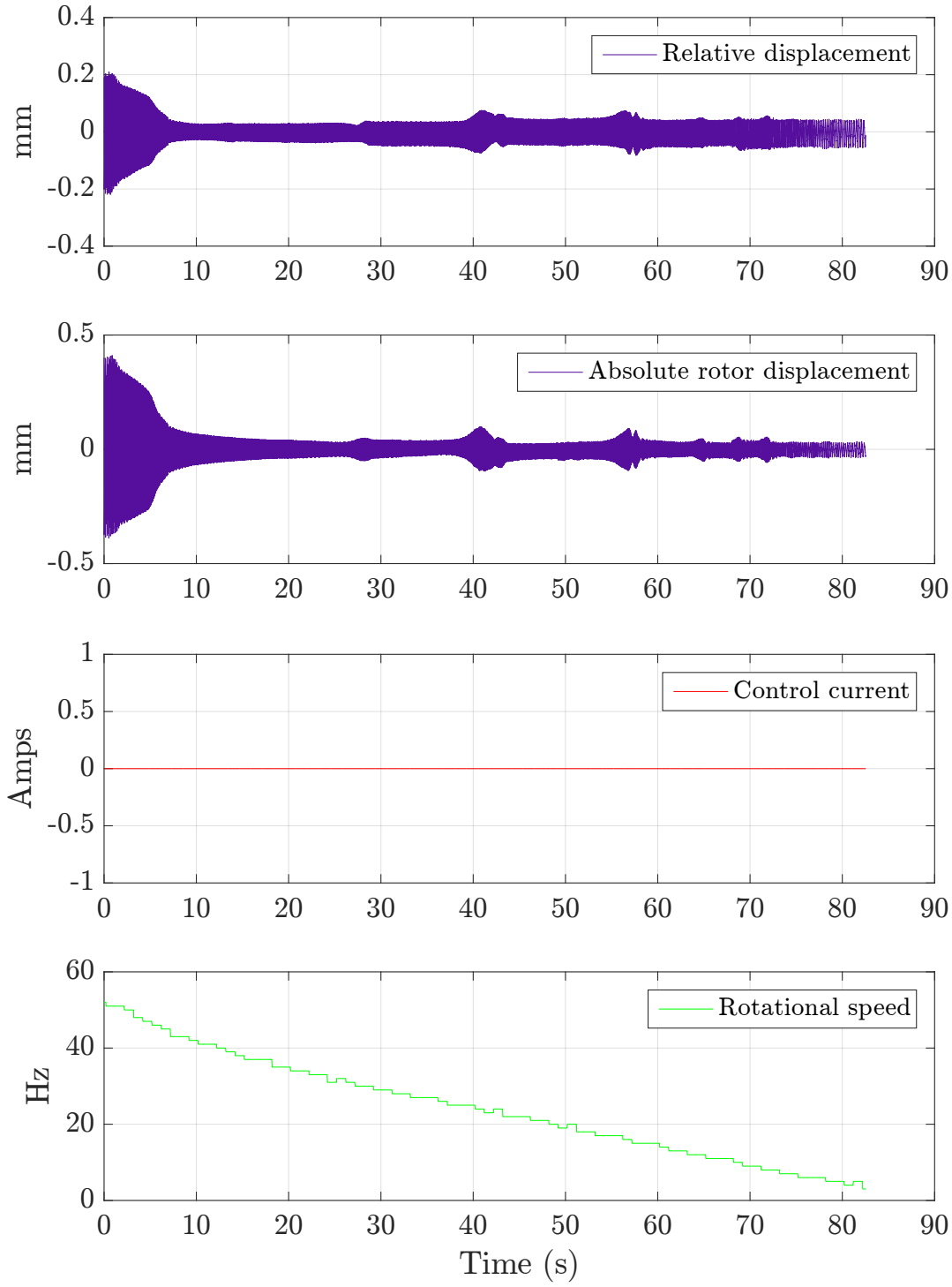

Figure 7.16: Data from uncontrolled rotor run-down, as seen in axis x2

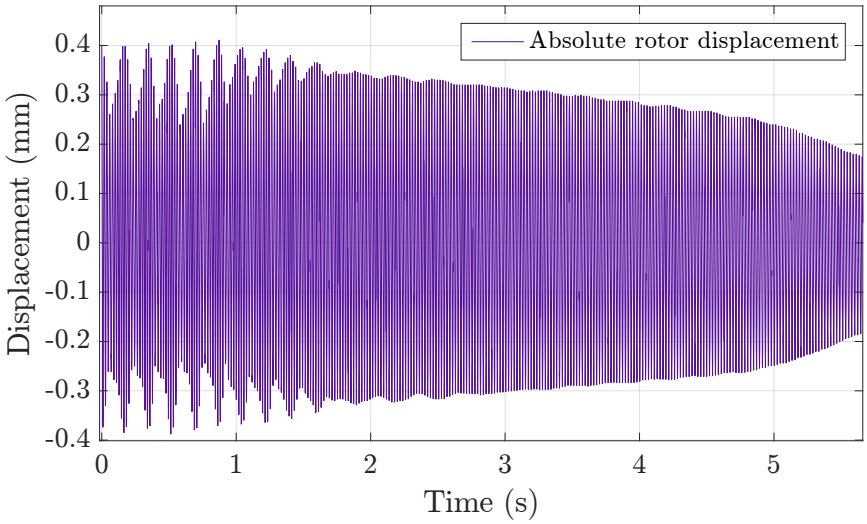

Figure 7.17: Enlargement of data from Figure 7.16, demonstrating touchdown motion superimposed on rotor whirling

7.3.3 PD Controlled Rig Behaviour

In a similar way to the uncontrolled rotor testing and characterisation described in Section 7.3.2, once a tuned PD controller was designed, the same tests were performed on the rig with the controller active.

As before, the fist test performed was an impulse test, and results of the FFTs of these are shown - from internal and external sensor sets respectively - in Figures 7.18a and 7.18b.

Comparing these responses to the analogue responses from the uncontrolled rig in Figures 7.9 and 7.10, it is immediately apparent that the controller is having a strong influence on the vibration at the rotor first critical speed around 50 Hz. It is observed, both by internal and external sensors, that this peak is both significantly smaller in amplitude when the magnetic bearings are active, as well as increasing in frequency by around 10 Hz.

Therefore the impulse test provides a good indication that less vibration may be experienced by the rotor as it approaches its critical speed.

To explore the pd-controlled system character further, it was then subject to forced vibration response testing. The same frequency range as was used with the uncontrolled system was applied, and plots of orbit against excitation frequency - to be compared to those shown in Figure 7.11 - are presented in Figure 7.19.

In comparison to the forced orbits of the uncontrolled system, it is seen that the PD control does indeed reduce the magnitude of the vibration observed in the rotor as its first natural frequency is passed, although it appears that as higher frequencies are reached (in the range of

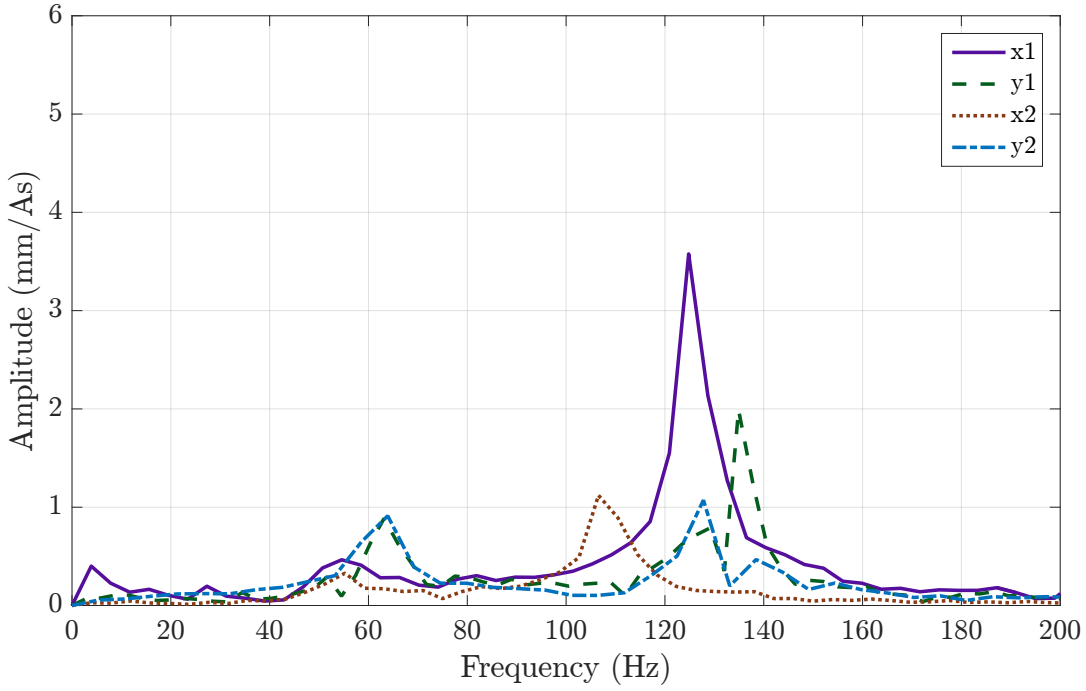

(a)

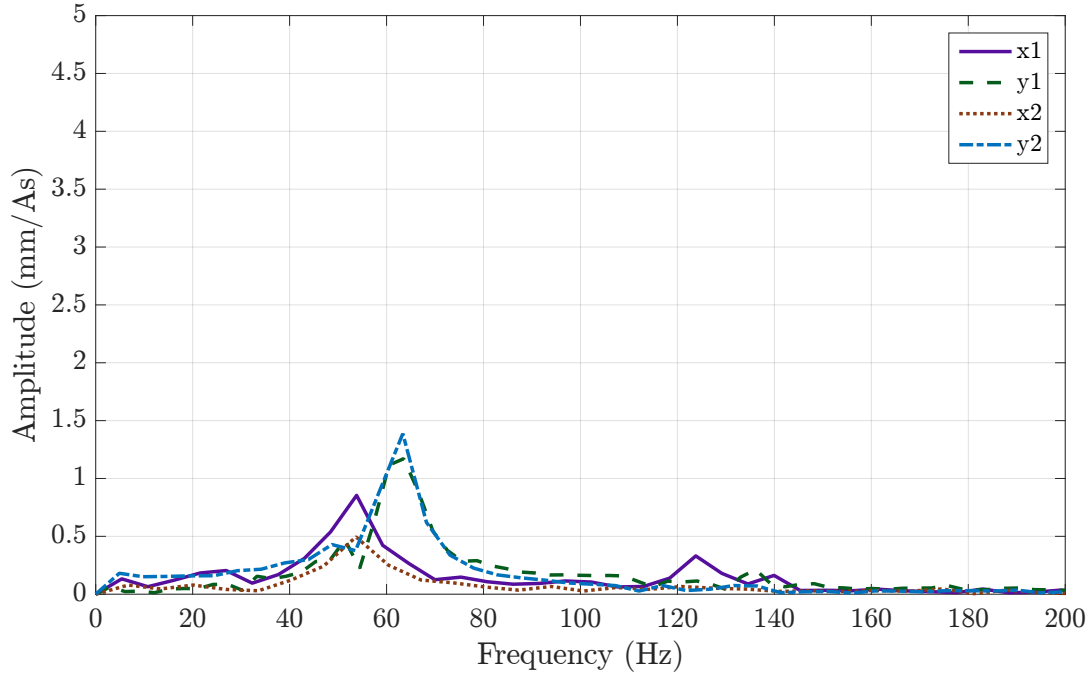

(b)

Figure 7.18: FFT of impulse response of rig under PD control (a) observing with internal sensors and (b) observing with external sensors

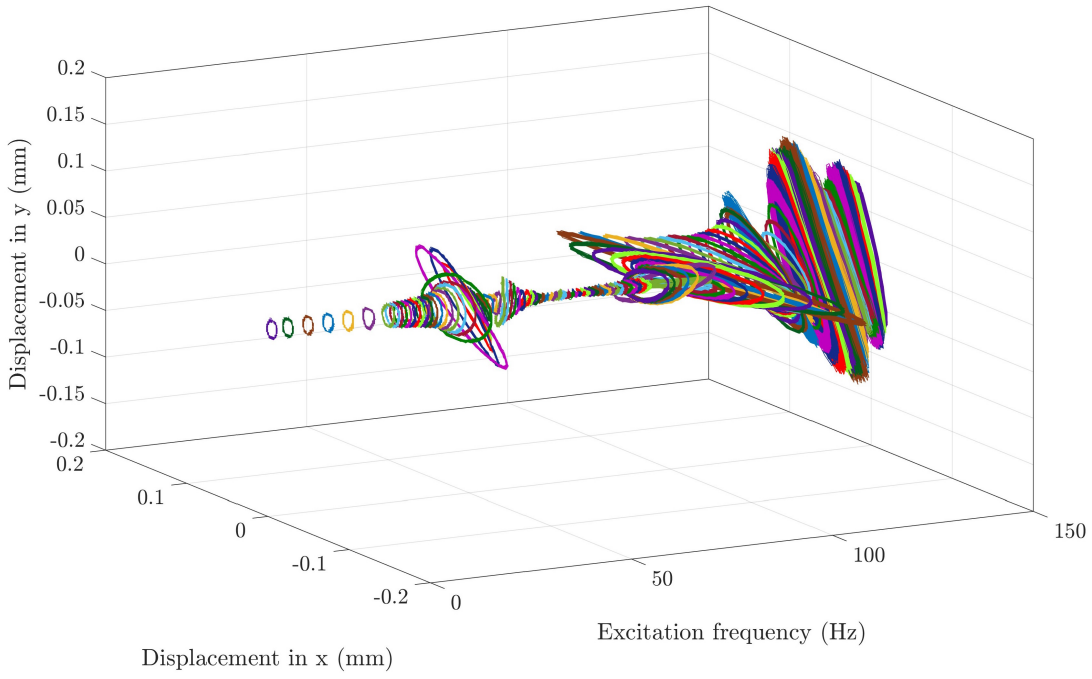

(a)

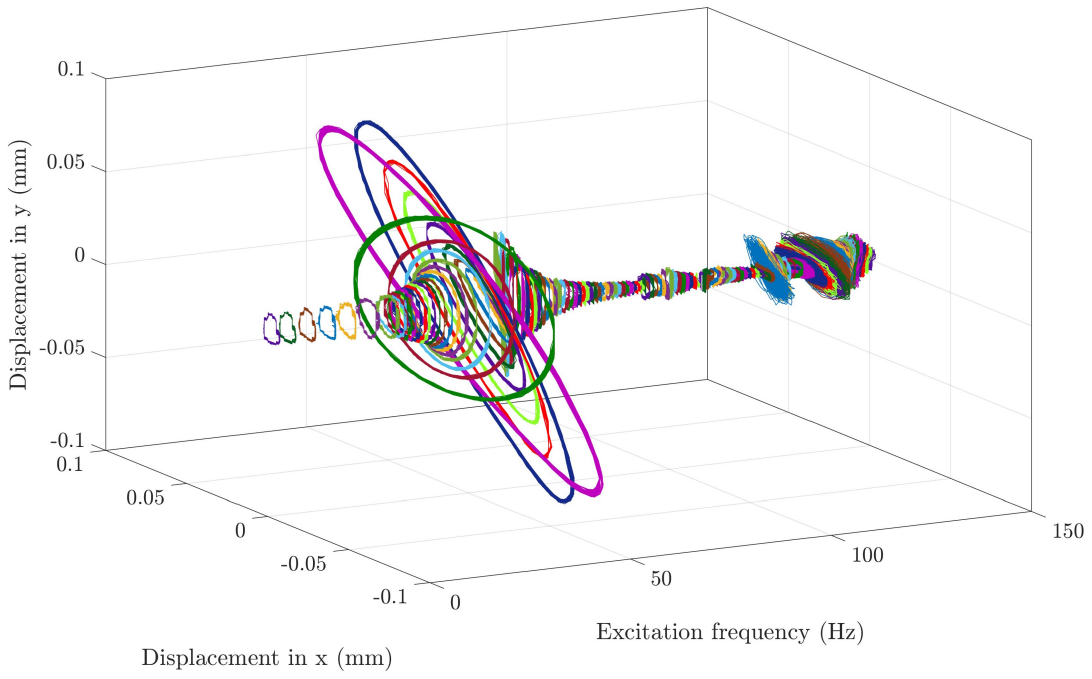

(b)

Figure 7.19: Forced orbits against forcing frequency at End 2 of the rotor, with PD control active. Orbits seen with internal sensors in plot (a) and with external sensors in plot (b)

the secondary shaft natural frequency), vibration of the secondary shaft in some axes is slightly amplified - particularly in the y direction - when compared to the uncontrolled system. This is not, however, likely to be problematic, as the goal of the system is to allow the passing of the *rotor* natural frequency, so speeds around the secondary shaft natural frequency of not of concern here.

The data of Figure 7.19 is presented as classic frequency response plots in Figure 7.20. Here the effects of the PD controller observed from the forced orbits on the amplitude of the response are demonstrated clearly. In addition one can see the increased frequencies of the resonance peaks, as indicated from the impulse response data.

Finally, the PD controller was tested on the system when rotating under unbalance. As before, the system was spun up slowly while the vibration was monitored. This time, the rotor was able to pass 52 Hz (the limiting speed without control active) without touchdown occurring - however, when a rotational speed of around 62 Hz was reached, touchdown was once more experienced. Consequently, the gas supply was shut off, and the rotor allowed to spin down. The data from this run-down is now presented.

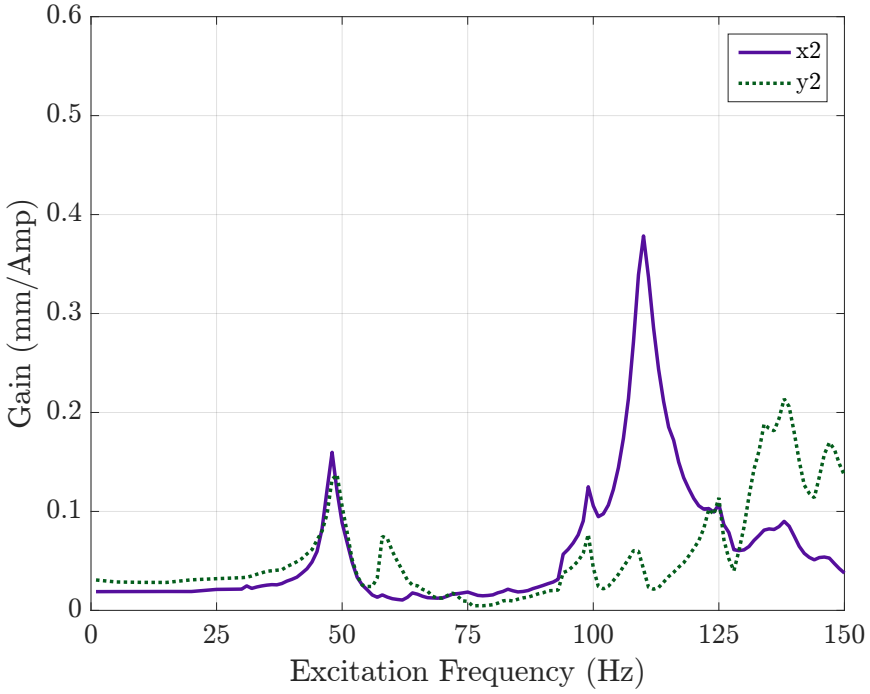

(a)

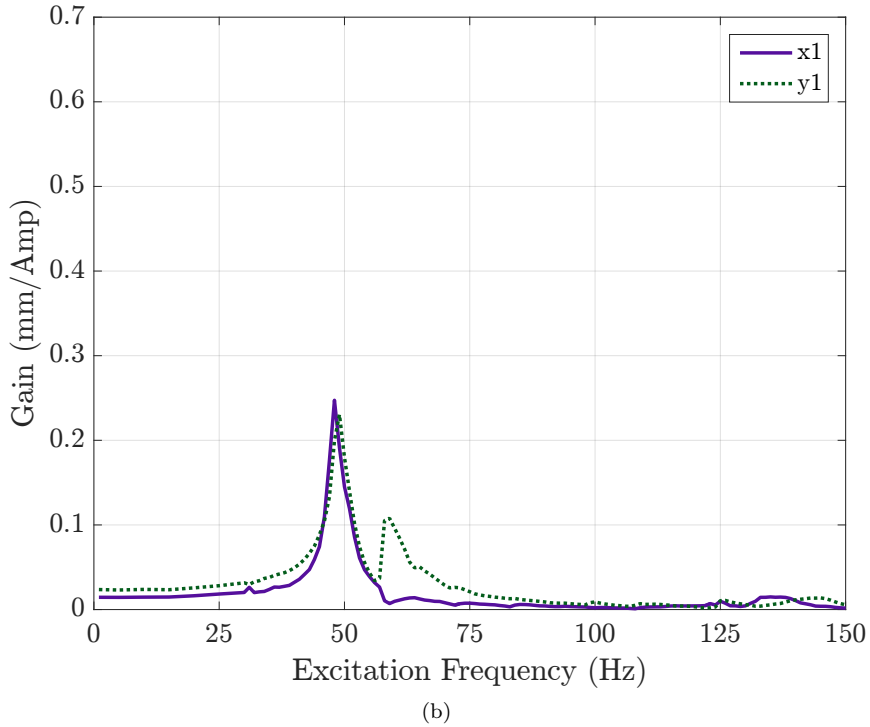

(b)

Figure 7.20: Current/displacement amplitude gain at End 2 of the rotor with PD control active, as seen by (a) internal and (b) external sensors

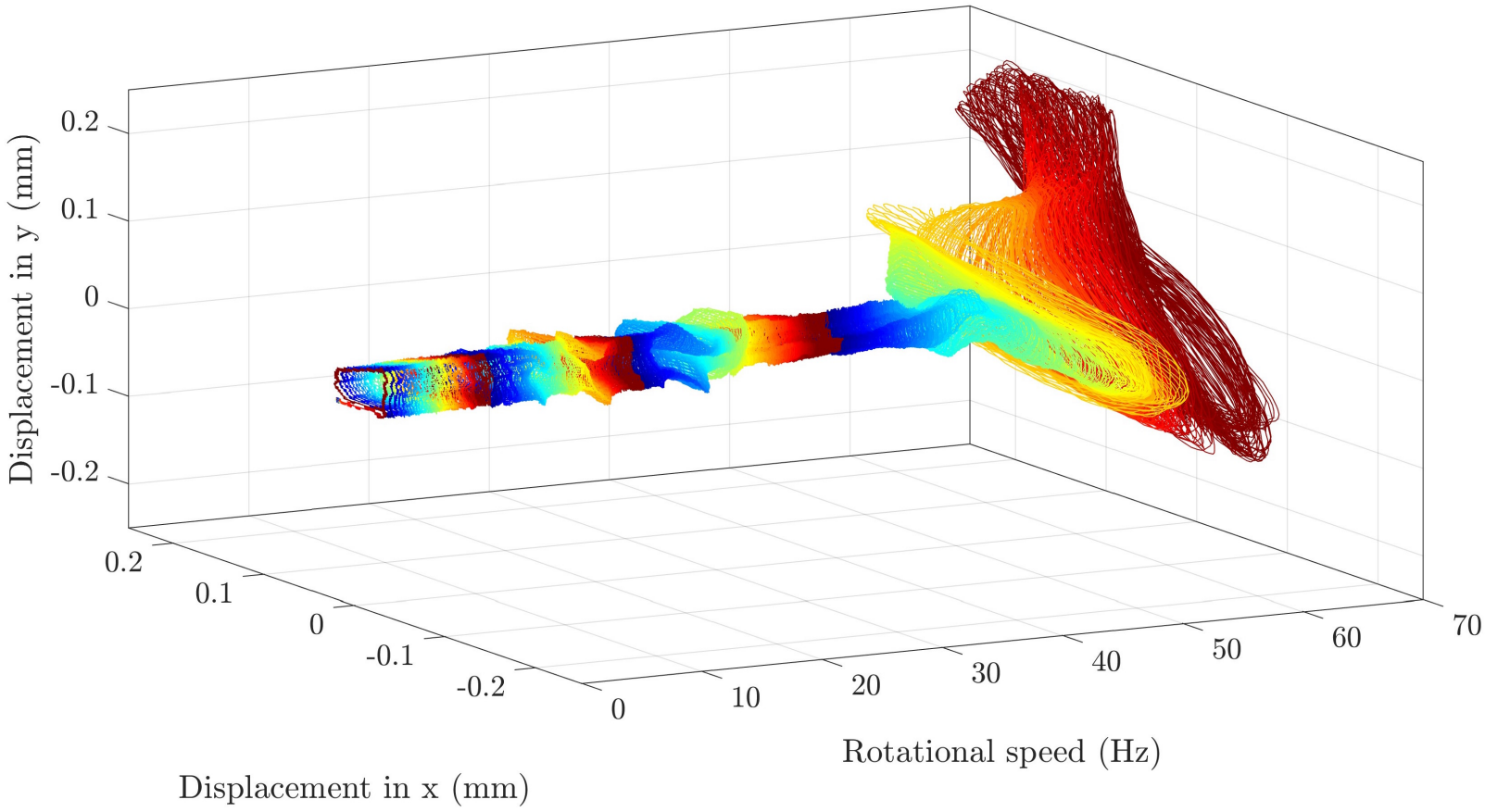

Figure 7.21: Rotor run-down with PD control active, as observed by internal sensors

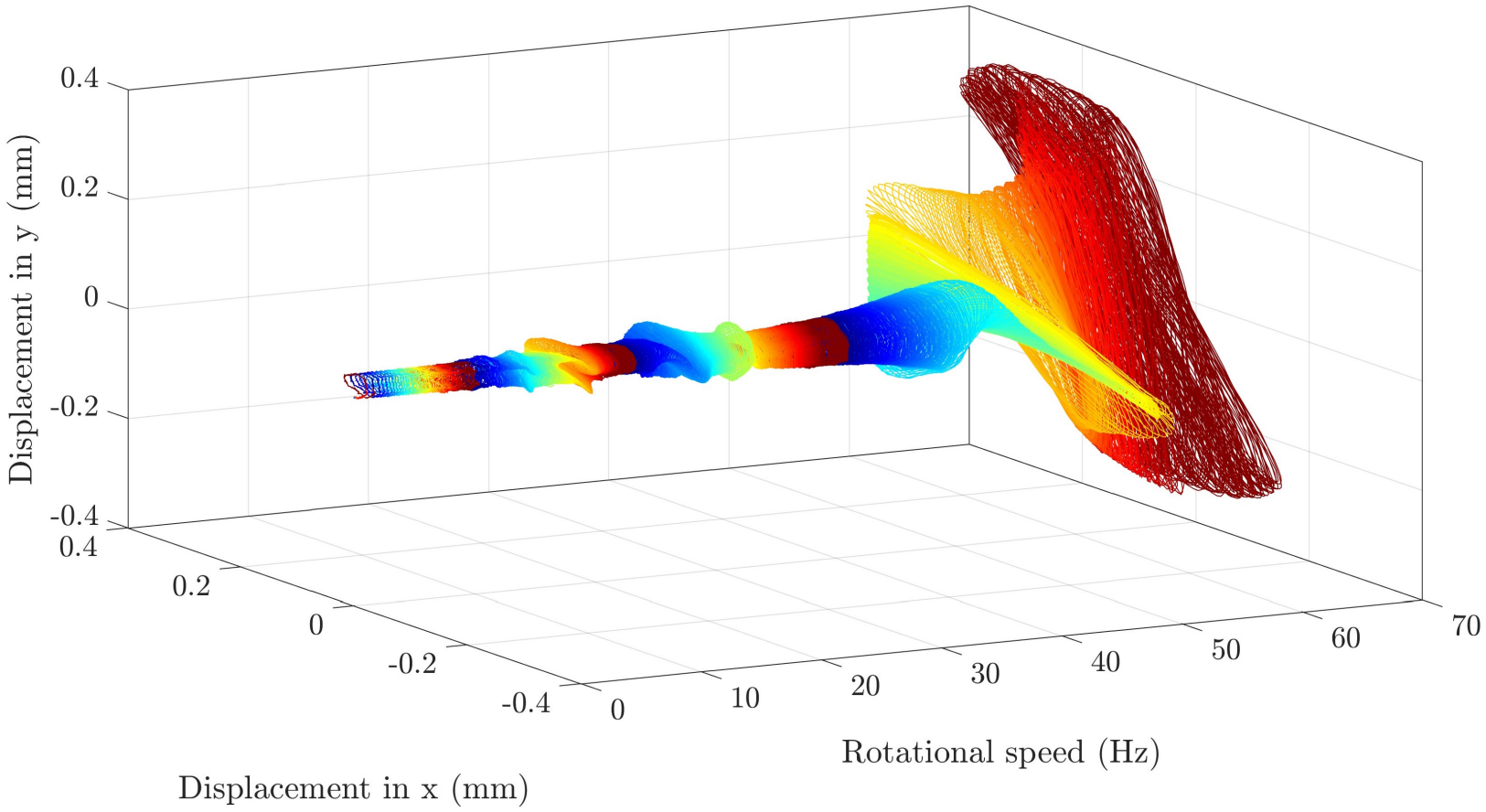

Figure 7.22: Rotor run-down with PD control active, as observed by external sensors

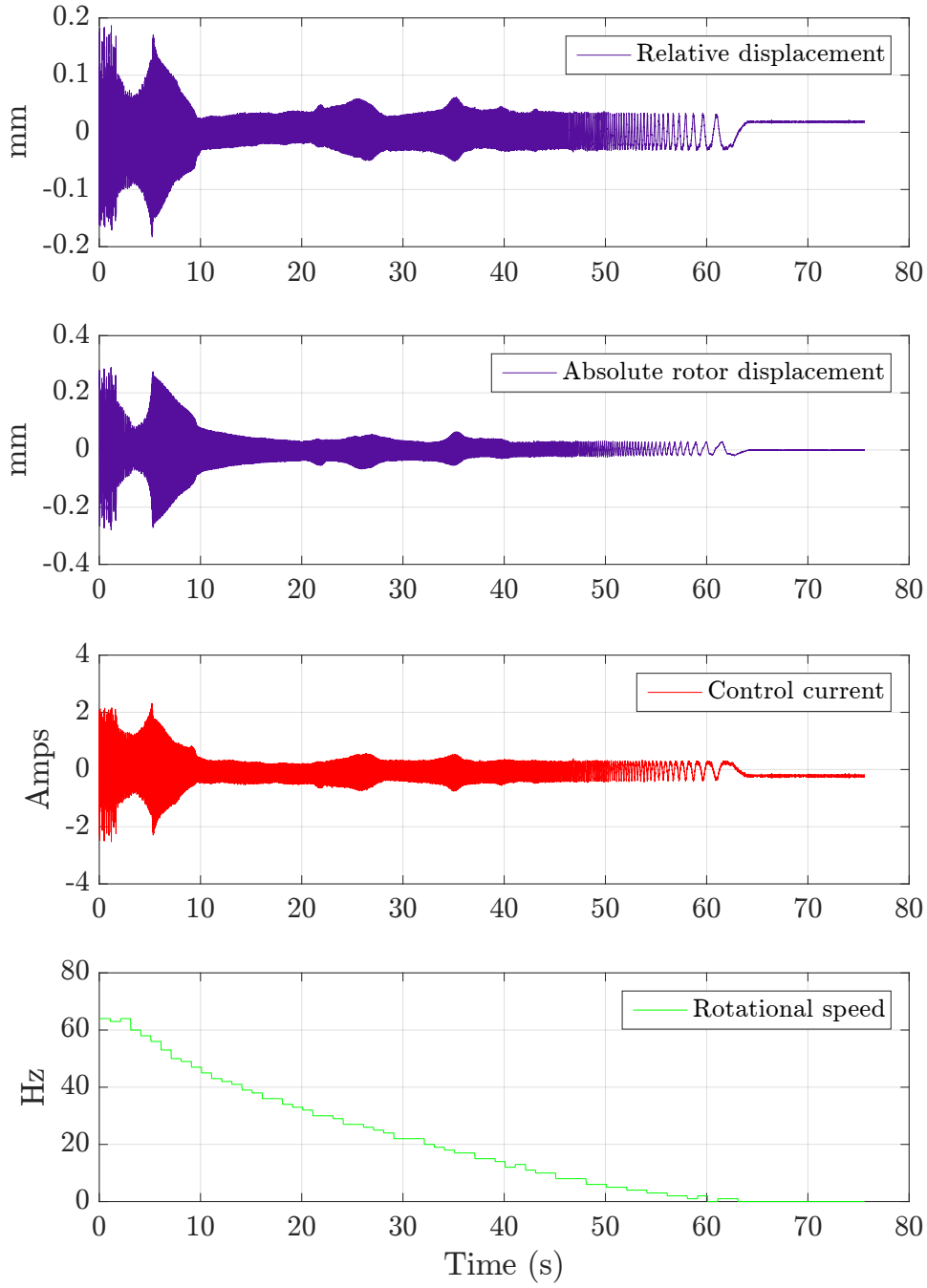

Figure 7.23: Detailed run-down data in axis x2 with rig under PD control.

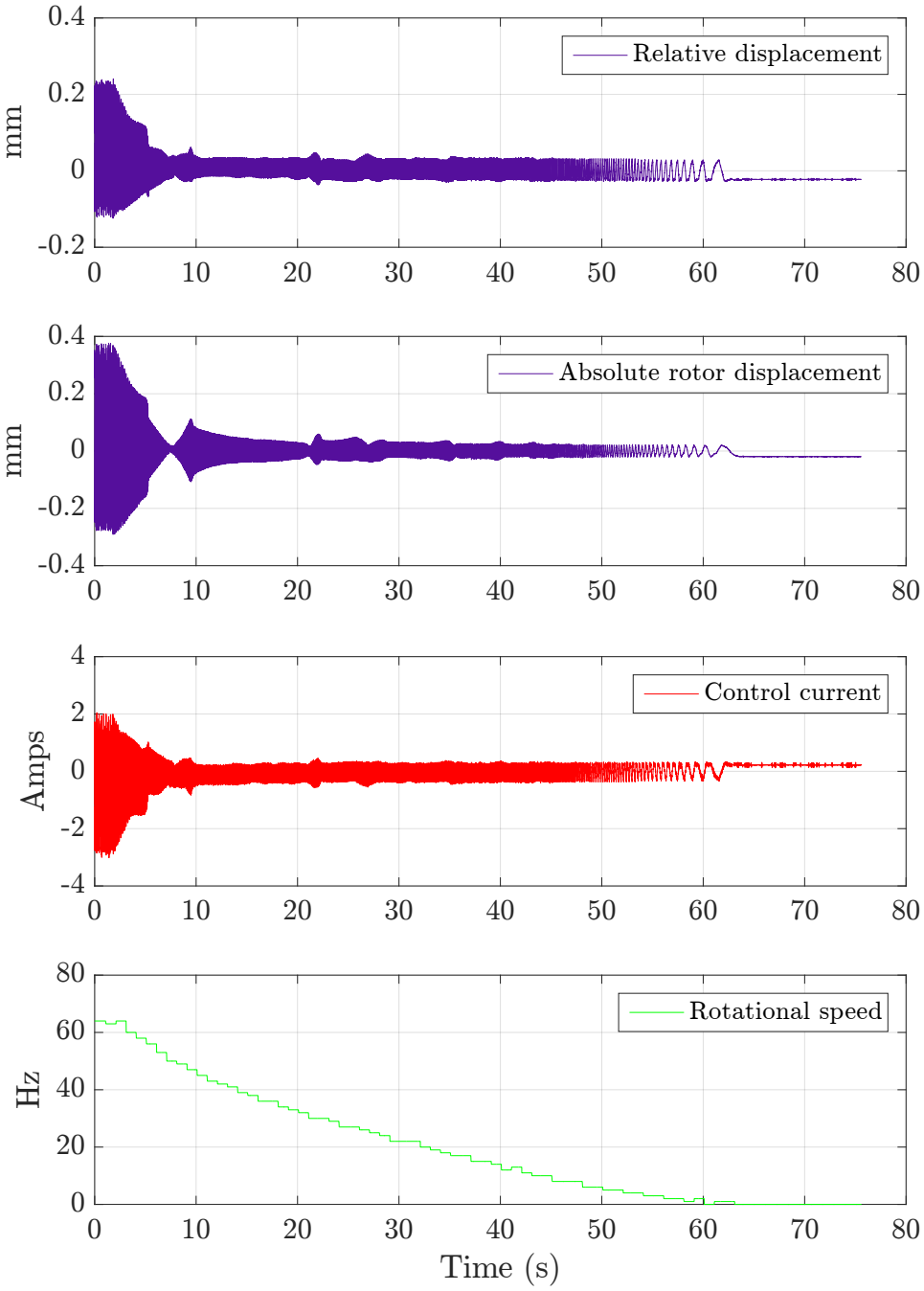

Figure 7.24: Detailed run-down data in axis y2 with rig under PD control.

7.3.4 H_∞ Controlled Rig Behaviour

With a finalised H_∞ controller in hand, the series of test used previously to assess the rig without control and with PD control were conducted under the H_∞ algorithm.

Impulse testing produced frequency responses somewhat similar to those seen with the PD controller. Specifically, significant reduction is seen in the rotor first natural frequency around 45 Hz, from both the point of view of the external and internal sensors. In contrast to the PD controller results however, there is no frequency change associated with the modification of this peak, suggesting that there is no directly proportional element to the controllers action. Furthermore there is very little change in the peaks observed by the internal sensors at higher frequencies (100 to 120 Hz) - this indicates that the controller is not attempting to control this behaviour, which is in line with the design goals specified in its formulation.

From these results then, it is expected that the controller will have at least some positive influence on rotor vibration behaviour, but it's difficult to determine how it may compare to the action of the PD controller.

The next set of tests performed was the forced vibration response. Here, certain differences are observed between the action of the H_∞ controller and the action of the PD controller. In particular, when under PD control, the rotor is seen to exhibit some substantially elongated oval orbits around the rotor first natural frequency. These are clearly based on the oval orbits observed in the uncontrolled system, which are themselves a results of system imperfections, including unequal stiffness in the axes, and imperfectly centred magnetic bearings. The H_∞ controller, on the other hand manages to greatly reduce the elongation of the orbits, and in doing so reduce the maximum vibration magnitude seen. It is likely that, as the H_∞ controller is build on an identified model, "knowledge" of these system imperfections is built into its structure, and thus it is able to counteract the phenomenon. It is also clear to see the change in phase of the orbits as the rotor natural frequency is passed.

Regarding the higher frequency excitations associated with the secondary shaft natural frequency, in agreement with the results of the impulse test, the H_∞ controller does not appear to attempt to control these, leading to a similar response to that seen in the uncontrolled system. Importantly, there is very little transmission of this excitation to the rotor.

On interpreting the forced response data into a more traditional frequency response, there are no real surprises. The peaks representing the rotor first natural frequency are a little lower than the corresponding peaks from the PD controlled system, but broadly speaking they are similar, and from these values it would be difficult to chose one over the other in terms of better performance.

The story become somewhat more dramatic, however, when actual rotation under unbalance is performed. Not only did the H_∞ controller allow the rotor to pass it's first critical speed *easily*, it also allowed it to surpass the resonant frequencies of the secondary shafts, and proceed to a

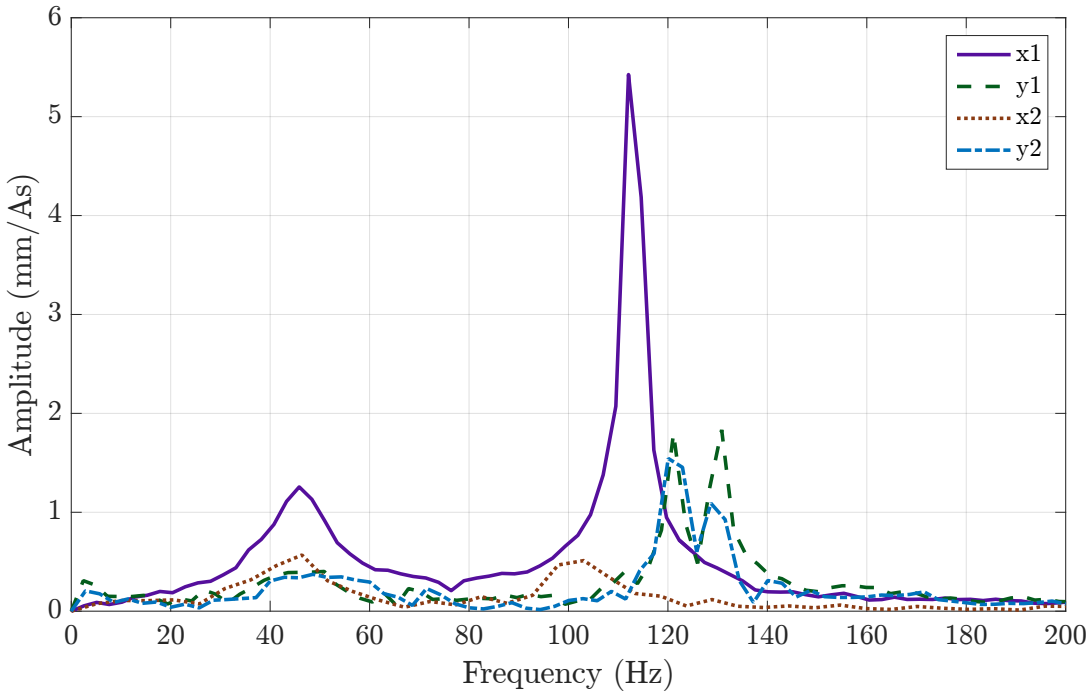

(a)

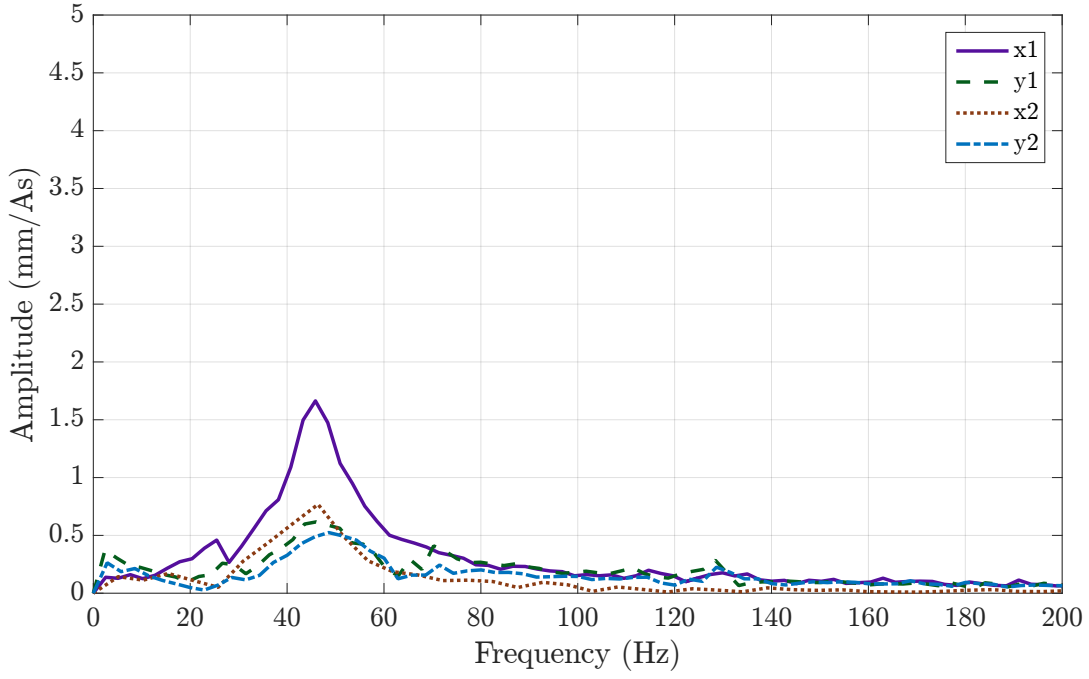

(b)

Figure 7.25: FFT of impulse response with rig under H_∞ control (a) observing with internal sensors (b) observing with external sensors

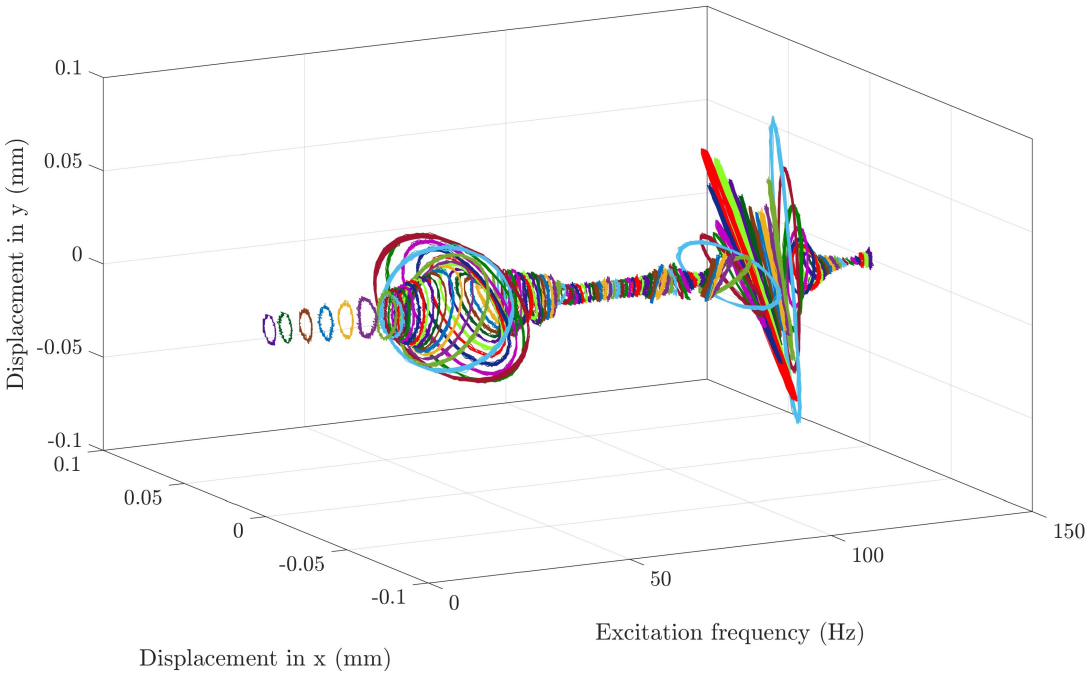

(a)

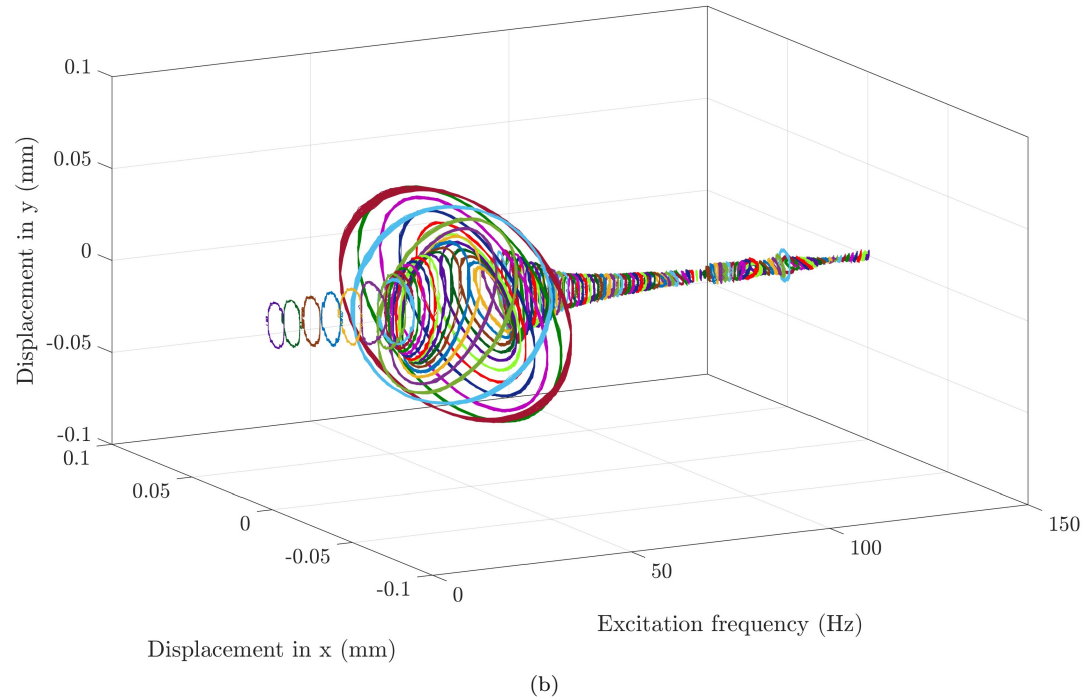

(b)

Figure 7.26: Forced orbits against forcing frequency at End 2 of the rotor, with H_∞ control active. Orbits seen with internal sensors in plot (a) and with external sensors in plot (b)

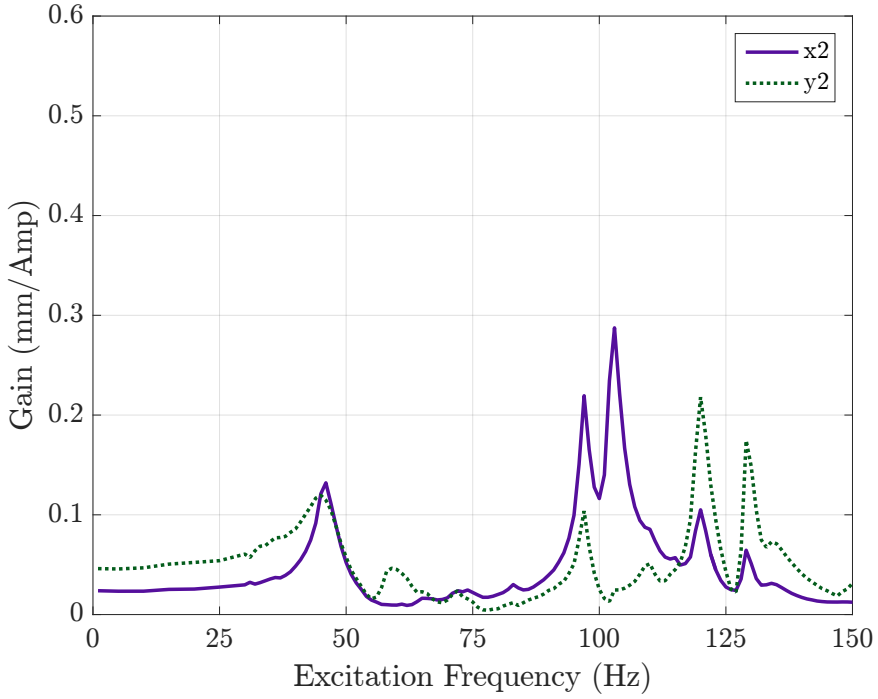

(a)

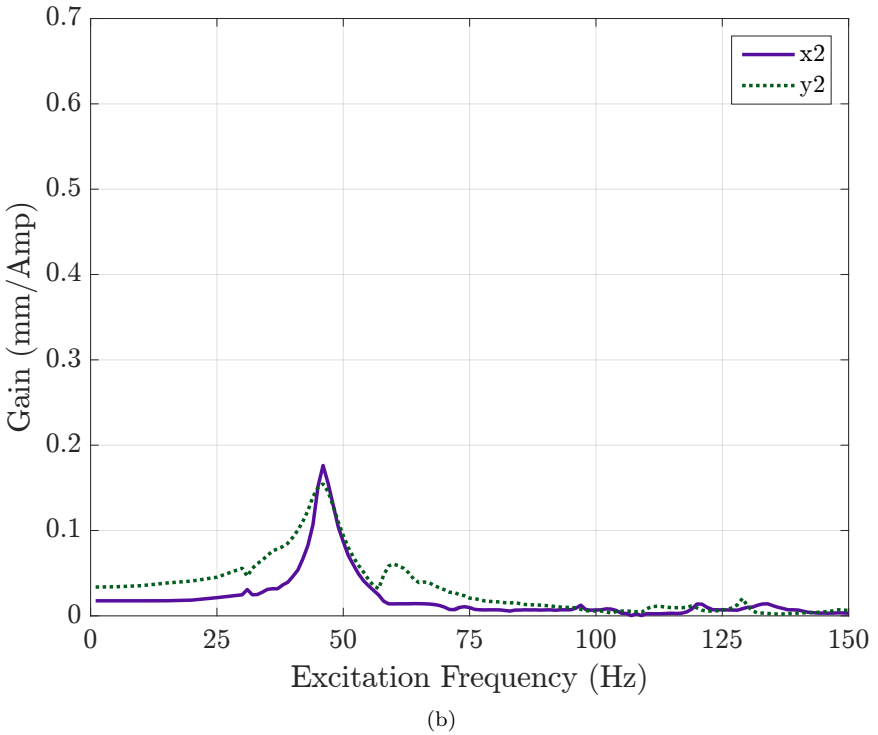

(b)

Figure 7.27: Current/displacement amplitude gain at End 2 of the rotor with H_∞ control active, as seen by (a) internal and (b) external sensors

speed three times higher than its critical speed - up to 150 Hz, or 9000 rpm. When building the rotor, it had not been considered that it would be operating at such a high speed, and thus it was deemed imprudent to continue increasing the speed further - for one thing the rolling element bearings are only rated to 10,000 rpm, and any unexpected behaviour at such speeds could lead to "exciting" consequences.

Thus the gas supply was turned off with the rotor at 150 Hz, and the run-down recorded. The 3D plots of this are provided for End 2 of the rotor, from relative and absolute displacement perspectives in Figures 7.29 and 7.30 respectively. The most instantly remarkable feature of these results is the consistency of the orbit size size across the speed range, or equivalently, the lack of any real resonance-like behaviour. The absolute rotor motion records a modest, yet restrained, increase in orbit size as the first critical speed is passes, but over the rest of the entire speed range, only minor fluctuations are seen. The relative displacement has a slightly more variable profile over the speed range, although this is largely in terms of observed orbit *shape*, rather than changes in orbit *size*. This is particularly noticeable as the orbit appears to "twist", both where the rotor critical speed is passed (50 Hz) and where the secondary shaft resonance is passed (100 - 120 Hz). A detailed view of the orbit shape twist as the rotor passes 50 Hz is provided in Figure 7.28 - it is seen here how the ellipse that forms the orbit rotates through 90° at the critical speed is passed.

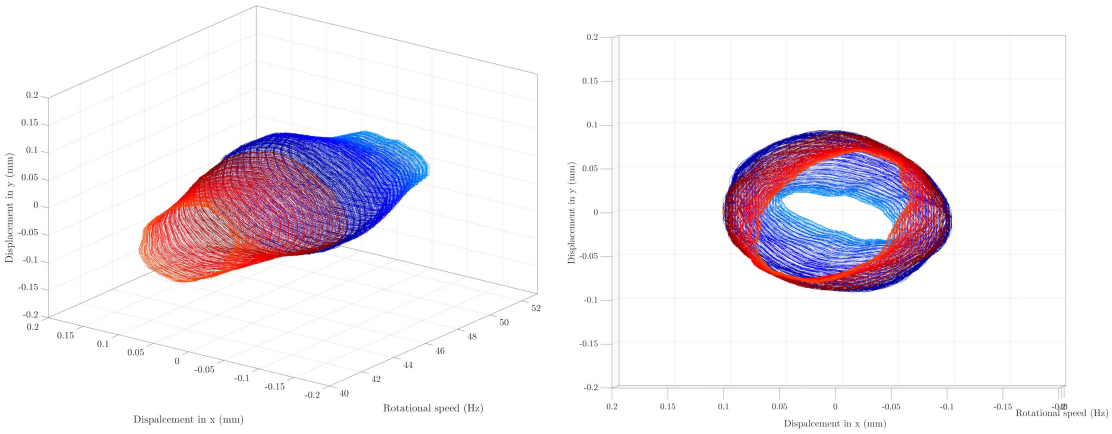

(a) (b)

Figure 7.28: Detailed illustration of the change in phase of the rotor orbit as the critical speed is passed. (a) shows a 3D view of the relevant section of data, with (b) showing an "end-view" along the length of the same data

There is one slight drawback seen in these results, however. At low rotation speeds, the controller appears to *amplify* the rotor run-out. This leads to recording slightly larger displacements at low speed than either in the uncontrolled or the PD controlled cases. This effect is not large enough to cause any performance concerns, and in spite of this the overall capability of the H_∞ controller makes it substantially the best option for vibration reduction of the project. It should also be possible to reduce or eliminate this run-out amplification quality

through adjustments to the weightings used in the augmented plant used for the controller design. Another option would be to use a continuous-position encoder on the rotor, and use this to subtract off the (pre-recorded) run-out profile from the sensor readings before passing them to the controller. These, however, are tasks for a future project.

Looking at the detailed, individual axis plots of the run-down test data, further information may be gleaned. One of the most noticeable, and impressive, findings the very modest control currents the H_∞ controller demands. Over the entire run, the maximum control current demanded was 0.5 A, and often substantially less than this. This is in contrast to the PD controller, which demanded in excess of 2 A of control current around the rotor critical speed, while achieving less vibration reduction. Thus it is determined that, in addition to better absolute performance, the H_∞ controller also acts in a far more efficient way than the PD controller. This increased efficiency confers a number of advantages in addition to the obvious energy saving - in the first case, smaller control currents will lead to less heating (through both copper and induced-eddy current effects), which is always advantageous, and sometimes operationally critical. Furthermore, the potential is open for the use of smaller, cheaper amplifiers, and indeed smaller, more compact magnetic bearings.

An interesting and unexpected phenomenon is observed in the detailed y-axis plot shown in Figure 7.32. It appears that at higher speeds, above around 75 Hz, the rotor undergoes an upward deflection. The cause of this effect likely to be from aerodynamic effects in the turbine. Specifically at these high speeds there is strong likelyhood of any slight non-concentricity of the turbine within its housing leading to a "pillow" of air forming in the narrower part of the clearance, leading to a displacement in the rotor. In any case it is reassuring that such an occurrence does not disturb the controller, which continues to perform well in spite of such an event.

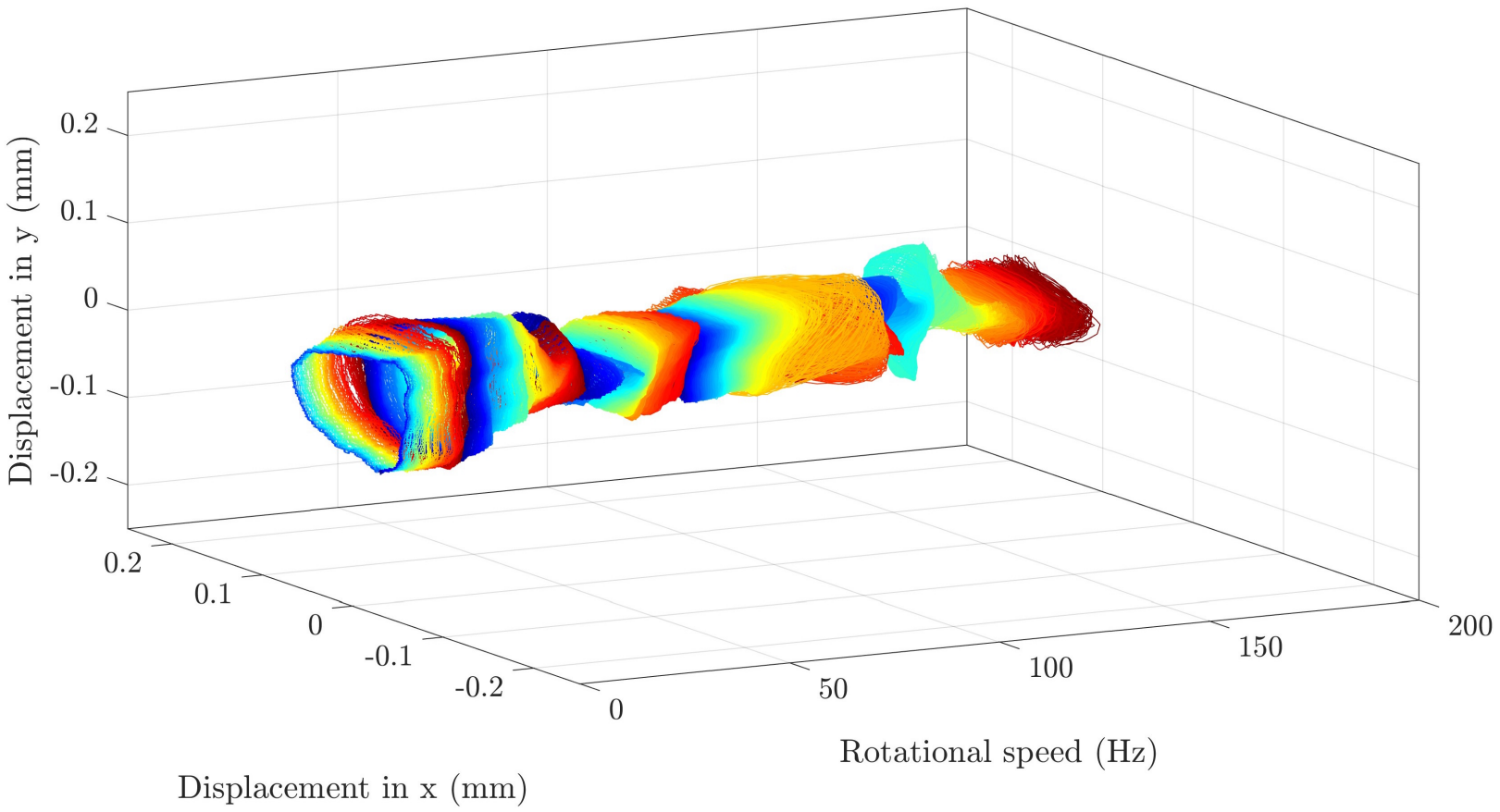

Figure 7.29: Rotor run-down with H_∞ control active, as observed by internal sensors

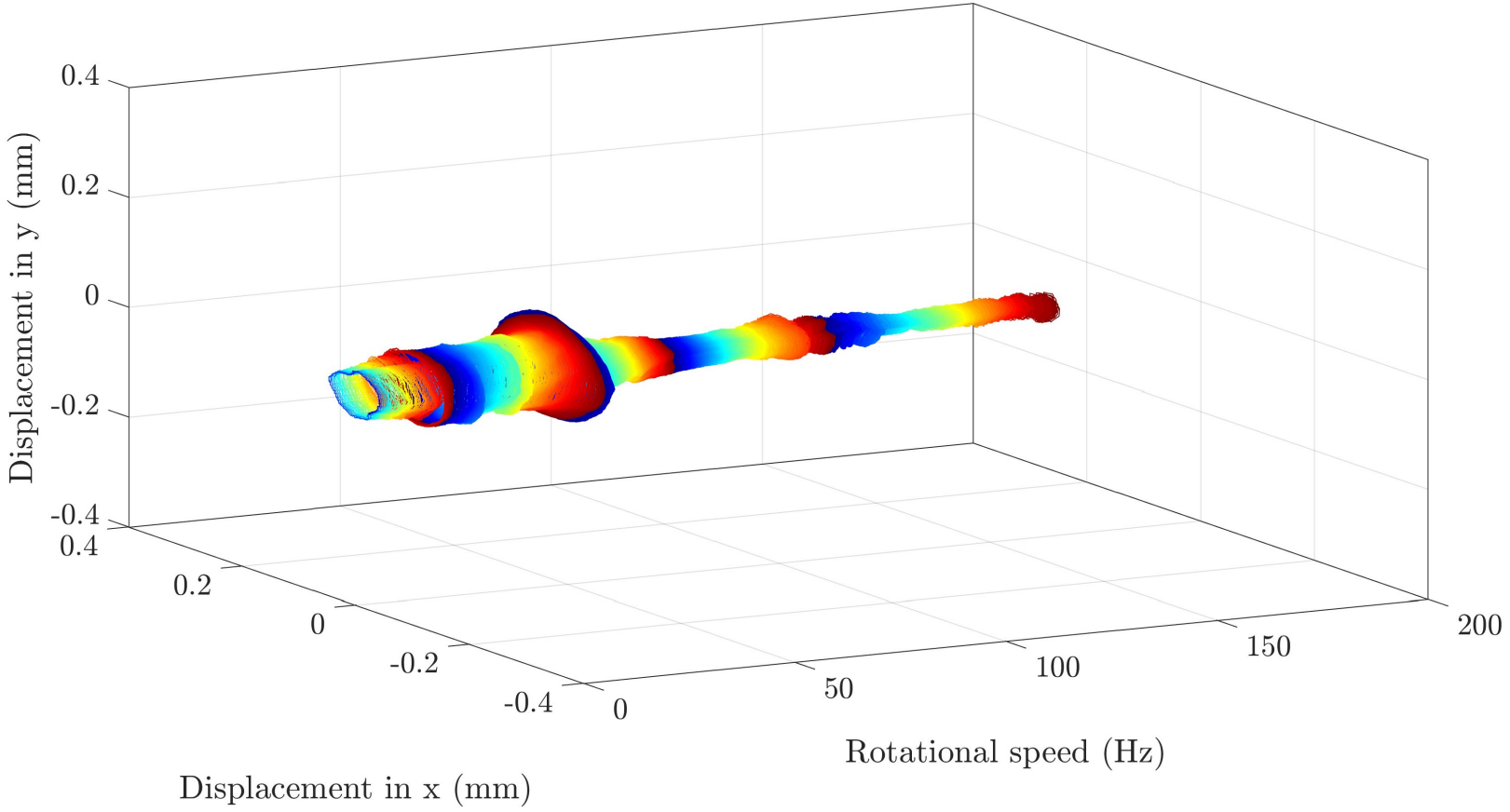

Figure 7.30: Rotor run-down with H_∞ control active, as observed by external sensors

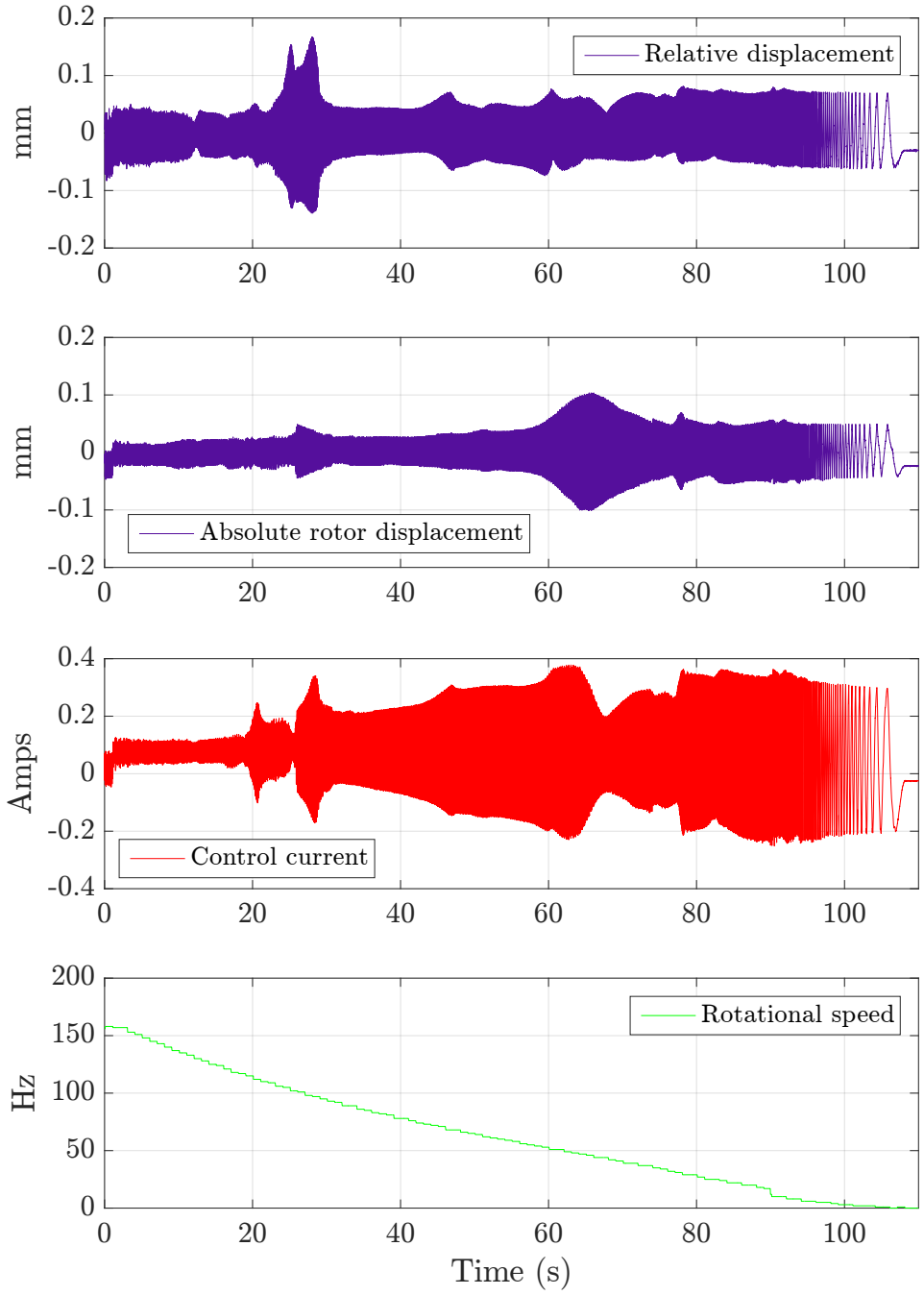

Figure 7.31: Detailed run-down data in axis x2 with rig under H_∞ control.

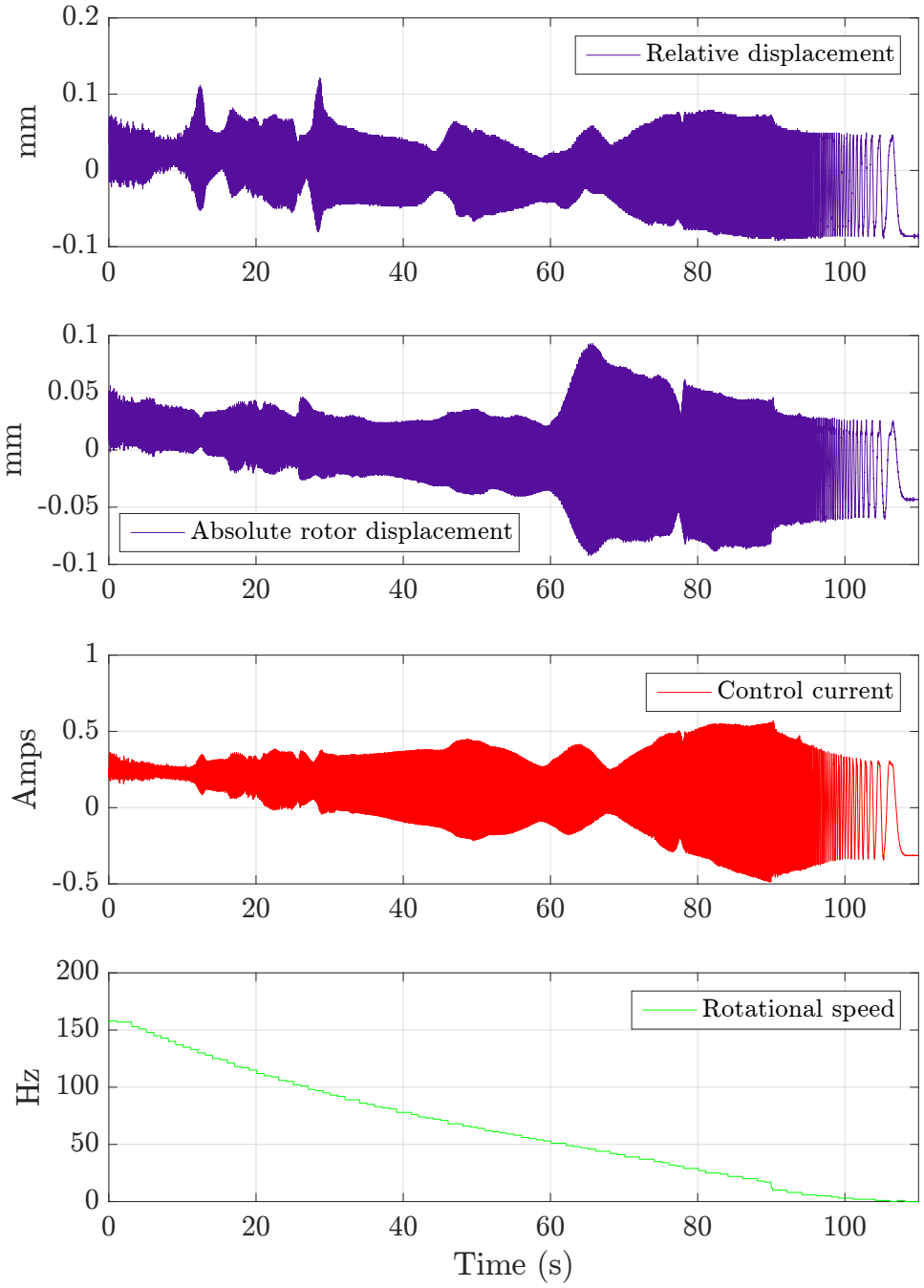

Figure 7.32: Detailed run-down data in axis y2 with rig under H_∞ control.

Chapter 8

Conclusions

8.1 Achievements and Key Results

This project has centred around a concept for a rotor system topology consisting of a hollow rotor which uses internal-stator, flexibly-mounted magnetic bearings for vibration reduction. The topic has been addressed mathematically via finite element modelling, which illustrated promising potential for the concept. This then progressed into a detailed test rig design, with both first and second generation test rigs constructed to enable useful assessment of the concept capabilities.

The completion of the successful, functional test rig was by no means trivial - the process was long and iterative. Each aspect of the design, manufacture, assembly and commissioning turned out to demand detailed attention, and frequently, numerous attempts. In the first place, it was discovered that basic choice of material is critical to success - for instance the use of a rolled, welded steel tube for parts of the rotor rendered it almost impossible to build a successful system owing to its non-uniform stiffness and high internal stresses. Only through the substitution of rotor sections fabricated from higher quality steel billets with isotropic and homogeneous properties was progress possible.

Furthermore, the importance of considering (and thereby minimising) unavoidable imperfections was found to be of critical importance to the design. For the first generation rotor design, while the design was *theoretically* sound, and could be assembled perfectly in a CAD model, in reality there were far too many parts with imperfectly located joints, leading to the introduction of many small imperfections/misalignments, which combined to make accurate assembly extremely arduous and inconsistent. Conversely, the second generation rotor design required only three main parts, which included in their design the facility to accurately and repeatedly join them together.

Another unanticipated - yet pivotally important - consideration was in relation to signal noise, especially that generated by digital amplifiers. For a considerable time, it was impossible to use any sensors in the lab while the amplifiers were active, owing to the noise interference swamping measurement signals. Only after various experiments with filters (physical and software), earthing points and cabling arrangements was it discovered that the best solution was to take each individual sensor signal in individual BNC cables directly from the conditioning units to the dSPACE processor.

Significant work was also required to achieve concentric alignment between the rotor and magnetic bearings, and indeed was a highly critical assembly considerations for successful operation. Lack of concentricity is a key contributor to instability of control action, as it results in unmodelled, non-linear bearing forces. The problem was addressed through a combination of precision machining of rotor and secondary shaft support stands, custom alignment tools and delicate in situ fine-tuning.

Particular consideration has been given to the design of the magnetic bearings for this application. Space limitations dictated a homopolar design (to avoid the need of a laminated collar on the rotor). In order to minimise eddy currents in the stator, SMC was investigated as a potential alternative to traditional laminations. Through the fabrication of sample heteropolar bearings with each material, it was demonstrated that SMC was capable of similar magnetic performance to laminations, and thus it was chosen as the material for the core, allowing a novel, compact bearing design to evolve.

On completion of the test rig, two different control strategies have been investigated - a "traditional" PD controller, and an H_∞ model based controller. It was found that the PD controller, while successful in subduing rotor vibration at low speeds, was not capable of permitting the rotor to pass its first critical speed. It is proposed that a stiffer PD controller may be able to achieve this, although stability issues were encountered trying to implement such a controller.

The design of the H_∞ was challenged by the desire to control rotor absolute motion, while only measuring a relative displacement between the rotor and the secondary shafts. Attempts made to use a controller based on a mixed sensitivity structure combined with a Luenberger observer suffered from stability issues. In response to this, a more elegant solution - taking full advantage of the model-based properties of the H_∞ controller - was conceived, removing the need for an observer entirely. After considerable tuning of the plant augmentation weightings in the new structure, a suitable, stable controller was achieved.

With the final H_∞ controller very successful results were obtained. Using its capability to express (and achieve) specific performance goals, the H_∞ controlled rig easily permitted the rotor to surpass its first critical speed with a minimum of vibration, and proceed all the way to a 150 Hz rotational speed - three times the first critical speed. It was also seen that the H_∞ controller achieved this performance while demanding materially smaller control currents than

the PD controller used, indicating far more efficient operation.

8.2 Proposed Continuation

There are two obvious paths that might provide interesting and useful extensions to the work presented here. The first would be physical changes to the system topology, and the second would be in the control algorithms behind the vibration reduction.

With regard to physical changes to the system, changes could include alterations to the number and axial location of the magnetic bearings. One particularly intriguing topic might be examining the feasibility of having axially mobile magnetic bearings, which has the potential to allow optimisation of the axial location dependent on the nature of the vibrations needing to be attenuated in a given circumstance. For instance, a different axial location may be desirable for passing a rotor second critical speed compared to the first. Alternatively, it is not difficult to image that a mass loss event at any of a number of locations (e.g. a blade loss from any of several turbine stages) may be best handled if the magnetic bearing(s) have the capacity to move.

A further logical extension to the work presented here would be to modify the system by removing the rolling element bearings, and use the magnetic bearings for a combination of both static support *and* vibration suppression. It is likely that - given the flexible nature of the system secondary shaft - it would be most effective to implement this via a model based controller, which should be capable of minimising transmission of excitation from the secondary shaft(s) to the rotor which may be unavoidable with, for instance, PID control.

On the control front, numerous investigations and extensions can be imagined. In the first place, the H_∞ controller presented in this report is by no means the only possible such controller, and it is possible that further performance improvements could be achieved with variations to the weightings / augmented plant structure.

Beyond this, the field of modern control techniques offers plenty of potential for adding extra features. For instance, the use of μ-synthesis controller design based on an uncertain plant and/or actuator model could be employed to build guaranteed robust performance into the system. There again, given the speed dependence of the system performance, linear parameter-varying (LPV) control techniques could be explored with a view to extending the range of usability of the control algorithm as higher speeds are reached.

One particularly interesting problem which could be explored is connected with previously-mentioned difficulty with achieving a perfectly concentric alignment between the independently-located rotor and magnetic bearings. This circumstance currently leads the magnetic bearings inevitably imparting a small force on the rotor, even when it is stationary or not significantly deflecting. In a recently presented paper, Caple et al. [79] have presented a technique for

eliminating such so-called “static force”, which would apply well to the test rig built in this project, potentially offering significant performance benefits.

In summary then, the topic of flexibly-mounted, internal-stator magnetic bearings for rotor vibration control has been introduced, and its viability conclusively demonstrated. From here, a multitude of possibilities for further research and development on the theme lie waiting to be explored, with numerous interesting and useful discoveries surely to be made.

References

[1] DJ Clark, MJ Jansen, and GT Montague. An overview of magnetic bearing technology for gas turbine engines. 2004.

[2] John M Vance, Daniel Ying, and Jorgen L Nikolajsen. Actively controlled bearing dampers for aircraft engine applications. *Journal of Engineering for Gas Turbines and Power*, 122(3):466–472, 2000.

[3] WA Rankine. On the centrifugal force of rotating shafts. *Engineer*, 27:249, 1869.

[4] G De Laval. Turbine for steam and other motive powers. US Patent Office - No. 285,584, September 1883.

[5] Stanley Dunkerley. On the whirling and vibration of shafts. *Philosophical Transactions of the Royal Society of London. A*, 185:279–360, 1894.

[6] A Föppl. Das problem der lavalschen turbinenwelle. *Der Civilingenieur*, 4:335, 1895.

[7] HH Jeffcott. Xxvii. the lateral vibration of loaded shafts in the neighbourhood of a whirling speed.—the effect of want of balance. *The London, Edinburgh, and Dublin Philosophical Magazine and Journal of Science*, 37(219):304–314, 1919.

[8] Maurice L Adams. *Rotating Machinery Vibration: From Analysis to Troubleshooting (Mechanical Engineering Series)*. CRC Press, 1 edition, 10 2000.

[9] Se Young Yoon, Zongli Lin, Chris Goyne, and Paul E Allaire. Control of compressor surge with active magnetic bearings. In *Decision and Control (CDC), 2010 49th IEEE Conference on*, pages 4323–4328. IEEE, 2010.

[10] JS Rao. *History of rotating machinery dynamics*. Springer, 2011.

[11] HD Nelson and JM McVaugh. The dynamics of rotor-bearing systems using finite elements. *ASME Journal of Engineering for Industry*, 98:593–600, 1976.

[12] HD Nelson. A finite rotating shaft element using timoshenko beam theory. *Journal of Mechanical Design*, 102:793, 1980.

[13] Agnieszka Muszynska. *Rotordynamics*. CRC press, 2010.

[14] Karl-Olof Olsson. Limits for the use of auto-balancing. *International Journal of Rotating Machinery*, 10(3):221–226, 2004.

[15] Marco Antonio Meraz, Andrés Yánez, Carlos Jiménez, and Raúl Pichardo. Self balancing system for rotating mechanisms. *Revista Facultad de Ingeniería-Universidad de Tarapacá*, 13(2):59–64, 2005.

[16] J Van De Vegte. Continuous automatic balancing of rotating systems. *IMechE Journal of Mechanical Engineering Science*, 6(3):264–269, 1964.

[17] J Van de Vegte and RT Lake. Balancing of rotating systems during operation. *Journal of Sound and Vibration*, 57(2):225–235, 1978.

[18] J Van De Vegte. Balancing of flexible rotors during operation. *IMechE, Part C, Journal of Mechanical Engineering Science*, 23(5):257–261, 1981.

[19] RED Bishop. On the possibility of balancing rotating flexible shafts. *IMechE, Part C, Journal of Mechanical Engineering Science*, 24(4):215–220, 1982.

[20] Z Gosiewski. Automatic balancing of flexible rotors, part i: Theoretical background. *Journal of Sound and Vibration*, 100(4):551–567, 1985.

[21] Z Gosiewski. Automatic balancing of flexible rotors, part ii: Synthesis of system. *Journal of Sound and Vibration*, 114(1):103–119, 1987.

[22] SW Dyer and J Ni. Adaptive influence coefficient control of single-plane active balancing systems for rotating machinery. *ASME Journal of Manufacturing Science and Engineering*, 123(2):291–298, 2001.

[23] S Zhou and J Shi. Active balancing and vibration control of rotating machinery: a survey. *Shock and Vibration Digest*, 33(4):361–371, 2001.

[24] IF Santos. Trends in controllable oil film bearings. In *IUTAM Symposium on Emerging Trends in Rotor Dynamics*, pages 185–199. Springer Netherlands, 2011.

[25] J Qiu, J Tani, and T Kwon. Control of self-excited vibration of a rotor system with active gas bearings. *ASME Journal of Vibration and Acoustics*, 125(3):328–334, 2003.

[26] AB Palazzolo, S Jagannathan, AF Kascak, GT Montague, and LJ Kiraly. Hybrid active vibration control of rotorbearing systems using piezoelectric actuators. *ASME Journal of Vibration Acoustics*, 115:111–119, 1993.

[27] AB Ortega, FB Carbajal, G Silva, and Marco AOS Navarro. Active vibration control of a rotor-bearing system based on dynamic stiffness (control activo de vibraciones en un sistema rotor-chumaceras basado en la rigidez dinámica). *Revista Facultad de Ingeniería Universidad de Antioquia*, 55:125–133, 2010.

[28] Nesbitt W Hagood, Walter H Chung, and Andreas Von Flotow. Modelling of piezoelectric actuator dynamics for active structural control. *Journal of Intelligent Material Systems and Structures*, 1(3):327–354, 1990.

[29] HG Horst and HP Wölfel. Active vibration control of a high speed rotor using pzt patches on the shaft surface. *Journal of Intelligent Material Systems and Structures*, 15(9-10):721–728, 2004.

[30] Yanhong Ma, Qicheng Zhang, Dayi Zhang, Fabrizio Scarpa, Baolong Liu, and Jie Hong. Tuning the vibration of a rotor with shape memory alloy metal rubber supports. *Journal of Sound and Vibration*, 351:1 – 16, 2015.

[31] Søren Enemark, Ilmar Santos, and Marcelo A Savi. Shape memory alloys applied to improve rotor-bearing system dynamics-an experimental investigation. In *XVII International Symposium on Dynamic Problems of Mechanics*, 2015.

[32] JL Nikolajsen, R Holmes, and V Gondhalekar. Investigation of an electromagnetic damper for vibration control of a transmission shaft. *Proceedings of the Institution of Mechanical Engineers*, 193(1):331–336, 1979.

[33] MEF Kasarda, PE Allaire, RR Humphris, and LE Barrett. A magnetic damper for first-mode vibration reduction in multimass flexible rotors. *ASME Journal of Engineering for Gas Turbines and Power*, 112(4):463–469, 1990.

[34] CR Burrows, MN Sahinkaya, and S Clements. Active vibration control of flexible rotors: an experimental and theoretical study. *Proceedings of the Royal Society of London. A. Mathematical and Physical Sciences*, 422(1862):123–146, 1989.

[35] G Schweitzer and R Lange. Characteristics of a magnetic rotor bearing for active vibration control. In *Institution of Mechanical Engineers Conference on Vibrations in Rotating Machinery, Cambridge*, number C239/76, pages 301–306, 1976.

[36] H Bleuler and G Schweitzer. Dynamics of a magnetically suspended rotor with decentralized control. In *IASTED Applied Dynamics and Control Symposium, Copenhagen*, 1983.

[37] D Vischer and H Bleuler. Self-sensing active magnetic levitation. *Magnetics, IEEE Transactions on*, 29(2):1276–1281, 1993.

[38] MD Noh and EH Maslen. Self-sensing magnetic bearings using parameter estimation. *Instrumentation and Measurement, IEEE Transactions on*, 46(1):45–50, 1997.

[39] PS Keogh, MOT Cole, MN Sahinkaya, and CR Burrows. On the control of synchronous vibration in rotor/magnetic bearing systems involving auxiliary bearing contact. *Journal of Engineering for Gas Turbines and Power: Transactions of the ASME*, 126(2):366–372, June 2004. ID number: ISI:000222192700022.

[40] PS Keogh and MOT Cole. Rotor vibration with auxiliary bearing contact in magnetic bearing systems part 1: Synchronous dynamics. *Proceedings of the Institution of Mechanical Engineers, Part C: Journal of Mechanical Engineering Science*, 217(4):377–392, 2003.

[41] MOT Cole and PS Keogh. Rotor vibration with auxiliary bearing contact in magnetic bearing systems part 2: robust synchronous control for rotor position recovery. *Proceedings of the Institution of Mechanical Engineers, Part C: Journal of Mechanical Engineering Science*, 217(4):393–409, 2003.

[42] M Komori, S Matsuoka, and S Fukata. Evaluations of a hybrid-type superconducting magnetic bearing system. *Applied Superconductivity, IEEE Transactions on*, 6(4):178–182, 1996.

[43] M Komori, M Kumamoto, and H Kobayashi. A hybrid-type superconducting magnetic bearing system with nonlinear control. *Applied Superconductivity, IEEE Transactions on*, 8(2):79–83, 1998.

[44] M Komori and C Shiraishi. A levitated motor with superconducting magnetic bearings assisted by self-sensing ambs. *Applied Superconductivity, IEEE Transactions on*, 13(2):2189–2192, 2003.

[45] CD Bradfield, JB Roberts, and R Karunendiran. Performance of an electromagnetic bearing for the vibration control of a supercritical shaft. *Proceedings of the Institution of Mechanical Engineers, Part C: Journal of Mechanical Engineering Science*, 201(3):201–212, 1987.

[46] CR Burrows and MN Sahinkaya. Vibration control of multi-mode rotor-bearing systems. *Proceedings of the Royal Society of London. A. Mathematical and Physical Sciences*, 386(1790):77–94, 1983.

[47] Carl R Knospe, R Winston Hope, Stephen J Fedigan, and Ronald D Williams. Experiments in the control of unbalance response using magnetic bearings. *Mechatronics*, 5(4):385–400, 1995.

[48] Carl R Knospe and Samir M Tamer. Experiments in robust control of rotor unbalance response using magnetic bearings. *Mechatronics*, 7(3):217–229, 1997.

[49] AG Abulrub, MN Sahinkaya, PS Keogh, and CR Burrows. Contact dynamics and recursive open loop adaptive control to recover rotor position. In *Proceedings of the Tenth International Symposium on Magnetic Bearings (ISMB10)*, 2006.

[50] Hooshang Heshmat, H Ming Chen, and James F Walton. On the performance of hybrid foil-magnetic bearings. In *ASME 1998 International Gas Turbine and Aeroengine Congress and Exhibition*, pages V005T14A027–V005T14A027. American Society of Mechanical Engineers, 1998.

[51] Sena Jeong and Yong Bok Lee. Vibration control of high-speed rotor supported by hybrid foil-magnetic bearing with sudden imbalance. *Journal of Vibration and Control*, 2015.

[52] Minh Nha Pham and Hyeong-Joon Ahn. Experimental optimization of a hybrid foil–magnetic bearing to support a flexible rotor. *Mechanical Systems and Signal Processing*, 46(2):361–372, 2014.

[53] Sena Jeong, Bok Seong Choe, and Yong Bok Lee. Rotordynamic behavior and performance of controllable hybrid foil-magnetic bearing. In *Proceedings of the 9th IFToMM International Conference on Rotor Dynamics*, pages 1465–1476. Springer, 2015.

[54] Jarir Mahfoud and Johan Der Hagopian. Investigations on the critical speed suppressing by using electromagnetic actuators. *smarts structures and systems*, 9(4):303–311, 2012.

[55] Eric Maslen, Gerhard Schweitzer, Hannes Bleuler, Matthew Cole, Patrick Keogh, Rene Larsonneur, Rainer Nordmann, Yohji Okada, and Alfons Traxler. *Magnetic bearings: theory, design, and application to rotating machinery*. Springer-Verlag Berlin Heidelberg, 2009.

[56] G Schweitzer. Applications and research topics for active magnetic bearings. In *IUTAM Symposium on Emerging Trends in Rotor Dynamics*, pages 263–273. Springer Netherlands, 2011.

[57] Erwin Krämer. *Dynamics of rotors and foundations*. Springer Berlin Heidelberg, 1993.

[58] Leonard Meirovitch. *Fundamentals of Vibrations*. McGraw-Hill Higher Education, 10 2000.

[59] MEF Kasarda, PE Allaire, C Mastrangelo, EH Maslen, and PM Norris. Experimentally determined rotor power losses in homopolar and heteropolar magnetic bearings. *ASME Journal of Engineering for Gas Turbines and Power*, 121(4):697–702, 1999.

[60] H Shokrollahi and K Janghorban. Soft magnetic composite materials (smcs). *Journal of Materials Processing Technology*, 189(1):1–12, 2007.

[61] E Fleischer and W Hofmann. Application of soft magnetic composites in active magnetic bearings. In *IECON 2011-37th Annual Conference on IEEE Industrial Electronics Society*, pages 1770–1775. IEEE, 2011.

[62] E Fleischer and W Hofmann. Linear and nonlinear control of a three pole combined radial and axial active magnetic bearing-a comparison. *Mechanical Engineering Journal (advance publication)*, DOI:10.1299/mej.15-00145, 2015.

[63] D Howe, P Mason, PH Mellor, ZY Wu, and K Atallah. Flywheel peak power buffer for electric/hybrid vehicles. In *Electric Machines and Drives, 1999. International Conference IEMD'99*, pages 508–510. IEEE, 1999.

[64] Torsten Söderström and Petre Stoica. *System identification*. Prentice-Hall, Inc., 1988.

[65] Lennart Ljung. *System identification - Theory for the user*. Springer, 1998.

[66] C Gähler, Manuel Mohler, and Raoul Herzog. Multivariable identification of active magnetic bearing systems. In *IUTAM Symposium on Interaction between Dynamics and Control in Advanced Mechanical Systems*, pages 127–134. Springer, 1997.

[67] José A Vázquez, Eric H Maslen, Hyeong-Joon Ahn, and Dong-Chul Han. Model identification of a rotor with magnetic bearings. In *ASME Turbo Expo 2001: Power for Land, Sea, and Air*, pages V004T03A059–V004T03A059. American Society of Mechanical Engineers, 2001.

[68] Manfred Schroeder. Synthesis of low-peak-factor signals and binary sequences with low autocorrelation (corresp.). *Information Theory, IEEE transactions on*, 16(1):85–89, 1970.

[69] Mehmet N Sahinkaya, Matthew OT Cole, and Clifford R Burrows. On the use of schroeder phased harmonic sequences for the multi-frequency vibration control of flexible rotor/-magnetic bearing systems. In *The Eight International Symposium on Magnetic Bearings ISMB-8, Mito, Japan*, pages 217–222. Citeseer, 2002.

[70] Jonas S Lauridsen, André K Sekunda, Ilmar F Santos, and Henrik Niemann. Identifying parameters in active magnetic bearing system using lft formulation and youla factorization. In *2015 IEEE Conference on Control Applications (CCA)*, pages 430–435. IEEE, 2015.

[71] Henrik Niemann, Jakob Stoustrup, and Niels Kjølstad Poulsen. Controller modification applied for active fault detection. In *2014 American Control Conference*, pages 1963–1968. IEEE, 2014.

[72] Henrik Niemann and Niels Kjølstad Poulsen. Estimation of parametric fault in closed-loop systems. In *2015 American Control Conference (ACC)*, pages 201–206. IEEE, 2015.

[73] Greg Wolodkin, Sundeep Rangan, and Kameshwar Poolla. An lft approach to parameter estimation. In *American Control Conference, 1997. Proceedings of the 1997*, volume 3, pages 2088–2092. IEEE, 1997.

[74] George Zames. Feedback and optimal sensitivity: Model reference transformations, multiplicative seminorms, and approximate inverses. *IEEE Transactions on Automatic Control*, 26(2):301–320, 1981.

[75] J William Helton. Orbit structure of the möbius transformation semigroup acting on h(broadband matching). *Topics in Functional Analysis*, 3:129–133, 1978.

[76] Allen Tannenbaum. Feedback stabilization of linear dynamical plants with uncertainty in the gain factor. *International Journal of Control*, 32(1):1–16, 1980.

[77] DE Bently. Forced sub-rotative speed dynamic action of rotating machinery. In *MECHANICAL ENGINEERING*, volume 96, pages 60–60. ASME-AMER Soc Mechanical Eng 345 E 47th St, New York, NY 10017, 1974.

[78] Dara W Childs. Fractional-frequency rotor motion due to nonsymmetric clearance effects. *Journal of Engineering for Power*, 104(3):533–541, 1982.

[79] M Caple, E Maslen, J Nagel, and J Wild. Control of an amb to zero static force. In *Proceedings of 15th International Symposium on Magnetic Bearings*, 2016.

Appendices

Appendix A

Finite Element Matrices

This appendix presents the mass, stiffness and gyroscopic matrices used in all rotor finite element modelling in this project.

Elements are modelled according to the equation:

$$\mathbf{m}\ddot{\mathbf{q}} - \Omega\mathbf{g}\dot{\mathbf{q}} + \mathbf{k}\mathbf{q} = \mathbf{f} \tag{A.1}$$

Where the degrees of freedom of q are arranged thus:

$$\mathbf{q} = [x_1, y_1, \theta_1, \phi_1, x_2, y_2, \theta_2, \phi_2]^T \tag{A.2}$$

where

$$\mathbf{m} = \frac{\mu l}{420}\begin{bmatrix} 156 & 0 & 0 & 22l & 54 & 0 & 0 & -13l \\ 0 & 156 & -22l & 0 & 0 & 54 & 13l & 0 \\ 0 & -22l & 4l^2 & 0 & 0 & -13l & -3l^2 & 0 \\ 22l & 0 & 0 & 4l^2 & 13l & 0 & 0 & -3l^2 \\ 54 & 0 & 0 & 13l & 156 & 0 & 0 & -22l \\ 0 & 54 & -13l & 0 & 0 & 156 & 22l & 0 \\ 0 & 13l & -3l^2 & 0 & 0 & 22l & 4l^2 & 0 \\ -13l & 0 & 0 & -3l^2 & -22l & 0 & 0 & 4l^2 \end{bmatrix} \tag{A.3}$$

$$\mathbf{k} = \frac{EI}{l^3}\begin{bmatrix} 12 & 0 & 0 & 6l & -12 & 0 & 0 & 6l \\ 0 & 12 & -6l & 0 & 0 & -12 & -6l & 0 \\ 0 & -6l & 4l^2 & 0 & 0 & 6l & 2l^2 & 0 \\ 6l & 0 & 0 & 4l^2 & -6l & 0 & 0 & 2l^2 \\ -12 & 0 & 0 & -6l & 12 & 0 & 0 & -6l \\ 0 & -12 & 6l & 0 & 0 & 12 & 6l & 0 \\ 0 & -6l & 2l^2 & 0 & 0 & 6l & 4l^2 & 0 \\ 6l & 0 & 0 & 2l^2 & -6l & 0 & 0 & 4l^2 \end{bmatrix} \tag{A.4}$$

$$\mathbf{g} = \frac{\mu(d_1^2 + d_2^2)}{240l}\begin{bmatrix} 0 & -36 & 3l & 0 & 0 & 36 & 3l & 0 \\ 36 & 0 & 0 & 3l & -36 & 0 & 0 & 3l \\ -3l & 0 & 0 & -4l^2 & 3l & 0 & 0 & l^2 \\ 0 & -3l & 4l^2 & 0 & 0 & 3l & -l^2 & 0 \\ 0 & 36 & -3l & 0 & 0 & -36 & -3l & 0 \\ -36 & 0 & 0 & -3l & 36 & 0 & 0 & -3l \\ -3l & 0 & 0 & l^2 & 3l & 0 & 0 & -4l^2 \\ 0 & -3l & -l^2 & 0 & 0 & 3l & 4l^2 & 0 \end{bmatrix} \tag{A.5}$$

Here the element has length l m, a mass per unit length μ kg/m, Young's Modulus of E Pa, second moment of area I m^4, inside diameter d_1 m (zero permitted for solid element) and outside diameter d_2.

Appendix B

Test Rig Technical Drawings

This appendix includes dimensioned technical drawings for the main components of the final version of the test rig. Note that these drawings are not to scale.

B.1 Magnetic Bearing Core

Material: Hoganas Prototyping SMC

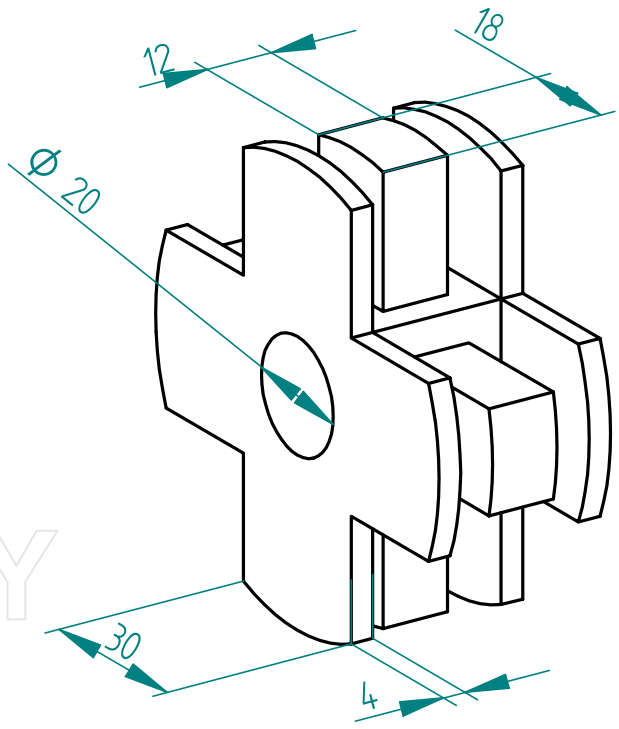

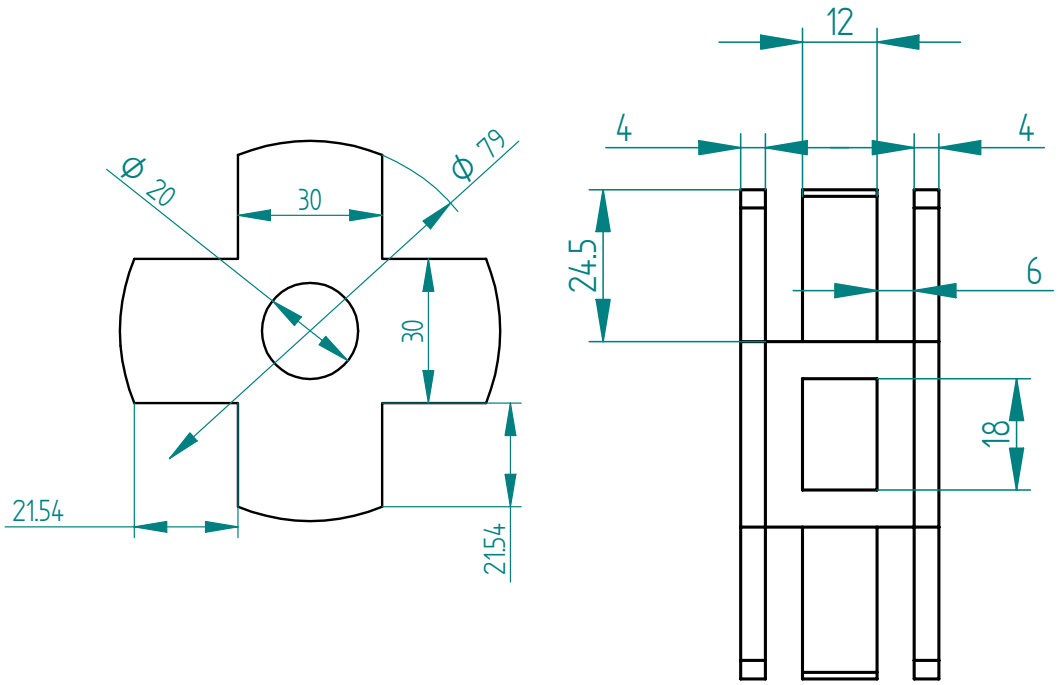

B.2 Rotor

Material: EN 32B steel

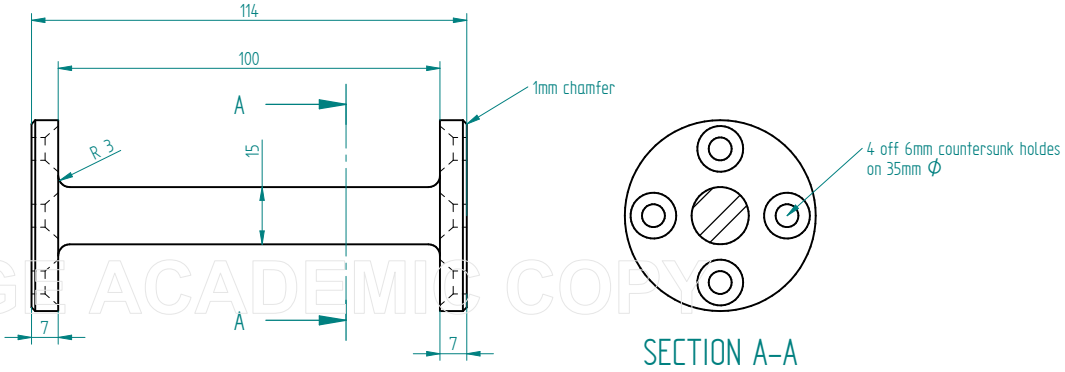

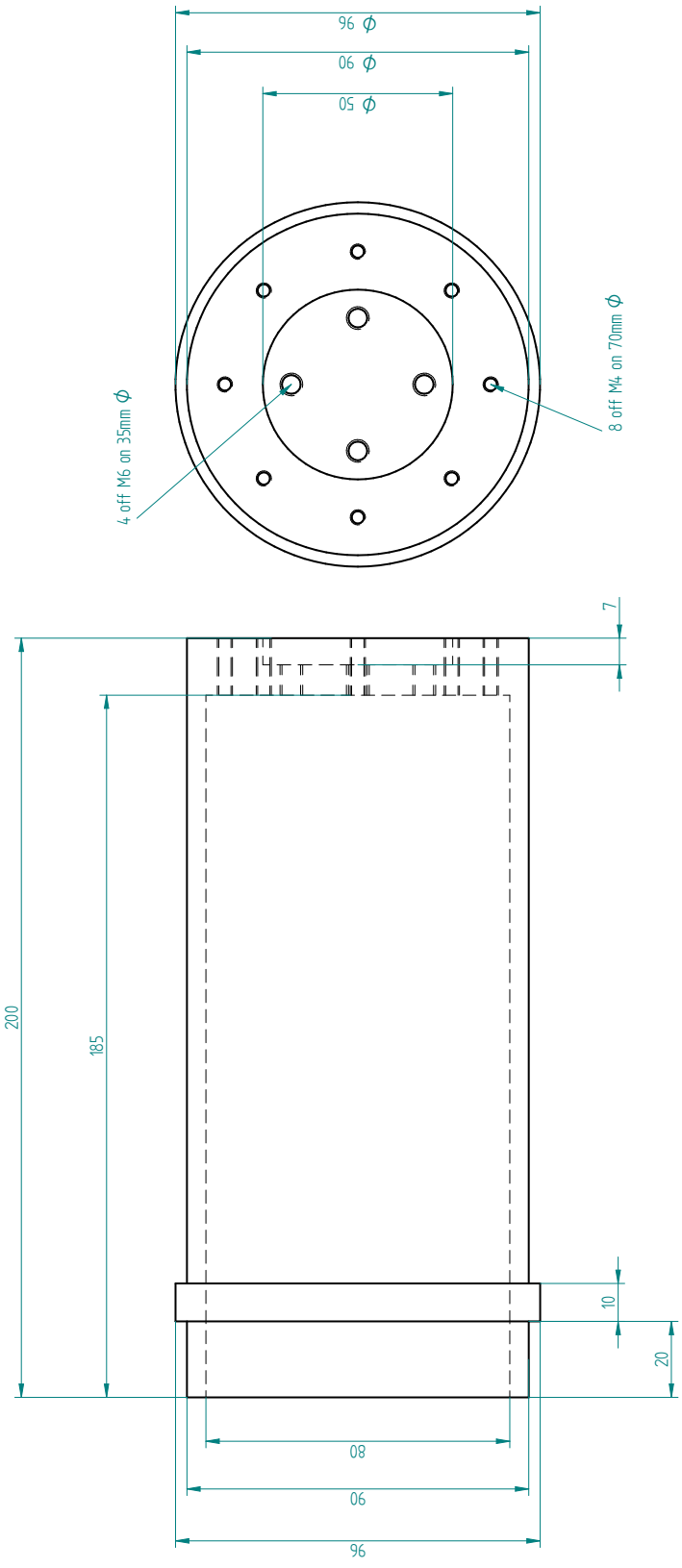
96 ϕ
90 ϕ
50 ϕ
4 off M6 on 35mm ϕ
8 off M4 on 70mm ϕ
7
200
185
10
20
80
90
96

B.3 Drive Turbine

Material: 6061 aluminium

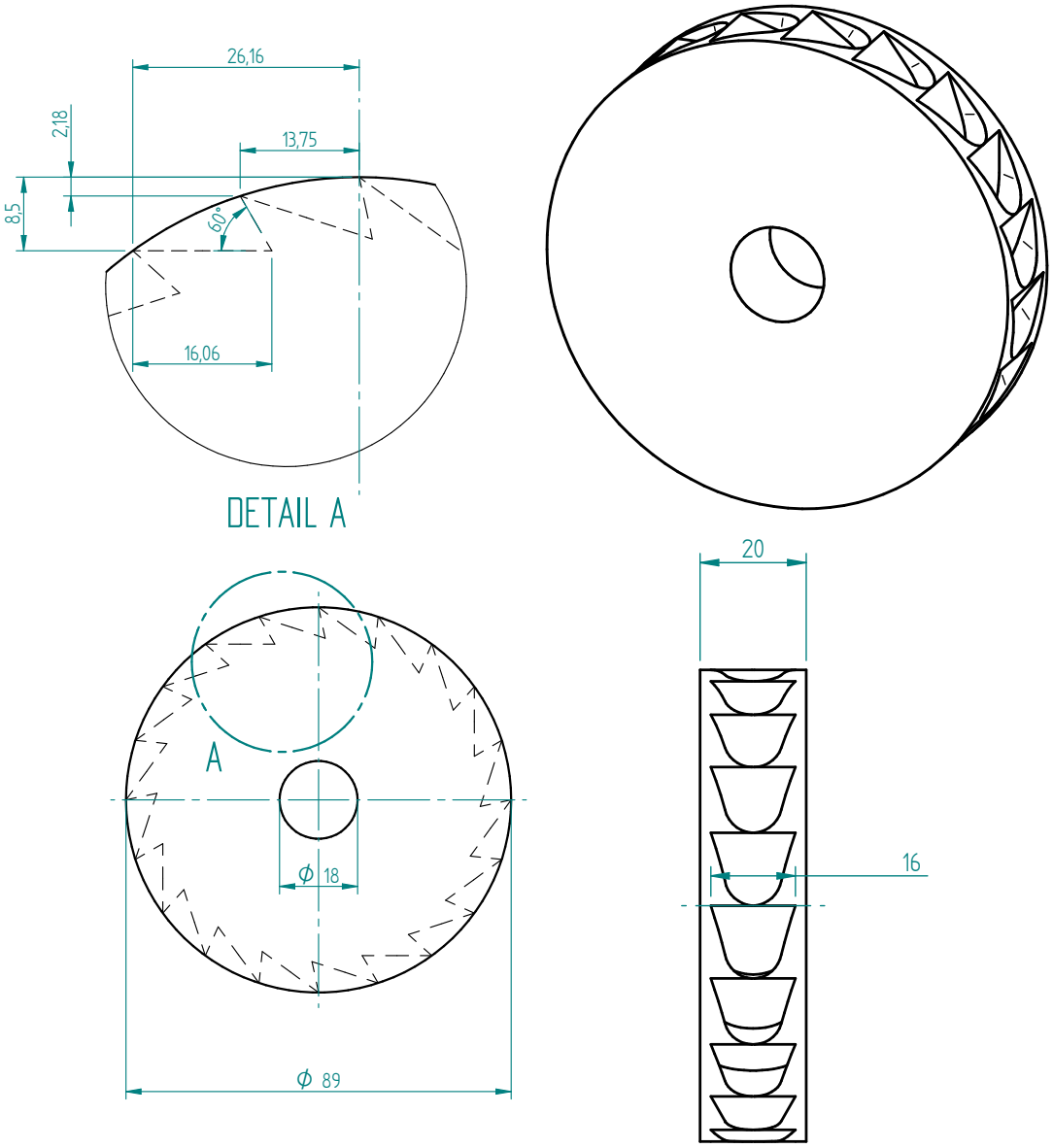

B.4 Secondary Shaft

Material: EN 24T steel

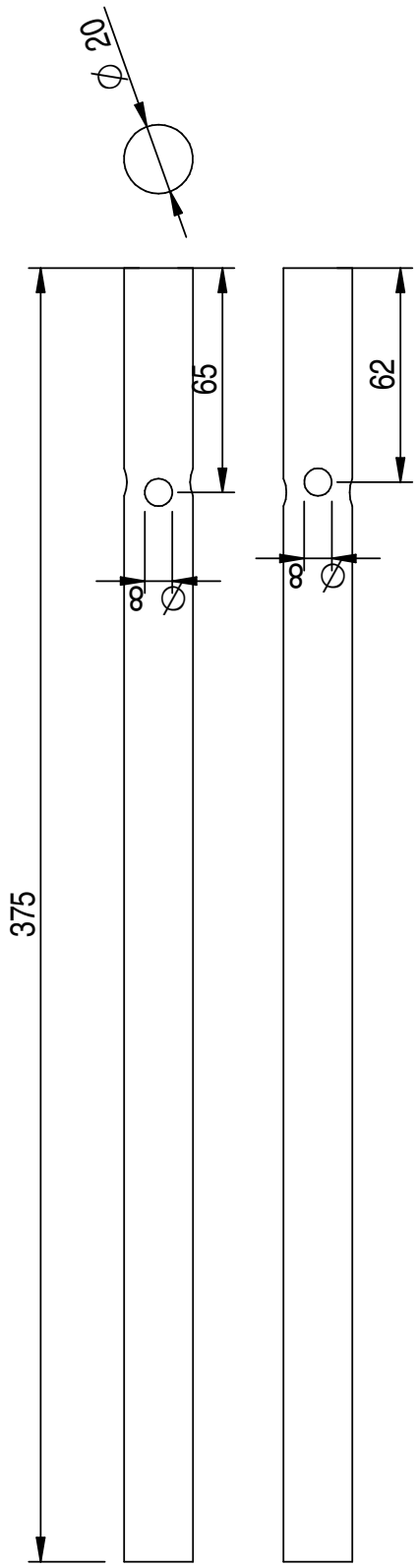
ϕ 20
65
62
375
8
∅
8
∅

B.5 Sensor Bracket

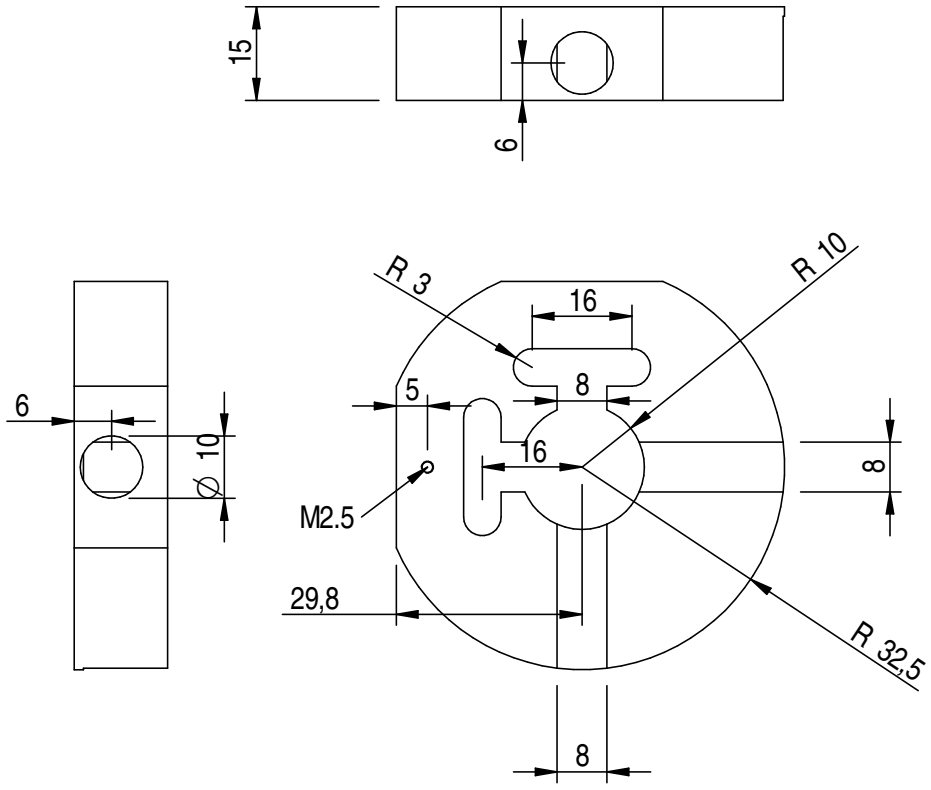

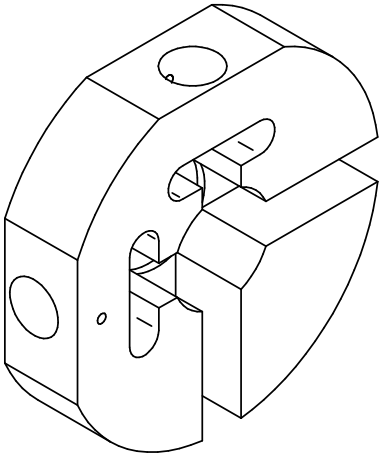

B.6 Touchdown Disk